DURBAN UNIVERSITY OF TECHNOLOGY

PROCESSING AND CHARACTERIZATION OF NANOCLAYS REINFORCED METAL (ALUMINIUM) MATRIX COMPOSITES

MWANGI, FESTUS MAINA

PROCESSING AND CHARACTERIZATION OF NANOCLAYS REINFORCED METAL (ALUMINIUM) MATRIX COMPOSITES

A THESIS SUBMITTED TO THE

DURBAN UNIVERSITY OF TECHNOLOGY

FOR THE DOCTOR OF ENGINEERING DEGREE

(IN MECHANICAL ENGINEERING)

BY

MWANGI, FESTUS MAINA

DEPARTMENT OF MECHANICAL ENGINEERING

FACULTY OF ENGINEERING AND THE BUILT ENVIRONMENT

DURBAN 4000, SOUTH AFRICA

2018

FINAL APPROVED SUBMISSION

_____ _____

Supervisor (Prof. K. Kanny) Date

_____ _____

Co-Supervisor (Dr. CN. Machio) Date

ABSTRACT

Aluminium is currently one of the most versatile and preferred engineering material of our times. It is the world's most abundant metal and is the third most common element on earth. The worldwide demand for aluminium has been growing steadily at an average rate of 5-7% annually. In fact, the demand has more than doubled up in the last decade. Despite the marked growth for aluminium, its alloys and composites, there is still a dire need to redesign this material's system if it is to enjoy progressive and diverse economic feasibility and acceptability in various industrial sectors.

This study opens up a new line of thought in the challenge of repositioning the material from an economic, industrial, and environmental perspective. It explores the efficacy of integrating a low-cost nanophased reinforcement system in the form of nanoclays into aluminium and/or its alloys. In the study, an experimental approach was adopted. The study called for an understanding of the intrinsic nature of both the aluminium and/or its alloys on one hand and nannoclays on the other. Based on that understanding, potential processing technologies were identified, with powder metallurgy eventually emerging as the most preferred processing route.

For the current study, AMB-2712 Al alloy was used as the matrix. Two nanoclays at 1% – 12.5%wt content were experimented with as the reinforcement system, i.e. *Nanofil 116* and *Cloisite Ca++DEV*. A conventional press and sinter approach was used to process the composites. Variables under investigation included the effects of green compaction pressure, sintering temperature profile, sintering atmosphere, and the percentage weight content of nanoclay. Besides physical inspection, hardness and tensile testing were used in comparatively evaluating the composites' structural integrity. Thermal behaviour was assessed using DSC-TGA. Additionally, thermal conductivity, thermal diffusivity, specific heat capacity, and thermal expansion were examined with thermal-management-applications in mind.

Results from the study show that nanoclays can feasibly be integrated into aluminium and/or its family of alloys and composites. Under the processing parameters used in this study, best results were obtained with 1%wt nanoclay addition. For better appreciation, both the load bearing capacity of the reference alloy and its percentage elongation to fracture were increased by more than 150%. Melting temperature was increased by 6.6%. It was also observed that the thermal conductivity, diffusivity, and specific heat capacity were not only significantly improved, but also more stable. While the results for reference sample were deteriorating after 220^0C, the composites were observed to be stable at 300^0C and still showing signs of potential to progress further. At 3%wt, content, the nanoclays were observed to demonstrate thermal barrier properties. Microstructural analysis portrayed the nanoclays as heat-sinks, thereby ideal for use in thermal management systems in areas such as the automotive engine components. Effects of nanoclays as revealed by microstructural analysis further demonstrated that the successful use of nanoclays as a reinforcement system for aluminium and/or its alloys presents a novel technique of preparing conventional aluminium alloys in a more economical way.

DECLARATION

This thesis is being submitted to the Durban University of Technology for the award of the degree of Doctor of Engineering (Mechanical Engineering). I declare that the thesis entitled **"PROCESSING AND CHARACTERIZATION OF NANOCLAYS REINFORCED METAL (ALUMINIUM) MATRIX COMPOSITES"** is a record of research work carried out by myself. The content of this thesis, in full or in parts, have not been submitted to any other Institute or University for the award of any degree or diploma. I further declare that the only part of this work that has been published is in the form of a conference papers with details as given below:

CONFERENCE PAPER

FM Mwangi, K. Kanny. Nanoclay-reinforced 2712 Al-Cu Alloy: Thermal Properties. Paper presented in 2nd International Conference on Composites, Biocomposites and Nanocomposites (ICCBN 2015). 28-30th October, 2015, Durban, South Africa.

_____ _____

Signature of Student Date

_____ _____

Signature of Supervisor Date

_____ _____

Signature of Co-Supervisor Date

To my beloved family
A Great Blessing in my life.

Acknowledgements

It is by the grace of the Almighty Living God that I have completed this study. Without His divine guidance, blessings, and hope, all my efforts would not have been as fruitful as they have. He laid up for me a couple of invaluably great, learned, and selfless people along the different stages of the research project and their contributory support has been incredibly awesome. I am and will forever be grateful to Him for nurturing me as His own child. All glory and honour belongs to Him.

Amongst the people that God put into my life in order to make the journey of this research project bearable is Prof. K. Kanny. He has been my supervisor and mentor. I would like to specially thank him for his selfless all-round support, guidance, constructive criticism, inspiration and motivation throughout the research programme. More than anything, I especially thank him for believing in me. I shall forever be indebted to him for bearing the load of making sure that I got access to any necessary piece of equipment required for the study and also ensuring availability of funds to facilitate any needful travel. I am also very grateful for my co-supervisor, Dr. TP Mohan who, in many ways, has always been readily available to support me from all possible perspectives. His brainstorming sessions and motivational support are hereby most appreciated.

I would like to specially thank Dr. Christopher Machio from the Council for Scientific and Industrial Research (CSIR) for his immeasurable support. While conducting my experiments at CSIR, he relentlessly saw to it that I got access to whatsoever piece of equipment that was necessary for my experiments, trained me in the use of such equipment, made any necessary bookings, and allocated me support staff to work with as and whenever the need arose. His constructive criticism, redirection and sharing of knowledge has been a beacon of strength. I have learnt a lot from him from a personal and academic perspectives. For his warm

brotherhood as engraved in his going out of his way towards making sure that I not only succeed but also excel in the research project, I shall forever remain grateful to him.

At the early stages of the study, I needed critical assistance with equipment that was at the time available in MINTEK. In that line, I am extremely grateful for the access and technical support accorded to me by Dr. Papo Jones, and Dr. Alain Mwamba with respect to measurement of apparent density and mechanical mixing of my powdered raw materials. Same goes to Mr. Erwin Royeppen from the metrology laboratory at TOYOTA (SA) for providing me with the much needed access and technical support with respect to their Tally-Surf piece of equipment. Similarly, I'd also like to acknowledge the role played Mr. Pradeep Suthan from the University of KwaZulu Natal (uKZN) with respect to their provision of specialist TEM and XRD services. On the same note, I hereby acknowledge Mr. Bruce Berger from CERMALAB for his specialty services with respect to experiments relating to thermal properties of my specimens.

My experience at DUT would have been incomplete without the exciting and rewarding interactions with fellow students and support staff comprising the Composites Research Group (CRG) based in the Mechanical Engineering Department. Their helpful discussions and moments shared with them in and off-campus during research workshops have been very fruitful in redirecting and pacing my study. On that note I'd like to thank Dr. Shalini Singh and Dr. Anisa Vahed for their supervisory role of the group, as well as my postgraduate colleagues including, but not limited to, Dr. Vimla Paul, Mr. Avinash Ramsaroop, Mr. Ken Okeke, Mr. Stanley Onwubu, Mr. John Olusanya, Mr. Joseph Oluwatoyin Gbadeyan, Ms. Sathie Chetty, Mr. Sifiso Nkosi, Mr. Mufaro Moyo, Mr. Rane Ajay, and Mrs. Maleni Thakur. The direct and indirect role of the post-doctoral research fellows (Dr. Mithilkumar Tammineni, Dr. Dani Jagadeesh, and Dr. Vimla) is also hereby acknowledged and most appreciated.

I am also grateful for the enormous support that I have received from DUT support staff members and their respective departments. I would like to specially thank Mr. Bruce Robert Graham and Mr. Graham Arthur Thurbon in their term-capacity as head of department of the mechanical engineering department during my study period. Their support in diverse ways and means including study leave and financial support through the TDG fund has been very helpful and invaluable. On the same note, I have been a recipient of DUT's financial support through the Higher Degrees Committee (HDC) and remission of tuition fees. Without all these channels of institutional support, I highly doubt if I would have successfully completed the programme.

Lastly and not the least, I am highly blessed and favoured to have been surrounded with every possible form of support from my big family – I hereby express my utmost gratitude to my dear loving wife, Philile, and my children; Sandiso, Emma, Henry, and Milani. They have been a great source of unconditional love, encouragement, motivation, inspiration, and understanding especially during difficult moments of our life together. Much gratitude also goes to my loving mom for having cultured in me a sense of pride in education despite never having been to school herself. Special thanks also go to my mother-in-law for her reliable presence at the centre of my family life. As for my big brothers, sister, nieces and nephews, they have indirectly been part of my academic journey since I was a child and it is with thanksgiving and humbling joy that I acknowledge their diverse roles, sacrifices, and selfless support towards my receiving of an education.

- May the Almighty Living God Superfluously Bless You All -

TABLE OF CONTENTS

LIST OF FIGURES

LIST OF TABLES

LIST OF ABBREVIATIONS

ABREVIATION	PARTICULARS
AMCs	Aluminium Metal-matrix Composites
MMCS	Metal Matrix Composites
DRA	Discontinuously Reinforced Aluminium
EU	European Union
NEDC	New European Driving Cycle
MPA	Megapascals
GPA	Gigapascals
ppm/°C	Parts Per Million per degree Centigrade
BCC	Body Centred Cubic
FCC	Face Centred Cubic
TBCs	Thermal Barrier Coatings
SPS	Spark Plasma Sintering
P/M	Powder Metallurgy
BUE	Built-Up-Edge
UK	United Kingdom
USA	United States of America
MSDS	Materials Safety Data Sheets
PTFE	Polytetrafluoroethylene
PE	Polyethylene
EBS	Ethylene Bisstearamide
MPIF	Metal Powder Industries Federation
DSC	Differential Scanning Calorimetry

TGA	Thermogravimetric Analysis
FTIR	Fourier Transform Infrared Spectroscopy
TEM	Transmission Electron Microscope
ESEM	Environmental Scanning Electron Microscope
EDX / EDS	Energy Dispersive X-Ray Spectroscopy
PSA	Particle Size Analysis
GSD	Geometric Standard Deviation
ASTM	American Society for Testing and Materials
LPS	Liquid Phase Sintering
SPLS	Supersolidus Liquid Phase Sintering
XRD	X-Ray Diffraction
SANAS	South African National Standards
ALS	Advanced Laboratory Supplies
HSS	High Speed Steel
JIS	Japanese Industrial Standard
BCC	Body Centred Cubic
FCC	Face Centred Cubic

CHAPTER 1:

INTRODUCTION

1.1 Preamble

Aluminium has become one of the most versatile and preferred engineering material of our times. It is the world's most abundant metal and is the third most common element comprising 8% of the earth's crust [1]. As of 2005, the worldwide demand for Aluminium was approximately 29 million tons per year. Of this demand, 22 million tons was primary aluminium while 7 million tons was recycled aluminium scrap. On average, world aluminium demand grows 5-7% annually. For instance when compared with 2013, the global consumption of primary aluminium in 2014 amounted to 54.8 million tonnes, which represented a 7% growth. And based on data in 2015, world demand is expected to increase by additional 6% – amounting to 58 million tonnes, which is double the demand in a decade [2]. The use of recycled aluminium is compelling, both economically and environmentally. This is because the remelting and recycling 1 tonne of aluminium only takes 5% of the power required to produce 1 tonne of new aluminium, yet there is no known difference between virgin and recycled aluminium alloys in terms of quality [1].

1.2 Aluminium the Material

One of the key driving forces behind the growth in demand for aluminium is its unique properties. Pure aluminium is soft, ductile, and corrosion resistant. It is also known to have a high electrical conductivity. In it pure form, it is widely used for foil and conductor cables. However, alloying aluminium with other elements is necessary in order to provide the higher strengths that are often needed for other applications. Further, aluminium is one of the lightest engineering metals. It has a superior strength-to-weight ratio as compared to steel. Through utilization of various combinations of its advantageous properties, aluminium has found

applications in an ever-increasing range of applications and industries [1]. These properties include strength, mechanical and thermal properties, high payload-to-weight ratio, corrosion resistance, recyclability and formability. These properties are further complemented by aluminium's versatility in processing techniques and compatibility with physical-properties enhancers, reinforcement, and alloying elements. These attributes attests to the feasibility of a wide array of products ranging from structural materials through to thin packaging foils [1]. Of significant interest is the diversity and increased growth in demand for aluminium in the transport, packaging, and the building and construction industry in that order [3]. However, it should be noted that, like most engineering materials, aluminium is hardly used in its pure metallic form but rather in an alloy or metal matrix composite system.

In alloyed context, aluminium is mostly alloyed with copper, zinc, magnesium, silicon, manganese and lithium. Small additions of chromium, titanium, lead, bismuth and nickel have also been made, while iron has invariably been present in small quantities as a remnant. To date, there are over 300 wrought alloys with 50 in common use [1]. Wrought alloys are commonly identified using a four-figure-system as 1XXX – 8XXX depending on the key alloying element(s). Cast alloys have similar designations and use a five-digit-system. For unalloyed wrought aluminium alloys designated as 1XXX, the last two digits represent the metal's purity. The second digit indicates modifications in impurity limits. For the 2XXX – 8XXX groups, the last two digits are used to identify different aluminium alloys in the group. The second digit indicates alloy modifications. On the other hand, a second digit of zero indicates the original alloy while integers 1 to 9 indicate consecutive alloy modifications [1]. For the purposes of the current study, AMB-2712 (a 2XXX series alloy) was used with the understanding that any favourable findings can be feasibly transferrable to other series of aluminium.

In Aluminium Metal-matrix Composites (AMCs), one of the constituent and primary ingredient is aluminium / aluminium alloy, which forms a percolating network and is termed the matrix phase. The other constituent, which is embedded in this aluminium / aluminium alloy matrix serves as the reinforcement. This latter phase is usually non-metallic and most commonly a ceramic such as Silicon Carbide (SiC) and Alumina (Al_2O_3) [4-6]. Properties of AMCs can be customized by varying the nature and volume fraction of constituents to suit the target application [7-9].

1.3 *Where* aluminium has been used and *why*

The automotive industry has been facing challenges (as early as in the 80s) with respect to five key aspects: (i) improving fuel economy, (ii) reducing vehicle emissions, (iii) increasing styling options, (iv) enhancing performance, and (v) maintaining safety, quality, and performance [10, 11]. Durability, quality, and recyclability aspects have also been factored into the cost's equation. To meet these challenges, the quest of developing new materials and technologies has been an ongoing one. Key to numerous efforts has been the focus on weight reduction, which has additionally been construed to interpret into direct and indirect costs savings. Costs in this context not only includes materials cost but also the manufacturing (including capex) and recycling. For better appreciation, *Figure 1-1* shows a comparative view of the various costs in a typical automotive component manufactured from steel and discontinuously reinforced aluminium (DRA).

Comparatively, it has positively been stated elsewhere [11] that aluminium and magnesium are relatively more costly than the currently used steels and the cast irons that they might replace. Accordingly, it has been suggested that their competitive edge lies in the ability to lower component manufacturing costs. In comparison to cast irons and steel, cast aluminium and magnesium products and/or components are potentially less costly to produce. This contention is based on their: (i) better machinability, (ii) reduced manufacturing cycle times, (iii) ability

to have thinner and more variable wall dimensions, (iv) closer dimensional tolerances, (v) reduced number of assemblies, (vi) less costly melting / metal-forming costs, and (vii) more ease in production into near-net-shape with the effect of decreasing the finishing costs [11].

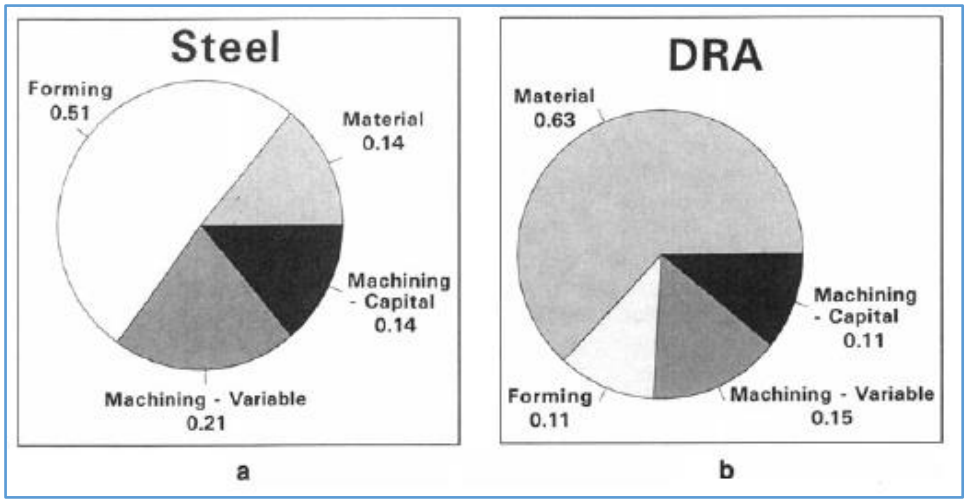

Figure 1-1: Proportions of the various costs in a typical automotive component manufactured from (a) steel, and (b) DRA [10].

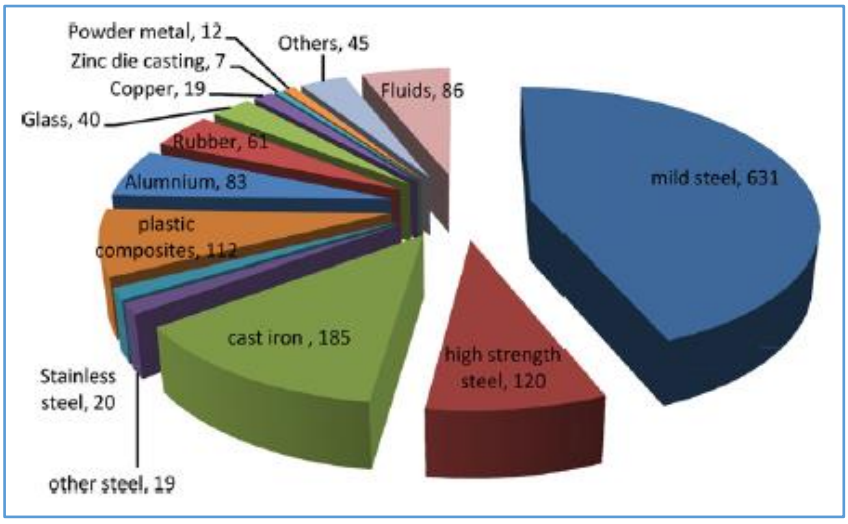

Figure 1-2: Material distribution of total vehicle curb weight in Kilograms [12].

Figure 1-2 shows the relative distribution of materials used in making a typical vehicle in 2011, with the iron and steel accounting for the majority weight while aluminium stands out as the preferred alternative metal for the automotive industry [12]. It is therefore reasonable to expect significant growth in the replacement of steel and iron with AMCs if the dream of light-weighting and related cost economies are to be realized.

In the drive for new markets, AMCs have found industrial applications primarily in areas where weight reduction is a key design consideration, especially in the aerospace and automotive industries. In light of the campaign towards greening our industries, light-weighting has often been advocated and perceived to interpret into less fuel consumption and carbon emissions [13, 14]. In fact, the drive towards this goal has seen to the introduction of carbon-tax in some economies such as, among many others, the United States, Canada, China, India, South Africa, and the European market [15]. The potential of aluminium as a mass reduction material becomes apparent when looking at its specific weight of 2.7 grams per cubic centimetre, which is significantly less than that of iron (7.8 g/cm3) and copper (8.9 g/cm^3) [13]. Besides direct weight reduction by material substitution, there are also additional possibilities for component light-weighting. An example of such possibilities relates to the aluminium-specific fabrication techniques, such as complex, multi-hollow extrusions or thin-walled, high-strength vacuum die castings that enable new design solutions [13].

Just for insightful reference purposes, when Audi designed the A8 model, it is reported that they had to choose between a steel body-in-white having a mass of 441 kg or an aluminium alternative of 247 kg. Upon deciding in favour of the aluminium aternative, further weight-saving measures were also realized. These included that realization that a smaller engine or a smaller fuel tank would effectively fulfil the given requirements for the car (acceleration, mileage per tank filling). In effect, Audi reported such "indirect" weight savings as 45 kg which represents 23% of the direct weight savings of 194 kg. This invariably means that the 247 kg aluminium body-in-white effectively reduced the car weight by 239 kg. Studies on other vehicle suggest a secondary weight saving in the range of 50 - 100% [13].

Similarly, the Jaguar XE is acclaimed to new levels of aluminium-intensive lightweight construction. It is projected to deliver fuel economy of less than 4 litres/100 km on the EU

combined cycle. The XE uses aluminium-intensive monocoque design that accounts for 75% of the vehicle's structure. The inherent reduction in weight ensures that the XE is currently the most fuel-efficient Jaguar yet, with fuel consumption and carbon dioxide (CO_2) emissions on the NEDC combined cycle of less than 4 litres/100 km and less than 100 g/km respectively. In line with the quest for innovative materials, the Jaguar XE is also reportedly the first car in the world to utilize RC 5754, which is a new grade of high strength aluminium. The alloy has been developed specifically for the XE. It features a high level of recycled material and also makes a significant contribution to Jaguar's target of using 75% recycled material by 2020 [13].

With due reference to safety in the automotive industry, it is most important to find a suitable compromise amongst key design aspects such as stiffness, crash performance and further body requirements (such as styling, package restrictions, etc.) in the development of a car body structure [16]. Aluminium is well suited to reach these targets with maximum performance and the lowest possible mass. It can be appreciated that the specific characteristics that aluminium alloys and AMCs offer do present the possibility of designing cost-effective, lightweight structures that have high stiffness, and excellent crash energy absorption potential.

Comparatively from a crashworthiness perspective, the mass-specific energy absorption capacity of aluminium is equivalent to double that of mild steel. Furthermore, it compares favourably to the newly developed grades of high-strength-steel. It should also be mentioned here that aluminium structures generally have a high rigidity as compared to a steel design. This is as a result of the relatively higher material thickness of aluminium structures. In essence, aluminium components generally have about 50% thicker walls than steel components fulfilling the same function. This is coupled with the favourable possibility of using closed multi-hole extrusions as well as high quality die castings of sophisticated design that allows the elimination of joints. Depending on the available package space, it is highly feasible to

improve the rigidity of an entire structure and still maintain a significant weight reduction of up to 40 – 50% [16].

One of the most important advantages of aluminium in the design of lightweight and cost-efficient structures relates to its ease of formability, i.e. versatility with respect to production technologies. Elaborate sheet-panels can efficiently be formed using various techniques. These range from high productivity stamping processes to low-cost tooling technologies that are suited to both high and low volume production. An interesting aspect compared to competing materials relates to the availability of extruded open and closed profiles that have intricate shapes and different wall thicknesses. Additionally, net-shaped and near-net-shaped aluminium parts can be produced using powder metallurgy, forging and other forming techniques [17-29]. Various casting processes acknowledging aluminium's flowability are readily available. The resultant cast aluminium parts can exhibit a wide range of sizes, shapes and properties depending on the applied method. Extruded and subsequently machined profiles, as well as high quality, thin-walled pressure die cast aluminium components, are not only beneficial for load-carrying and/or stiffening functions, but can be applied simultaneously as joining elements. It is noted that their proper use facilitates the development of new, innovative structural design solutions and that, as a result, significant weight and cost savings are realized by parts integration as well as the incorporation of additional functions [17].

The assembly step is a critical success-factor in the transportation market. The assembly tasks range from the joining of individual aluminium components of different alloys and product forms (stamped sheet, castings, machined extrusions, forgings, etc.) to multi-material joining of aluminium to steel, magnesium, plastics and composites. Inevitably, mixed material designs bring additional complications, since the selection of the applicable joining methods is restricted. Additionally, other factors such as differences in thermal expansion coefficients or

potential galvanic corrosion effects have to be taken into consideration. Most of the joining processes that have been developed over many years for steel structures are also applicable to aluminium. However, the ever increasing use of aluminium and, in particular, the growth of mixed-material designs has led to the introduction of innovative joining techniques. These include laser welding, friction-stir welding, self-piercing-riveting, and adhesive-bonding. As a result, diversely appropriate joining methods are readily available for all aluminium applications today. Nonetheless, selection of the proper method for optimal technical performance and economic viability is still a challenging task [17].

As vehicle manufacturers increasingly apply aluminium to lightweight their vehicles, the focus is increasingly being directed towards the system cost and life cycle cost analysis in order to obtain the desired outcome as encompassed in improved driving performance, reduced fuel consumption and/or reduced emissions. The manufacturer is increasingly considering avenues of fully exploiting the weight reduction in one or more parts, while allowing this weight reduction to offer additional weight or cost savings in other vehicle components [30]. Research has shown that cost-effective solutions do exist with aluminium-intensive cars as well as trucks. Under the right conditions, and in comparison to steel, these vehicles can be economically viable especially for high-volume vehicles. During their useful life, the fuel savings can be significant and directly or indirectly offer a real benefit to the consumer.

From another perspective, metals, aluminium being the most significant, do play an important role in funding the end-of-life processing of vehicles, through their high scrap value [30]. In fact, aluminium is already part of an established recycling system and the aluminium so recycled can be utilized for almost all applications, thereby preserving raw materials as well as reducing emissions and leading to considerable energy savings [31]. This value-chain underscores the cost-effectiveness of aluminium throughout a vehicle's useful life and beyond.

From an environmental-context of design considerations, aluminium components and assembled structures resist corrosion as long as they are properly designed and manufactured with appropriate alloys. This makes aluminium the material of high preference whenever it comes to transport applications due to its durability. Aluminium is known to be a highly reactive metal that oxidizes readily and quickly in air. In that process, a very thin, transparent, protective, layer of aluminium oxide is formed. This layer effectively hinders deeper intrusion of oxygen and other gases or liquids. The layer clings strongly on to the surface of aluminium and it does not flake off. It therefore prevents exposure of more fresh surfaces to further oxidation. Just in case the layer get damaged, it will "regenerate" itself, thus providing a continuous protection. It is recommended that aluminium components should be designed and constructed in a manner that avoids as much as possible the presence of entrapment areas for agents of corrosion that include moisture, salts and dirt [32].

Besides technical functionalities, it is not surprising that some of the most stylish vehicles (and indeed buildings, consumer products, fashion items and accessories) of the last two centuries, have employed aluminium – both for its functional and also for its aesthetic properties; its durability, formability and wide range of finishes. The Airstream trailer, London's Eros, Philippe Starck's 1006 chair, the iPod, and the BMW 328 racing car are outstanding examples – they all diversely make full use of aluminium's light-weight, the strength and durability. At the same time, they all have creatively been transformed from functional objects to cultural icons of our times through their stylish look and feel [33]. The inherent design concept of streamlining has been realized through the combination of technology and design aesthetics in commercially innovative ways. It is noted that although streamlined objects have been and are still popular in the home and workplaces, the design aesthetics aspect has found a niche in transportation industry because of its obvious association with aerodynamic movement. Aluminium has been suggested to be the perfect material for the streamlined age

by virtue of its clean, smooth, sleek, new, and ease of casting or extrusion into the seductive curves that defines the look. Most importantly, aluminium's lightness translates into, among other benefits, greater speed – some all-aluminium streamlined trains have been reported to provide a smooth comfortable ride and have even broken speed records [33].

1.4 What has changed about the strengths and weaknesses?

The characteristic behaviour of a material is normally highly reflective of the interdependence / correlation of the material's intrinsic properties. For the purposes of this study and in the particular context of automotive engine components, aluminium has been selected as the candidate material for an investigation towards improving its performance and/or optimizing its suitability as a candidate light-weight design material. Despite the diverse use and portfolio of favourable properties of aluminium, the full potential use of aluminium is yet to be realized. Great hope of exploiting this incumbent potential lies in the development of AMCs. AMC material systems present a superior combination of properties in such a way that today no existing monolithic material can rival [4]. Over the years, AMCs have been tried and effectively used in various applications in different engineering sectors. These include both structural and non-structural applications as well as functional applications. Driving forces for the noted utilization of AMCs in these diverse sectors include performance, economic and environmental benefits. In the context of the transportation sector, key benefits of AMCs include less noise, lower fuel consumption, and associated lower airborne emissions. With the increasing stringent environmental regulations by key stakeholders, and the emphasis on improved fuel economy, an increased use of AMCs in the transport sector will be almost inevitable and irresistibly desirable in the coming years.

Other major advantages of AMCs compared to monolithic materials include greater strength, improved stiffness, reduced density (weight), improved high temperature properties, controlled thermal expansion coefficient, thermal/heat management, enhanced and tailored electrical

performance, improved abrasion and wear resistance, control of mass (especially in reciprocating applications), and improved damping capabilities [4]. These advantages can be quantified for better appreciation. For instance, the elastic modulus of pure aluminium can be enhanced from 70GPa to 240GPa by reinforcing it with 60 vol% continuous alumina fibre [34, 35]. On the same note, incorporation of 60 vol% alumina fibre in pure aluminium results into a decrease in the coefficient of thermal expansion from 24 ppm/°C to 7 ppm/°C [34, 35]. It is also possible to process Al-9% Si-20 vol% SiCp composites that have a wear resistance equivalent to, or even better than, that of grey cast iron [34, 35]. All these examples demonstrate the possibility of altering several technological properties of aluminium or aluminium alloy by more than two–three orders of magnitude through the incorporation of appropriate reinforcement in suitable volume fractions [5].

1.5 Problem Statement (The Research Gap)

It is understood that reinforcement of light metals, especially aluminium, opens up the possibility of their being used in areas where weight reduction is first priority. Karl U. Kainer [36] identifies development objectives for light metal composite materials as: (i) Increase in yield strength and tensile strength, both at room temperature and at elevated temperatures while still maintaining the minimum ductility / toughness, (ii) Increase in material's creep resistance at higher temperatures as compared to that of conventional alloys, (iii) Increase in fatigue strength, especially at elevated temperatures, (iv) Improvement of thermal-shock resistance, (v) Improvement of corrosion-resistance, (vi) Increase Young's modulus, and (vii) Reduction of thermal percentage elongation. Since these objectives in themselves are not mutually exclusive especially in the context of engineering design, efforts need to be made towards ensuring that an improvement in one does not necessitate a trade-off with another *per se*.

From a general perspective, AMCs are intended to substitute monolithic materials including aluminium alloys, ferrous alloys, titanium alloys and polymer based composites in several

applications. It has been acknowledged that although increasing development activities have led to improved system solutions using metal composite materials, the use of especially innovative systems, particularly in the niche area of light metals, has not yet been realized [5]. The reason for this is said to be insufficient process stability and reliability, combined with production and processing problems as well as inadequate economic efficiency. Over the years, it has been recognized that in order for AMCs substitution for monolithic materials in engineering system to be wide spread, there is a compelling need to re-design the whole system in order to gain additional weight-and-volume savings as well as reduced production costs. These goals need also embrace processing stability, reliability, and adequate economic efficiency [5].

It is hereby considered that an opportunity for re-designing AMCs system lie in effective use of innovative reinforcement system(s). With particular reference to the automotive and aerospace industry where light-weighting is currently a primary design consideration, other costing-related factors validate the quest for new approaches to AMCs formulation and processing technologies. One area that is bound to benefit most from innovative AMCs system is the engine and its peripheral systems. Bearing that in mind, it is worth noting that automotive engines are nowadays more often than not operated at high speed and high temperature [34]. While at it, they are also expected to meet stringent emission regulations. As such, engine components are required to be tighter and lighter [34]. Therefore in this quest, density and thermal-mechanical properties are bound to play a critical role in the materials engineering process.

At the on-set, it is hereby further contended that improving thermal properties of the material for automotive engine components such as engine-blocks, cylinder-heads, connecting rods, and other associated components can increase the engine's operating temperatures, potentially

yielding improved operational efficiency, lower fuel consumption, and lower carbon footprint on the environment. This contention is founded in the fundamental *Law of Conservation of Energy*, which states that the total amount of energy in a closed system remains constant [37]. This implies that "Energy cannot be created or destroyed, it can only be changed from one form to another" – *Albert Einsten*. Considering the thermal energy from a combusted unit of fuel to be constant, this energy can either be converted to useful work of driving the vehicle or dissipated through heat losses avenues such as the exhaust gases, the water coolant and oil cooling systems. It is therefore easy to appreciate that engine thermal management systems do play a great role in the development and calibration of engines towards optimization of performance in terms of power output, fuel consumption, and emissions.

The engine thermal management system may be considered to be constituted of three eminent sub-systems. (i) *The fuel-combustion system*, i.e., thermal profile during the fuel injection-combustion-exhaustion cycle inside the internal combustion chamber - The normal operating temperature for most engines is in a range of 90^0C (195^0F) to 105^0C (220^0F) [38], (ii) *The water-cooling system* – The coolant mixture can reach up to 135 °C (water's standard boiling point of 100 °C can be exceeded since the cooling system is both pressurised and uses a mixture with antifreeze), which is then cooled with 20 °C air [39], and (iii) *The oil-cooling system* - A quality conventional motor oil may tolerate oil sump temperatures of up to 121^0C (250^0F), but starts breaking down over 135^0C (275^0F) [40]. Although professional racing teams have been reported to experiment with full-synthetic oils withstanding 177^0C (350^0F) or more, the traditional approach has been to try holding oil temperatures between 110^0C (230^0F) and 127^0C (260^0F) [40].

As of today, the latter two sub-systems present a significant limitation to the engine's feasible operating temperature. Holding the role and settings of the latter two sub-systems as a constant,

a window of opportunity to improve the engine's thermal management system exists in managing the heat transfer between the first sub-system and these latter two sub-systems. This opportunity is encompassed in thermal engineering of the material(s) used to make the constitutive engine components and peripheral systems. To date, design engineers are normally limited by the properties of materials that are available and the technique that can be used for fabricating the end-product or its components [1]. The mission of the current study is to challenge this *status quo* by re-engineering the thermal profile of the constitutive AMCs for engine applications by way of re-designing their reinforcement system. It is hoped that for every unit of combusted fuel, less energy dissipation will be necessary towards achieving optimum performance of the engine with reference to costs, vehicle weight / payload, fuel consumption, and emissions.

1.6 Aim of the study

In this study, primary interest is on the potential application of the material so developed in the automotive and aerospace industries and particularly in the engine components. The study encompasses an experimental exploration into the efficacy of using nanoclays as an economically competitive ingredient for enhancing thermal, mechanical, and machinability properties of aluminium and/or aluminium alloys. The objective is to characterize nanoclays-reinforced aluminium-based metal matrix composites (AMCs) and gain an insight into viable processing techniques.

Clay minerals have long been used in several applications, ranging from industrial materials to consumption in health-related products [41]. Clay belongs to a wider group of minerals that may simply be described as hydrous silicates that occur naturally as either residual clay or transported (sedimentary) clay. Residual clays are produced from the surface weathering of rock or shale (a dark fine-grained sedimentary rock composed of layers of compressed clay, silt, or mud) through various means, and they are generally found in the place of origin. They

could also be formed by the chemical decomposition of rocks. A common characteristic of clay minerals is their fine-grained (nanoscale) natural structure with sheet-like geometry.

The essential nanoclay raw material is montmorillonite and several researchers have explored the general nature of nanoclays from various perspectives. Amongst them, Uddin Faheem [41] reported on the structural, chemical, thermal, and electrical properties of Clays, Nanoclays, and Montmorillonite. Other relevant studies on nanoclays [231-238] are cited in *Chapter 4*. From an industrial perspective, the introduction of nanoclays as fillers or additives in polymers for various desired effects has been of enormous interest for research and development studies [41]. As a result, there has been a significant viable commercial interest in the use of nanoclays for the modification of polymeric material for numerous applications [41, 44-47].

To date, use of nanoclays as a reinforcement for aluminium-based metal matrix composites (AMCs) has not yet been reasonably explored. One notable limitation of nanoclays relates to their low functional threshold temperature, i.e. organic layered silicates begin to decomposion above 200^0C, which is relatively low compared to processing temperatures for most industrially used metals [41]. However, two nanoclays (*Nanofil 116* and *Cloisite C++DEV*) have been engineered for higher temperature regime applications and introduced into the market by *Southern Clay Inc. USA*. It is envisaged that their relatively improved threshold decomposition-temperature present a new set of possibilities towards the development of novel Nanoclay-infused Metal Matrix Composites.

For this study, and with due reference to alloying elements known to influence thermal-mechanical properties of aluminium, a copper-based heat-treatable 2xxx-series alloy has been selected as the preferred matrix. As the nanoclays consists of alumino-silica structure, it is expected that the clays can induce properties of alumina and silica reinforcement in the aluminium alloy matrix. By virtue of the selected nanoclay's chemical elements being

significantly similar to most of those found in the selected matrix alloy (Al, Si, and Mg), it is envisaged that the nanoclay can compatibly be integrated into the matrix, thereby inducing the inherent advantage of being nano-structured and chemically coherent with the matrix. For the sake of simplicity of this study, *Nanofil 116* was adopted as the datum nanoclay while *Cloisite C++DEV* was used for the purposes of supplementary comparative analysis.

The incumbent potential in use of the nano-phased *Nanofil 116* to especially improve thermal properties of aluminium alloys lies in: (1) the potential to optimize surface area of interfacial interactions – nanoclays are known to exhibit a very high aspect ratio [41], (2) As bentonite is the primary ingredient in *Nanofil 116*, there are traces of ceramic particles such as Al_2O_3 and ceramics are known to exhibit relatively low thermal conductivity [42], hence their typical use as refractory materials, (3) There is potential for chemical reactions between *Nanofil 116's* functional groups and aluminium – since Aluminium has a high affinity for oxygen, it could have chemically gained some oxygen atoms from the silicate layers of *Nanofil 116* through a localized thermally induced oxidation process, thereby increasing ceramic particles %wt content and distribution, and (4) *Nanofil 116* comprises of a layered structure – this could significantly optimize heat transfer resistance especially if these layers are perpendicularly oriented to the direction of heat flow especially between the matrix and alloying elements [43].

Interestingly at comparative level, nanoclays have been used as reinforcement particles in polymer matrix composites [44-46]. Superior improvement in properties of polymer has been observed in tensile, wear, and thermal properties due to the alumina/silica hard structure of clay. Such increase in properties has been observed at relatively low clay concentrations, with added advantage of low cost of commercially available nanoclays compared with SiC, Al_2O_3, WC and other hard ceramic particle reinforcement [47]. Considering the cost effective benefits of clay particles and the superior property enhancement in clay-filled polymer material, it is

hoped that the success in use of nanoclays in polymer systems can be replicated in metal systems. Accordingly, it is envisaged that a new breed of economically efficient AMCs with enhanced mechanical, thermal and machinability properties will hereby materialize. Further, it is hoped that a new direction can be pointed towards viable innovative processing technique(s) for AMCs and/or Nanoclay-AMCs.

1.7 Impact and/or significance of the study

From a hypothetical perspective, a significant improvement of one property of the alloy without compromising other properties can open up incredible opportunities for the automotive industry. For example, a significant improvement of thermal properties of the selected alloy can potentially interpret into a number of possibilities: (1) making of engine parts and/or components with thinner walls, with the knock on effect of direct weight reduction, (2) raising the temperature at which engines operate, thereby resulting to (3) improved operational engine efficiency by minimizing energy lost through the exhaust gases and cooling systems, (4) increased power output per unit of fuel intake through enhanced fuel combustion cycle efficiency, and (5) a resultant reduction in the automotive industry's carbon print, and (6) Improvement on mechanical properties such as tensile strength would similarly interpret to use of thinner-walled structural components with additional direct weight savings. For general reference, a typical rule-of-thumb estimate for the trade-off between weight and fuel economy has been that a 10% reduction in vehicle weight yields approximately 5.5% improvement in fuel economy [10].

Another significant potential impact relates to the reduction of production costs. Since some of the chemical elements in the nanoclays are also found in some aluminium alloys, e.g. magnesium and silicon, there is an embedded possibility that we can produce nanophased standard alloys using only elemental aluminium powder and nanoclays as the feed stock without necessarily adding on those elements independently. Such powder blends would then

simply need to be compacted and sintered into end products with properties that are either similar to (or even better than) those of conventionally processed alloys.

All these benefits would be fully realizable upon effective transfer of the favourable improvement(s) on properties of AMB-2712 alloy to other aluminium alloys without significantly compromising their current properties.

1.8 Scope and structure of study

Despite the broad focus on the automotive industry applications and potential transferability of properties to the building and construction industry, the scope of properties of interest has been focused on relevance to the context of engine components. Powder metallurgy has been used as the primary processing technique. Effects of nanoclay content on mechanical, thermal, and machinability properties have been investigated. The study encompasses development of economically viable nanoclay-reinforced AMCs. The AMCs sensitivity to inherent processing variables has been explored. Potential use of alternative processing techniques has also been evaluated based on acquired understanding of the characteristics of AMCs developed herein.

Towards unlocking the inherently enormous potential, the study's experimental process has been segmented into three progressively integrated phases. *Firstly*, the suitability, compatibility, and processability of raw materials are assessed based on the materials' respective physical and chemical properties. This content constitutes the chapters on literature review, research methodology and design, and materials analysis. *Secondly*, the effect of nanoclays on the AMC are investigated from the functional perspective of thermal, mechanical, and machinability behaviour. This content is reported in the succeeding three chapters. *Thirdly*, focus is shifted onto the processability of the AMCs towards optimization of the processing variables. This makes up the chapter on processability, which is then followed by a conclusions and recommendations chapter.

CHAPTER 2:

LITERATURE REVIEW

2.1 Introduction

Material selection is a key element in the multifaceted engineering design space. In pursuit of meeting the functional demands of a design product or component, the material's physical, chemical, mechanical, and processing requirements or limitations play a critical role. To ascertain that the candidate material does meet at least the bare minimum design requirements, experimental analysis comes in handy by way of providing a means of characterizing the material quantitatively and qualitatively beforehand. Important reference performance indicators that are commonly used can broadly be classified into three clusters based on the material's response to:

(1) *Thermal energy* – phase change, microstructure, coefficient of thermal expansion, thermal diffusivity, specific heat capacity, etc.,

(2) *External loading* – direct, shear, bending, impact, quasi-static loading, cyclic loading, etc., and

(3) *Processing Variables* – formability, rheology, machinability, safety considerations, processing costs, physical-chemical properties, compatibility with other materials, etc.

The characteristic behaviour of a material as measured against the aforementioned indicators is normally highly reflective of the interdependence / correlation of the material's intrinsic properties. For the purposes of this study and in the particular context of automotive engine components, aluminium has been selected as the candidate material for an investigation towards improving its performance and/or optimize its suitability as a candidate light-weight design material. The ensuing background check is woven around the aforementioned three broad clusters. Based on limitation of scope for the current study, review relating to the three

clusters have been addressed and respectively reported under the sub-headings of thermal properties, mechanical properties, and machinability.

2.2 Thermal Properties

It is envisaged that improvement of thermal properties of the material for automotive engine components such as engine-blocks, cylinder-heads, connecting rods, and other associated components can increase the engine's operating temperatures, potentially yielding improved operational efficiency, lower fuel consumption, and lower carbon footprint on the environment. This is founded on the understanding that an engine's thermal management systems play a great role in the development and calibration of engines towards optimization of performance in terms of power output, fuel consumption, and emissions as discussed in *Chapter 1*. In that chapter, three constitutive sub-systems were identified, being the *fuel-combustion system*, *water-cooling system,* and the *oil-cooling system*. Thermal engineering of the material(s) used to make the constitutive engine components and peripheral systems was identified as an opportunity for managing heat transfer amongst these systems towards improving the engines performance.

In the technical design space, design engineers are normally limited by the properties of materials that are available and the technique that can be used for fabricating the end-product or its components [48]. In the quest for light-weight materials in the context of engine components for the automotive and aerospace industry, density, thermal, and thermo-mechanical properties play a critical role in the materials selection process.

2.2.1 Density – Light Weighting

Density is a function of the mass of the atoms making up the materials and the distance between them [49]. Research shows that a material's processing technology and parameters do have a significant impact on its densification as well as the thermo-mechanical properties [50-62]. For better appreciation, Zeng, R. with the colleague Rand, B. [53] and Forrester, J.S. et al [54]

investigated the effect of particle size distribution and particulate agglomeration in alumina. The former sought to understand the effect of particle size distribution, powder aggregation, and their effect on sinterability of alumina powders. They found that a wider particle size distribution generally leads to a lower true porosity, i.e. while agglomeration plays an important role, usually it restrains the packing, resulting in a higher true porosity. They further observed that a smaller mean primary particle diameter and lower true porosity does not guarantee a higher final density of sintered ceramics. In general, they noted that a higher level of agglomeration will cause poorer sinterability [53].

Forester, J.S et al [54] sought to determine the suitability of milling of alumina for the production of a sufficiently small grain size to promote sintering at lower temperatures. With the understanding that temperatures around 1700^0C are normally required to sinter alumina powder into useful ceramic monoliths, they hypothesized that grain size reduction using high energy mechanical milling could be used to promote sintering at lower temperatures. They further reiterated that agglomeration promotes uneven sintering, which sometimes results in mechanically weak and porous products. In their study, a significant reduction in sintering temperature to below 1200^0C was realized. Besides their results, they identified with the work of Inada et al [63] who reported that alumina powder particles in agglomerates do increase the volume and size of pores in green compacts, thereby causing a decrease in the densification rate in the compact. Since the target AMB-2712 matrix and nanoclay reinforcement systems are in powder form, the potential effect of agglomeration and its possible elimination thereof should be borne in mind.

Iwaoka, T. and Nakamura, M. investigated the effect of warm- versus cold-compaction of magnesium and aluminium powders. They examined the effect of compaction temperature in the range of 301K – 423K while subjecting the specimens to 489MPa compaction pressure.

They observed that lamination cracks occurred in pure magnesium compacts during the compaction process. This behaviour was not observed in other conditions. At the higher temperature limit, comparatively smaller pores were observed to disappear. Porosity of the compacts decreased with increasing temperature. Addition of aluminium powder (into magnesium powder) was observed to decrease the spring-back effect and also reduce porosity. This was attributed to aluminium's better deformability compared to magnesium. The warm compaction was observed to reduce expansion of the compacts in the radial direction. Upon sintering, it was observed that the bonding between powder particles was stronger due to warm compaction than the bonding due to cold compaction.

2.2.2 Implications of thermal properties

Since heat is generated in an engine through combustion of fuel, it is imperative that the engine material should be able to either withstand the resultant high temperatures and/or conduct away the heat to avoid localized melting or microstructural phase change. All factors being held constant, an engine material with enhanced thermal resilience would be relatively more fuel-efficient than one with relatively low thermal resilience. Thermal resilience may be perceived as the derivative sum-total of the interaction between heat-transfer and the bulk body of an engineering material. Reference quantitative measures of this interaction may be considered to include thermal conductivity, thermal diffusivity, specific heat capacity, melting point, glass-transition temperature, coefficient of linear thermal expansion, thermal shock resistance, and creep resistance [64].

In many materials, thermal profile of a material has a significant effect on the material's mechanical properties such as strength, elastic limit, proportional limit, yield strength, ultimate tensile strength, ductility, toughness, fatigue ratio, and loss coefficient [65]. These properties can be traced back to the material's atomic packing. For instance in crystalline materials, toughness, which is a derivative of strength and ductility, is strongly dependent on the

material's crystal structure. For example, Face Centred Cubic (FCC) materials such as aluminium are typically ductile while hexagonal close packed materials tend to be brittle [65, 66]. On the other hand, Body Centred Cubic (BCC) materials often display dramatic variation in the mode of failure with temperature; they are more brittle at lower temperatures and more ductile at higher temperatures [42, 65].

2.2.3 Heat Transfer

In engine components, heat transfer with respect to the constitutive materials is mostly through conduction, which is the transport of energy due to molecular vibrations. Other modes such as radiation and convection, (energy transfer modes involving molecular motion and interaction) may be deemed relatively negligible. Nonetheless, these latter modes are actively involved in the fluids-based cooling systems of the engine by way of carrying away heat from the engine and dissipating it elsewhere [67, 68]. Accordingly, the material's thermal conductivity and/or barrier properties are critical design considerations. In a composite material system, it is envisaged that these thermal properties are influenced by a heat-transfer-matrix comprising of five key factors: (1) The chemical element(s) constituting the matrix and reinforcement, (2) Relative content and distribution / dispersion of the alloying or reinforcing elements in the system, (3) Interfacial boundary conditions and geometry of the dispersed phase relative to the matrix, (4) The atomic and/or granular packing density, and (5) The dimensions, densification, and nature of microstructure.

Firstly, different chemical elements have different thermal conductivities. For instance, aluminium is reported to have relatively higher thermal conductivity than beryllium, magnesium, tin, and zinc, while on the other hand its conductivity is lower than that of Copper [69]. This aspect is intertwined with the contextual temperature, i.e. the thermal conductivity of some materials is known to vary with temperature [42]. For example, the thermal conductivity of aluminium and gold at reference temperature of 25, 125, and 225^0C, are

reported to have maximum conductivity at the 125^0C while their respective conductivities at both 25^0C and 225^0C are the same and relatively lower. Copper and iron on the other hand have their conductivity declining at these same reference temperatures. Contrary to this latter trend, the thermal conductivity of platinum and stainless-steel is shown to increase over the same reference temperatures [42].

Secondly, alloying elements in composite materials systems are purposely used to induce one or more of their respective properties. One of the approaches for improving thermal conductivity involves the use of reinforcement elements with higher thermal conductivity [70]. For instance, the use of copper (401 W/m.K) as an alloying element in aluminium implicitly improves the alloy's thermal conductivity whereas silicon carbide (120 W/m.K) would lower the thermal conductivity despite having the highest thermal conductivity amongst the existing structural ceramics [3, 42]. It is expected that the percentage weight content and distribution of the dispersed phase relative to the matrix affects the bulk material's properties from one point to another. Accordingly, a homogenous dispersion would be preferred for uniform thermal-conduction or thermal-barrier properties. It should be noted here that the requirements and/or choice of thermal properties, e.g. thermal-conduction versus thermal-barrier properties, do vary from one industrial application to another.

Thirdly, heat transfer is a phenomenon that is dependent on interfacial boundary conditions [43] just like most other properties of materials. In general, Metal Matrix Composites (MMCs) intrinsically exhibit diverse interfacial boundary conditions dependent on the constitutive chemical elements and varying geometry of the dispersed phase. Research shows that, for composite materials consisting of a continuous matrix phase with dilute concentrations of dispersions with spherical, cylindrical, and/or flat geometry with a thermal barrier resistance at

the interface between the components, the effective thermal conductivity not only depends on the volume fraction of the dispersed phase [71-75], but also on the dispersion size [43].

The effective thermal conductivity of composites can be affected by a thermal barrier resistance at the interface between the individual composite's elements [43, 75, 76]. In studies conducted by B. R. Powel et al [76] and D. P. H. Hasselman et al [77], thermal barrier resistance was attributed to the combination of a poor mechanical or chemical adherence at the interface and a mismatch in the coefficients of thermal expansion thereby possibly causing an interfacial gap. This contention was affirmed by comparative experimental data for thermal diffusivity, which depicted strong temperature dependence as the composites were heated towards the original processing temperature.

Through mathematical modelling, it has been shown that interfacial thermal barriers are expected to be effective if they are non-parallel to the direction of heat flow [43]. The mathematical model indicated that, when compared to spherical and cylindrical phase geometry, a flat-plate geometry for heat flow perpendicular to the plane of the plate will be most effective in lowering the thermal conductivity of a material as the boundary conductance tends to zero. The studies on effect of interfacial barriers on conductive properties can be correlated to earlier studies on the effective thermal conductivity of single-phase materials with cracks [43, 78, 79].

Fourthly, the fundamental atomic and/or granular packing mechanisms significantly affect the effectiveness of efforts towards enhancing thermal properties. An insightful understanding of the dynamics involved therein can be derived from studies on thermal barrier coatings (TBCs). Even though the study of TBCs is outside the scope of the current study, the heat-transfer implications of the interfaces in TBCs and AMCs contexts are similar and a great opportunity lies in the ability to connect the macroscopic failure phenomena to the microscopic properties.

These coatings are most commonly used on aircraft engines to protect the engine from the extreme combustion environment [80, 81]. The TBCs are comprised of ceramics, with favourably low thermal conductivity, deposited on the engine metals. The ideal engine would operate at very high temperatures without failure in order to have the highest fuel efficiency [81]. Typically, the combustion gas is held at temperatures above 1370^0C, while the metal super-alloys that constitute the engine components have melting points ranging from 1230 – 1315^0C. This makes it imperative to either cool the metal components for instance by drilling holes and flowing cool air, or to provide thermal protection from the combustion gas [81, 82].

Unlike the automotive industry where ideas for optimizing the cooling techniques and engine metal alloy compositions are still feasible, this concept reached a point of diminishing returns long ago with respect to the aerospace industry [81, 83]. As a result, engineers have since looked to ceramic materials as a means of providing a TBC that will: (i) extend the life of gas turbine components, (ii) reduce cooling requirements, (thereby decreasing fuel consumption), or (iii) allow for an increase in inlet temperatures (thereby increasing thrust) [81, 84].

The challenge of working with ceramics is that they typically have completely different thermo-mechanical properties from the material to which they are expected to adhere, namely a metallic alloy [81]. As a result, the usual thermal cycling that such Metal-Ceramic interfaces undergo tends to stress these interfaces to the point of fracture and spallation (chipping-off) [81, 82]. A. Christensen et al [81] sought to characterize the Metal-ceramic interfaces at an atomic level with the aim understanding the exact mechanisms by which the interface is formed, stressed, fractured, and spalled. They sought to understand what roles circumstantial phenomena such as oxidation and temperature plays in stabilizing or destabilizing the interface. Central to the factors identified for failure of TBCs is the induced strains caused by thermal expansion mismatch at the interfaces. Other factors noted include the build-up of thermally

grown oxide layers (some of which are very brittle), contaminants-induced stresses (which decrease adhesion during thermal expansion), migration of ions (leading to formation of chemical bonds under reducing conditions at high temperatures), segregation of components, phase transitions, porosity, the coating fabrication procedure used, and residual stresses after thermal treatment. It can be appreciated that this interfacial challenge can be extended to interfacial relationship between the matrix and reinforcement particles in an AMC.

Lastly, the dimensions, densification, and nature of microstructure of the composite material are dependent on the processing temperature profiles [85]. This is further amplified by the relative percentage weight content of alloying elements that render the alloy to be either heat-treatable or not [86, 87]. For instance, small amounts of magnesium added to any silicon-containing alloy will render it heat-treatable, but the converse is not true because excess magnesium over that required to form Mg_2Si sharply reduces the solid solubility of this compound [87]. Heat-treatment on the other hand has been shown to affect thermal conductivity of some aluminium alloy systems. For better appreciation of the impact of heat treatment, it has been demonstrated that the thermal conductivity of some Al-Si-Cu alloys can be increased by more than 60% when adopting T7 heat treatments [88, 89], which entails solution heat treatment and overaging. It has been mentioned that effects of heat treatment on the microstructure, such as grain refinement in aluminium alloys, increases the number of grain boundaries [88]. Since grain boundaries are considered as defects in a crystal structure, it has been suggested that their increase can be expected to reduce both electrical and thermal conductivity. Materials with coarse grains have been observed to exhibit relatively poor mechanical properties as compared to ones having fine grains [88]. However, the thermal conductivity of a rheocast AlSi10Mg (globular microstructure) has been measured to be about that same as that of a corresponding traditionally cast alloy (dendritic microstructure). Therefore, it has been concluded that the alloy composition and thermal history (heat

treatments associated with precipitation) constitute the most important factors that determine thermal conductivity while melt treatments do not have appreciable effect [88].

Resultant effects of the proposed heat-transfer-matrix manifest themselves in the end-product in various ways. For example, the aluminium alloys used in cylinder heads will anneal at 350^0C, but considerable softening begins at around 290 – 310^0C [90]. Similarly, it has been reported that a magnesium-free aluminium alloy yielded improved elevated temperature properties (especially at 300^0C), combined with good ductility and high fatigue strength at room temperature [91]. Evidently, the product's behaviour in the thermal-mechanical design space significantly depends of the heat-transfer-matrix. Bearing in mind the diversity of factors and/or variables that influence a material's heat-transfer-matrix, it is imperative that quantification of the effects attributable to key factors / variables does have a significant potential towards optimization of a material's heat-transfer-matrix.

Useful quantitative measures of this effect of heat-transfer-matrix include thermal conductivity, coefficient of linear thermal expansion, thermal diffusivity, specific heat capacity, wear rate, and thermo-mechanical test results. Analytical evaluations include phase change and microstructural analysis. Directly related failure mechanics include galling, thermal fatigue and creep. These resultant effects interpret to engineering design implications and economics. For instance, optimizing the thermal properties of an engine-block and cylinder head material can interpret into: (a) designing engines with thinner wall thicknesses, interpreting into using less material and lighter-weight engines, (b) creating an opportunity to possibly design engines that run at a relatively higher temperature, thereby enhancing their performance efficiency and useful life, and (c) potential fuel economy and reduced carbon emissions.

2.2.4 Heat Transfer Matrix Optimization

Three broad areas are hereby envisaged to directly present an opportunity for optimization of the heat-transfer-matrix of an AMC–system. With particular reference to thermal properties, *firstly* there is materials engineering [36, 90-103] – combination of the intrinsic physical, chemical, mechanical, thermal, and other properties and with due consideration of the inherent synergies amongst the different materials. Significant advancements in this respect can be identified with the development of advanced MMCs [7, 21, 35, 104, 105]. Thus far, materials that have been used to improve the properties of aluminium and its alloys include ceramics such as SiC, Al_2O_3, AlN, WC, TiB2, $ZrSiO_4$, and Boron Carbide [4-7, 22, 100, 106-108]. Despite their having low thermal conductivity and improving the metal's mechanical properties, these ceramic reinforcement systems have been associated with intolerable tool wear due to the particles' abrasive properties [108].

Relatively recent research publications document the use of Carbon fibre, Carbon Nanotubes, Fly Ash, and Nanoclays [4, 97, 98, 108-112]. However, in the case of using carbon fibres, carbon reacts with aluminium to generate a brittle and water soluble compound, Al_4C_3, on the surface of the fibre [4]. To prevent this reaction, the carbon fibres are coated with nickel or Titanium Boride. The use of Fly Ash has been discredited due to its insufficient chemical and mechanical stability [5]. From the reviewed scanty literature relating to the use of nanoclays in aluminium, nanoclay particles that were preheated to 500^0C were introduced to a molten Al-6061 metal pool through a vortex created in the melt using an alumina-coated stainless steel stirrer [110-112]. Since no details of the nanoclay are given whatsoever, it is difficult to establish if the nanoclay was still actively functional at the fabrication temperature as it interacted with the metal in a molten state.

Secondly there is the role of availability and choice of processing technology [113-115]. Given the same set of ingredients, different technologies require working at different temperatures, pressures, and environmental conditions, thereby yielding end-products that have diverse sets of properties. Examples include, among others, the semi-solid metal casting technologies, spark-plasma sintering, and conventional powder metallurgy, i.e:

(1) Semi-solid metal casting technologies such as thixocasting and rheocasting are associated with relatively finer microstructure compared to conventional stir casting [116].

(2) Spark-Plasma-Sintering (SPS) [109, 117-120] is identified with (i) typical operational or "monitored" temperatures (200-2400^{0}C) that are commonly 200 to 500^{0}C lower than with conventional sintering, thereby being classified as a lower-temperature sintering technology, (ii) high heating rates (up to 1000^{0}C/Minute), (iii) High compaction pressures (up to 1000 MPa), (iv) relatively short processing times (approximately 5 to 25 minutes) with high uniformity and without changing the particles' characteristics, and (v) significant influence on microstructure of the consolidated material and thereby mechanical response.

(3) Powder Metallurgy (P/M) and related processes [98, 99, 104, 121-124] are generally associated with (i) Product cost effectiveness, and (ii) Product uniqueness. Amongst other considerations, some combinations of chemical constituents, control over microstructure and porosity, and choice of feasible working temperatures can be achieved by starting from a powder feedstock, which would otherwise be very difficult or sometimes impossible in conventional processing routes.

Thirdly, heat treatment and aging of the finished product affects a broad spectrum of properties including the microstructure and thermal-mechanical properties [87, 110, 125]. Heat treatment

is normally used to refine the grains structure of the material. The mere fact that a material can be heat-treated to improve its microstructure is reflective evidence that the material's thermal properties significantly relate to the material's constitutive construction at grain level.

2.3 Machinability

Machining is a common integral aspect in several manufacturing processes especially when working with metals. Conventional machining operations include turning, milling, drilling, and their respective related machining operations [126-130]. Advanced machining technology includes the use of, among others, electron beam, plasma, laser technologies, and Wire-Electrical-Discharge-Machining [126, 131]. Machinability of a material quantifies the machining performance of that material, which may be defined for a specific application by various criteria such as tool life, surface finish, chip evacuation, material removal rate and machine-tool power [132]. Elsewhere [133, 134], machinability of a metal is reported to relate to the ease with which the metal can be machined to an acceptable surface finish. Besides environmental considerations of machining processes, machinability of a metal affects the costs dynamics of a production process with a knock-on effect on the absorption costing of the end-product. It is imperative, therefore, that it is considered as a pivotal factor in the design space.

2.3.1 Quantification of Machinability

Different automotive engine components require machining to different surface finish and tolerances. To aid comparative analysis, various approaches have been used in quantifying machinability of aluminium and its alloys. The most commonly used approaches include, among others (1) the tool wear rate / tool-life, (2) tool-force and power consumption, and (3) the surface finish method [128, 132, 133]. Each of these has unique advantages and disadvantages. For instance, the tool-wear rate approach can be useful when comparing materials that have similar properties and power consumptions but one of the materials happens

to be more abrasive, thereby decreasing the tool-life [133]. The major disadvantage of this approach is that tool-life is dependent on more than just the material the tool is machining and is influenced by other factors such as the cutting tool material, tool geometry, machine condition, tool clamping, cutting conditions, i.e. the speed, feed, and depth of cut. Furthermore, machinability for one tool type cannot be compared to another tool type [133]. From an economic perspective, it can be expected that this approach also necessitates the use of relatively large test specimens, which may be considered onerous and wasteful of resources.

The other two methods may be effective even with relatively small experimental specimens. In the tool-force and power consumption approach, tools forces are often given in units of specific energy, which leads to a rating method where higher specific energies equal lower machinability. The advantage of this method is that outside factors have little effect on the rating [133]. Surface finish method has the advantage that it is easily measured with an appropriate instrument. Nevertheless, it has the limitation that its relevance is tiered with the need to use only the finish cuts which often requires a certain accuracy that is naturally acclaimed to achieve a good surface finish. Consequently, surface finish during rough cuts is often irrelevant. This rating method also does not always agree with the other approaches [133].

Reference to chip formation is often effectively used to mitigate limitations associated with the surface finish approach. However, it should be noted that chip formation is a derivative of the material's properties and cutting conditions [126]. To appreciate this, brittle materials are known to form discontinuous chips when machined at low cutting speeds. On the other hand, ductile materials cut at high speeds and relatively small feeds and depths tend to form long continuous chips resulting to a good surface finish. To the contrary, when ductile materials are machined at low-to-medium cutting speeds, friction between the tool and chip tends to cause part of the work material to adhere to the rake face of the tool near the cutting edge [126]. This

tendency results into cyclical formation, growth, instability and eventual break-off of a built-up-edge (BUE). Much of the detached BUE is carried away with the chip, sometimes taking portions of the tool rake face with it, which reduces the life of the cutting tool. Portions of BUE not carried off with the chip become imbedded in the newly created work surface, thereby causing the surface to become rough [126]. It is reported that aluminium alloys as well as materials with a high shear zones typically do not tend to form BUE and would generally rank as more machinable [133]. It is elsewhere averred that, aluminium alloys as a class are considered as the family of materials offering the highest levels of machinability, as compared to other families of lightweight metals such as titanium and magnesium alloys [132]. Nonetheless, there is still a room for improvement.

2.3.2 Enhancement of AMCs Machinability

Several researchers have evaluated machinability of aluminium and aluminium Metal Matric Composites (AMCs) from diverse perspectives with due consideration of variables that affect machinability. It is generally understood that in order to meet the diverse target output benchmarks of a machined surface for a particular application, a variety of variables come into play. These can broadly be categorized into two groups: (1) variables related to the machining process, and (2) variables related to the material.

The *first* category includes key variables such as: (a) the effect of machining conditions such as the cutting speed, feed rate, depth of cut, and lubrication [135, 136], (b) effect of the cutting tool material, tool design, and tool surface modification [127, 128, 137-140]. On the other hand, the *second* category includes factors such as: (c) effect of material's processing techniques and the inherent processing variables [141-143], and (d) the effect of additives or alloying elements [129, 130, 144-148]. Of significance is the versatility and impact offered by the approach of using alloying / fortifying ingredients towards improving the machinability of AMCs [94].

Relating to the *second* category and with significant simplicity, Schneider [133] broadly categorised factors affecting machinability into two clusters. The *first* cluster relates to the *condition-of-work-materials* comprising of eight factors identified as microstructure, grain size, hardness, chemical composition, fabrication process, heat treatment, yield strength, and tensile strength. The *second* cluster constitutes the *physical-properties* of the individual material groups such as the modulus of elasticity, thermal conductivity, thermal expansion, and work hardening. Other identified factors considered important include the operating conditions, cutting tool material and geometry, as well as the machining process parameters [133]. The current study is focused on harnessing the synergies embodied in the *first* cluster of factors with particular emphasis on microstructure, grain size, hardness, and chemical composition.

In pursuit of improving the machinability of aluminium / aluminium alloys / AMCs, a variety of chemicals, both metal and non-metal, have been added to make the material easier to cut. These additives generally work by lubricating the tool-chip interface, thereby decreasing the material's shear strength or increasing the brittleness of the chip. Examples include nano-ceramic particles such as carbides, nitrides, oxides as well as carbon nanotubes [128, 136, 140, 143, 149]. The main issue of concern for the synthesis of the nano-ceramic materials consists in the low wettability of the reinforcement phase by the molten metal, which does not allow the synthesis by conventional casting methods [149]. Furthermore, it is reported that many ceramic particles of interest are thermodynamically unstable when they are in contact with pure metals and will react to form reaction compounds at the interface between the particles and the surrounding matrix [146]. These findings agree with observations made by A. Christian et al [81] even though in the context of TBCs.

Besides ceramic particles, minor elements like Lead, Bismuth, and Cadmium have been found to improve machinability of AMCs [150]. Other additives such as Titanium (Ti) and Boron (B)

have been shown to impart grain refinement on aluminium [151], thereby imperatively affecting the machinability. Originally, the processing methods were associated with risks such as generation of toxic fumes and residual spent salt in the melting furnace. However, these additives are still relatively expensive even after overcoming these risks [149]. Elsewhere, minor additions of Scandium and Zirconium have been reported to improve the Machinability of Al-Mg Alloys through grain refinement [152]. On the other hand, the rare-earth metals are not economically savvy especially at the face of driving demand for aluminium to mass market consumption. To mitigate the cost factor, some researchers have explored the possibility of using industrial waste such as fly-ash and agricultural waste such as breadfruit seed hull ash [108, 148, 153, 154]. However, fly-ash is reportedly associated with insufficient chemical and mechanical stability [154], while agricultural waste inherently requires significant processing (and costs) before integration into the metal matrix. The effect of nanoclays on the machinability of aluminium is not yet satisfactorily known.

2.4 Mechanical Properties

In almost all industrial applications, AMCs are required to have sufficient mechanical strength besides other contextual properties. Besides intrinsic physical-chemical properties of the matrix, mechanical properties of AMCs depend on a variety of factors / variables including, but not limited to, the relative quantity, size, geometry, chemical, and physical properties of the alloying element(s), AMC's processing route / technology, and any post-processing heat treatments. In order to optimize mechanical properties, control of these variables is normally design-oriented towards the envisaged application(s) and often plagued by trade-offs amongst other properties such as thermal, thermal-mechanical, electrical, physical, wear, fatigue, weldability, corrosion, and machinability properties. Accordingly, the costs-benefit matrix is not always universally transferrable across industries and this aspect makes the selection of an AMC for a particular design rather complex. However, it should be appreciated that mechanical

properties are predominantly a common reference in applications such as in aerospace and automotive industries where structural strength and lightweight are key design considerations. Furthermore, some mechanical properties are easily transferable to other industries such as the building and construction industry subject to costing considerations.

Over the years, significant strides have been made by several researchers towards improving the mechanical properties of aluminium by way of focusing on the alloying ingredients in their pure elemental form or as ceramic compounds. The choice and quantity of alloying ingredients is always reflected on the cost-benefits matrix of the resultant alloy or AMC. Major alloying elements targeted at improvement of mechanical strength include Copper, Magnesium, Manganese, Iron, Silicon, and Zinc [155-172]. Minor elements include Calcium, Titanium, Vanadium, Zirconium, and Boron for recrystallization / grain refinement [173-182], while Indium, and Tin have been used for improved heat treatment through artificial ageing and/or reduction of ageing time [156, 183, 184]. As a matter of fact, different combinations of these major and minor elements have been used in creating standardized alloys with a clearly defined nomenclature of wrought or cast alloys, and heat-treatable or non-heat-treatable alloys [185].

Additional elements such as Nickel and Lithium have been integrated into the formulation of super-alloys for the aerospace industry [163, 167, 186, 187]. Besides elemental alloying elements, ceramic compounds have also been used with positive structural strength and wear resistance results, including SiC, WC, Al_2O_3, AlN, TiB_2, $ZrSiO_4$, and B_4C [7, 100, 108, 153, 154, 188-205]. It should be noted here that one element (or fortifying ingredient) might be considered as a major ingredient in one alloy whereas the same element is considered a minor or remnant element in another alloy. Nonetheless, it can be appreciated that the resultant effect(s) of a particular element may vary depending on the relative %wt content, complementary elements in the matrix, and processing route - cum - atmosphere [60, 206-208].

By virtue of these alloying ingredients tending to be relatively more expensive compared to the aluminium matrix, the end AMC products tends to be either economically infeasible for the broad aluminium market or limited to special applications. The general trend has been in favour of using the relatively cheaper transitional metals such as Nickel in favour of rare earth metals [187]. To mitigate the cost factor further, efforts have evidently been made towards using relatively low-cost ingredients such as fly ash, which is an industrial waste [108, 153, 154]. However, results for this ingredient have been discredited due to insufficient chemical and mechanical stability [154]. Once again, the efficacy of using nanoclays as an alternative low-cost reinforcement system has not sufficiently been explored.

2.5 Summary

From the afore-going review, it is evident that there is a need for novel reinforcement system(s) and processing technologies for aluminium to gain further market share from an economics perspective. Despite transferability of a material's properties from one industry to another, the absorption of the material's cost along the life cycle may be feasible in one industry and yet infeasible in another. In the currently existing feasible niche markets such as the automotive and aerospace industry, there is still a phenomenal room for increased demand for aluminium in the quest for light-weighting. It is still possible to raise the benchmark for the knock-on effects such as increased fuel economies, lower carbon print, and improved performance and/or efficiencies. To optimize these knock-on effects as well as lower the cost of AMCs (and hence diversify their industrial feasibility), re-design of reinforcement systems and/or processing techniques is inevitable.

Towards this quest, it is envisaged that nanoclays can have favourable impact on the aluminium family of materials from the following perspectives: (a) Besides having aluminium as the primary chemical element, nanoclays have other elemental ingredients that are often

substantially used in alloying aluminium, e.g. magnesium and silicon; this similarity increases the probability of physical and chemical compatibility. (b) By virtue of being nano-phased, nanoclays stand to have a favourable structural impact on the matrix, and (c) nanoclays are relatively more affordable and available across the globe compared to the nano-ceramic particles and/or rare-earth metals.

In this study, the efficacy of using nanoclays in AMC-systems has experimentally been explored. Experimental results and discussions are embodied in the ensuing chapters with particular focus on thermal, machinability, and mechanical properties *Firstly*, the chapter on thermal properties documents an experimental investigation into the viability of using nanoclay particles towards enhancing thermal properties of AMCs for automotive industry applications. *Secondly*, the chapter on machinability documents a comparative study that explores the efficacy of using nanoclays as an economically attractive candidate for development of Nano-phased AMCs with particular focus on their influence on machinability. *Thirdly*, the chapter on mechanical properties documents a preliminary experimental exploration into the effect of using nanoclays as an economically competitive alloying ingredient for enhancing mechanical properties of AMCs.

An additional chapter on processability of Nanoclay-infused AMCs is presented towards the end of this report. Processing parameters explored during the experimental investigation and analysis may not necessarily be the optimal settings. They are however deemed sufficient for the scope of analysis and do serve as an insightful foundation for further developments.

CHAPTER 3:

RESEARCH METHODOLOGY AND DESIGN

3.0 Introduction

Through literature review, it was established that there currently exists a gap in the knowledge base and technology relating to enhancement of properties of Aluminium towards its gaining a broad-based economic application as a light metal. Insight was obtained relating to various material systems that has thus far been applied to enhance the materials performance. These included rare earth metals, ceramic particles, organic particles, and hybrid combinations thereof. Performance benchmarks revolved around, among other aspects, the mechanical, thermal, machinability, and processing. Potential avenues for closing up the gap were identified relating to re-designing the AMCs reinforcement systems. Focus was re-directed to applications in the automotive engine components with the target of harnessing the material's thermal properties. Secondary aspects such as machinability and mechanical properties were also highlighted.

The current study sought to stretch boundaries of the aforementioned body of knowledge with respect to reinforcement systems and processing technologies. In that pursuit, and in similarity to most of the reviewed work of other researchers, an experimental approach was used and anchored on comparative analysis. Quantitative and qualitative analysis were used to derive an understanding of the effect of various input variables towards characterizing Nanoclay-Aluminium composites. Relevant quality assurance standards and work procedures were used as a guide and means of ensuring repeatability of the reported results.

Since properties of engineering materials are known to influence the nature of application and feasible processing and/or manufacturing technologies, this chapter has been demarcated into

two main sections. The first section focuses on insights and characterization aimed at understanding the nature and limitations of candidate materials for the current study. The second section focuses on the techniques explored in this study to process and characterize new aluminium metal matrix composites.

SECTION A: MATERIALS

3.1 Overview

Most metals, including Aluminium are hardly used for engineering applications in their pure form but rather in alloyed or composites form [126]. *A priori* set of raw materials of interest in this study comprised of: (1) *Matrix*: constituting a standard Aluminium alloy, (2) *Reinforcement*: constituting a low-cost, nano-phased material system, and (3) *Binder-cum-Lubricant*: constituting a medium for facilitating in part the handling of powdered matrix and reinforcement system. Choice of the particular materials used was based on contemplated contextual applications in the automotive engine components sector. This chapter gives an insight into the take-off materials with the objective of understanding their physical, chemical, and thermal behaviour. The objective of the ensuing characterization was to establish a potential portfolio of feasible processing parameters and techniques.

3.2 Raw Materials

3.2.1 MATRIX – Standard Aluminium Alloy

Pre-alloyed aluminium powders were sourced from *AMPAL INC (USA)*. Three sets of composition were available as shown in *Table 3-1*. Based on understanding from the preceding chapters, and with due reference to alloying elements known to enhance key properties of aluminium, a copper-based heat-treatable 2xxx-series alloy was pre-selected as the preferred matrix for the current study. Of the three sets, AMB-2712 alloy was pre-selected as the matrix of choice based on three factors. *Firstly*, copper-based aluminium alloys have been observed

Table 3-1: Candidate Metal Matrices for the current study.

REF	Heat-Treatable	Composition		Key Alloying Element			
	Yes / No	Element	(%)		[1]Density (g/cm^3)	[2]Cash Price (1 Year Ave.) US$/Kg	[1]Young's Modulus (GPa)
Al		Al	100	Al	2.7	1.984	69
AMB-2712 [3](Theoretical Density = 2.7546 g/cm^3)	YES	Cu, Mg, Si, Al	3.8% 1.0% 0.75% Balance	Cu	8.96	6.371	117
AMB-2905 [3](Theoretical Density = 2.7482 g/cm^3)	YES	Cu, Mg, Si, Sn Al	2.98% 1.2% 0.26% 0.6% Balance	Cu	8.96	6.371	117
AMB-6711 [3](Theoretical Density = 2.6864 g/cm^3)	YES	Cu, Mg, Si, Al	0.25% 1.0% 0.8% Balance	Mg	1.738	2.260	45

Sourced on 8th August 2017 from: [1] https://en.wikipedia.org ; [2] http://www.infomine.com ; and [3] http://www.indium.com/blog/interest-in-formula-for-calculating-alloy-density-still-keen.php

to exhibit relatively higher mechanical strength than the counterpart magnesium-based [209] and silicon-based alloys [210]; strength is a significantly important property in key engine components, especially on components such as connecting rods due to their dynamic mode of

operation. *Secondly*, despite magnesium's favourable higher resistance to corrosion, lower density, higher specific strength, and lower cost as compared to copper, Al-Cu alloys have been observed to show better performances than Al-Mg alloys at both room and high temperatures [209, 210]. *Thirdly*, high levels of magnesium have been associated with embrittlement of AMCs [211] and since the contemplated reinforcement system also has magnesium in its formulation, minimal or no magnesium in the matrix would be preferable. Since all the three powders look the same, *Figure 3-1* shows a sample of the AMB-2712 as a representative sample. Nonetheless, additional supplier's information for the alloys is herewith attached as *Appendix A1 - A3*.

Figure 3-1: AMB-2712 Alloy powder.

3.2.2 REINFORCEMENT SYSTEM – Low Cost and Nano-phased

For this study, two natural montmorillonite nanoclays with high thermal stability were sourced from *Southern Clay Inc. (USA)*. This company has since been acquired by *BYK Additives & Instruments*. Their respective compositions were as shown in *Table 3-2*. As a datum for this study, *Nanofil 116* was pre-selected as the take-off nanoclay. Nonetheless, the effect of *Cloisite* Ca^{++}*DEV* was at a later stage comparatively evaluated against the performance of *Nanofil 116*. *Figure 3-2* shows samples of these nanoclays. For additional information, their respective

Product's Bulletin from the supplier are herewith attached as *Appendix B1 – B2*. Similarly, *Nanofil 116* was pre-selected as the preferred datum nano-phased reinforcement system.

Table 3-2: Candidate nanoclays for the current study.

	Bentonite	**Quartz**	**Price**
Nanofil 116	99 - 100%	0.1 - 1%	US$ 10.13
Cloisite Ca^{++}DEV	97 - 100%	<3%	US$ 10.13

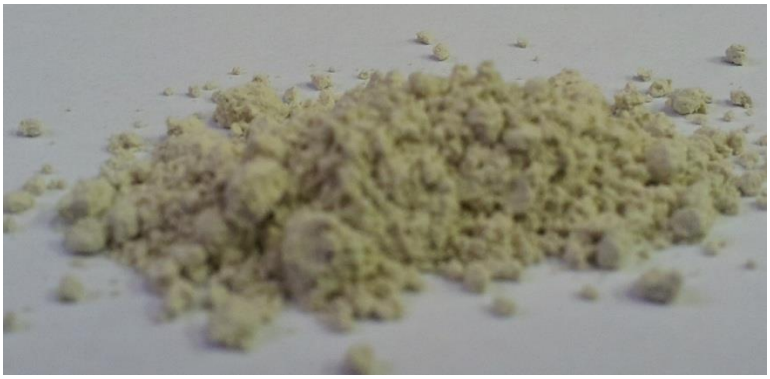

(i)

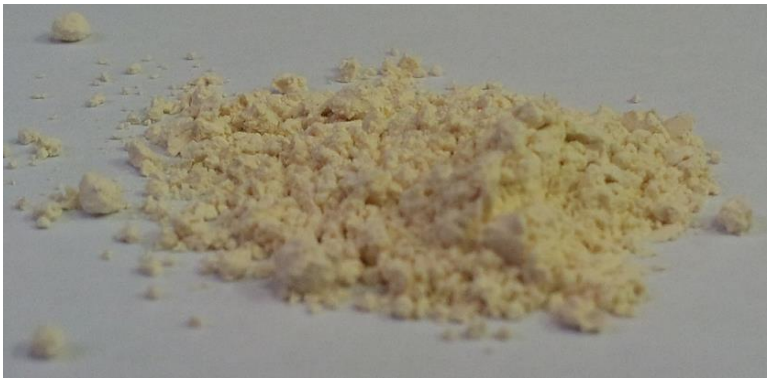

(ii)

Figure 3-2: Images of (i) *Nanofil 116*, and (ii) *Cloisite Ca^{++}DEV*

As alluded to in the literature review chapter, various reinforcement systems do exist for aluminium and its alloys. Materials that have been used to improve the properties of aluminium and its alloys include ceramics [4, 6, 7, 22, 52, 100, 107, 108], carbon fibre, carbon nanotubes, fly Ash, nanoclays [4, 97, 98, 108-112]. The respective limitations associated with the use of these reinforcement systems have also addressed [4, 52, 108] and reported in the literature

review chapter. With reference to the use of nanoclays in aluminium, only limited literature relating to the use of nanoclays in aluminium, has thus far been reported [110-112]. Since no details of the nanoclay were given whatsoever, it was difficult to establish if the nanoclays were still actively functional at the processing temperature as they were introduced to a molten metal matrix metal.

With reference to the relative prices of reinforcement materials systems, nanoclays and nanomaterials have been noted to be more expensive than technical ceramics and glasses [212]. Of this class of materials, nanoclays are the cheapest when compared to single-walled, multi-walled, and functionalized carbon nanotubes. This has been attributed to the processing requirements such as application-targeted functionalization. As economic logistics would dictate, the pricing has been noted to vary with quantities of use and level of purity. Nonetheless, quantities required for any real application would necessarily be quite large and costs would correspondingly decrease [212]. From another perspective, the high pricing may also be correlated to the research and development costs absorption by virtue of the materials being in the early years of technological advancements and applications. However, it should be borne in mind that direct comparison of pricing with bulk materials, such as the matrix into which they are integrated, should be viewed in the light that quite small quantities of nanomaterials may normally be actually used [212].

3.2.3 LUBRICANT – Cum – BINDER

Since powder metallurgy was one of the contemplated processing methods, a means of lubricating the dies and/or facilitating green compaction of the powdered raw materials was required. Researchers have in the past used lithium and zinc stearates, stearic acid, stearic acid in acetone, liquid paraffin, glycerol, polytetrafuloloethyren (PTFE), polyethylene (PE), Acrawax / ethylene bisstearamide (EBS), graphite-organic binder, and paraffin wax among others [50, 51, 55, 60, 62, 123, 213]. Since the afore-discussed matrix and nanoclay-

reinforcement system were essentially sourced in powder form, atomized acrawax was pre-selected as the preferred lubricant-cum-binder in order to facilitate in part the handling of these powders. The rationale for pre-selection of acrawax was that its light-weight and atomized nature were hypothetically perceived to complement the blending and binding process of the other (nano- and micro-scale) particulate raw materials. For the current study, atomized *Acrawax-C* was used on the basis 1.5% of every powder-mix [95]**.** Materials Safety Data Sheet for *Acrawax-C* is herewith attached as *Appendix C*.

3.3 Characterization of Raw Materials

It is understood that a material may behave differently and exhibit diverse physical, chemical characteristics depending on whether it is in solid or powder state [214-216]. For instance, physics of granular material in ambient gases is governed by interparticle forces, gas-particle interaction, geometry of particle positions and geometry of particle contacts [214]. In the context of low consolidations, these aspects are strongly dependent on the external forces, boundary conditions, and on the assembly procedure.

In the bulk context, the scale of reference matters. At nanoscale, a dominant mechanism of deformation is the rearrangement of free nano volume and exchange of momentum between bulk and grain boundary space [216]. Comparatively at microscale, the most common mechanism of deformation is dislocation motion. Then at macroscale, deformation patterning normally occurs by the transport of strain from region of the deforming material to another. This understanding has led to various classes of material behaviour including a gradient theory of elasticity, a gradient theory of defect dynamics, and a gradient theory of macroscopic plasticity [216].

Based on the afore-going understanding, the selected constituent materials were characterized using various methods before processing them into Nanoclay-infused AMCs. This was done

with the hope of gaining insight into their specific behaviour in their form and scale as received from their respective suppliers.

3.3.1 Apparent Density

Arnold Meter was used to determine the powders apparent density according to *MPIF 48* standard. The standard is suitable for both free and non-free flowing powders, premixes, and blended mixes.

3.3.2 Differential Scanning Calorimetry (DSC) / Thermogravimetric Analysis (TGA)

Materials are known to have different behavioural properties upon exposure to heat. Signature thermal properties of materials includes phase changes, fluctuations in weight, thermal expansion, diffusivity, and heat capacity. In order to understand and/or evaluate the temperature-dependent properties of the selected constituents, DSC-TGA thermal analysis was conducted using a *Thermal Universal Analyser Model: V4.5A* (Supplied by *TA Instruments*). Temperature was ramped up at 10^0C/minute to a maximum of 900^0C and immediately left to cool back to room temperature in the heating chamber. As most commercially available organoclays are known to decompose at temperatures higher than 212^0C [217], this procedure was especially important towards gaining an insight into the nanoclay's thermal behaviour in the extreme context of taking aluminium matrix to liquidous phase (>650^0C) as is normally the case in most processing techniques [218, 219]. With reference to Cloisites, it is further noted that degradation of the nanoclays may involve several mechanisms including the Hoffman elimination reaction, SN_2 nucleophilic substitution, thermal degradation of tallow residue, and the thermal decomposition of unexchanged surfactant [217].

For purposes of comparative analysis with respect to processing of Nanoclay-infused AMCs and bearing in mind the different views on processing atmosphere(s) for aluminium alloys such as vacuum, dissociated ammonia, argon, nitrogen, nitrogen/argon, and nitrogen/hydrogen mixtures [60, 121, 123, 220], an in-active processing atmosphere was preferred as a datum.

Accordingly, argon was chosen as the datum processing atmosphere at a flow rate of 2L/min [221]. However, it should be noted here that in powder metallurgy, argon is noted to be only effective at high green densities when magnesium is present [121] as was the case with the current study. This is mostly because, unlike a nitrogen atmosphere which promotes densification through nitridation, argon is inert and therefore has no associated chemical reactions in the alloy's constituents. Accordingly, any densification and sinterability relies heavily on cold welds created during green compaction, subsequent diffusion bonding process, and possible formation of liquid phases.

3.3.3 Fourier Transform Infrared Spectroscopy (FTIR)

FTIR spectrometer Model: Scimitar 800 FT-IR (Supplied by *Varian Inc.*) was used in order to verify any potential temperature-dependent chemical transitions of the nanoclays. For reference purposes, a sample of each of the nanoclays was analysed as supplied. The next set of samples was heated in argon atmosphere at 10^0C/minute to a maximum temperature of 635^0C and held at that temperature for 45 minutes before analysis. This temperature was selected based on DSC-TGA results for nanoclays and further fits into the supersolidus temperature range as depicted by *Figure 3-3*, which shows a representative Al-Cu binary phase diagram for AMB-2712. Two other follow-up sets of samples were similarly heated as the preceding set of samples but up to maximum temperatures of 590^0C and 550^0C, which respectively correspond to the solidus and eutectic temperature (548.2^0C) of the AMB-2712 alloy matrix. All the heated samples were left to cool down to room temperature in the heating chamber before FTIR analysis.

To facilitate FTIR analysis, each of the powder samples was mixed with 0.1g potassium bromide (KBr) as a carrier in the ratio of 1:100. The mixture was ground and blend manually using a set of ceramic mortar and pestle. The homogenous fine mixture was then put into a Beckman KBr Die with a maximum load rating of 10 Tons. In order to compact the powder

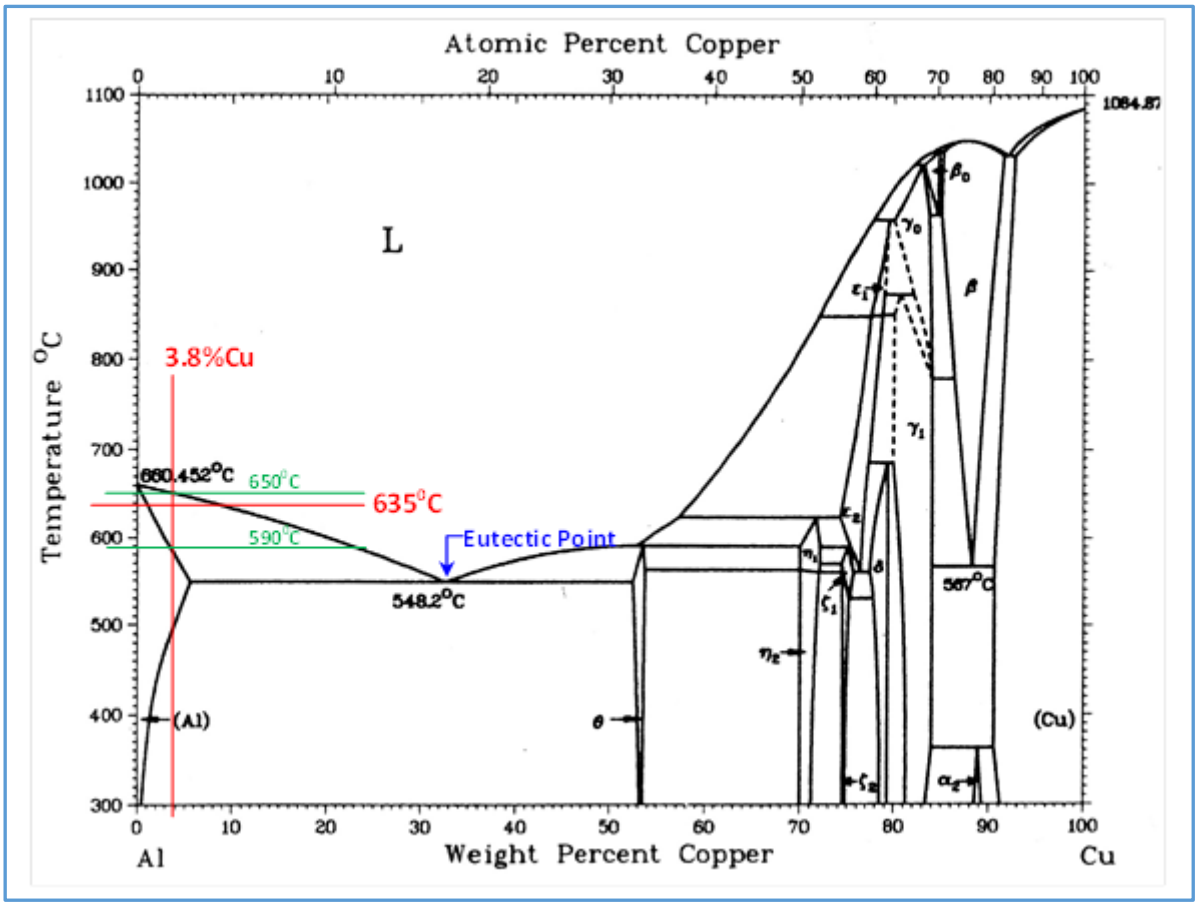

Figure 3-3: Al-Cu binary phase diagram [218, 219].

into a pellet, air pressure at 10 MPa was passed through the die for 8 minutes by means of a customized instrument supplied by the *Instrumentation Centre, Technicon Natal*. FTIR procedure was then run on the pellet with the intention of gaining an insight into thermal-resilience of nanoclay's constituent functional groups in the context of a thermal profile similar to that contemplated for the sintering of test specimens.

3.3.4 Optical Microscopy, TEM, SEM, and EDX

Powder's morphological analysis was conducted using a Transmission Electron Microscope, *TEM Model: Jeol TEM-1010*. Optical Microscope supplied by *Olympus Corporation, Japan*, and an Environmental Scanning Electron Microscope, *ESEM Model: S-3000N* (Supplied by *Karl Zeiss – Germany*) were used for microscopy. The latter equipment was further used to extract Energy Dispersive X-Ray Spectroscopy (EDX) results for the test samples.

3.3.5 Particle Size Analysis (PSA)

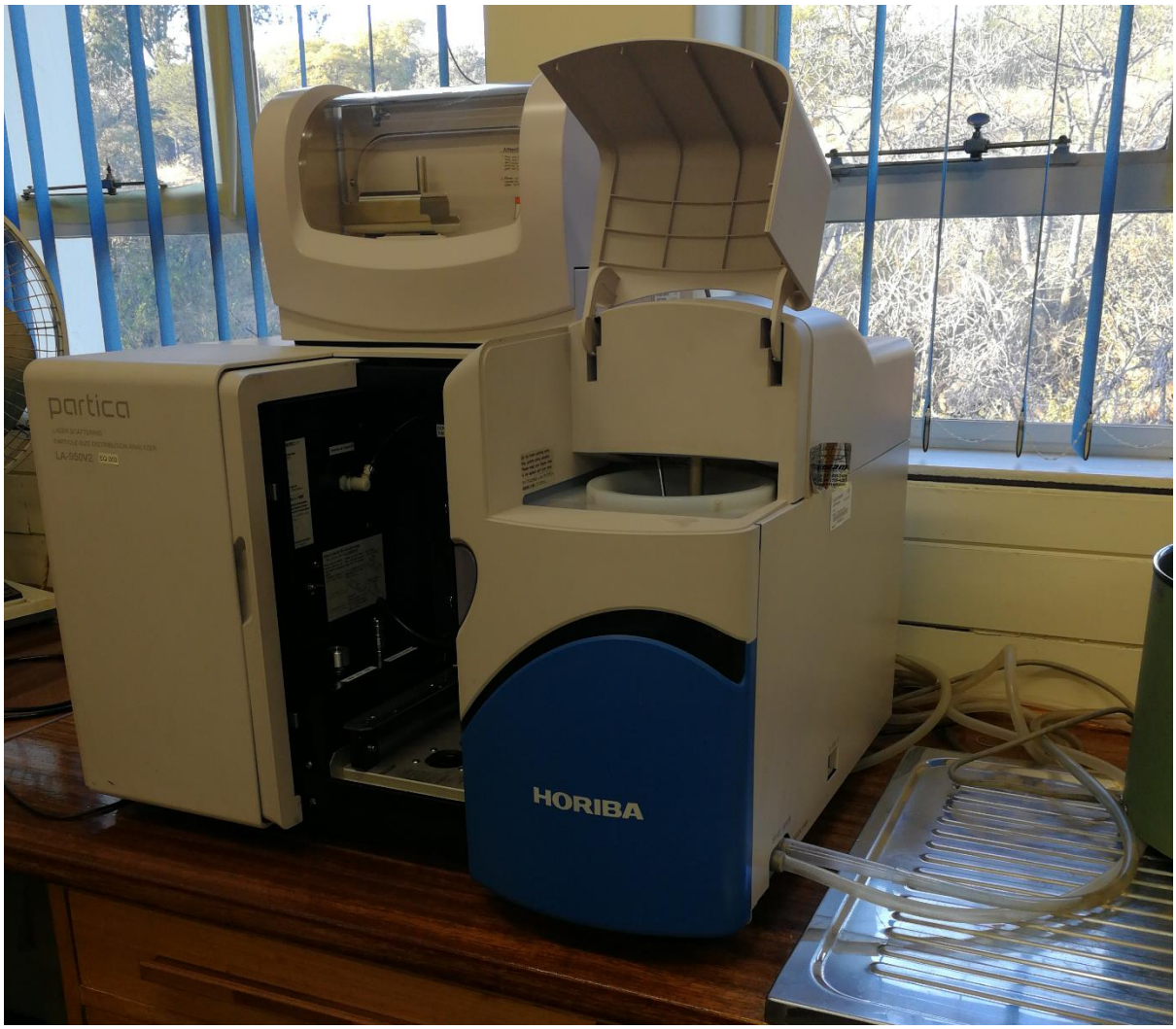

Figure 3-4: Particle Size Analysis Equipment located at CSIR, Pretoria.

Distribution of particles sizes is reported to affect the sinterability of Aluminium powders [59], whereby green density of compacts was observed to increase linearly with particle size distribution. This phenomenon was attributed to the smaller particles filling up the interstices between the larger ones, thereby increasing the overall density of the compact. In general, a narrow-size-distribution powder is preferred to monosized or broad-size-distribution powders for high sinterability and microstructure control of powder compacts provided that agglomerates in the starting powder are removed by appropriate means. In their work, J Ma and L.C Lim observed that powders with a higher geometric standard deviation (GSD = 1.6 and 1.9) exhibit superior sinterability compared to the near-monosized (GSD = 1.2) and broader

size distribution (GSD = 2.1). Despite there being an optimum range of particle size distribution for best sinterability of a given powder system, they noted that the resultant grain size at the final stage of sintering is very much determined by the sintering condition used but not the particle size distribution of the starting powder [59].

Since the atomized Acrawax-C was expected to only serve as a binder and lubricant during the green compaction stage and thereafter burn out, particle size distribution / analysis was conducted only on the AMB-2712 powder and *Nanofil 116* powders. *Figure 3-4* shows a *Laser Scattering Particle Size Distribution Analyzer LA-950* that was used to do the analysis according to *ASTM C1070* standard.

SECTION B: PROCESSING AND CHARACTERIZATION OF AMCs

3.4 Processing of Nanoclay-AMCs

Based on findings from DSC-TGA results with respect to temperature-dependent stability of the nanoclays, it was determined that the feasible processing temperature had to be below the liquidous temperature of Aluminium or AMB-2712 alloy. At the on-set, candidate processing techniques were: (i) *Spark-Plasma Liquid Sintering (SPLS)*, which is reported to allow sintering at relatively low temperatures under shorter time intervals [118] such as 500^0C with a holding time of 120 Seconds [119], (ii) *Conventional Powder Metallurgy (P/M)* processing, which similarly does not necessarily require the material to enter the liquidous phase and rather entails solid-state-sintering [50, 94], (iii) *Liquid Phase Sintering (LPS)*, a variation of conventional powder metallurgy process in which one of the admixed powders melt or reacts upon heating to form a liquid between the particles and thereby engulfing the more refractory phase, [61, 222] - the process consists of several overlapping steps involving solid-state diffusion, particle rearrangement, solution reprecipitation, and solid skeleton rearrangement, and (iv) *Supersolidus Liquid Phase Sintering (SLPS)*, a variation of *LPS* whereby pre-alloyed

powders are heated to a temperature between the solidus and liquidous temperature [50, 61]. Based on available raw materials, the latter option was chosen as the datum processing technique for the current study.

From a general perspective, powder metallurgy encompasses three key steps namely the blending of powders, green compaction of the powders, and sintering at a selected temperature profile and atmosphere. Advantages of powder metallurgy include, but are not limited to: (i) Efficient material utilization, (ii) Enables close dimensional tolerances, i.e. near-net shapes are possible, (iii) Good surface finish, (iv) Manufacture of complex shapes possible, (v) Hard materials used to make components that are difficult to machine can be readily made, e.g. tungsten wires for incandescent lamps (vi) Environment friendly, energy efficient, (vii) Suited for moderate to high volume component production, (viii) Powders of uniform chemical composition - reflected in the finished part, (ix) wide variety of materials - miscible, immiscible systems, refractory metals, and (x) Parts with controlled porosity can be made. It's limitations include the high cost of powder material & tooling, the parts thus made being less strong than wrought ones, and the process is less well known [223].

3.4.1 Blending of Powders

Table 3-3: Powder Mixture Sets

Mix Sets	**REF**	**1**	**2**	**3**	**4**	**5**	**6**
Nanofil 116	0%	1%	3%	5%	8%	10%	12.5%
Aluminium (AMB 2712 Alloy)	100%	99%	97%	95%	92%	90%	87.5%

The AMCs were prepared by mixing *AMB-2712* powder with varying amounts of *Nanofil 116* in %wt ratios. *Table 3-3* shows the most commonly used mixes used in this study. Other combinations include and these are not exhaustive. Atomized *Acrawax-C* powder was added into the composite powder mix on basis of 1.5% of the mix-set weight [224]. In order to achieve

a homogenous mix, every mix set of mixture was mechanically mixed using a *TURBULA System planetary mixer Type T2C* for 20 minutes [121]. Alternative mixing time used by other researchers was noted to vary from 10 minutes [108] to 30 minutes [50].

3.4.2 Green compaction of powders

Figure 3-5: Green compaction hydraulic machine, housed at CSIR, Pretoria.

Green compact samples for the datum sintering process were made from the homogenous powder mixtures using the biaxial hydraulic press shown in *Figure 3-5*. The press, located at the *Council for Scientific and Industrial Research (CSIR)* in Pretoria, had a rated maximum capacity of 100 Tons / 700 Bars / 1000 kN. Green compacts were cylindrical in shape based on available compaction dies. Based on compaction gauge pressure of 160, 200, and 240 Bars and a die cavity of Ø17.5mm, effective green compaction pressures of 950, 1187, and 1425 MPa were used, respectively. With an average feedstock powder of 7g, the corresponding resultant green compacts measured to an average height of 11.5mm, 11.0 mm, and 10.5mm, respectively. For ease of reference, these specimens were named *Batch 1*. All the dies used in this study were made from high-speed-tooling-steel.

3.4.3 Sintering of green compacts

For the sintering stage, a sintering boat made of Zirconia (Zr) was used. Interior dimensions of the boat measured 17.5 mm (height) by 20 mm (width) by 95 mm (length). It has an average wall thickness of 2.5 mm. Four Al-Nanoclay composite specimens were packed in the sintering boat for every of the sintering cycles with an approximate equal spacing between any two adjacent specimens as well as from the boat's interior end-walls along the boat's length. Care was taken to position them centrally with reference to the 20 mm width, thereby leaving an approximate 1mm-spacing between the specimens and the boat's interior side-walls.

Figure 3-6 shows a horizontal tube furnace *Model No. STF16/180* supplied by *Carbolite, UK*, which was used for sintering all the AMCs. The furnace is housed at CSIR in Pretoria and has a maximum temperature of 1600^0C. Sintering was done at 635^0C for 45 minutes; a sintering profile closely aligned to those used elsewhere [52, 60, 121, 123, 124, 220]. The sintering temperature was chosen in consultation with the Al-Cu binary phase diagram and with due reference to DSC-TGA results for *Nanofil 116*. This selective reference to copper was based

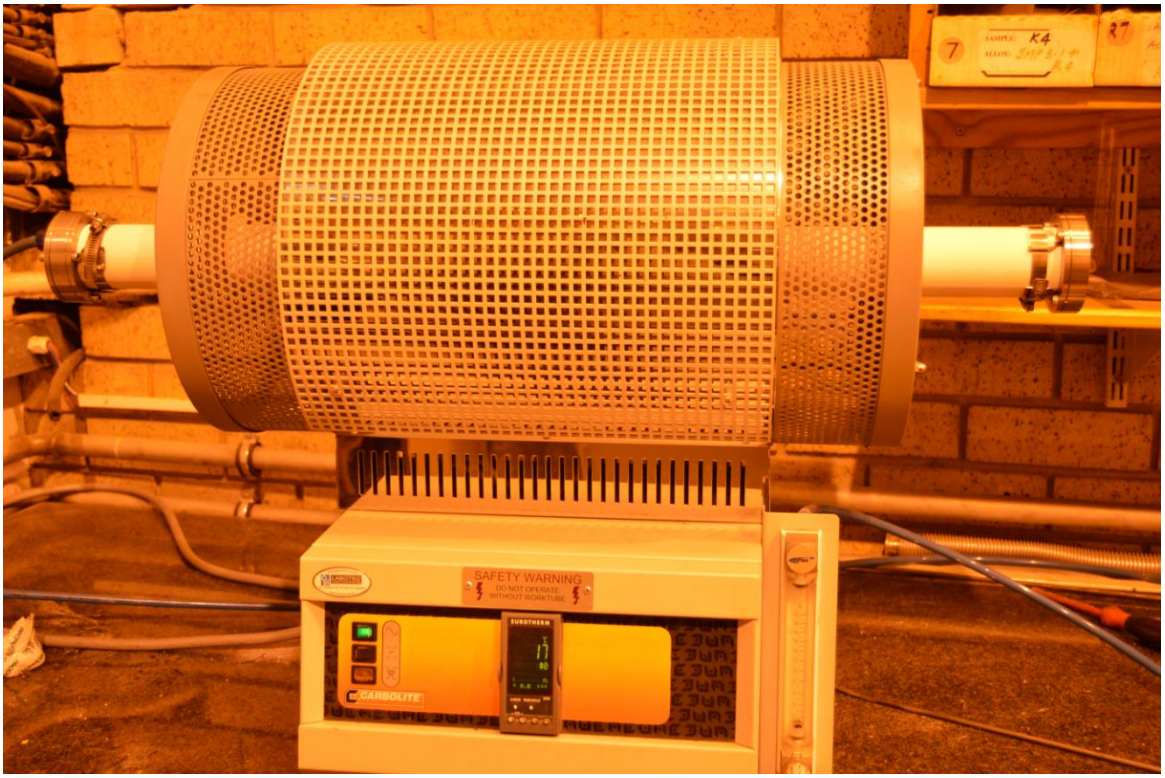

Figure 3-6: Horizontal tube furnace, housed at CSIR, Pretoria..

on the fact that Copper constitutes the highest proportion amongst all the alloying elements in Al-2712. *Figure 3-7* illustratively summarises the experimental datum sintering-profile, namely *Set "A" Run*.

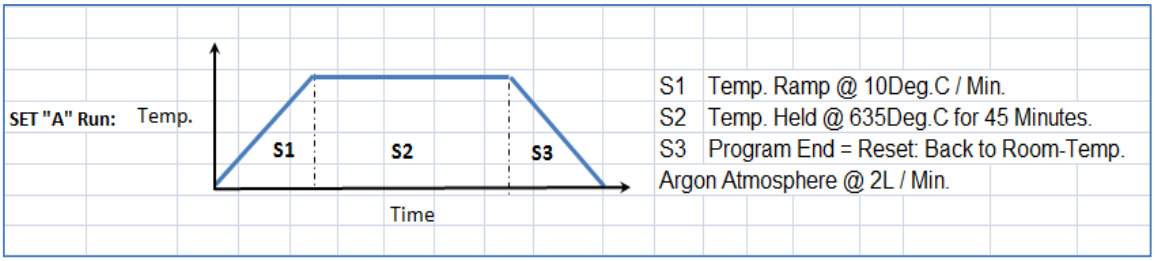

Figure 3-7: Datum sintering profile (*Set "A" run*).

3.5 Characterization of Nanoclays - AMCs

3.5.1 The Sintered Samples

3.5.1.1 Physical inspection

The samples were inspected for any visible deformities. A preliminary grinding test was also conducted to assess if the samples were sufficiently sintered.

3.5.1.2 Sintered density and Porosity

Sintered density of the specimens was determined using the Archimedes principle. The process entails weighing a sample in air and then weighing it while immersed in a liquid, which can either be water or oil (for highly porous samples). For a fully immersed object, the sintered density is then calculated using the formula [225]:

$$\frac{Density\ of\ object}{Density\ of\ fluid} = \frac{Weight}{Weight - Apparent\ Immersed\ Weight}$$

As a follow-up parameter, porosity of the respective sintered AMC specimens was quantified using the formula:

$$Porosity = \frac{(Theoretical\ Density\ of\ Alloy - Sintered\ Density)}{Theoretical\ Density\ of\ Alloy} \times 100\ \%$$

3.5.1.3 DSC-TGA

Figure 3-8 shows the sampling schematic for DSC-TGA analysis. Of the three samples, two randomly selected samples were used for analysis. The ensuing reference numbering of samples as 1 or 2 was independent of the original location.

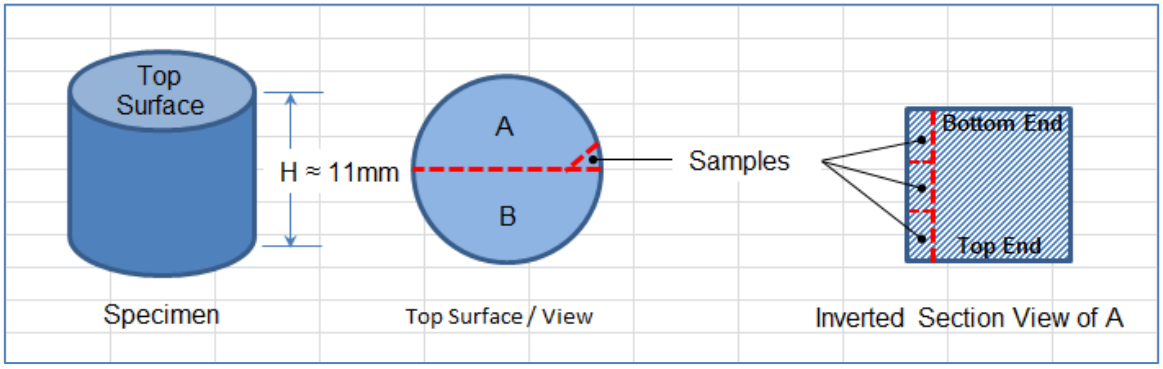

Figure 3-8: DSC-TGA Sampling schematic.

3.5.1.4 Optical Microscopy, SEM, EDX

With reference to *Figure 3-8*, the flat rectangular plane of section B of the sintered specimens was used for microscopy. Metallographic preparation of the samples was executed using *Struers MD-System*^{TM} involving four steps: (1) Grinding on SiC foil with a grain size of *46µm*, (2) Polishing using MD-Largo (hardness: HV 40 – 150) with *9µm* diamond suspension

(Allegro Largo), (3) Polishing using MD-Mol (Woven 100% wool) with *3μ* diamond suspension (Diapro Mol B3), and (4) Polishing using MD-Chem (Porous Neoprene) with *0.04μm* colloidal silica suspension (OP-S). No etching was used on the samples.

As with the raw materials, an *Optical Microscope* supplied by *Olympus Corporation, Japan*, and an *Environmental Scanning Electron Microscope, ESEM Model: S-3000N* (Supplied by *Karl Zeiss – Germany*) were used for microscopy. Similarly, the latter equipment was further used to extract *Electron-Dispersion X-Ray (EDX)* results for the sintered AMC samples.

3.5.1.5 X-Ray Diffraction (XRD) analysis.

Samples measuring Ø10mm by 2mm in thickness were machined from the datum reference specimens and subjected to an XRD analysis. The phase compositions were determined using a Phillips X-Ray Diffractometer operated at 40kV and 20mA, in the 2Theta range 20 – 90º. The objective was to investigate any chemical transitions as a result of infusion of *Nanofil 116* and the datum sintering process.

3.5.2 Thermal Properties

Another set of specimens named *Batch 2* was prepared for assessment of additional thermal properties, in particular the coefficient of thermal expansion, thermal conductivity, thermal diffusivity, and specific heat capacity. Green cylindrical compacts having Ø8mm were prepared for coefficient-of-thermal-expansion samples, which were then machined to Ø6mm x 25.4mm length after sintering. The die used had an internal diameter of 7.5mm.

Similarly, green compact discs measuring approximately Ø43mm x 3mm thickness were prepared. After sintering, smaller discs measuring Ø19mm x 3mm were wire-cut as specimens for thermal conductivity, thermal diffusivity, and specific heat capacity. A common green compaction pressure of 550MPa was used for both the rods and discs, a value closer to the regime used on AMB-2712 by other researchers [108, 222]. *Table 3-4* shows the portfolio of

samples compacted and sintered for thermal properties analysis. For consistency, sintering of these specimens was accomplished using the datum *Set-"A"-Run* profile in argon atmosphere.

Table 3-4: Thermal properties samples matrix

Composition →	Geometry	REFERENCE	1%	2%	3%	4%	5%
Pressure ↓							
16.5 Bars (550 MPa)	 Ø = 8mm, Length = 25mm	✔	✔	✔	✔	✔	✔
558.8 Bars (550 MPa)	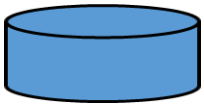 Ø = 43mm Height = 3mm	✔	✔	✔	✔	✔	✔

Based on preceding results for *Set-"A"-Run* samples, it was deemed necessary to only further test three representative samples. Accordingly, specimens subjected to further testing included the Reference, 1%wt, and 3%wt *Nanofil 116* specimens. Nonetheless, other relevant data such as the sintered density, optical micrographs, SEM, and EDX analysis was collected for all samples in order to aid in comparative analysis of the entire batch.

The thermal properties tests were done in a *South African National Standards* (SANAS) accredited laboratory. The measurement of thermal expansion was done in accordance with work procedure MSM-LM-WP-317 Rev 01 for measurement of thermal expansion, which is in alignment with section 5.3 of BS 1902. Determination of thermal conductivity was by laser flash method according to work procedure MSM-LM-WP-307 Re 04, which is in alignment with ASTM E 1461. The laser flash method entails heating the front side of a small, usually disk-shaped plane parallel sample by a short (61 ms) laser pulse. The temperature rise on the

rear surface is measured versus time using an infrared detector. All samples were coated on both faces with a very thin layer of colloidal graphite. The thermal diffusivity *a*(T) values can then be converted to thermal conductivity ʎ(T) by using the specific heat Cp(T) and bulk density ρ(T) of studied material according to [226]:

$$ʎ(T) = a(T).Cp(T).ρ(T)$$

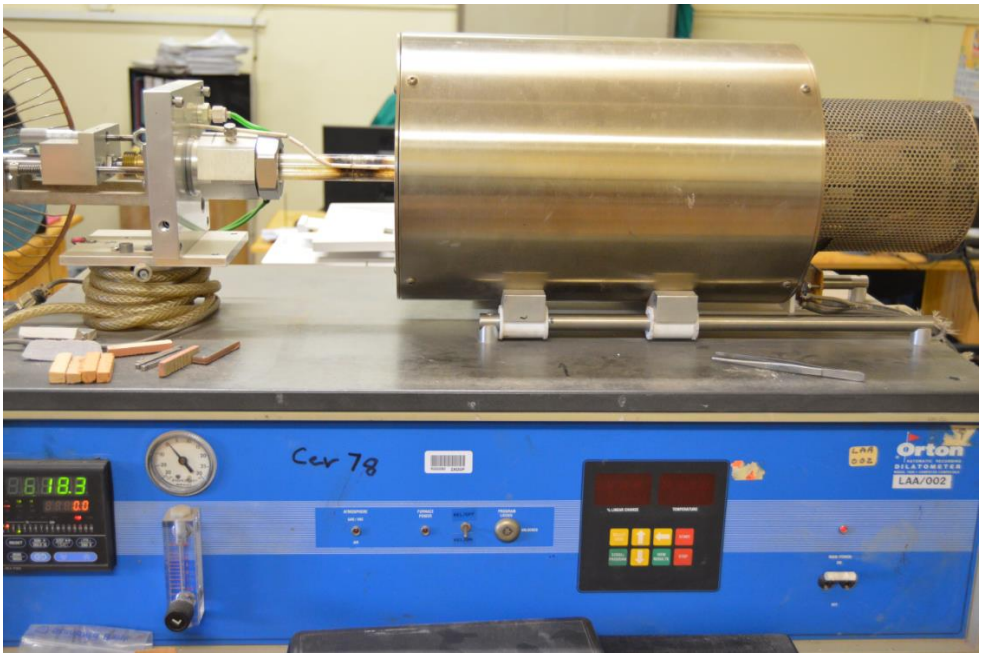

Figure 3-9: Orton Automatic-Recording Dilatometer.

Figure 3-10: Anter Flashline 3000 apparatus.

In the case of Reference specimens, thermal expansions were first carried out to 520^0C in argon atmosphere. After that, the three categories of specimens were tested in air to 320^0C. *Figure 3-9* shows the computer-compatible *Orton Automatic Recording Dilatometer Model 1600* that was used for recording of thermal expansions data while *Figure 3-10* shows the *Anter Flashline 3000* apparatus that was used for thermal conductivity work (conductivity, diffusivity, and specific heat capacity), which was carried out at three different temperatures (120, 220, and 320^0C) in argon atmosphere. All these tests were conducted in line with procedures accredited by the *South African National Standards* (SANAS) for Cermalab / Light Metals Collaboration laboratory.

In order to gain further insight into results for this set of specimens, metallurgical samples were hot mounted at 165^0C (max.) in Bakelite using *ATA-Opal 450* supplied by *Advanced Laboratory Supplies (ALS)*. They were then prepared for microscopy using *ATA Saphire 550* supplied by *ALS*. Since this exercise were performed at a different site with a different set grinding and polishing facilities, the following steps were used. (1) grinding with 800-grit SiC paper in water for 4 minutes at 300 revolutions per minute (rpm) and 25N load, (2) grinding with 1200-grit SiC paper in water for 3 minutes at 300 rpm and 15 N load, (3) grinding with 2400-grit SiC paper in water for 3 minutes at 300 rpm and 15 N load, (4) grinding with 4000-grit SiC paper in water for 3 minutes at 300 rpm and 10 N load, (5) polishing with 50nm alkaline colloidal silica for 10 minutes at 150 rpm and 10N load, (6) cleaning in water for 10 minutes at 150 rpm and 10N, and (7) drying using 5.3-bars compressed air. Optical microscopy was conducted on un-etched samples using a *Leica* optical microscope while SEM and EDX were conducted using a JEOL Scanning Electron Microscope.

3.5.3 Machinability

With reference to *Figure 3-8*, the flat rectangular plane of section A (*Batch 1* specimens) was used for machinability testing. The samples were mounted using *Fast-Cast*^{TM} resin system

supplied by *AMT South Africa*. The sampling surfaces were milled using Ø20mm High Speed Steel (HSS) cutting tool (0.00GRAD). Final cutting conditions comprised of a cutting speed of 1910 rpm (Ø20 @ 120 m/min), feed rate of 382 mm/min (0.1 mm/Tooth), and a 0.5 mm depth of cut. As with machining of other comparable materials, no cutting fluid was used [227].

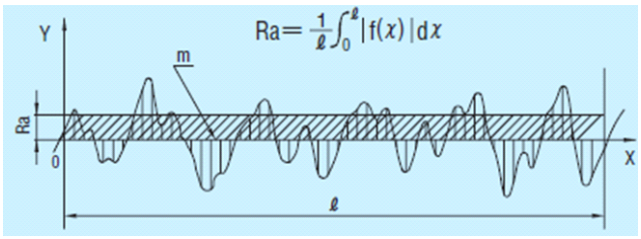

(a) R_a Criterion

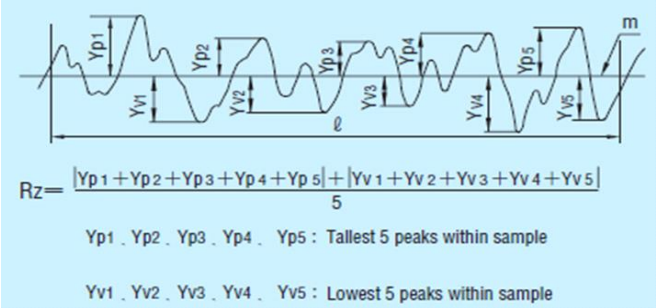

(b) R_z Criterion

(i) (ii)

Figure 3-11: (i) Surface finish profilometer, and (ii) Quantification criteria $\boldsymbol{R_a}$ & $\boldsymbol{R_z}$ [228].

Figure 3-11(i) illustrates the set-up for machinability rating with reference to surface finish as was determined using a *Taly-Surf*^{TM} profilometer, while *Figure 3-11(ii)* explains the surface finish quantification criteria R_a and R_z as given on an excerpt from *Japanese Industrial Standards (JIS) B 0031(1994)* [228]. These reference values were used throughout the analysis. Ten readings were taken for each sampled surface and arithmetically averaged to get a representative mean value for the sample and standard deviation.

3.5.4 Mechanical Properties

3.5.4.1 Hardness Testing

Since experimental procedures were carried out at different geographical sites based on the

availability of equipment, hardness testing of specimens was conducted using either Rockwell B Hardness or Vickers scale depending on the available equipment at the respective locations.

Rockwell B Hardness

After microscopy, the metallographically prepared surface of samples was further used for hardness testing. The assumption here was that no significant residual stresses emanated from the preparation process of the specimens. The test procedure was in alignment with *ASTM E18-02*. A spherical ball indenter (Ø1.588mm) was used with a 588N load being applied for a pre-set dwell time of 8 seconds. For each sample, at least five readings were taken, arithmetically averaged, and a standard deviation from the mean calculated thereof.

Vickers Hardness

The testing was in alignment with *ASTM E92-17*. A load of 2Kg force was used and a dwell time of 15 seconds. For each sample, at least five readings were taken, arithmetically averaged, and a standard deviation from the mean calculated thereof.

3.5.4.2 Tensile properties

Batch 3:

Based on on-site available equipment, dumbbell-shaped green compact samples were made from the homogenous powder mixtures using a 30kN biaxial hydraulic press (*MTS Criterion Model 43*) in accordance with *ASTM B965-03*. Surface area of the dumbbell profile face was 1 square inch (645.16mm^2). *Gauge Length* (L) of the samples was 25mm and the target cross-section *Width (W)* and *Thickness (t)* at the mid-section were 6mm by 5mm respectively. The maximum load capacity of the machine was used as the green compaction load, interpreting to a compaction pressures of 46.5 MPa. Datum sintering profile and atmosphere were used to sinter this batch of specimens.

Gauge length of the sintered samples was 25mm. Cross-sectional area was calculated based on measured width and thickness at the mid-section of the gauge length. Tensile testing was

conducted using the *MTS Criterion Model 43* universal testing machine having a maximum loading capacity of 30kN. A strain rate of 1mm per minute was used for all the samples. Three compacts were successfully sintered and duly tested. The maximum load values were recorded net of the preloads.

Batch 4:

The primary objective of *Batch 4* was to optimize the processability of nanoclay-AMCs through iterative experimental assessments. For the sake of consistency in processing of datum specimens, the pre-mixed powder was biaxially compressed into cylindrical green compacts measuring ø43mm using a 1000kN, 700-Bar hydraulic press. Aluminium powder with *Nanofil 116* as the fortifying ingredient were biaxially pressed in a Ø43mm die using green compaction pressures of 350, 438, and 525 Bars. These compaction pressures were selected on the basis of 50, 63, and 75% of load capacity of the then available press machine. Choice of the die size was based on targeted post-sintering wire-cutting and machining of tensile testing samples from the successfully sintered specimens.

Compacts were then sintered in the tube furnace using the sintering profile illustrated in *Figure 3-12*. This profile was chosen after a series of trials as detailed in the succeeding section on processability. The delubrication temperature was set at 450^0C based on the DSC results for the atomized *Acrawax-C*. The sintering atmosphere for this batch was switched from argon to nitrogen for 30 minutes in *S4* stage, with the end of the 30 minutes marking the start of *S5* stage. The switching of atmosphere was founded on the understanding that an addition of 0.1-1 wt-%Mg has been reported to facilitate break-up of the surface oxide layer on aluminium and its alloys through the development of $MgAl_2O_4$ phase [229]. At elevated Mg contents however, it is reported that the inferior phase does not completely dissolve in solid solution and therefore stays as a complex at the grain boundaries resulting to embrittlement of the alloy [230]. This sintering profile was named *Set-"AD"-Run* for ease of reference.

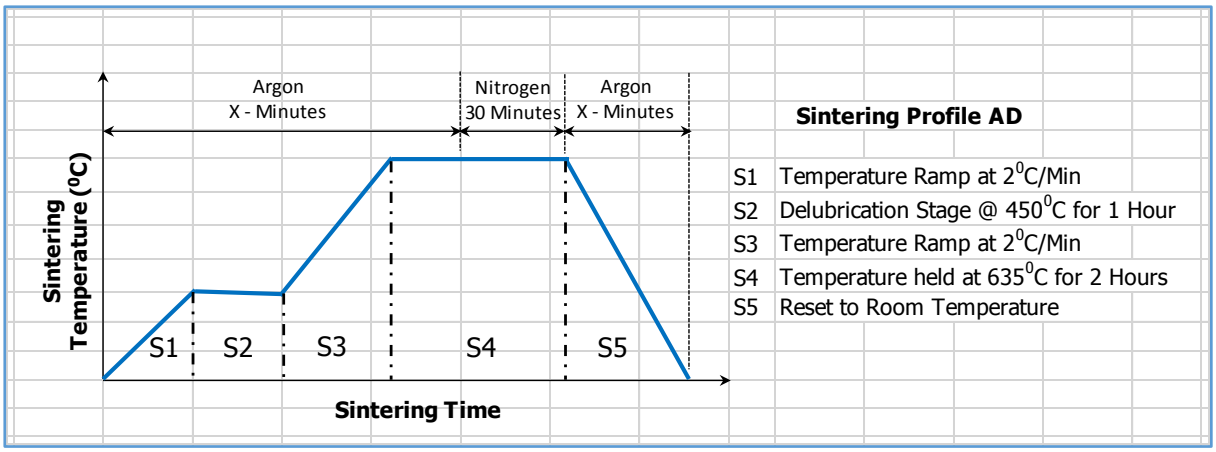

Figure 3-12: Sintering profile for *Batch 3* (*Set-"AD"-Run*).

From the sintered specimens, Ø10mm cylindrical samples were wire-cut and machined to a dumbbell-shape for tensile testing. The dimensions of test samples and testing procedures were in alignment with *ASTM E63-01* standards. However, the samples diameter at the gauge length was only machined to Ø5mm instead of the standard's Ø2.5mm. This modification was deemed necessary after observed fracture of some of the specimens during the trial stages of turning. The tensile testing results there-off were further deemed relevant and valid based on four aspects: (1) this was a comparative study on the samples, (2) the modification was uniformly applied entirely to this batch of samples, (3) the samples were for tensile testing, yet turning entails axial loading on the test samples, and (4) tensile test results are fundamentally normalised, i.e. they are based on relative measurements between load and cross-sectional area at every data point.

After wire-cutting the tensile test samples, the remaining shell of each specimen was used for sampling of test samples for either *Rockwell-B* hardness testing, assessment of sintered density, DSC-TGA, and/or microstructural analysis.

3.6 Processability of Nanoclay-AMCs

Using *Batch 4* specimens, and further relating to results from the preceding other batches, the effect of a variety of processing variables was evaluated, including: (i) Sintering temperature

limitations (ii) Type of nanoclay used, i.e, effect of composition of the reinforcement system, (iii) Sintering profile, and (iv) Sintering atmosphere. The objective of this stage was to gain an insight into the effect of different processing variables and optimize the processing settings for Nanoclay-AMCs.

3.6.1 Sintering temperature and time

A set of samples of the matrix alloy as supplied were pressed at the same green compaction pressures as the datum reference samples, i.e. same as *Batch 1*. However, this set was sintered using the profile shown in *Figure 3-13*, whereby the temperature ramping was similar to that of datum *Set-"A"-Run* profile but with a higher holding temperature of 650^0C for a duration of 2 hours. This sintering profile was for general reference purposes and named the *"Trial-Run"*. Two sets of processing parameters were used. Its objective was to tentatively assess, deduce, and / or establish a feasible range of process settings with respect to sintering temperature and time for the alloy under study. In essence, *Set-"A"-run* sintering parameters were conceptualized in consultation of the preliminary visual inspection and destructive-testing (grinding) results from the *Trial-run* samples.

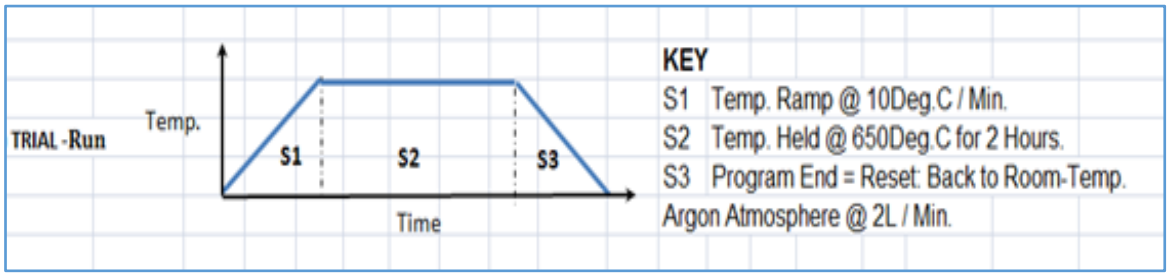

Figure 3-13: "*Trial-Run"* sintering profile representing evaluation of sintering temperature thresh-hold.

3.6.2 *Nanofil 116* versus *Cloisite* Ca^{++} *DEV*

Specimens were processed using *Cloisite* Ca^{++}*DEV* as the reinforcement ingredient under similar processing conditions as those used for the datum samples, i.e. similar to *Batch 1*. These specimens were then evaluated comparatively against results for *Nanofil 116*.

3.6.3 Effect of processing parameters

Table 3-5: *Nanofil 116*-AMCs green compaction and composition optimization matrix.

Composition →	REFERENCE	1%	2%	3%	4%	5%	10%
Pressure ↓							
350 Bars	✔	✔	✔	✔	✔	✔	✔
438 Bars	✔	✔	✔	✔	✔	✔	✔
525 Bars	✔	✔	✔	✔	✔	✔	✔

Table 3-5 shows the matrix of (*Batch 4*) green compaction pressures and compositions of the evaluated AMCs. On the other hand, *Figure 3-14* shows the different sintering profiles and atmospheres that were used in processing these specimens.

Specimens were then sampled for further characterization in terms of sintered density, optical micrographs, SEM–cum–EDX analysis, DSC-TGA, *Rockwell-B* hardness, and/or tensile strength properties. The sampling was necessitated by the need to prioritize samples and thereby minimize the number of samples in view of the time-duration required for sintering each specimen and demand for use of the sintering facility by other users. Accordingly, the sampling was done aimed at the following objectives:

(1) To assess the effect of %wt of *Nanofil 116* on the AMCs.

(2) To assess the effect of green compaction pressure on the AMCs.

(3) To assess the effect of sintering profile and atmosphere.

(4) To deduce threshold %wt *Nanofil 116* and green compaction pressure for sinterability of the AMCs.

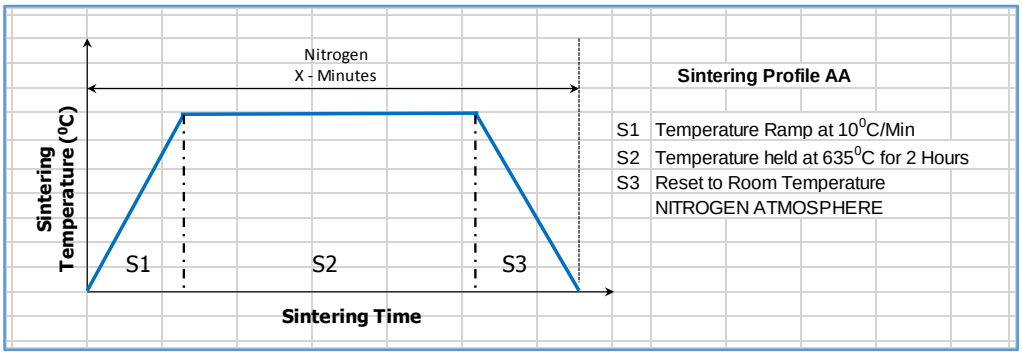

(i) Set-"AA"-Run

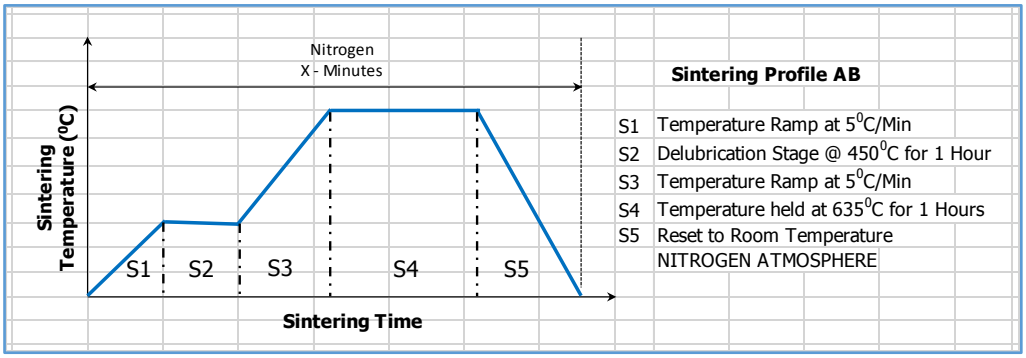

(ii) Set-"AB"-Run

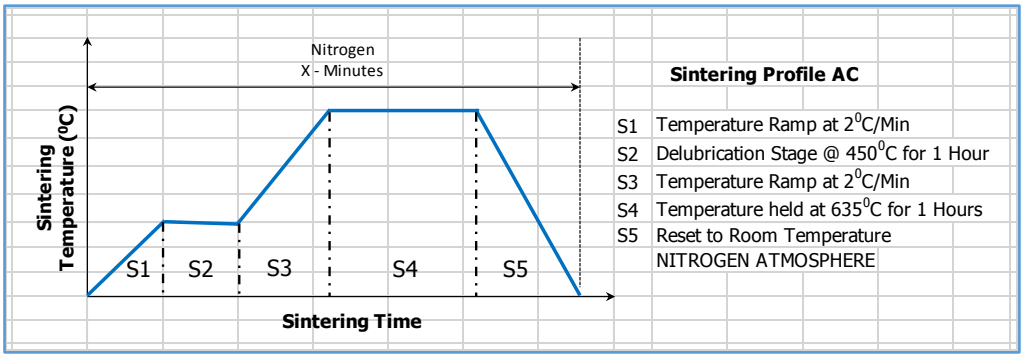

(iii) Set-"AC"-Run

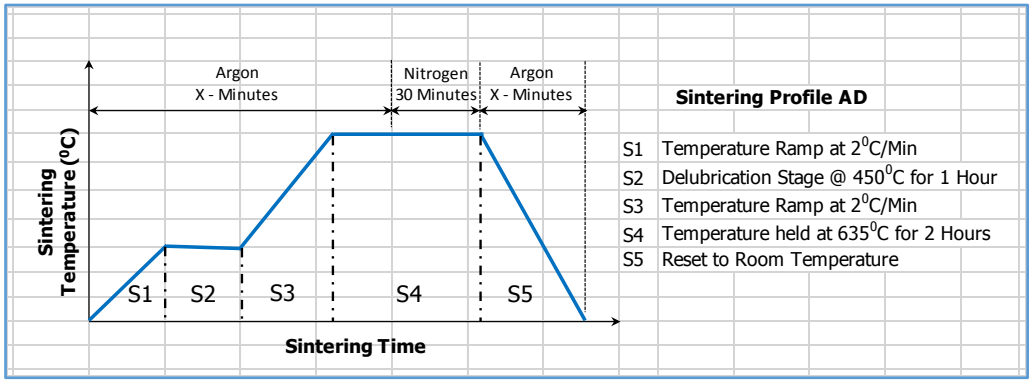

(iv) Set-"AD"-Run

Figure 3-14: Optimization sintering profiles and atmospheres for *Nanofil 116*-AMCs.

3.7 Summary

The experimental processes used in this study were aligned as much as possible to generally accepted work procedures and test standards. They may not be exhaustive but have been deemed sufficient for an understanding of Nanoclay-AMCs. For ease of reference, *Table 3-6* shows a summary of the pressed green compacts, their respective sintering conditions, and the eventual use in different chapters. Further examinations and/or test procedures may be adopted towards specific target applications of the AMCs thus developed, for instance electrical properties and tribological analysis aimed at electrical and wear-related applications, respectively. The possibilities are diverse, unlimited, and do present an opportunity for future work.

Table 3-6: Summary of green compacts, sintering profiles, and targeted use.

Sintered Specimens	Sintering Profile	Targeted Use
BATCH 1 **(160 / 200 / 240) Bars** **(950 / 1187 / 1425) MPa**  Ø = 18 mm Height ≈ 11 mm Sampled for sintered density, microstructural analysis XRD, DSC-TGA (Thermal Behaviour), Hardness, and Machinability tests	**(i) SET-"A"-RUN** 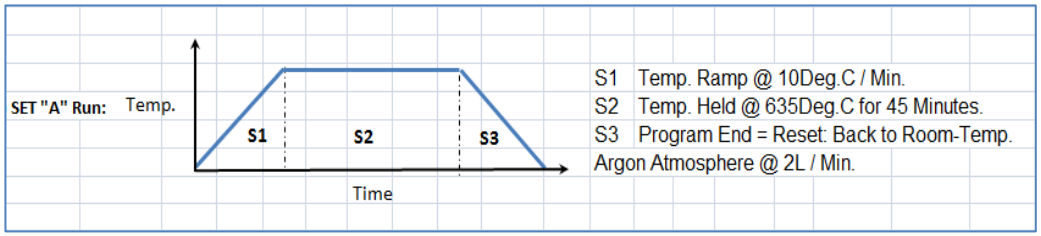	**(i) Characterization of:** Nanofil 116-AMCs • **Chapter 5** Physical inspection, Sintered density, Microstructures, XRD. • **Chapter 6** DSC-TGA (Thermal behaviour). • **Chapter 7** Hardness. • **Chapter 8** Machinability. & **Processability:** Nanofil 116-AMCs - Versus - Cloisite Ca^{++}DEV-AMCs • **Chapter 9** Machinability.

<table>
<tr>
<td></td>
<td><u>(ii)</u> TRIAL-RUN
 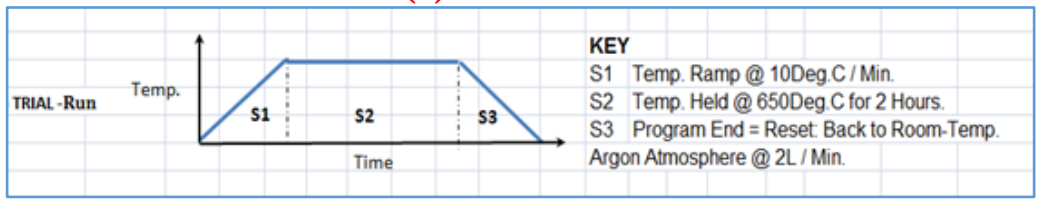
</td>
<td><u>(ii)</u> Processability:
Trial-Run
- Versus -
Set-“A”-Run
• Chapter 9
Physical inspection,
DSC-TGA,
Machinability.</td>
</tr>
<tr>
<td>BATCH 2
<u>Rods</u>: 16.5 Bars (550 MPa)
 
Ø = 8mm, Length ≈ 27 mm
Turned into Ø6mm x 25.4mm
<u>Discs</u>: 558.8 Bars (550 MPa)
 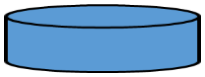
Ø = 43mm
Height = 3mm
Wire-cut to obtain discs measuring Ø19mm x 3mm.</td>
<td>SET-“A”-RUN
 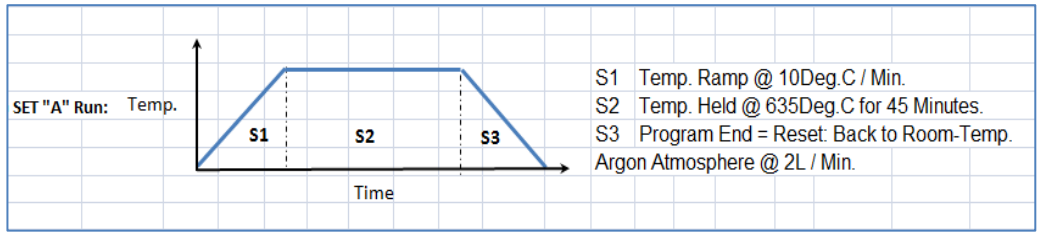
</td>
<td>Characterization of:
Nanofil 116-AMCs
• Chapter 5
Physical inspection,
Sintered density,
Microstructures,
SEM/EDX.
• Chapter 6
<u>Rods:</u>
Thermal Expansion.
<u>Discs:</u>
Thermal Conductivity,
Thermal Diffusivity,
Specific Heat Capacity.
• Chapter 7
<u>Discs:</u> Hardness</td>
</tr>
</table>

BATCH 3 **(46.5 MPa)** Dumbbell-Shaped Specimens (*Rectangular* cross-section) 	**SET-"A"-RUN** 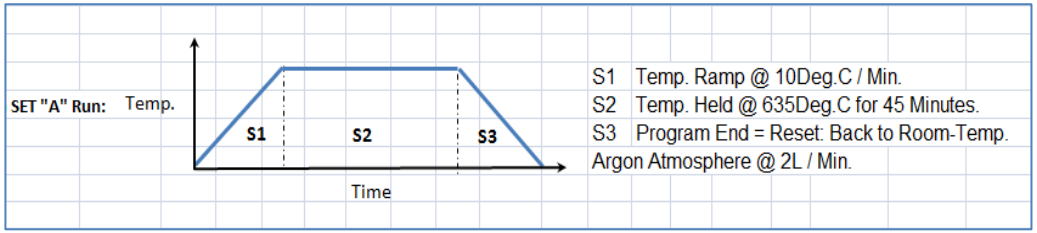	**Characterization of:** Nanofil 116-AMCs • **Chapter 7** Physical inspection, Sintered density, Tensile tests.
BATCH 4 **(350 / 438 / 525) Bars** **(344 / 431 / 516) MPa** 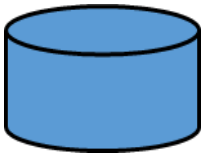 Ø = 43mm Height ≈ 15 mm Wire-cut and turned into *Cylindrical* dumbbell-shaped tensile test specimens.	**SET-"AA"-RUN** TO **SET-"AD"-RUN** 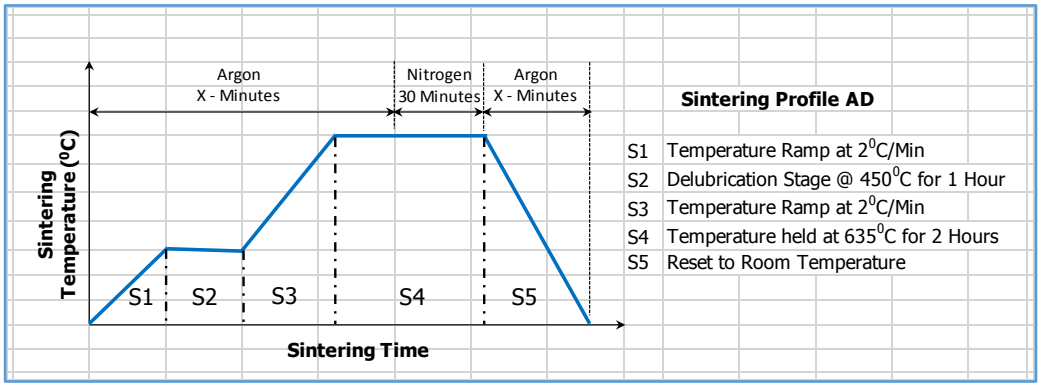	**Processability of:** Nanoclay-AMCs • **Chapter 9** Physical inspection, Sintered densities, Tensile tests, Microstructures, SEM/EDX.

CHAPTER 4:

RAW MATERIALS - CHARACTERIZATION

4.0 Introduction

This chapter details the results and discussions on the characterization of raw materials used in the current study. Aspects covered include the apparent density, differential scanning calorimetry and thermogravimetric analysis (DSC-TGA results), fourier transform infrared spectroscopy (FTIR), optical microscopy, transmission electron microscopy (TEM), scanning electron microscopy (SEM), electron-dispersion X-Ray (EDX), and particle size analysis.

4.1 Apparent Density

Average mass of AMB-2712 powder for the Arnold Meter samples was 25.272g with a standard deviation of 0.231g. Apparent density of the plain powder was determined to be 1.264 g/cm^3.

4.2 DSC - TGA

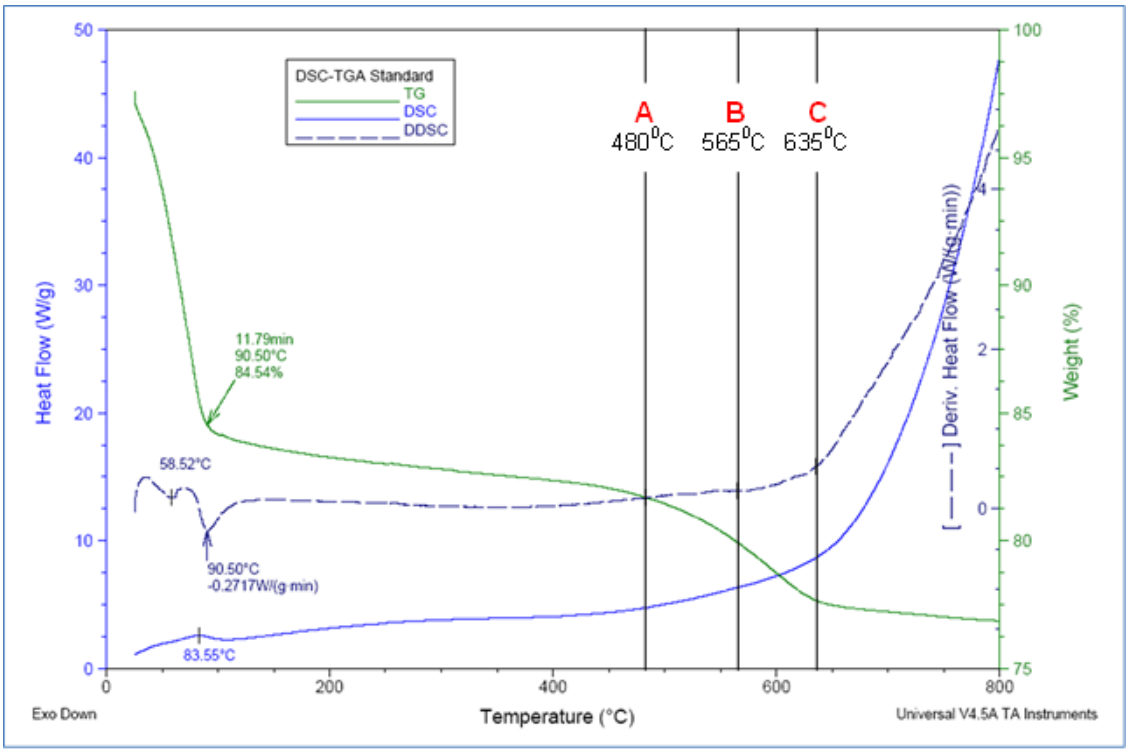

Figure 4-1: DSC-TGA Results for *Nanofil 116*.

Figure 4-1 shows DSC-TGA results for *Nanofil 116* as-received from supplier. Lines A, B, and C correspond to the temperature at 480^0C, 565^0C and 635^0C respectively. The graph shows that the nanoclay lost 15.46% of its weight at 90^0C. This dominant mass loss was due to dehydration of interparticle water, adsorbed water and interlayer water [231, 232]. Elsewhere [217], water in nanoclays is said to be in the form of free water (generally released below 100^0C), bound water (below 300^0C), and structural water (near 600^0C). A heat flow endothermic peak corresponding to the 15.46% weight loss was observed at the 90^0C. From 100^0C to about 450^0C, the nanoclay lost an additional 1% weight. This may be attributed to burn out of organic compounds in the nanoclay. Another 5% weight was lost within the 450^0C and 650^0C temperature range after which there was no significant weight loss corresponding to the increase in temperature. This latter mass loss was due to dehydroxylation of the nanoclay [231].

Of significance was the observation that the lines A, B, C map the maximum gradient zone on the TG curve, which falls within the 450-650^0C temperature range that befit with the supersolidus phase according to the Al-Cu binary phase diagram at 3.8%wt Cu content [218, 219]. A corresponding sharp rise in heat flow at around 650^0C was observed, being related to the end of release of OH groups from the octahedral layer [231]. The slight change in gradient of the heat flow graph at around 800^0C possibly marks the start of recrystallization. According to supplier's specifications, the nanoclay has a moisture content of 11% and was subject to 8% weight loss on ignition. These two sets of information comparatively imply that, besides the weight loss attributable to moisture content, *Nanofil 116* may be deemed functionally active upto a temperature of 650^0C, inclusive of a 200^0C temperature-window during which thermally-instigated chemical-reactions and/or transformations may be considered to occur. It was on basis of this temperature-dependent-stability of nanoclays that powder metallurgy or its variants was determined to be the most feasible processing route, i.e. the possibility of processing nanoclay-AMCs at temperatures below the liquidus temperature of the matrix.

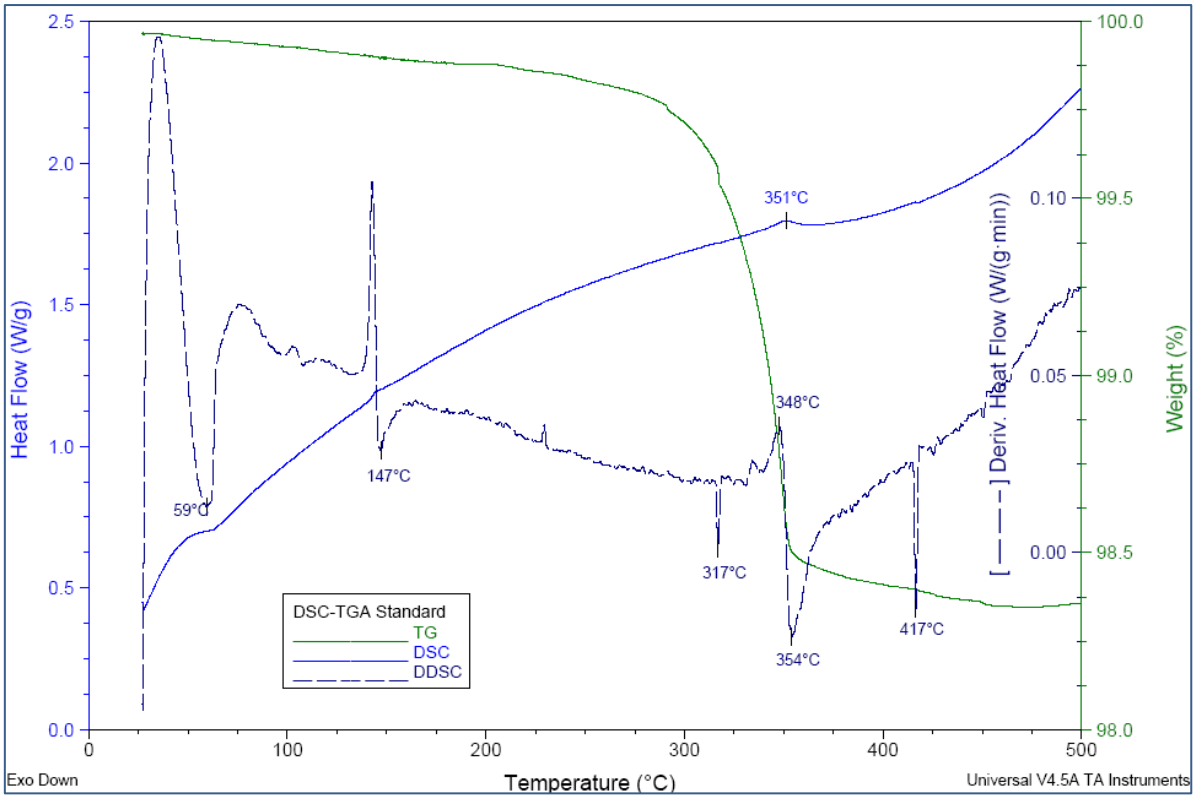

$0^0C - 500^0C$

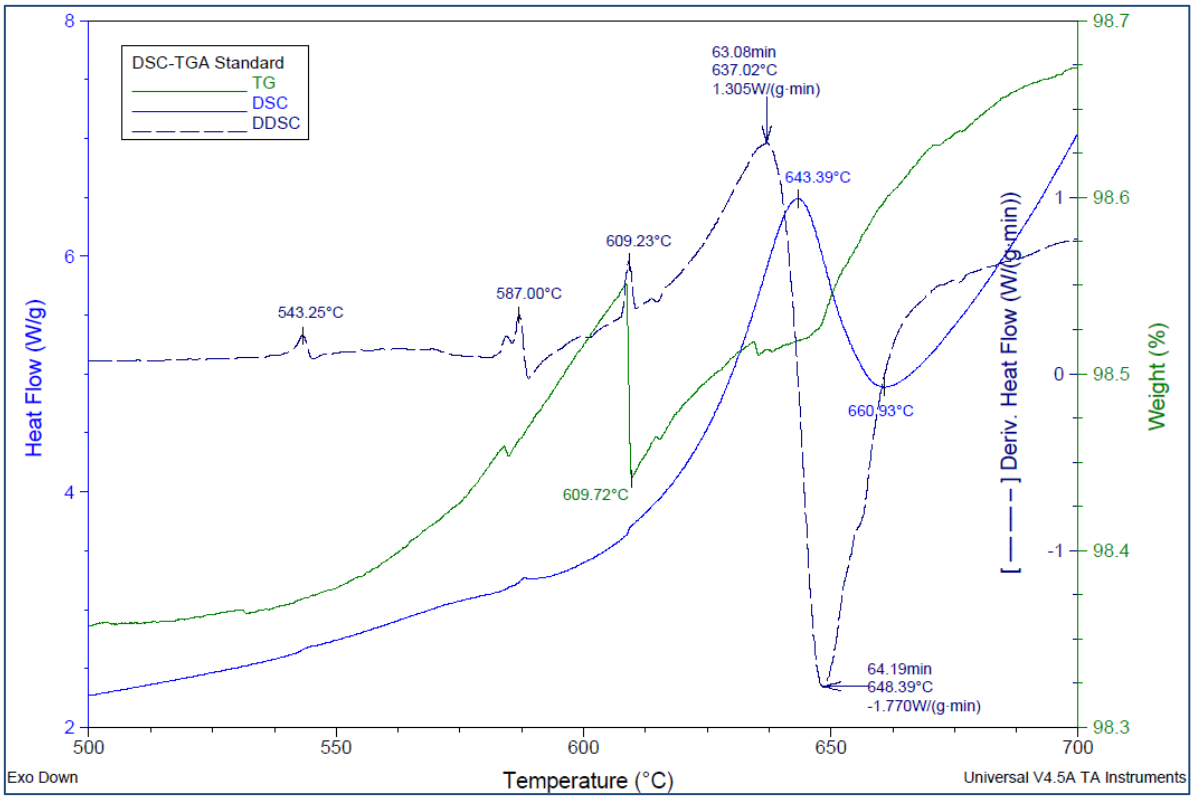

$500^0C - 700^0C$

Figure 4-2: DSC-TGA Results for AMB-2712 Alloy as received from supplier.

Figure 4-2 shows DSC-TGA results for AMB-2712 alloy as-received from supplier. Phase changes considered significant were those that occurred at 350^0C, 609^0C, and 643^0C by virtue of being accompanied by noticeable physical changes as reflected by the thermogrametric (TG) graph. The 1.5% weight loss in the test sample was due to the loss of Acrawax. Additionally, since the powder used in this study was produced through air atomization, it has been related that such powders are invariably coated in a thin film that is principally based on aluminium oxide together with adsorbed and chemisorbed water [56]. The release of a portion of that water either through direct evaporation or thermally triggering its release via the decomposition of $Al_2O_3.3H_2O$ [56] may partly be related to the first phase change at 350^0C and contributory to the 1.5% weight loss in the test sample. The 609^0C and 643^0C approximate to the solidus and liquidous temperature of the Al-Cu binary phase [218, 219].

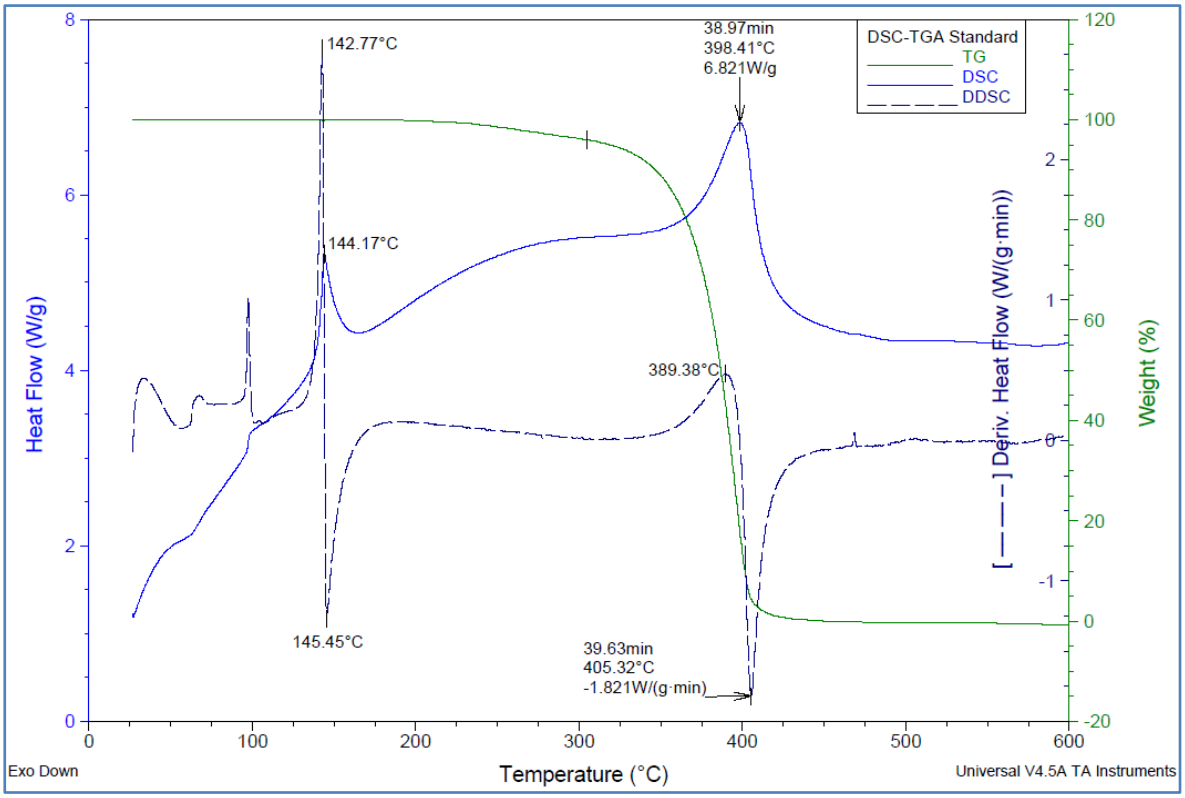

Figure 4-3: DSC-TGA Results for atomized *Acrawax-C* as received from supplier.

Figure 4-3 shows DSC-TGA results for the atomized *Acrawax-C* selected as the preferred binder. This ingredient does not form part of the targeted AMCs as it is meant to be fully

eliminated during the processing. This occurs during a delubrication phase whereby the ingredient is ideally meant to melt away out of the blended mixture and burn out without leaving any remnants. Even though other researchers [95] have achieved the delubrication objective at temperatures and duration as low as 300^0C for 20 minutes, the DSC-TGA indicates that a temperature within the range of 300 – 500^0C should suffice. It can be expected that the delubrication duration might have a correlation with the particulate packing density and the heating rate, i.e. in the case of processes such a powder metallurgy, high green compaction pressures would require relatively slower heating rates and longer durations than low green compaction pressures. Other factors such as relative particle sizes and chemical composition may also be perceived to play a role in the efficiency of the delubrication phase.

4.3 FTIR

According to the supplier's *Product Bulletin*, *Nanofil 116* is a natural montmorillonite with no organic modifier and contains 0.1 – 1% Quartz and 99-100% Bentonite (***Appendix B1***). The chemical formula for Bentonite is given as $Al_2O_3.4SiO_2.H_2O$ [233]. *Figure 4-4 (i)* and *(ii)* shows the FTIR results for *Nanofil 116 before* and *after* heating to a temperature of 635^0C with a holding time of 45 minutes, respectively. The absorption band at $A_{3623cm-1}$ was due to the stretching vibrations of structural OH groups of the nanoclay [231, 234, 235]. The peak at $B_{3452cm-1}$ was attributed to H_2O stretching vibrations [231]. Peaks at $C_{2925cm-1}$ and $D_{2855cm-1}$ were attributed to CH_2 vibrations [234], i.e. C-H stretching mode of the organic matter in *Nanofil 116*. This is rather strange because organic materials typically do not survive temperatures above 600^0C (see C and D in *Figure 4-4(ii)*). Nonetheless, this phenomenon may be related to structural modifications of the nanoclays [236] or remnant constituents. Peak at $E_{2365cm-1}$ was assigned to O-Si-H and Si-H vibrations [237]. The band at $F_{1638cm-1}$ was assigned to

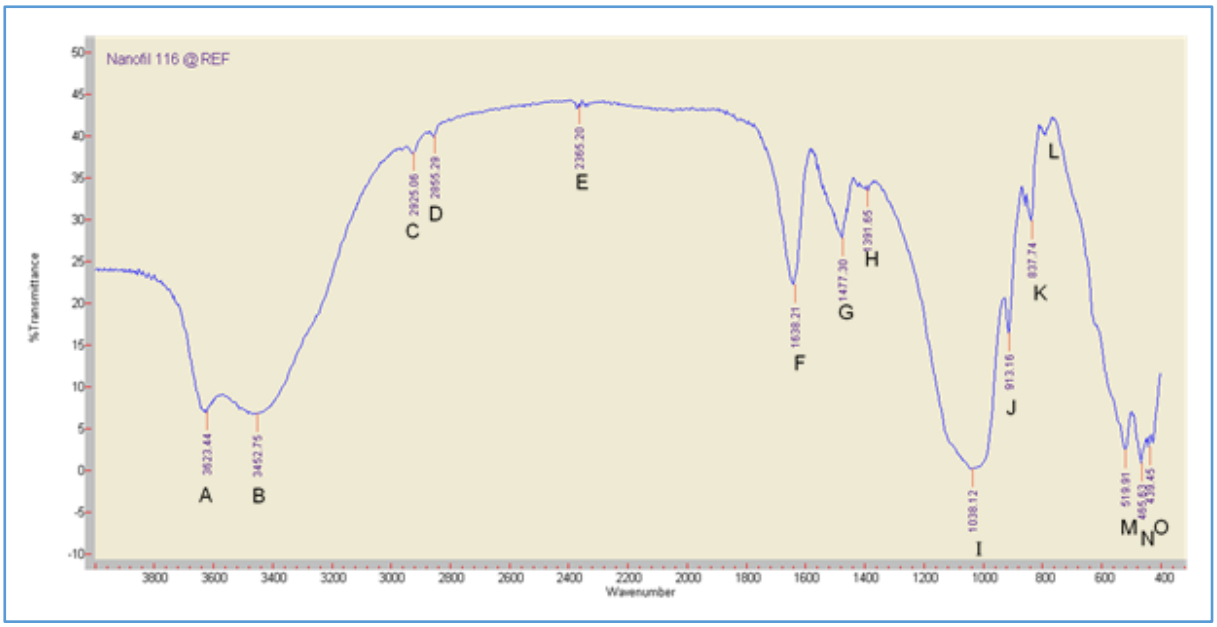

(i)

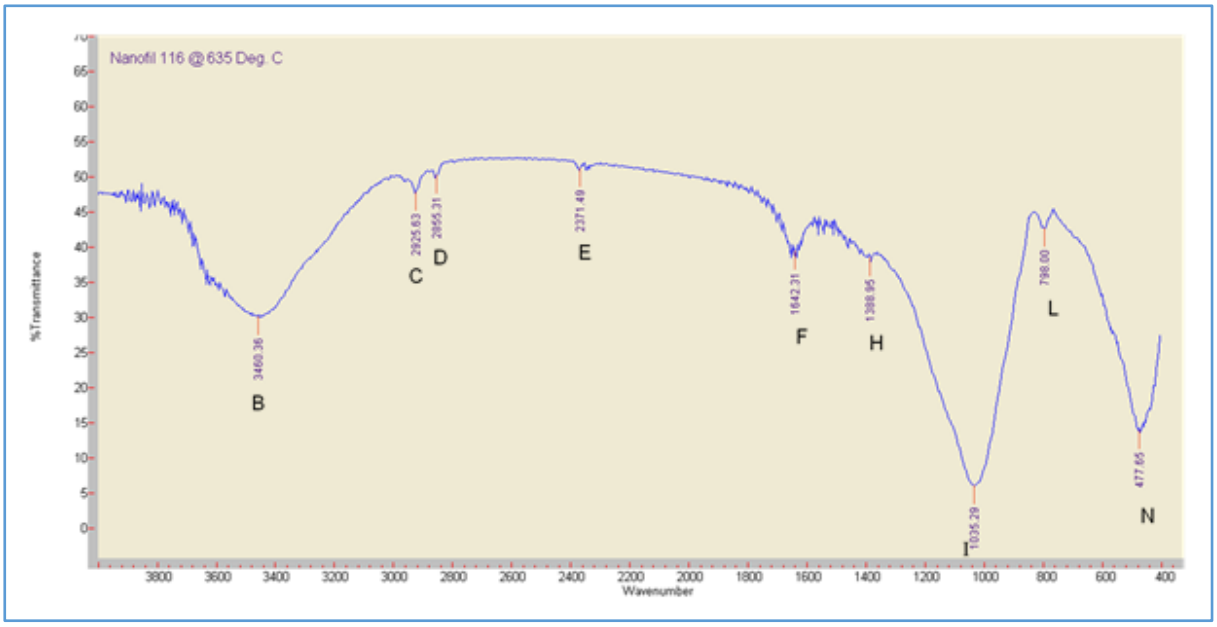

(ii)

Figure 4-4: FTIR results for *Nanofil 116* (i) *Before*, and (ii) *After* heating to 635^0C and holding for 45 minutes.

deformation vibration of adsorbed water (H_2O) in the structure of silicate [235] with an overtone at around 3250 [234]. Similarly, the band at $G_{1477cm-1}$ was assigned to H_2O [238]. The band at $H_{1391cm-1}$ at H was attributed to CH_3 vibrations [239]. The intense band at $I_{1038cm-1}$ was assigned to the stretching of siloxane (Si-O-Si) groups [236]. Elsewhere, this band is attributed to Si-O stretching [231, 238]. The band at $J_{913cm-1}$ was assigned to the deformation mode of the

Al_2OH group, i.e. deformation of OH linked to $2Al^{3+}$ [231, 234-236]. Similarly, the band at $K_{837cm-1}$ was assigned to the deformation mode of AlMgOH group exhibiting the deformation of OH linked to Al^{3+} and Mg^{2+} [231, 236]. The peak at $L_{798cm-1}$ was attributed to the presence of Quartz (SiO_2) [234]. Bands at $M_{519cm-1}$, and $N_{465cm-1}$, correspond to bending vibrations due to Al-O-Si and Si-O-Si respectively [231, 235, 238] while the band at $O_{439cm-1}$ correspond to Si-O vibrations [235].

Comparing the two graphs, it was evident that some functional groups (A, G, J, K, M and O) were destroyed or altered after exposure to heat at 635^0C. In particular, the functional groups at A and G were destroyed, thereby leaving only remnant residue as implicitly depicted by the replacement of those previously smooth and long peaks with several short peaks. Shoulders previously at J and K were completely destroyed. This observation was consistent with findings elsewhere [231], whereby the Al_2OH peak at J was found to be absent in sample of natural bentonite heated to 650^0C. Functional groups represented by M and O were also affected, with a seemingly resultant effect of refinement towards adding on to the group at N.

It was further observed that, of those functional groups that remained after heating to (and holding the temperature at) 635^0C, their transmittance generally increased. The increase in transmittance by 23% at B was relatively the highest. This relates to the dominant dehydration of water near the 100^0C temperature. Corresponding increase at N was by 15%, while transmittance at both C and D increased by 10%. Similarly, transmittance of groups at F, H, and I increased by 6%. Lowest increases of 3% and 2% were noted at E and L respectively, attributable to the thermally stable Si-O bonds in siloxane groups and quartz [240].

All the aforementioned differences in functional groups as a result of the nanoclay's exposure to heat represents a potential for chemical reactions and/or alterations as the nanoclay interacts with the AMB-2712 matrix.

4.4 TEM and SEM analysis

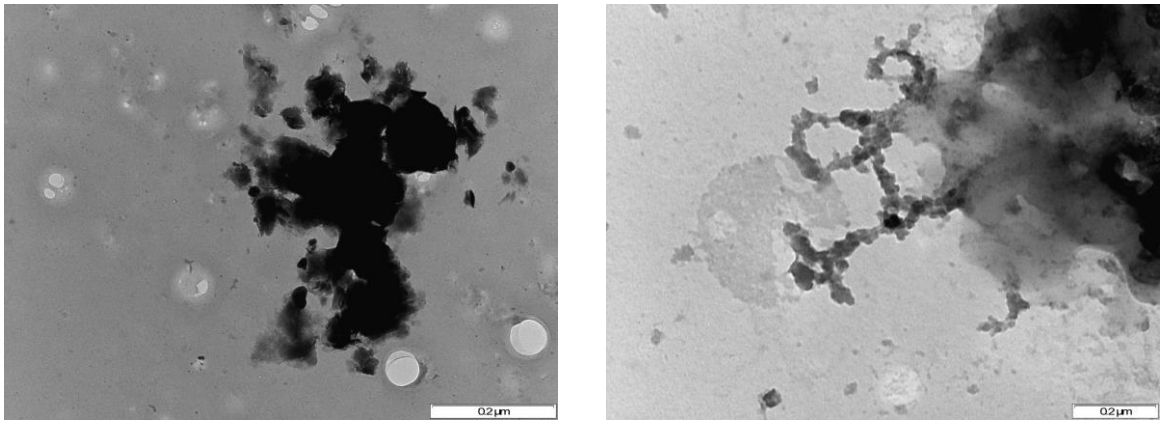

(i) (ii)

Figure 4-5: TEM Micrographs of (i) *Nanofil 116*, and (ii) Plain AMB-2712 powders.

Figure 4-5 (i) and *(ii)* shows TEM micrographs of plain AMB-2712 Al powder and *Nanofil 116* powder, respectively. Both powders are comprised of smooth-edged particles that seem to be predominantly agglomerated. The smooth edges for AMB-2712 alloy particles may be attributed to the associated gas atomization processing of the powder from molten stock. The agglomeration phenomenon is consistent with the behaviour of powders constituting very small particle sizes. Varying intensity in shades represents various levels of layered stacking of platelet particles.

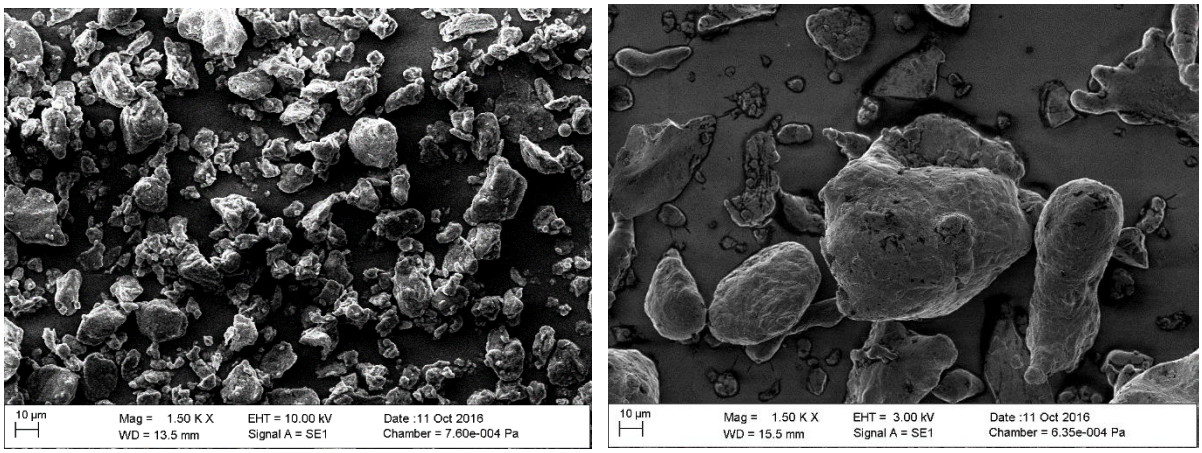

Figure 4-6: SEM micrographs of (i) *Nanofil 116*, and (ii) Plain AMB-2712 powders.

To complement the TEM results, *Figure 4-6* shows respective SEM images captured at a common magnification of 1500 times. Two observations were eminent: (1) Particles in both

powders exhibited smooth, rounded surface profiles. These features generally account for the degree of variation in local particle parking and the resultant green-compacts densities [59]. (2) At the common magnification, significantly higher disparity in particle sizes was noticeable in aluminium powder than in the nanoclay powder.

4.5 Particle Size Analysis (PSA)

Table 4-1 shows the particle size analysis results for both *Nanofil 116* and AMB-2712. Despite the observed agglomeration from TEM results, almost a quarter of the *Nanofil 116* particles were less than 10µm (22%). Results further indicate that the AMB-2712 particles were generally 4 times the size of *Nanofil 116* particles. It can be expected that mechanical blending of these powders and/or ball milling and can potentially have a positive effect on the relative particle sizes and distribution. The variance in diameter of aluminium particles was found to be even bigger than the powder's mean particle size. This phenomenon reiterates the observed disparity in the particle size results as presented in *Figure 4-6*. Regardless of the observed disparities, both powders showed a normal particle size distribution as presented in *Figure 4-7* in the form of histogram and S-curve.

Table 4-1: Particle size analysis results

Analysis → **(Units)**	%PM10	D10	D50	D90	Mode	Mean	Std. Dev
	(%)	µm	µm	µm	µm	µm	µm
Powder ↓							
Nanofil 116	22	8.22	13.48	21.75	14.08	14.39	5.54
AMB-2712 Alloy	6	13.04	48.22	116.96	55.25	65.85	100.75

The *Nanofil 116* and AMB-2712 alloy were found to have a GSD of 1.46 and 2.42 respectively. At individual ingredient level, the determination of optimal particle size distribution for these powders is outside the scope of this study. However, from the perspective of blending the

powders in the process of making AMCs, their difference in GSD presents an opportunity for the nanoclay particles to physically serve as interstitial filler for the aluminium powder matrix.

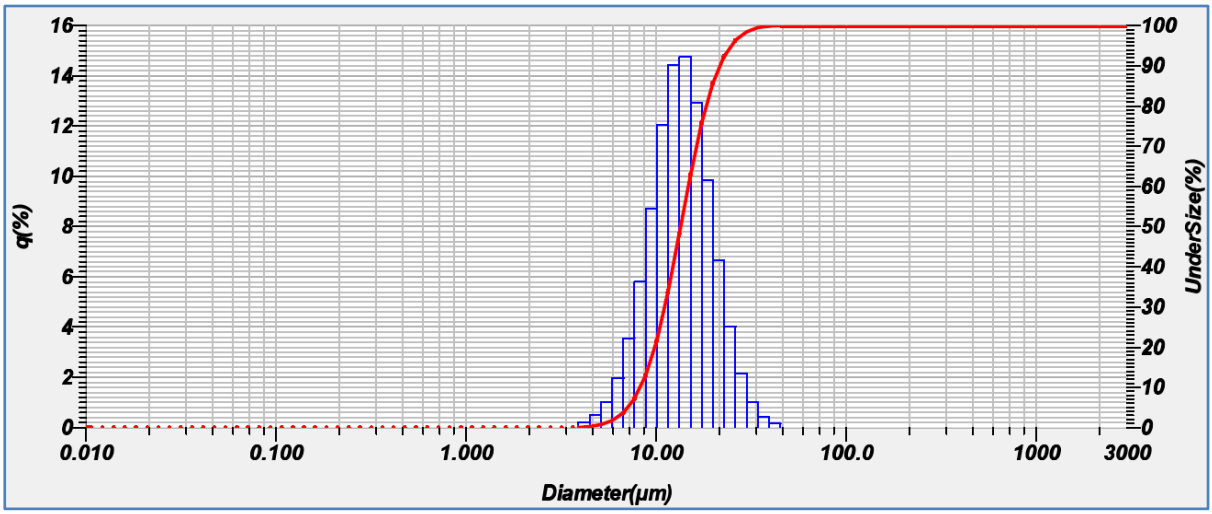

(i) *Nanofil 116*.

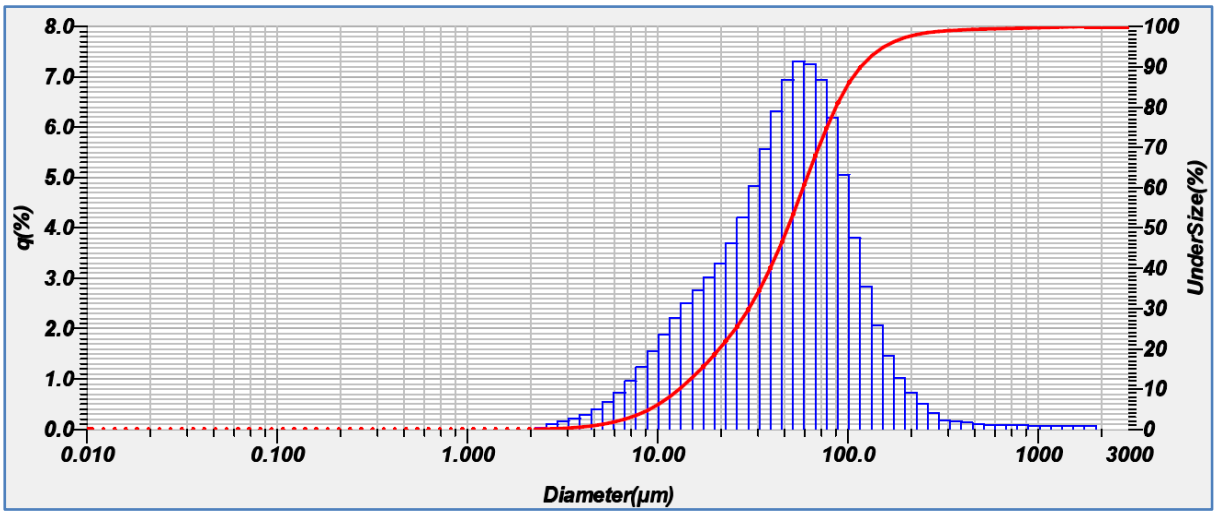

(ii) AMB-2712 Alloy.

Figure 4-7: Particle Size Distribution for (i) *Nanofil 116* powder, and (ii) AMB-2712 Alloy Powder.

4.6 Summary

With due reference to alloying elements known to enhance properties of aluminium, a copper-based heat-treatable 2xxx-series alloy was pre-selected as the preferred datum matrix for the current study, i.e. AMB-2712 in particular. Similarly, *Nanofil 116* was pre-selected as the preferred datum nano-phased reinforcement system. Since these materials were originally

sourced in powder form, atomized *Acrawax-C* was pre-selected as the preferred lubricant-cum-binder in order to facilitate in part the handling of these powders.

As alluded to and hereby verified, *Nanofil 116* comprises of chemical elements similar to some of those found in the selected matrix (Al, Si, Mg, etc). It was therefore envisaged that nanoclays can compatibly be integrated into the matrix, thereby inducing the inherent advantage of being nano-structured and chemically coherent with the matrix. To accommodate the relatively lower temperature range for the nanoclay compared to aluminium, powder metallurgy processing route was selected as the preferred processing technique. The following chapters detail explorative characterization processes revolving around evaluation of the efficacy of using nanoclays as a preferred reinforcement system for aluminium and its alloys.

CHAPTER 5:

NANOFIL 116 – AMCs: Physical Properties and Microstructures

5.0 Introduction

This chapter is documents the nature of sintered *Nanofil 116*-AMCs as characterized using physical inspection, sintered density, microstructural analysis, and SEM / EDX / XRD analysis. Any underlying and/or contributory factors relating to observed trends and features have been discussed wherever deemed to be significant.

5.1 Physical inspection

5.1.1 Batch 1

Figure 5-1(i), (ii), and *(iii)* show the respective top-, side-, and bottom-view of reference samples (no nanoclays) as processed using *Set-"A"-run* settings. The bottom view images were taken after a preliminary grinding test meant to check whether the green compacts were fully sintered. The images in *Figure 5-1(iii)* show that all the specimens were sufficiently sintered. *Figure 5-1(i)* and *(ii)* show that the specimens as sintered exhibited no noticeable geometrical distortion. Since SLPS is time-temperature sensitive [241], this geometrical stability depicts suitability of the selected sintering conditions.

Figure 5-2 shows the side-view of sintered specimens with varying nanoclay content as compared to the reference specimens. No defects such as cracks and/or physical deformations were observed irrespective of the green compaction pressure and nanoclay content. Nonetheless, varying hues of colour were observed on the surfaces of the specimens containing 1%wt. and 3%wt. content of *Nanofil 116*. This phenomenon points to potentially ineffective delubrication of the specimens during sintering, which may be attributed to the following contributory factors: (1) At the 10^0C/minute heating rate towards the sintering temperature, the

Set-A-Run sintering profile did not have a dedicated stage for delubrication, (2) the green compactions used in making these specimens, e.g. 950MPa and 1425MPa, were approximately

(i)			
	160 Bars	200 Bars	240 Bars
(ii)	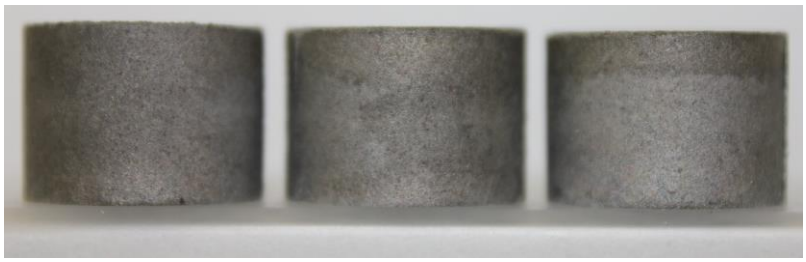		
	160 Bars	200 Bars	240 Bars
(iii)	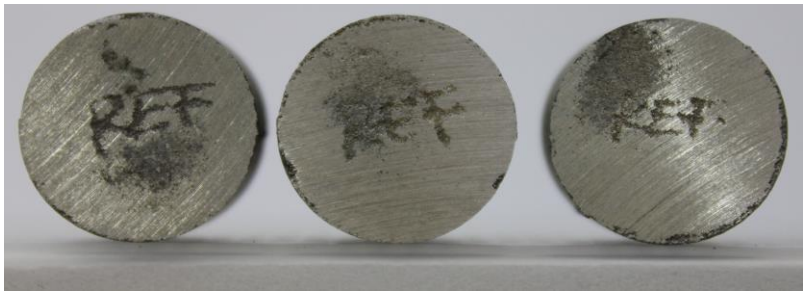		
	160 Bars	200 Bars	240 Bars

Figure 5-1: Set "A" Run Reference Samples: (i) Top view, (ii) Side view, and (iii) Bottom view.

double and triple the magnitude of those used elsewhere on the same material, respectively [108, 222] - the effect of this would be enhanced closure of the very pores that would otherwise aid delubrication, (3) The nanoclay particles, whose sizes were observed to be significantly smaller than those of the AMB-2712 matrix powder, would serve to fill-up the interstitial vacancies, thereby creating less opportunities for the lubricant to escape. For further appreciation, AMB-2712 with the same amount of 1.5%wt Acrawax has effectively been

processed using a green compaction pressure of 200MPa, a delubrication temperature of 300^0C for 20 minutes, and a sintering temperature of 600^0C for 30 minutes.

REF	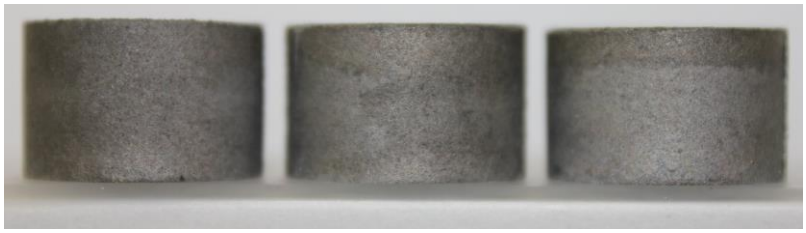		
	160 Bars	200 Bars	240 Bars
1%N	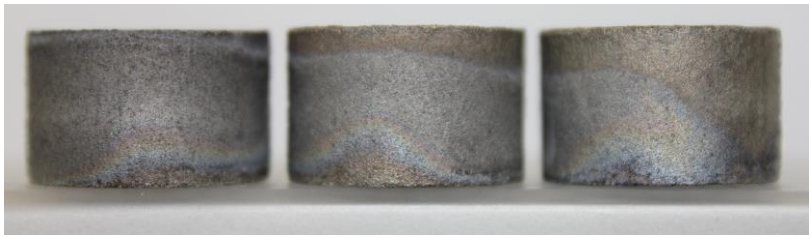		
	160 Bars	200 Bars	240 Bars
3%N			
	160 Bars	200 Bars	240 Bars
8%N			
	160 Bars	200 Bars	240 Bars
12.5%N	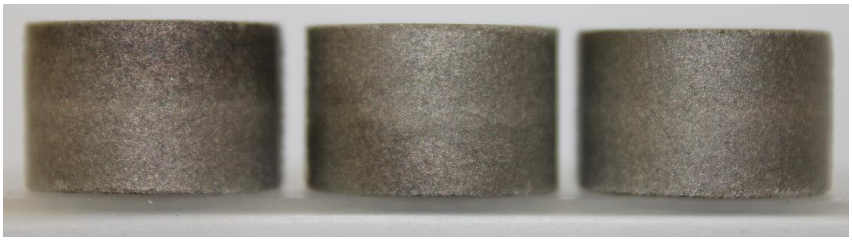		
	160 Bars	200 Bars	240 Bars

Figure 5-2: Side view of *Set "A" Run* Specimens.

Interestingly, it was noticed that these hues of colour were absent in the 8%wt. and 12.5%wt. specimens. This was perceived to be indicative of an improved delubrication process in these latter categories. This perception is based on the understanding that, at higher contents of the nanoclay, there would inevitably be a relatively higher number and size of nanoclay's particulate agglomeration sites. Agglomeration of particles on the other hand has been reported to result into increased volume and size of pores in green compacts [54, 242]. It is further said to promote uneven sintering, which sometimes results in mechanically weak and porous products [54]. Accordingly, there must have been relatively increased level of porosity in these latter specimens as a result of the agglomeration, thereby providing sufficient routes for escape of Acrawax.

5.1.2 Batch 2

Table 5-1 shows the second batch of sintered specimens for thermal analysis. Exudation and warpage were observed in specimens containing 1% through to 4%wt. content of *Nanofil 116*. The extent of warpage corresponded with the extent of exudation. Exudation in itself has been associated with poor wettability of aluminium oxide in the absence of magnesium when sintering Al-Sn alloys [121]. In their work, German and Hall [121] found that exudation was apparent in Al-Sn alloys when samples were sintered without magnesium in the furnace. They showed that the phenomenon could largely be avoided by placing magnesium filings in the furnace upstream of the samples. They further reported that the use of an argon or nitrogen atmosphere had no effect on whether exudation occurs. However, there is no indication of the exudation phenomenon being observed in the case of Al-Mg specimens [121]. It is therefore hereby suspected that the primary cause for exudation in the current study was directly related to the addition of *Nanofil 116* and the loading conditions of the specimens.

Table 5-1: *Batch 2* of sintered specimens.

REF	
1%N	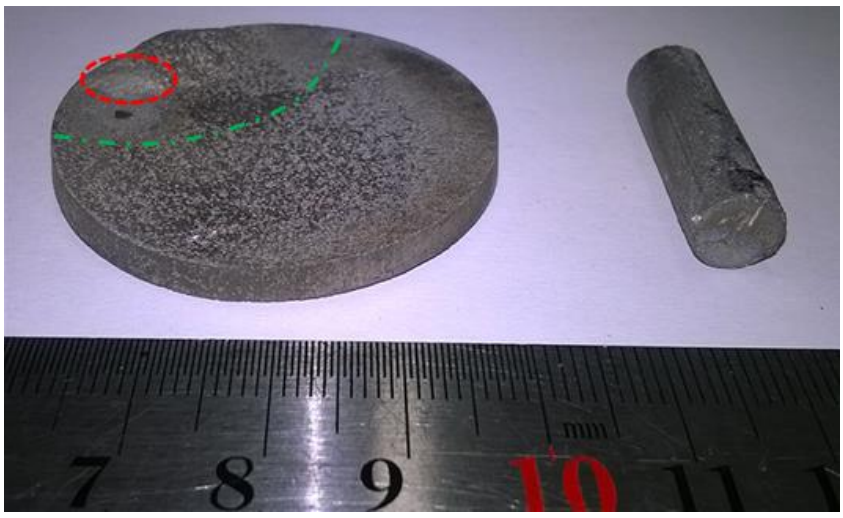
2%N	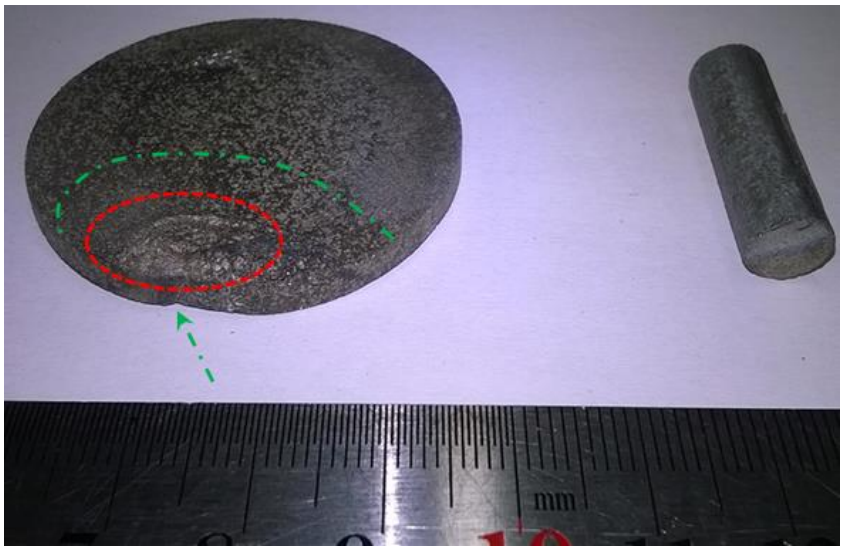

3%N	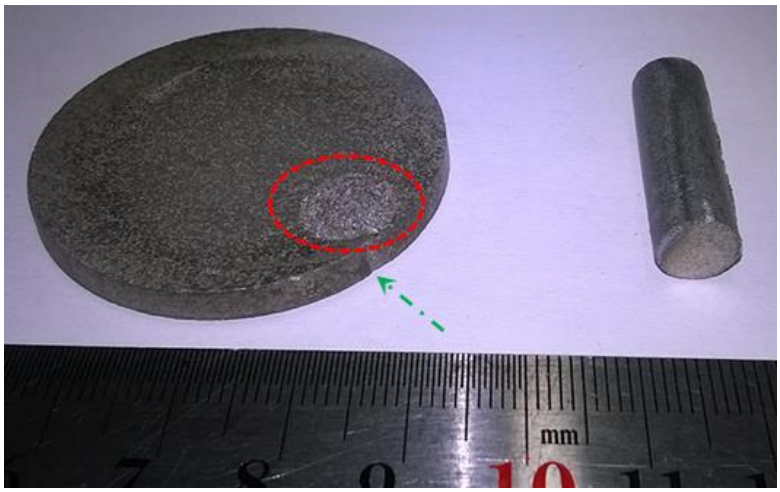
4%N	
5%N	
	KEY: Exudation Warpage

In the current study, the issue of wettability was ruled out because (i) the phenomenon was not observed in any other batch of specimens, (ii) both the matrix and nanoclay contained magnesium, and (3) there was no tin (Sn) in the alloy, which is mentioned to experience difficulties in wetting alumina [121]. Two factors were considered to have contributed to these phenomena. *Firstly*, since the discs could not seat flat inside the relatively narrow sintering boat, they were rather placed at angle and thereby being supported on their edge at the bottom of the boat. This aspect was perceived to induce localized pressure at the lower support points. An arrow has been used to show the respective pressure points.

Secondly, since these phenomena only occurred in the specimens containing nanoclay and the sintering was conducted in the supersolidus temperature range, it is imperative that the nanoclays significantly impacted on the thermal properties of the material, thereby resulting in increased liquid ratio in the specimens. With the specimens seating at an angle, the resultant effect of specimens own weight and mushy granular structure would inevitably cause the observed warpage. This proposition is further validated by the fact that the phenomena was not observed in the reference specimen and that the effects thereof became less profound with increasing nanoclay content.

5.2 Sintered density of specimens

5.2.1 Batch 1

Table 5-2 shows sintered densities for the cylindrical specimens compacted to 200-bars and processed using *Set-A-Run* sintering profile. It was observed that there was no significant difference in porosity between Reference sample and the sample containing 1%wt nanoclay content. The porosity quantifications seemed to follow no particular pattern.

It was observed that the sintered density decreased with increasing nanoclay content, except the density value for the 8%wt specimen. This decreasing trend was attributed to nanoclay's

partial role of adversely affecting the delubrication process as it was notable that: (1) The reference sample posted the highest sintered density value, which progressively declined upon addition of 1%wt and 3%wt nanoclay, and (2) With improved delubrication as discussed earlier on for samples having 8%wt and 12.5%wt content of *Nanofil 116*, the sintered density pick-up again at the 8%wt content and decreased thereafter with further increase of the nanoclay content.

Table 5-2: Sintered density of *Batch 1* specimens

Nanofil 116 Content	SINTERED DENSITY (g/cm^3)					POROSITY
	Sample 1	Sample 2	Sample 3	AVERAGE	Std. Dev.	
%	0.0000	0.0000	0.0000	0.0000	(g/cm^3)	(%)
REF	2.4887	2.4837	2.4799	2.4841	0.0036	9.82
1%N	2.4657	2.4652	2.4660	2.4656	0.0003	10.49
3%N	2.3575	2.3556	2.3683	2.3605	0.0056	14.31
8%N	2.4557	2.4570	2.4605	2.4577	0.0020	10.78
12.5%N	2.3191	2.3020	2.3393	2.3201	0.0152	15.77

5.2.2 Batch 2

Table 5-3: Sintered density of *Batch 2* specimens

Nanofil 116 Content	SINTERED DENSITY (g/cm^3)					POROSITY
	Sample 1	Sample 2	Sample 3	AVERAGE	Std. Dev.	
%	0.0000	0.0000	0.0000	0.0000	(g/cm^3)	(%)
REF	2.3679	2.3693	2.3808	2.3727	0.0058	13.87
1%N	2.4095	2.3979	2.3635	2.3903	0.0195	13.23
2%N	2.4062	2.4110	2.4279	2.4150	0.0093	12.33
3%N	2.3821	2.3600	2.3760	2.3727	0.0093	13.86
4%N	2.3626	2.3610	2.3417	2.3551	0.0095	14.50
5%N	2.3782	2.3681	2.3838	2.3767	0.0065	13.72

Table 5-3 shows sintered densities for the disc specimens compacted to 16.5-bars and processed using *Set-A-Run* sintering profile. It was observed that the sintered density increased with increasing nanoclay content, peaking at 2%wt content. Thereafter the density generally decreased with further increase in nanoclay content except at 5%wt content, which could represent the onset of a microstructural transition resulting into observed densification. From an alternative perspective, porosity decreased with increase in nanoclay content up to 2%wt content, after which a tendency to increase with nanoclay content was then observed.

5.3 Microstructure of sintered specimens

Follow-up inspection as done using an optical microscope further confirmed that the samples were significantly sintered. *Figure 5-3*(i) and (ii) shows the microstructure of specimen previously compacted at 160 Bars and viewed at the mid-section of the edge of cylindrical wall and at the central axis, respectively. Both images were taken in the mid-zone along the height of the specimens. No expressly discernible difference in porosity was identified, potentially implying an even distribution of green density and heat flow matrix, i.e. the microstructures after sintering were uniform throughout the specimen. This observation is in agreement with observations made by Min Ho Kyung et al [222] whose work was on AMB-2712 delubricated at 400^0C for 30 minutes and sintered at 630^0C in dry nitrogen for 30 minutes. Nonetheless, the effect of processing conditions such as the green compaction pressure and %wt. content of lubricant / binder do have knock-on effects on other factors such as the porosity, interparticle residual stresses, and bulk hoop stresses [51, 53, 62] .

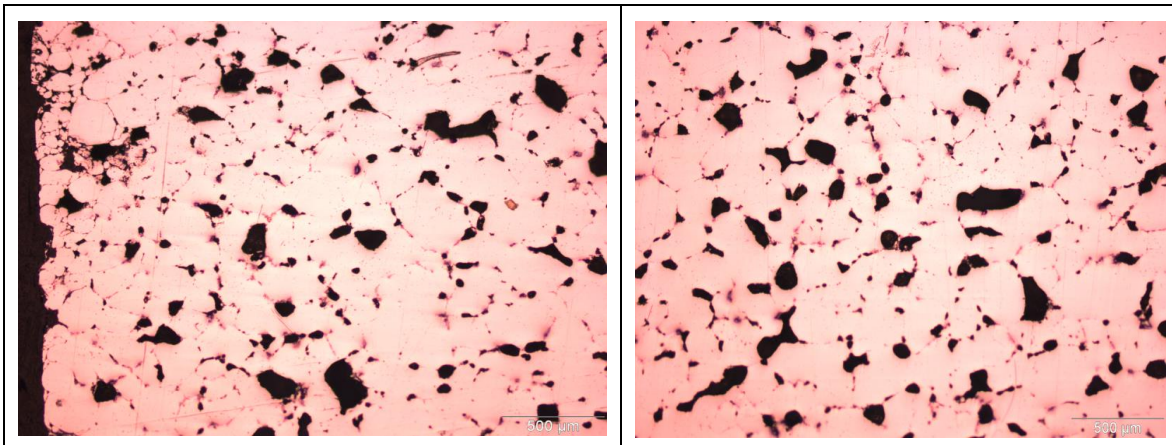

(i) Edge	(ii) Central

Figure 5-3: Microstructure of 160 Bars reference specimen sintered under *Set-"A"-run* settings and viewed at: (i) Edge of Cylindrical wall, and (ii) Central Axis.

Figure 5-4 shows the microstructure of specimens with 1%wt. content of *Nanofil 116* as previously compacted to 160, 200 and 240 bars. It was evident that porosity decreased with the green compaction pressure as seen in (i) towards (iii). This behaviour was attributed to: (1) increase in green compaction pressure may be expected to have increased the cumulative inter-particle contact's surface area for conductive heat transfer as a result of cold-welding induced by the compaction pressure, hence the observed thermal behavioural trend relative to compaction pressure, and (2) the role of residual stresses, i.e. these stresses may reasonably be expected to potentially affect the level and significance of thermally instigated lattice vibrations with a knock-on effect of increasing the system's entropy.

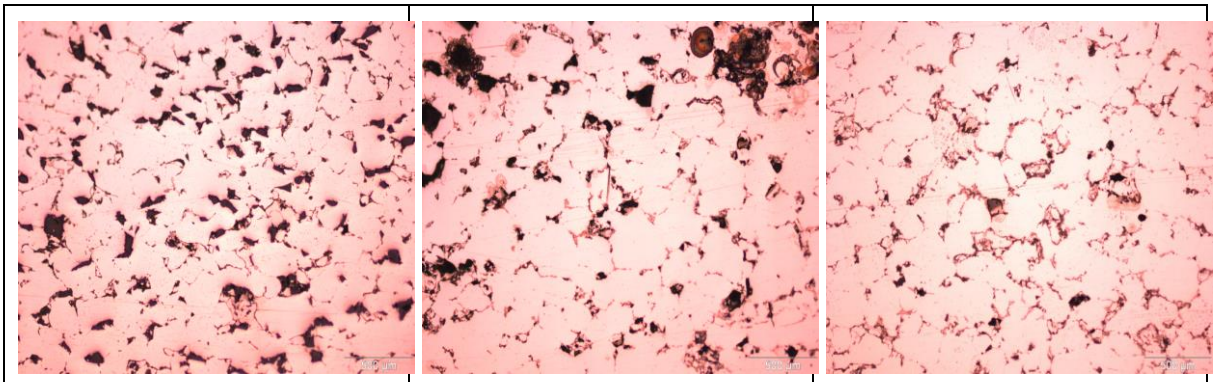

(i) 160 Bars	(ii) 200 Bars	(iii) 240 Bars

Figure 5-4: Microstructure for *Set-"A"-run* specimens with 1%wt *Nanofil 116* showing decreasing porosity with increasing compaction load seen in (i) towards (iii).

Figure 5-5 shows the effect of *Nanofil 116* on the microstructure of specimens previously subjected to green compaction pressure of 160 Bars. The images were captured at the central axis region of the respective polished surfaces. In comparison to the reference sample, it was observed that the level of porosity in terms of pore-size and population declined with increase in nanoclay content as evident in the samples with 1%wt and 3%wt. This phenomenon was attributed to filler-effect of the nanoclay at the grain and inter-particle boundaries. In effect, this could increase the material's compressive strength and possibly also the tensile strength. However, this favourable trend was observed to diminish at the relatively higher nanoclay contents of 8%wt and 12.5%wt content. In the latter pair, porosity was characterised by relatively fewer but larger diameter pores accompanied by smaller segregated grains. The trend depicted by these results was consistent and equally representative of the specimens previously subjected to green compaction pressures of 200 and 240 Bars.

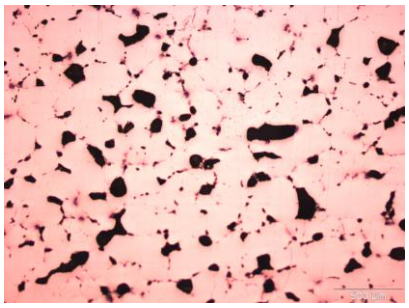

REF

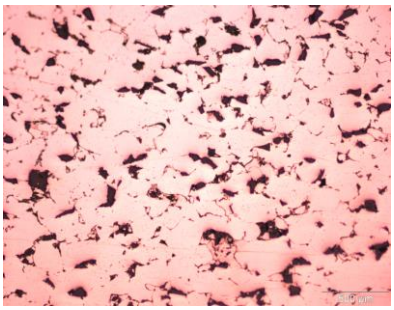

1%wt.

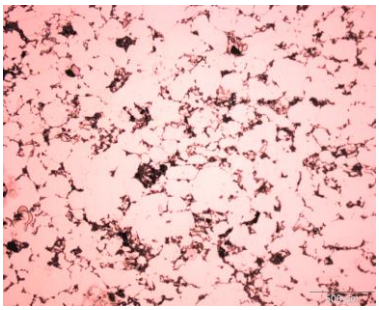

3%wt.

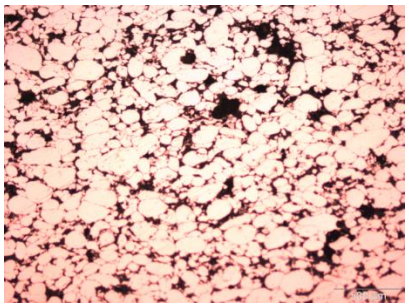

8%wt.

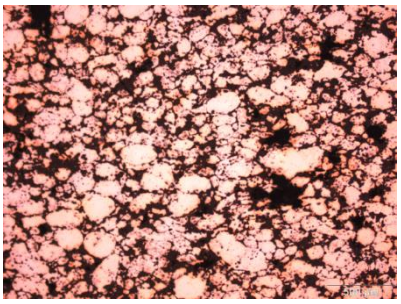

12.5%wt.

Figure 5-5:
Microstructure for specimens previously subjected to 160 Bars.

Table 5-4 shows the evolution of microstructures with changes in the %wt. content of *Nanofil 116* and the green compaction pressure. The trend for both the 160-bars and 240-bars

specimens was observed to be similar as compositions changed from the reference samples through to the 12.5%wt. nanoclay samples. At every comparative composition, microstructural features in the 240-bars specimens were observed to be more amplified than in the 160-bars specimens. This was perceived to infer into the role of the green compaction pressure on the heat-transfer-matrix, which on the other hand relates to the system's tendency to seek thermodynamic equilibrium. This tendency is in accordance with the second law of thermodynamics [243], which states that the total entropy for an isolated system can only increase.

Table 5-4: Microstructure for *Set-"A"-run* specimens with varying %wt *Nanofil 116* and previously compacted at 160 Bars and 240 Bars.

	160 Bars	240 Bars
A	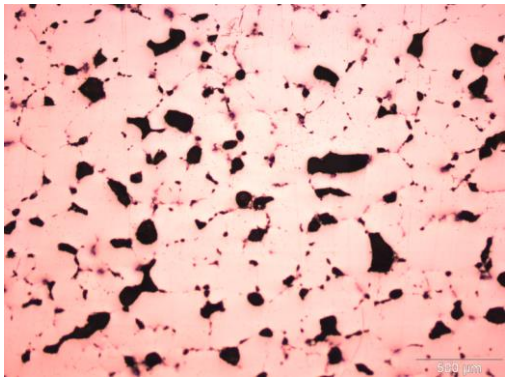	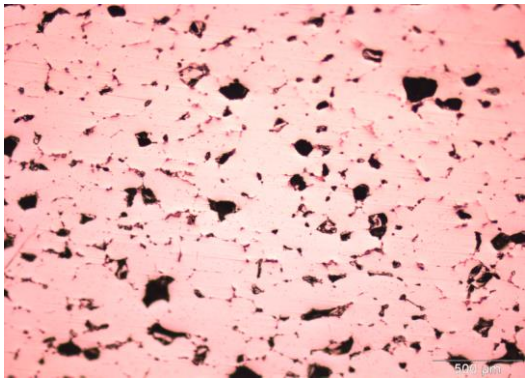
1%	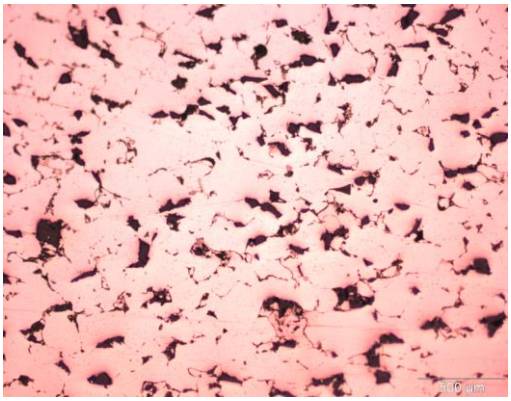	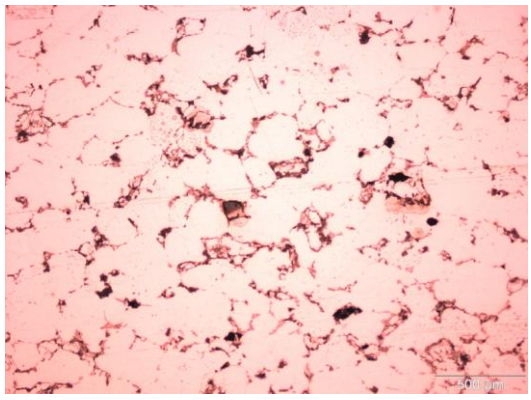

3%	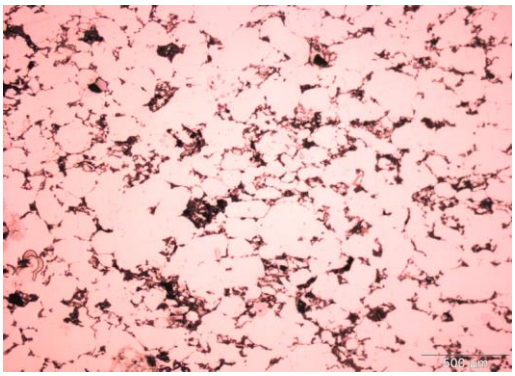	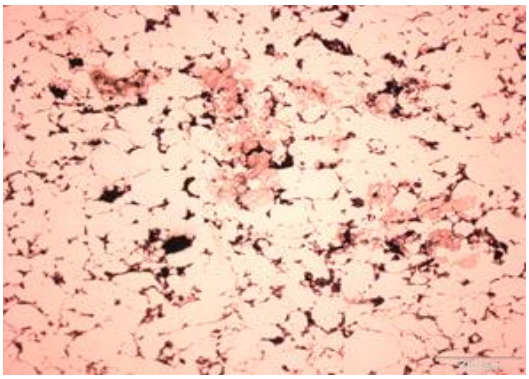
8%	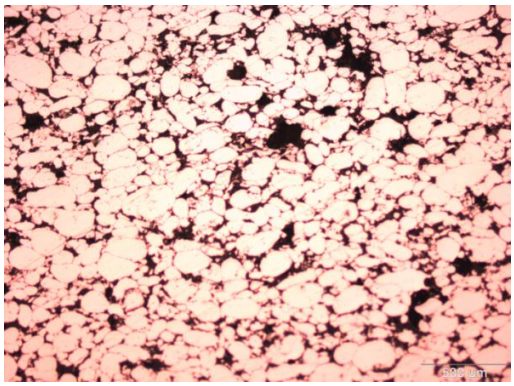	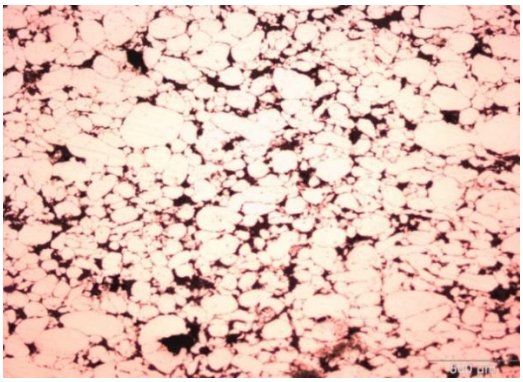
12.5%	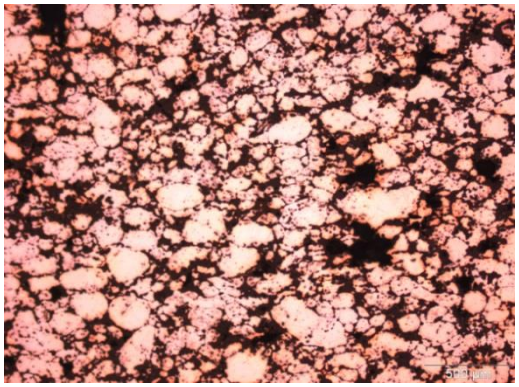	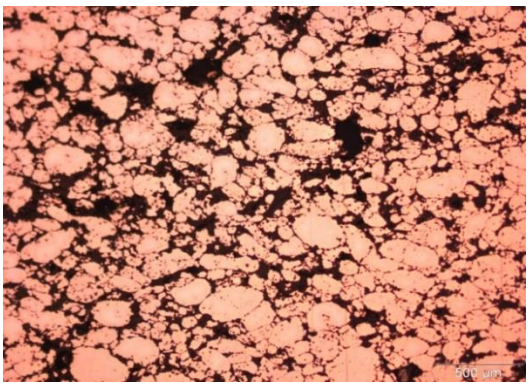

A closer look at the microstructure of the sample with 3%wt nanoclay content showed an on-set of particulate disintegration into individual grains potentially due to thermal stresses concentration at both the grain- and interparticle-boundaries. This was accompanied by noticeable discolouration of the grains and eminent concentration of a dark-looking phase, some features suspected to alloying elements and/or chemical compounds at the boundaries. From magnified microscopic sites as shown in *Table 5-5(i)* to *(iv)*, four significant observations were made, respectively.

Firstly, *Nanofil 116* had a resultant filler effect. Upon addition of nanoclays, porosity was significantly reduced irrespective of the green compaction pressure especially in lower nanoclay contents such as 1 and 3%wt.; at relatively higher contents such as 8 and 12.5%wt., the pores were very scarcely distributed but relatively much larger in size. This validates the observed effective delubrication in these specimens in comparison to those containing 1%wt. and 3%wt. nanoclay.

Secondly, for the same %wt content of nanoclay, increased green compaction pressure effectively changed the heat transfer dynamics as depicted by thermally induced granular collapse illustrated in figure *(ii)* of *Table 5-5*. Further evidence was as shown in *Table 5-4*, e.g. sites of granular collapse were more prevalent in the 3%wt specimen previously compacted to 240 Bars as compared with 3%wt specimen previously compacted to 160 Bars.

Table 5-5: Magnified microscopic sites of *Nanofil 116*-AMCs.

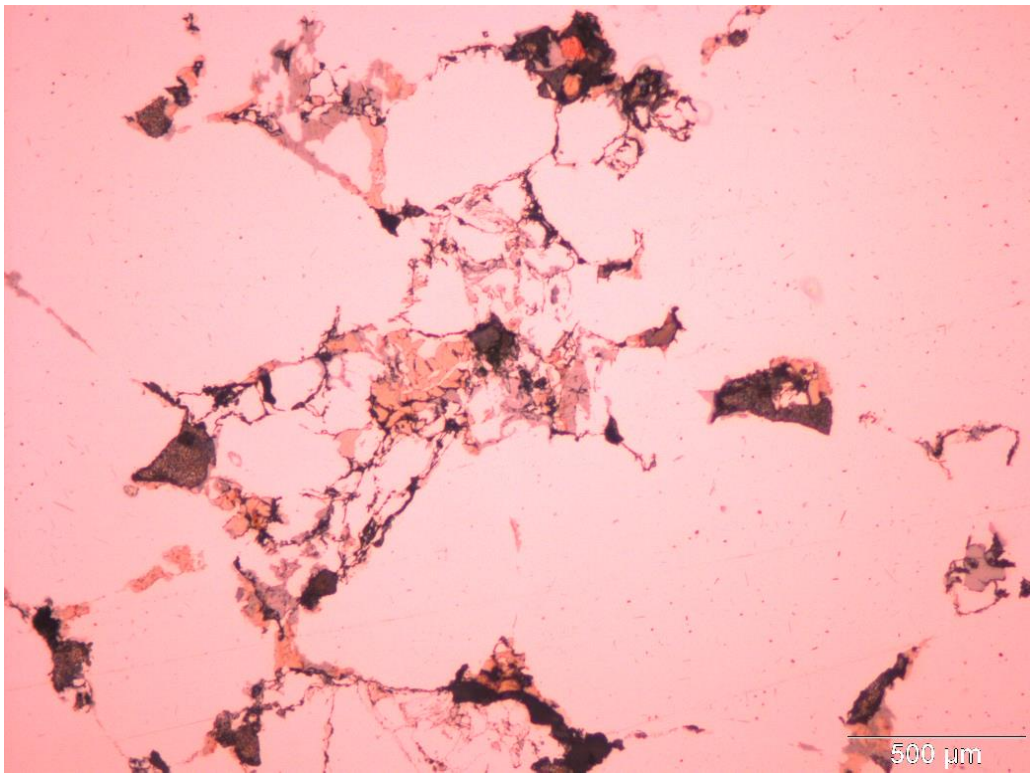

(i) *Nanofil 116* as a filler (1%wt *Nanofil 116* @ 240 Bars).

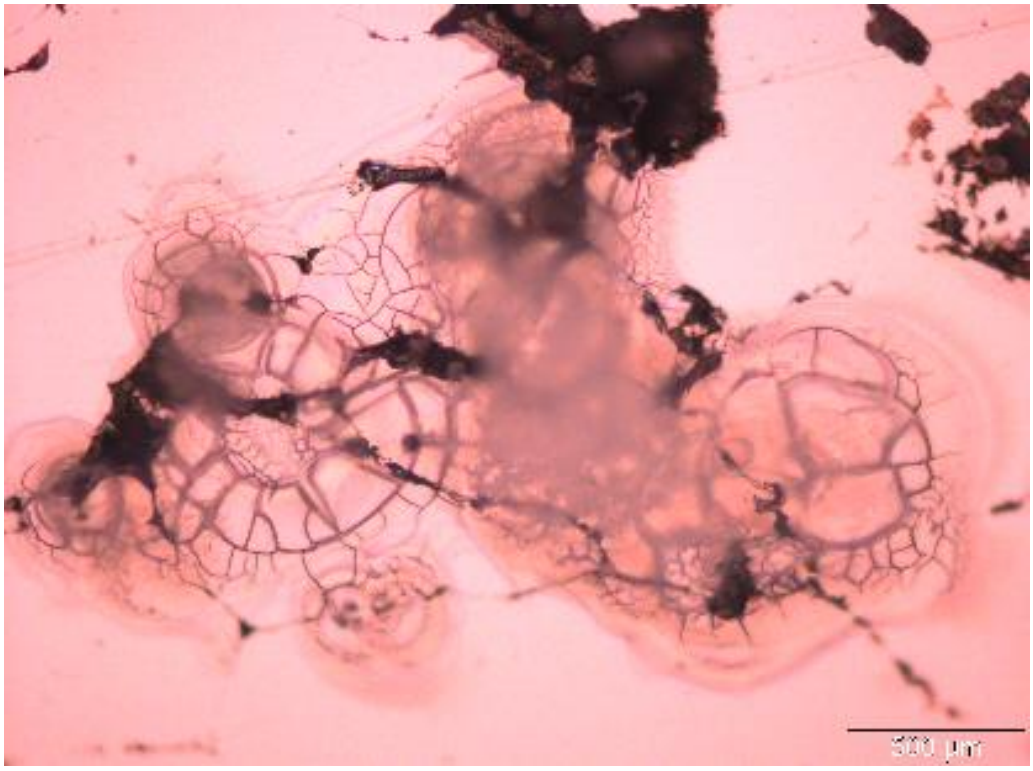

(ii) Thermally induced granular collapse (3%wt *Nanofil 116* @ 200 Bars).

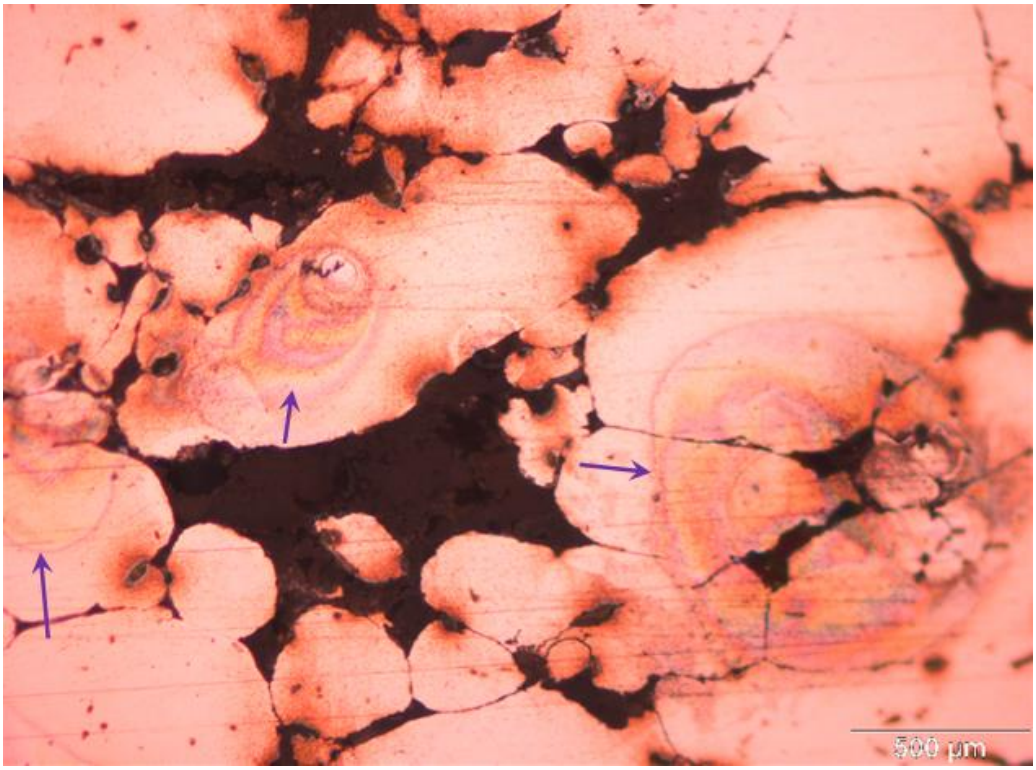

(iii) Thermal stress concentrations (8%wt *Nanofil 116* @ 200 Bars).

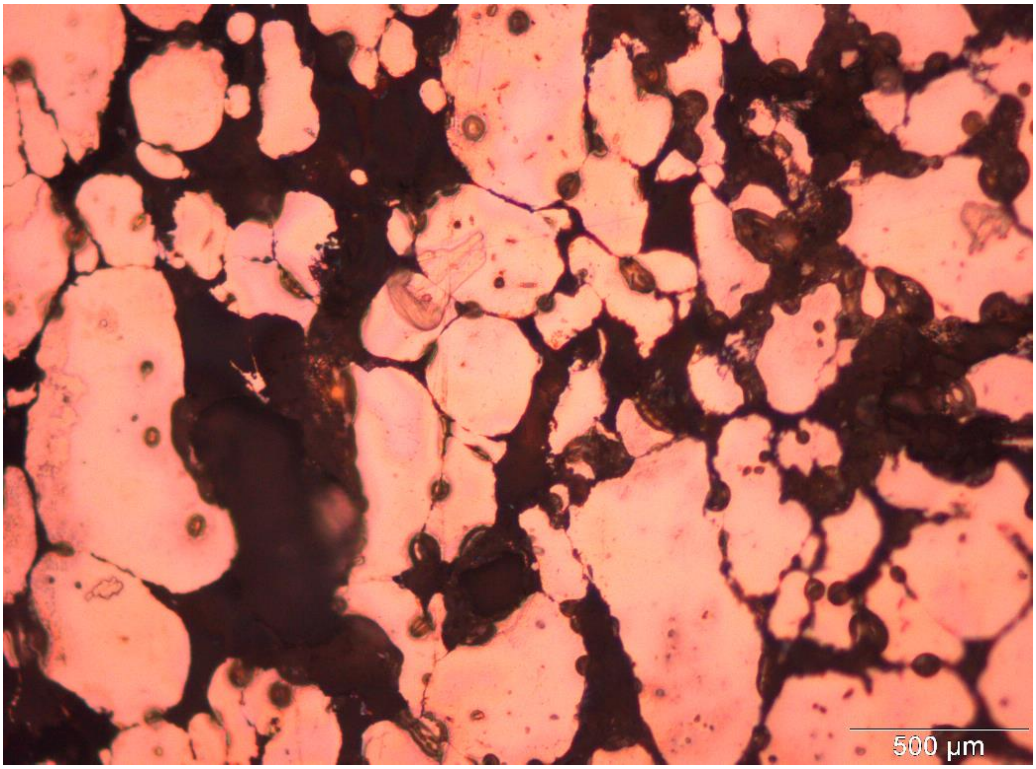

(iv) Granular disintegration (12.5%wt *Nanofil 116* @ 240 Bars).

Thirdly, local temperature gradients. There was a noticeable inference to potential disparities in thermal properties (conductivity, diffusivity, and specific heat capacity) between the matrix and the filler nanoclay (or chemical compounds formed due to its integration into the matrix), thereby creating a cross-border heat transfer gradient and thermal stress concentrations as implied by thermal-stress-bands (pointed out by arrows) evident in figure *(iii)* of *Table 5-5*.

Lastly, increased nanoclay presence progressively changed the heat transfer dynamics as characterized by extensive granular disintegration at 8%wt. and 12.5%wt. content. At relatively high contents, the nanoclay in effect served as heat dissipation sites due to potentially having a relatively lower thermal conductivity, lower diffusivity, and a corresponding higher specific heat capacity compared to the matrix. This thermal-barrier-effect would lead to local temperatures becoming high enough to burn out some of the chemical elements and/or reactively create other chemical compounds. In addition, this can be expected to have an effect

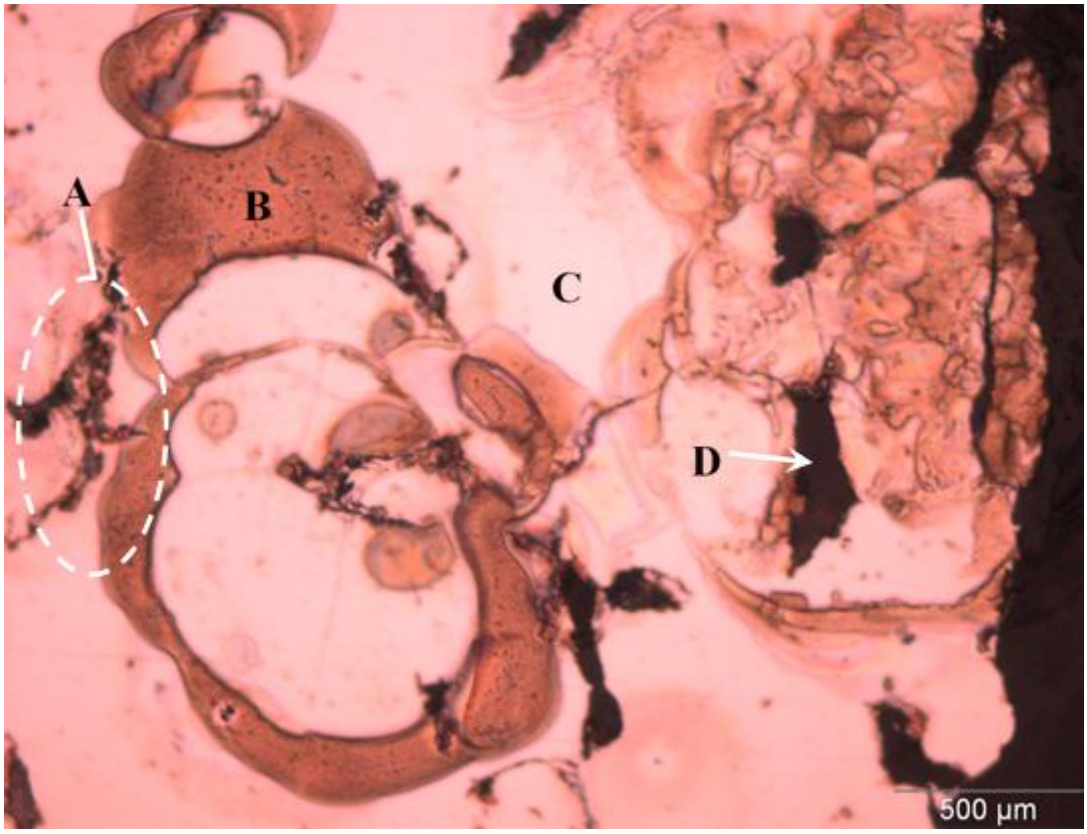

(i)

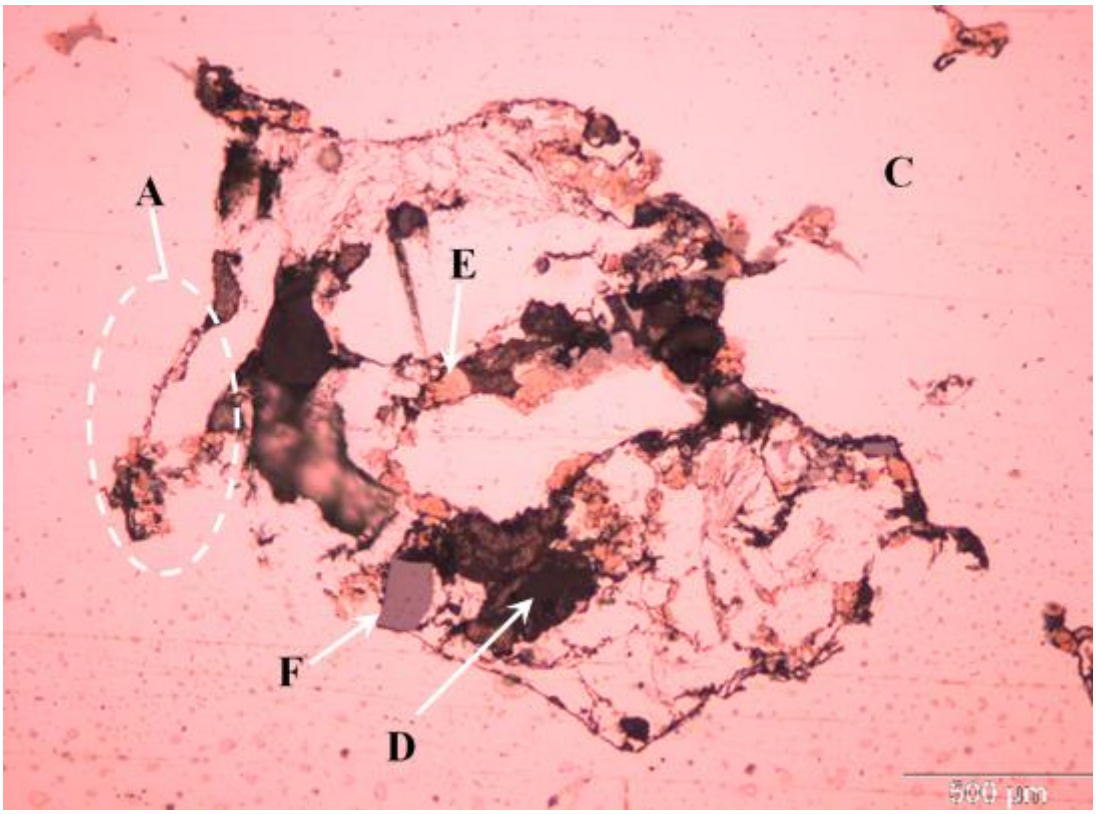

(ii)

Figure 5-6: Sample phases and interfaces in a 240-bars specimen with 1%wt *Nanofil 116* requiring SEM / EDX for better identification.

on the relative proportion of liquid phase, effective granular dislocation, extent of densification, and the resultant material's physical-chemical properties.

Figure 5-6 illustratively shows sample phases and/or interfaces in a 240 Bars Specimen with 1%wt content of *Nanofil 116.* A higher magnification and/or etching would be necessary in order to enhance and/or identify the phases or interphases of interest especially as alphabetically marked from A to F. For this purposes, results from SEM / EDX / RXD analysis have been provided in the succeeding section.

It should be noted here that microstructural analysis of samples from *Batch 2* using JEOL microscope revealed similar trends and features as observed and discussed above with respect to *Batch 1* samples. The only notable difference was that *Batch 2* samples showed signs of precipitation. Both representative microstructures and precipitation can be seen in the images used for SEM analysis in the immediate next section.

5.4 SEM analysis of the sintered specimens

Comparable secondary-electrons images for *Batch 2* specimens are given in *Table 5-6* shows the evolution of microstructure with respect to nanoclay content. The general trend and features were similar to those observed from optical microscope imaging for *Batch 1* specimens. Two observations were considered significant. *Firstly,* unlike the reference specimen, grain boundaries for the specimen containing 1%wt nanoclay were not easily discernible other than by deciphering from the patterns of precipitates. This signified a relatively higher degree of sintering and superior heat-flow-matrix compared to the reference specimen. Attenuation of the level of porosity was also noted. From 2%wt nanoclay content onwards, grain boundaries appeared to gradually become more defined as well as distribution of pores. At 4%wt and 5%wt content, the boundaries were clearly defined, with the latter showing the onset of granular fragmentation into globular shape. This was accompanied by a relative increase in the number

and size of pores, a phenomenon linked by other researchers [54, 242] to agglomeration of particles.

Secondly, the prevalence of precipitates both at the grain boundaries and within the grains was observed to increase with the nanoclay content especially from 1%wt through to 3%wt content. From images taken at a relatively higher magnification as presented in *Table 5-7*, it was observed that the precipitates were becoming relatively fewer but larger in size with increase in the nanoclay content and getting more concentrated at the grain boundaries.

Table 5-6: Secondary electron images for *Batch 2* specimens showing the evolution of microstructure.

REF	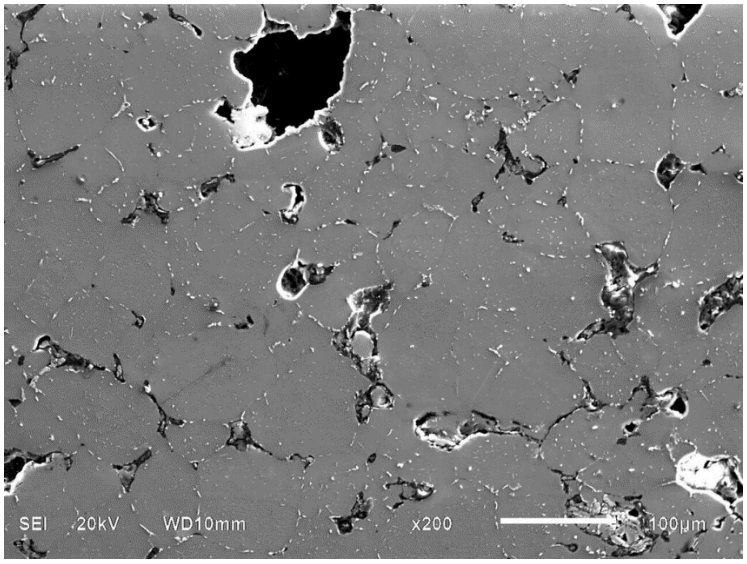
1%N	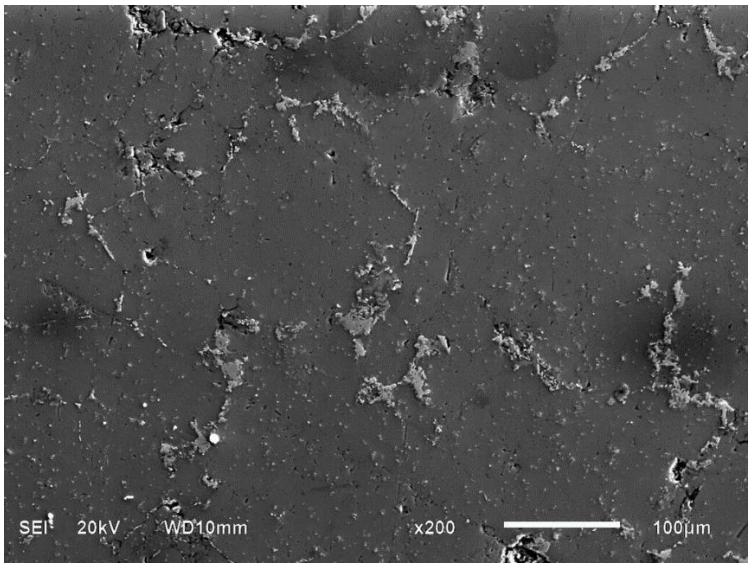

2%N	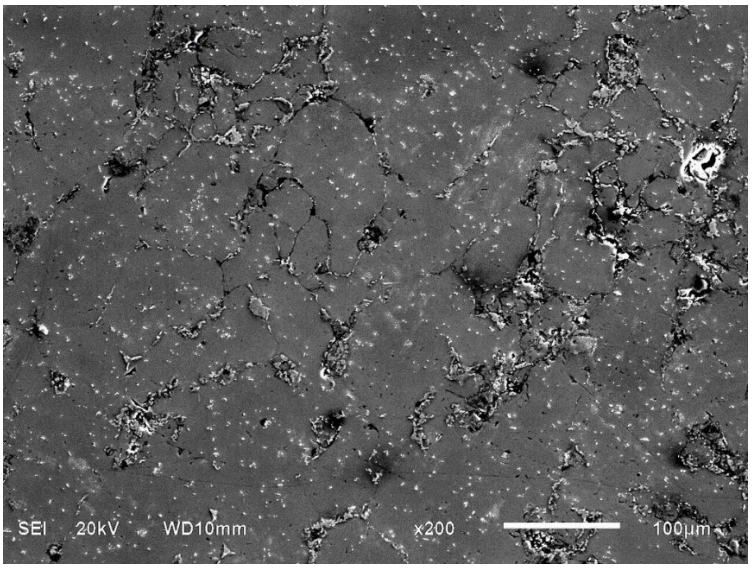 SEI 20kV WD10mm x200 100µm
3%N	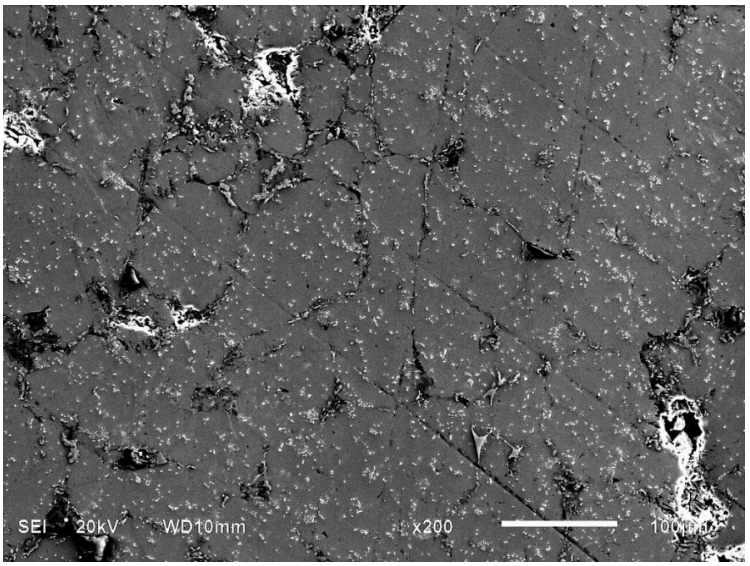 SEI 20kV WD10mm x200 100µm
4%N	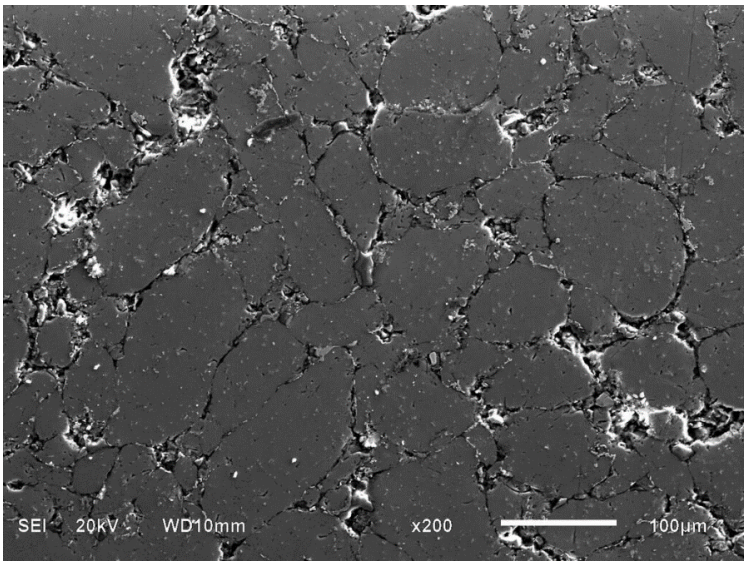 SEI 20kV WD10mm x200 100µm

5%N	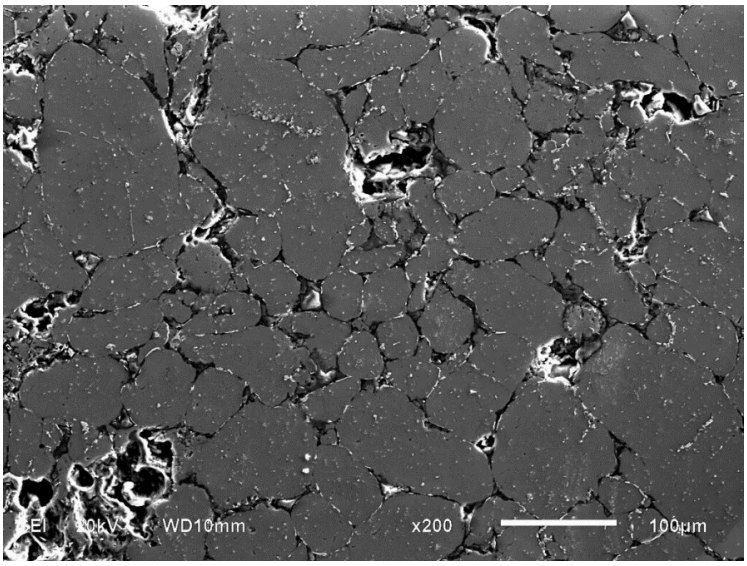

In addition to precipitates, it was further observed that the reference sample had micro-cracks in one of the phases located at the grain boundary as shown in *Table 5-7*. This phase was observed in both the reference samples as well as in all the samples containing nanoclay. This implies that the presence of this phase was not caused by addition of nanoclays. The cracking of this phase was deemed to imply that the phase was brittle. The cracking possibly occurred due to disparities between thermal properties of the phase relative to the neighbouring phases. EDX and XRD analysis results gave more information about this phase and the precipitates as detailed in the succeeding sections.

Table 5-7: Back scattered images of *Batch 2* specimens showing precipitation trend and micro-cracks.

REF	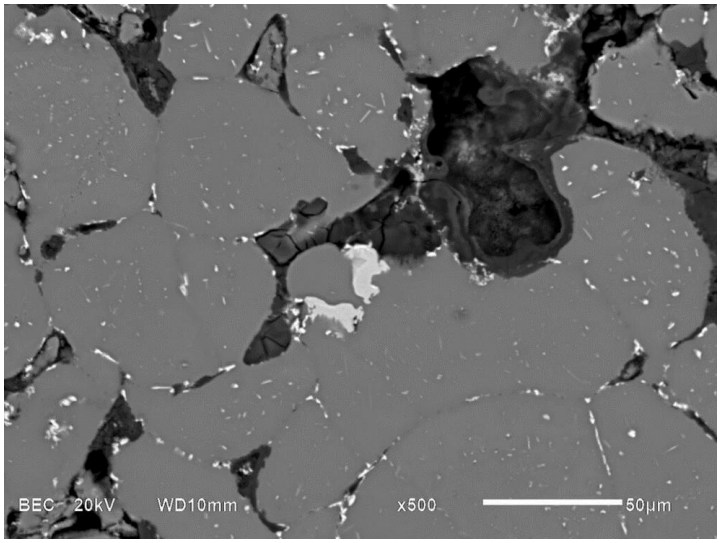

1%N	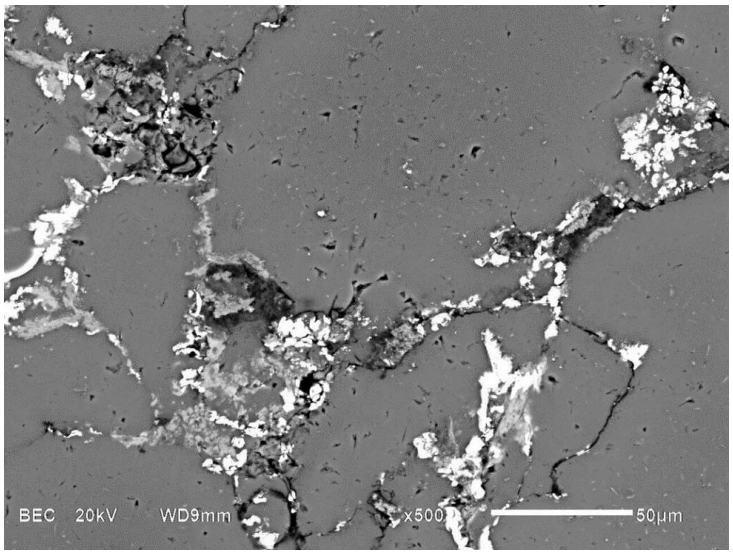 BEC 20kV WD9mm x500 50µm
2%N	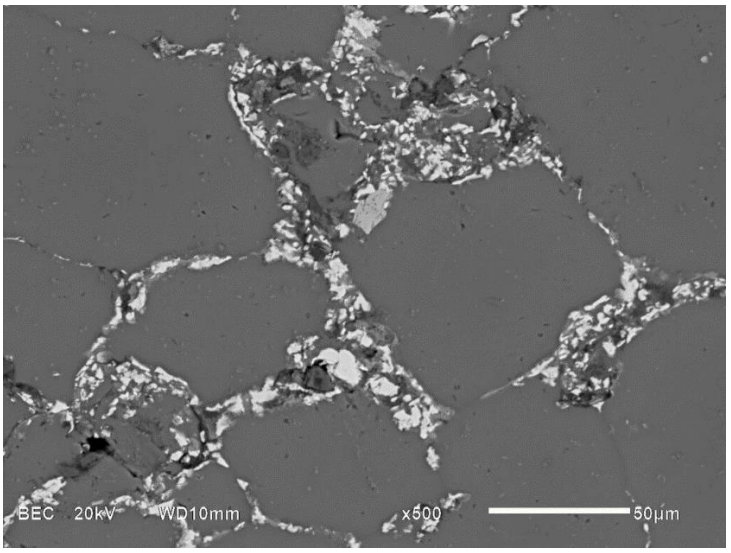 BEC 20kV WD10mm x500 50µm
3%N	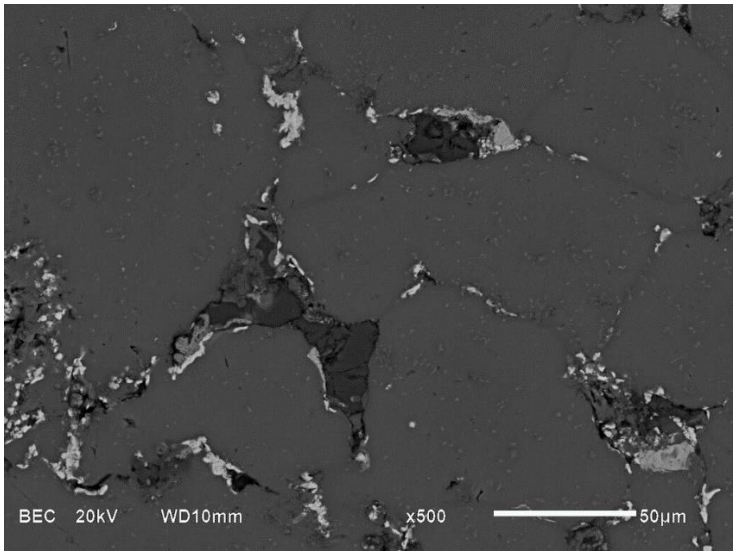 BEC 20kV WD10mm x500 50µm

4%N	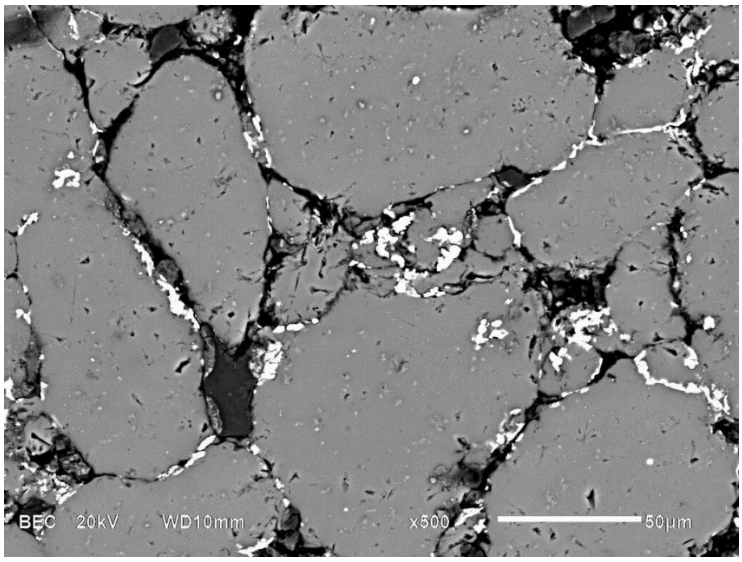
5%N	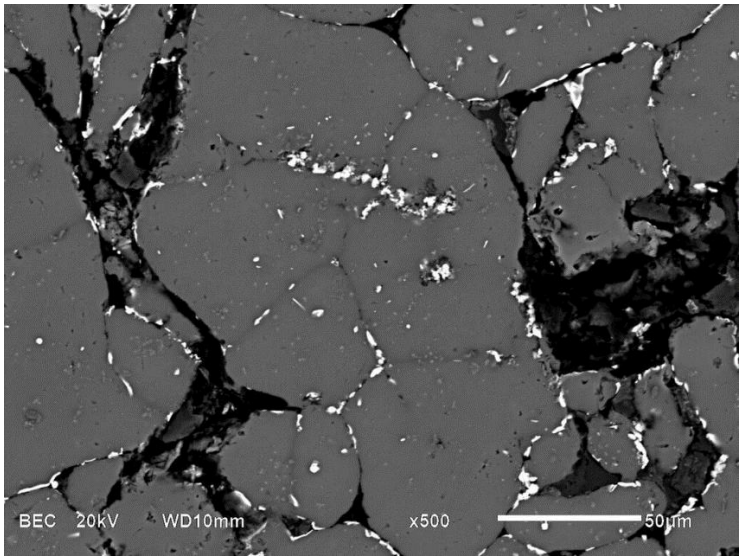

5.6 Phase composition: EDX and XRD analysis

5.6.1 EDX Analysis

EDX analysis was used as a follow-up investigating into two significant observations: (i) a dark phase appearing in all the specimens and seemingly plagued by microcracks, and (ii) precipitations in the microstructure at both the grain boundaries and within the grains.

5.6.1.1 The dark phase with micro-cracks

Table 5-8 shows magnified sites with the dark phase present in all categories of specimens. Of interest was the identification of a dark cracked phase in the sample as this phase. Sample locations of this phase are shown with an arrow.

Table 5-8: Dark phase observed in all categories of specimens.

REF	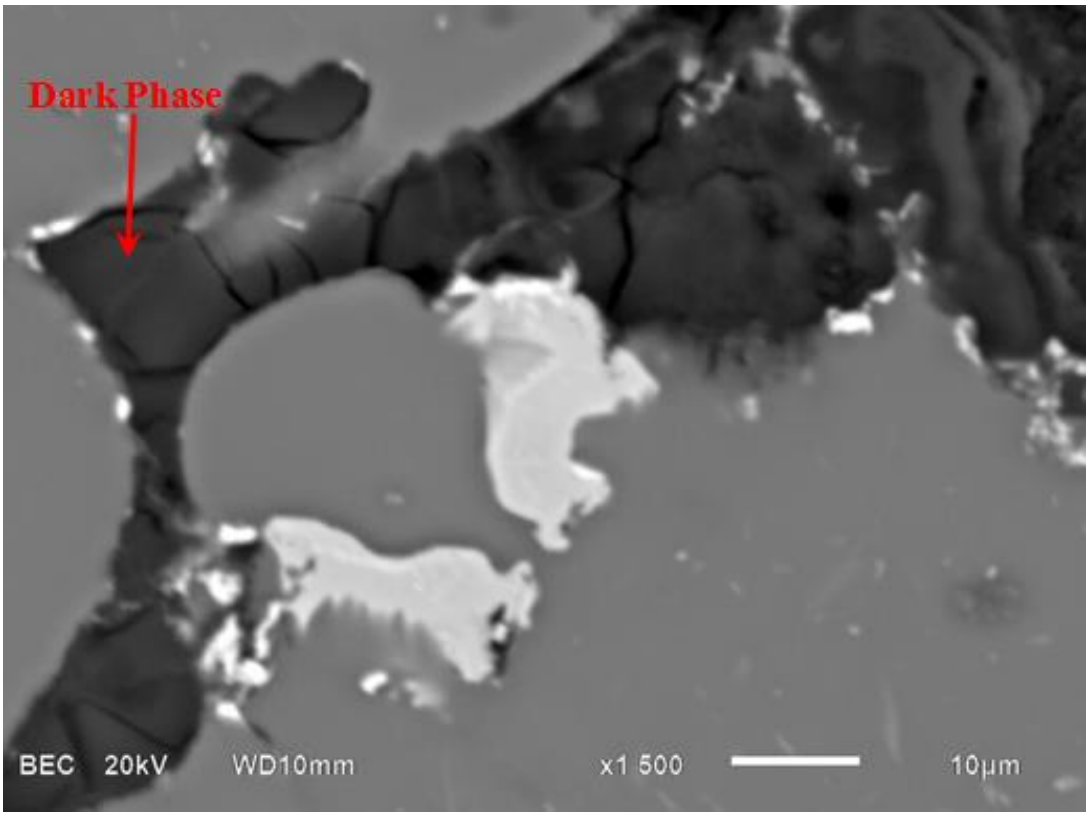
1% N	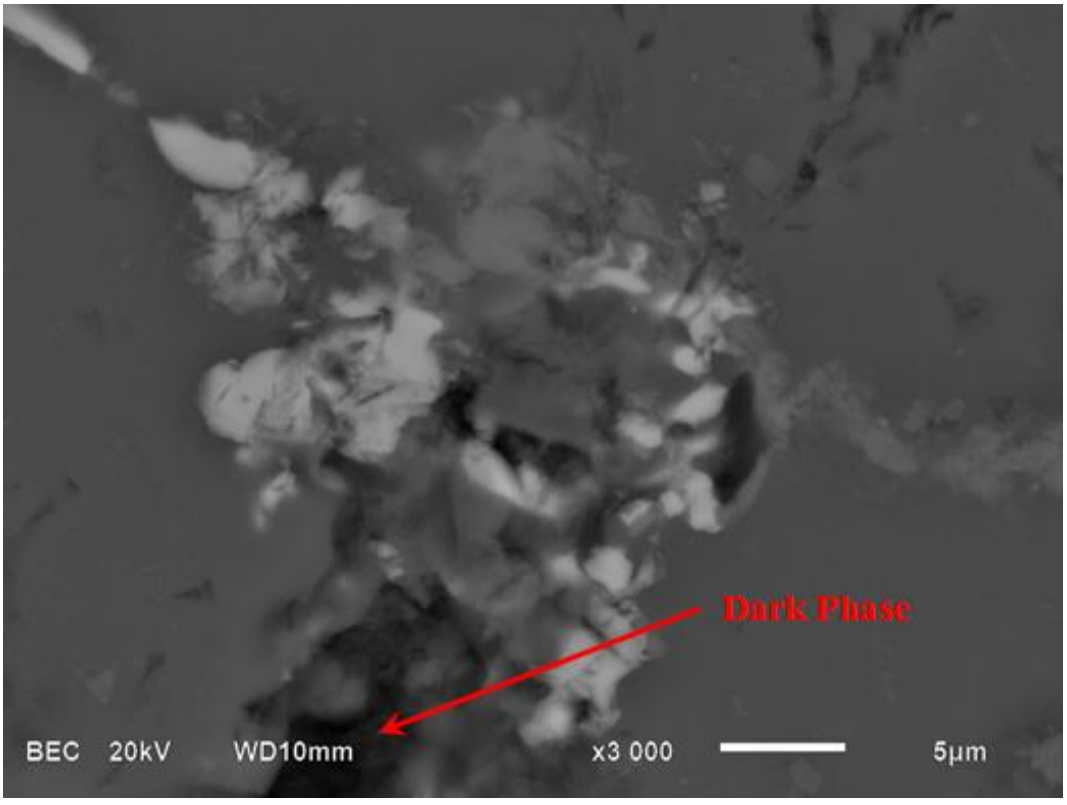

2% N	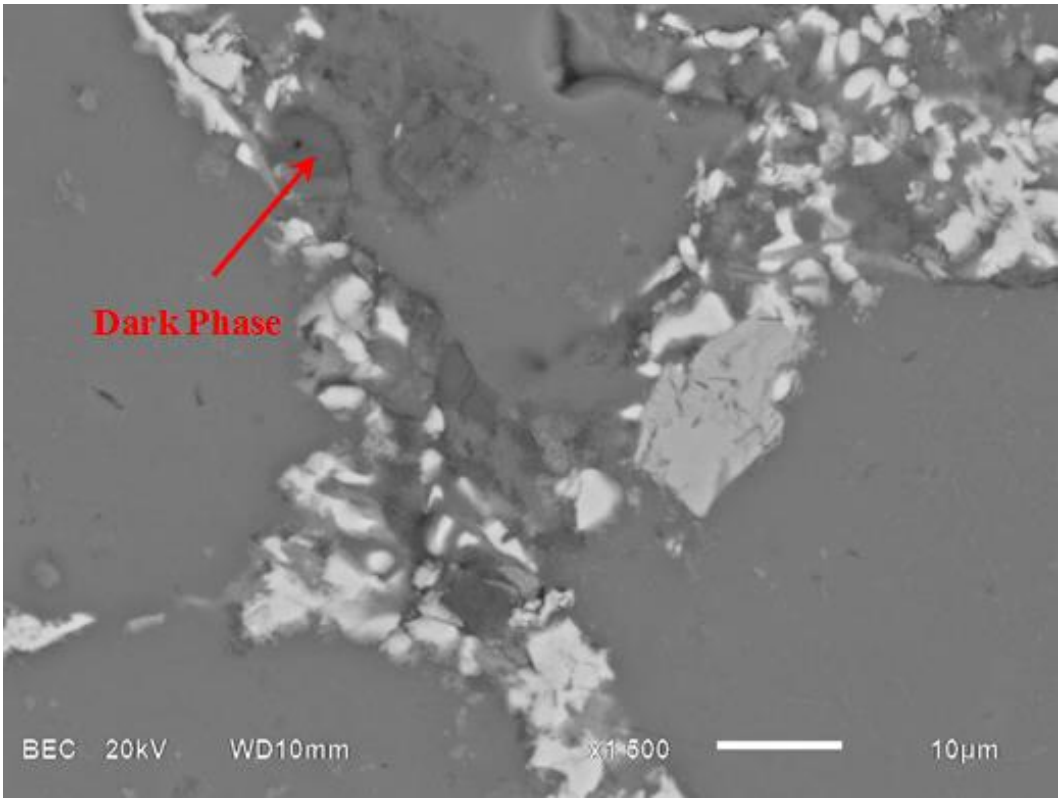 Dark Phase BEC 20kV WD10mm x1 500 10µm
3% N	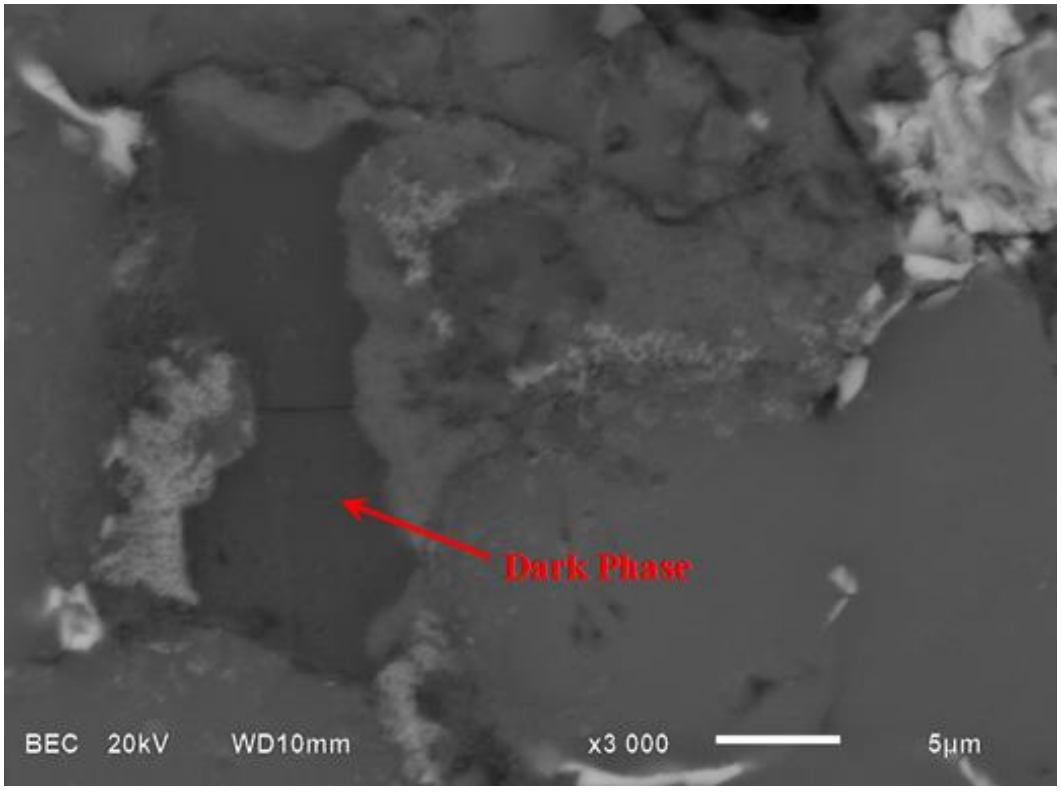 Dark Phase BEC 20kV WD10mm x3 000 5µm

4% N	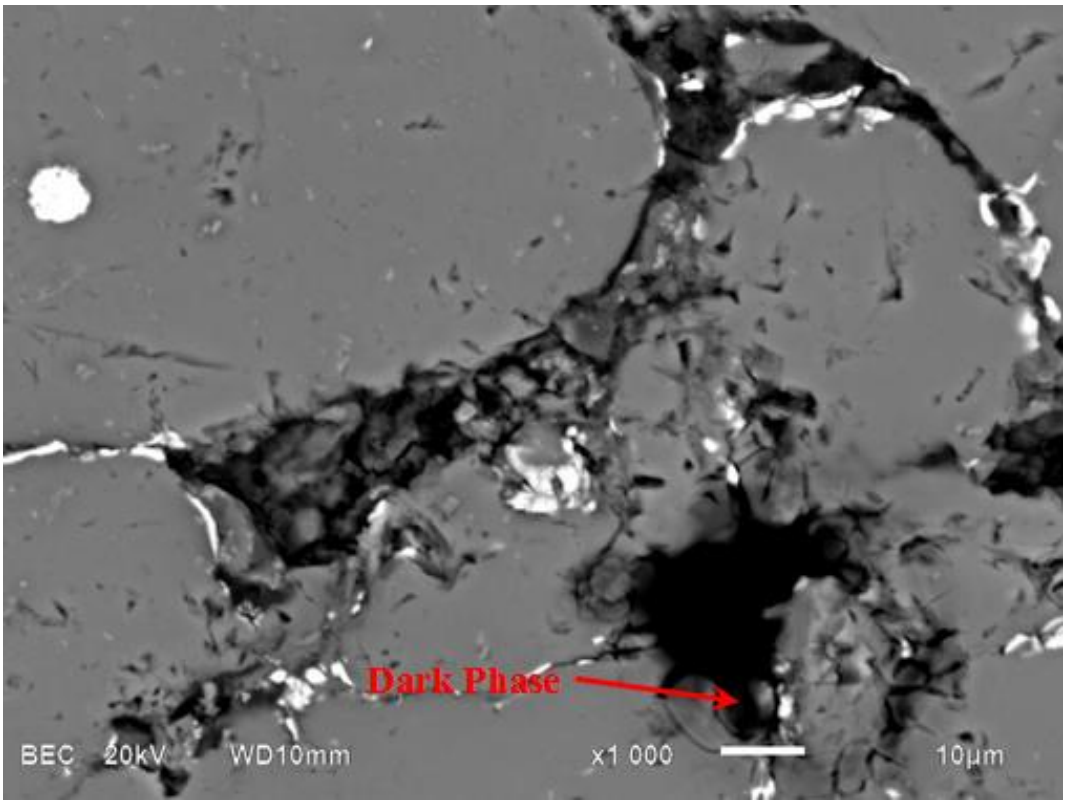
5% N	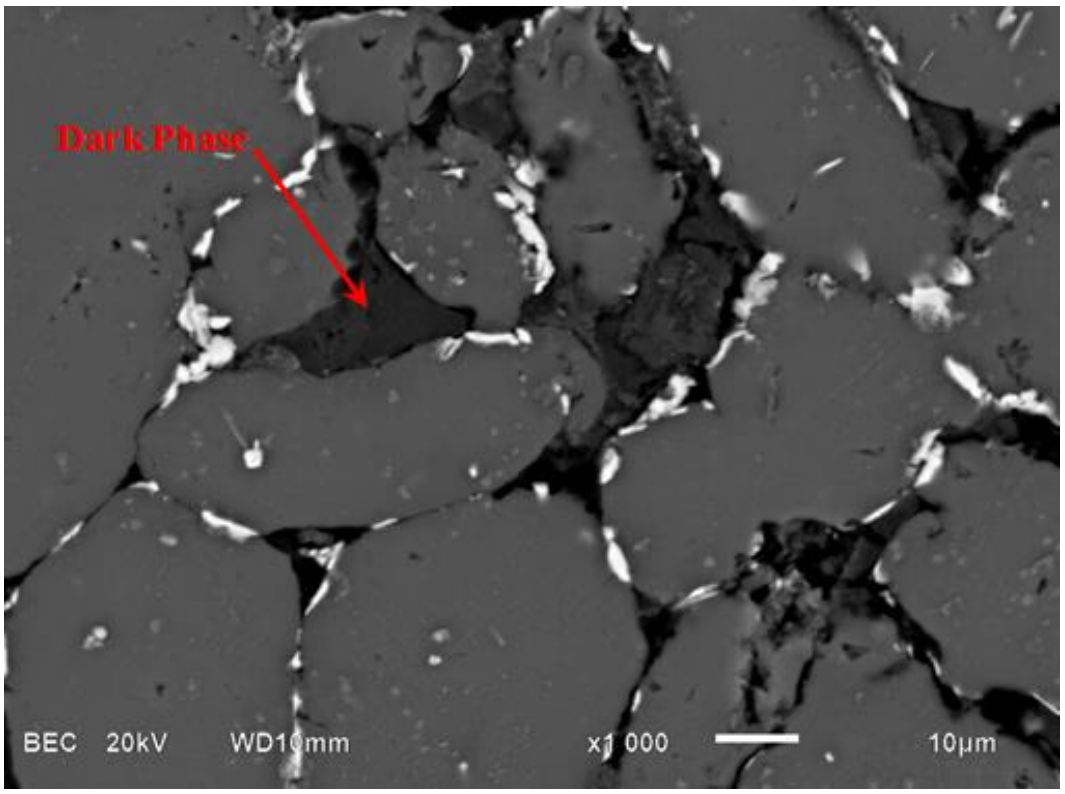

Figure 5-7 shows a secondary electron image corresponding to the back-scattered image shown in *Table 5-8* for the sample with 3%wt nanoclay. From this figure, it was evident that this dark phase had solidified from a liquid state. Of significance was the observation that the extent of

cracking of this phase in the nanoclay-AMCs was to relatively less compared to that observed in the reference sample.

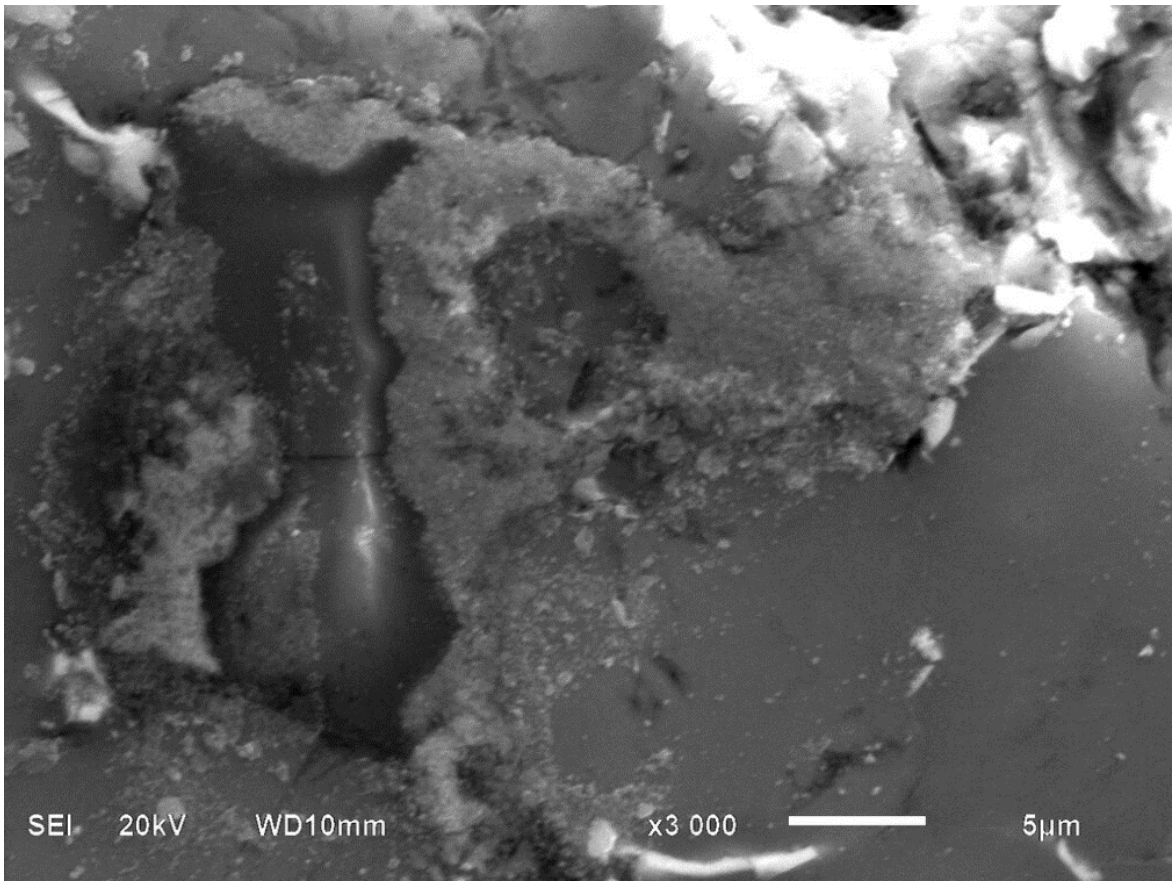

Figure 5-7: Secondary electron image showing the dark phase in sample with 3%wt nanoclay.

For identification of chemical composition of the dark phase, *Figure 5-8* was used for EDX spectral analysis. The site shown was from the reference sample. Alongside the dark-phase, the figure was used to identify composition of other compounds as differentiable by the different shades of colour. EDX spectra mapping identified the dark phase to be dominantly composed of MgO and SiO_2. Additional phases were also observed as detailed in *Chapter 9*. Meanwhile, it is worth noting that the phase was primarily found at the grain boundaries and seemingly played a significant role in filling up the pores, and hence aiding the densification process. Spectra overlays were used to decipher the elemental composition of different locations on the microstructure. These compositions are provided in the key to the figure. It should be noted that the major elements in section marked as B was Silicon (83%wt content).

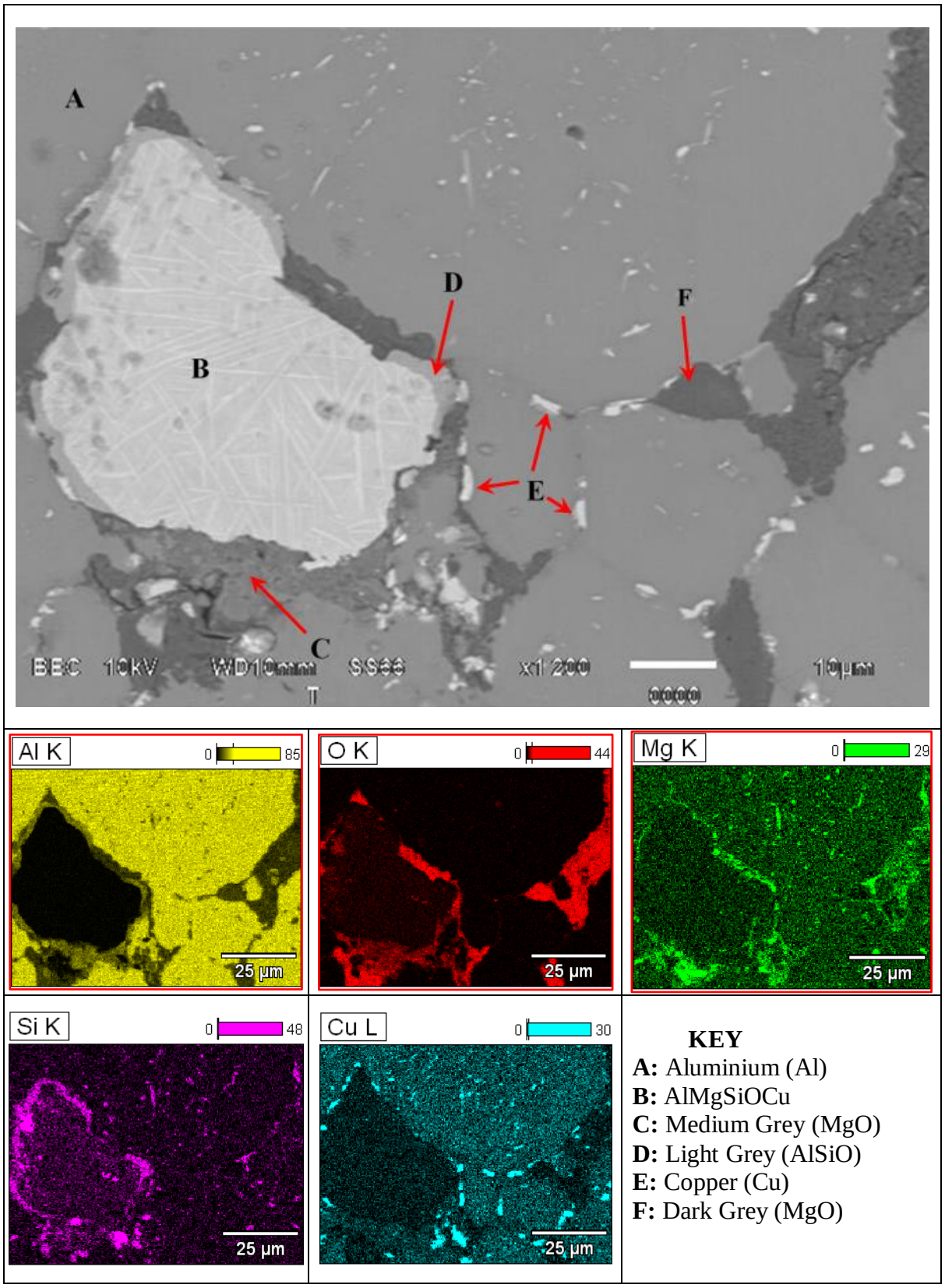

Figure 5-8: EDX spectral overlays identifying elemental compositions.

5.6.1.2 Precipitations

REF	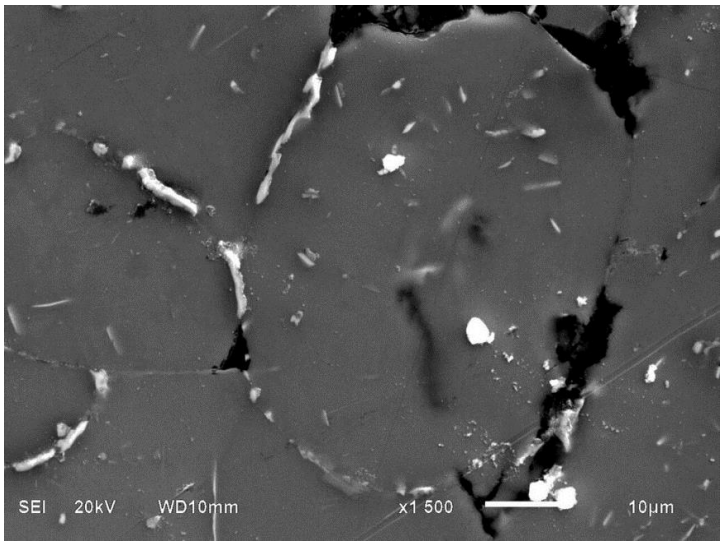
1%N	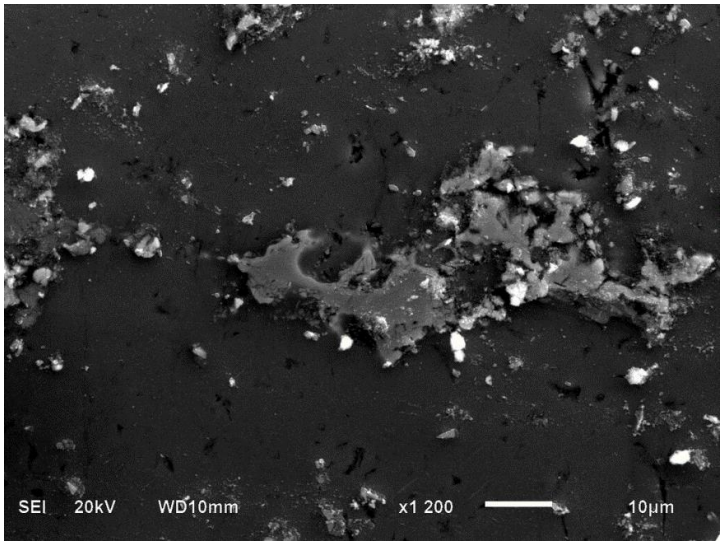
3%N	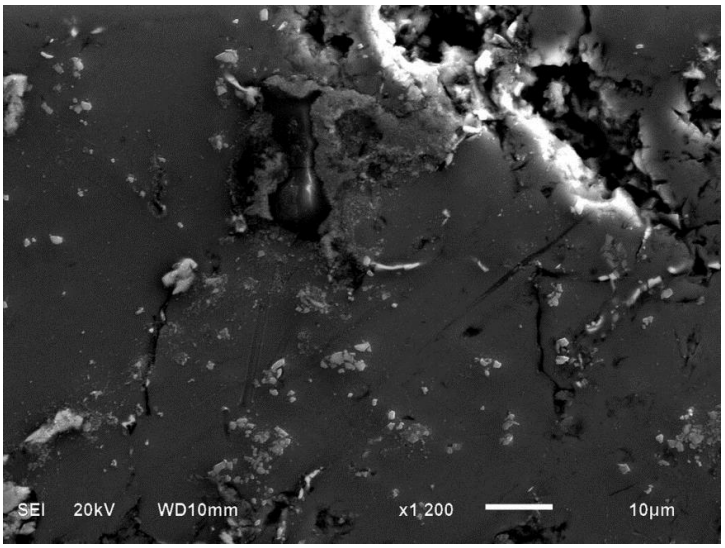

Figure 5-9: Evidence of nanoclays effectively increasing the occurrence of precipitations.

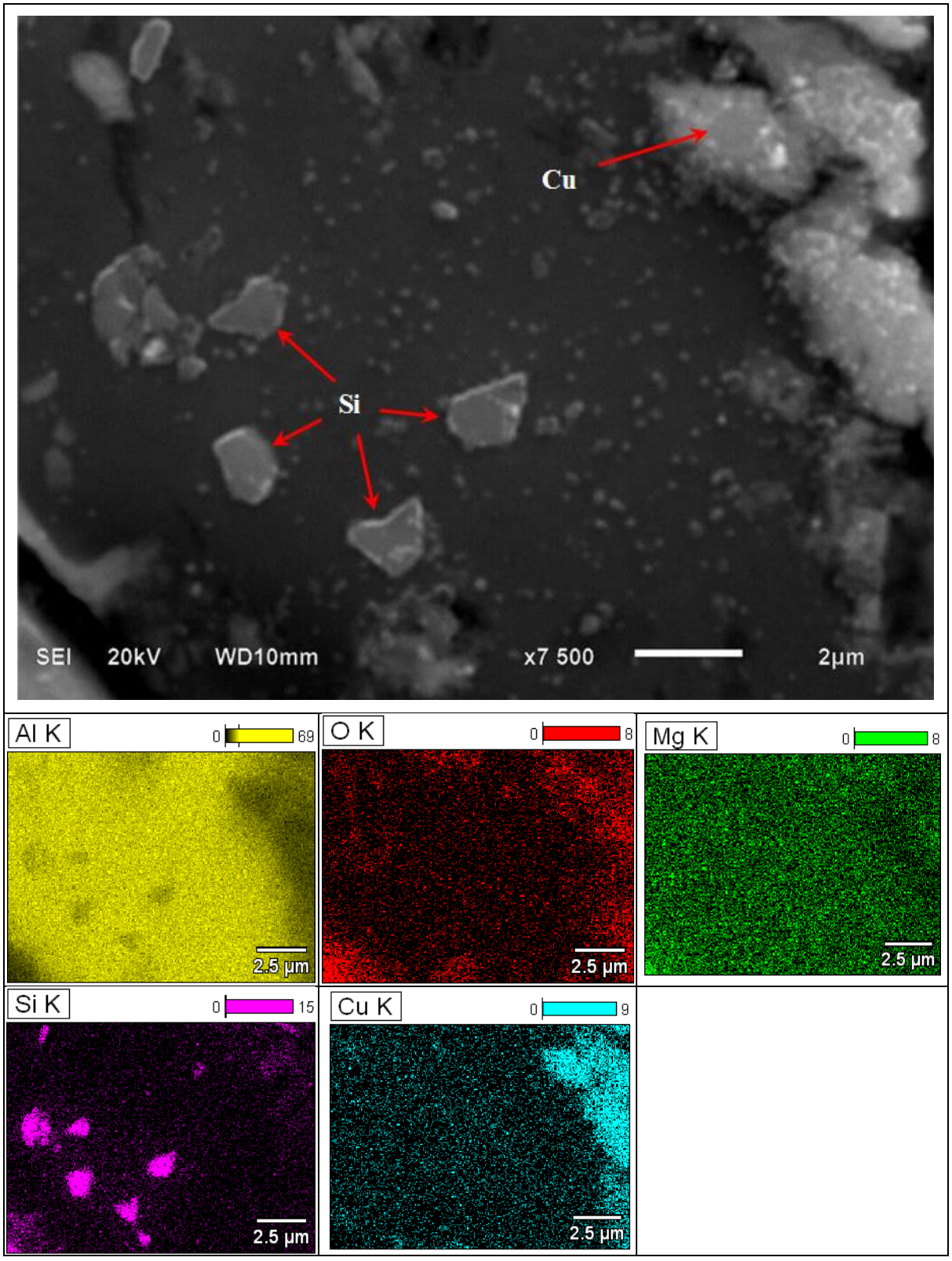

Figure 5-10: EDX spectra showing sample large silicon precipitates within grains.

A look at *Figure 5-8* shows that copper, silicon, and magnesium precipitated both at the grain boundaries and within the grains. However, precipitation was more dominant in the boundary

grains especially as demonstrated by the copper-precipitates appearing as white particles in high contrast from the background. This trend was also visible from *Table 5-7* where the distribution of precipitates was observed to become less but accompanied by increase in size of the precipitates. *Figure 5-9* exemplifies the observed trend of precipitates increasingly appearing within the grain besides their concentration at the grain boundaries as a result of increase in nanoclay content in the system. Even though the magnification for the reference sample was higher than the counterparts, it was evident that the relative intensity of precipitates distribution within the grains increased with increasing nanoclay content.

EDX revealed the precipitates within the grains to be largely comprised of silicon. *Figure 5-10* shows the distribution of copper and silicon precipitates in the sample containing 5%wt nanoclay. As observed on all other samples, copper is seen predominantly precipitated at the grain boundary. Interestingly, in addition to presence at the grain boundaries, large silicon precipitates were clearly evident within the grains. For this to happen, the silicon solubility in aluminium must had been exceeded beyond the 1.65% limit [244]. Since the AMB-2712 only has 0.6-0.9%Si according to the supplier, the excess silicon must had been from the nanoclay. Therefore, this precipitation phenomen presents evidence to the effect that nanoclays can innovatively be used as an effective source of silicon in the formulation of conventional aluminium alloys and composites.

5.6.2 XRD Analysis

The different versions of cracks or phase discontinuities observed were further investigated using XRD. Irrespective of the magnification used, it was noted that in the absence of nanoclay (*Figure 5-11(i)*) as well as at relatively low nanoclay contents (*Figure 5-11(ii)*), any visible microcracks were observed to be entirely contained within the grain-boundaries and distinct from the inherent porosity evident in most materials processed through powder metallurgy. They either constituted instances of incomplete fusion or separation of a solidified liquid phase.

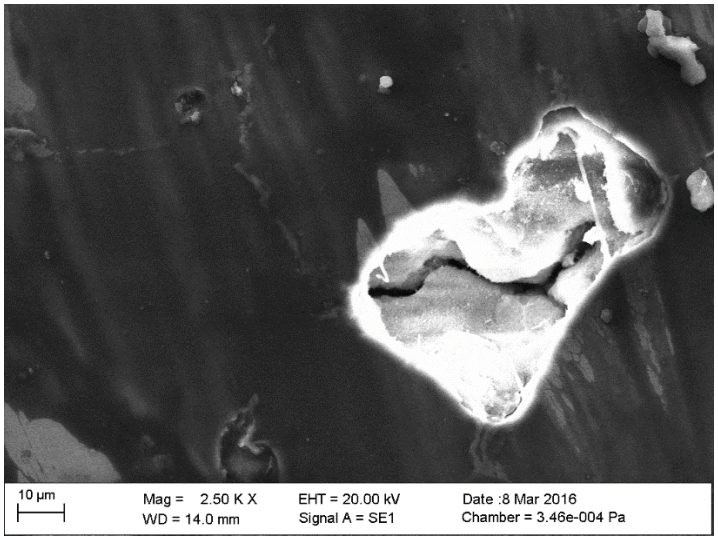

(i)

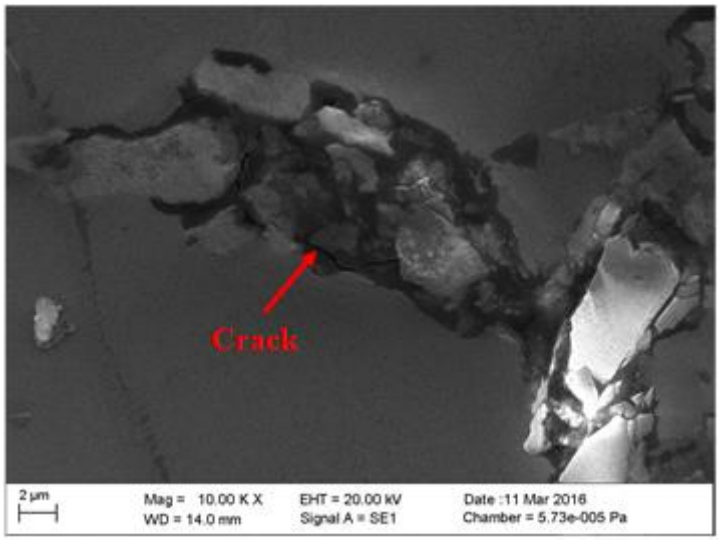

(ii)

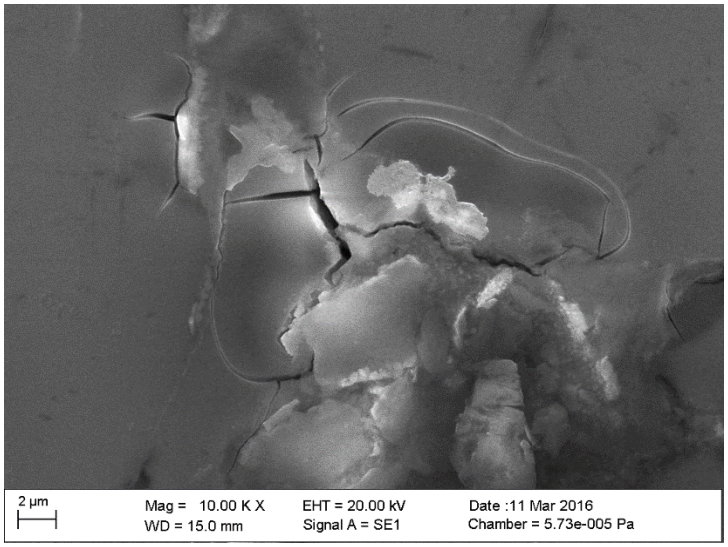

(iii)

Figure 5-11: SEM images: (i) Reference, (ii) 1%wt, (iii) 12.5%wt *Nanofil 116* sample.

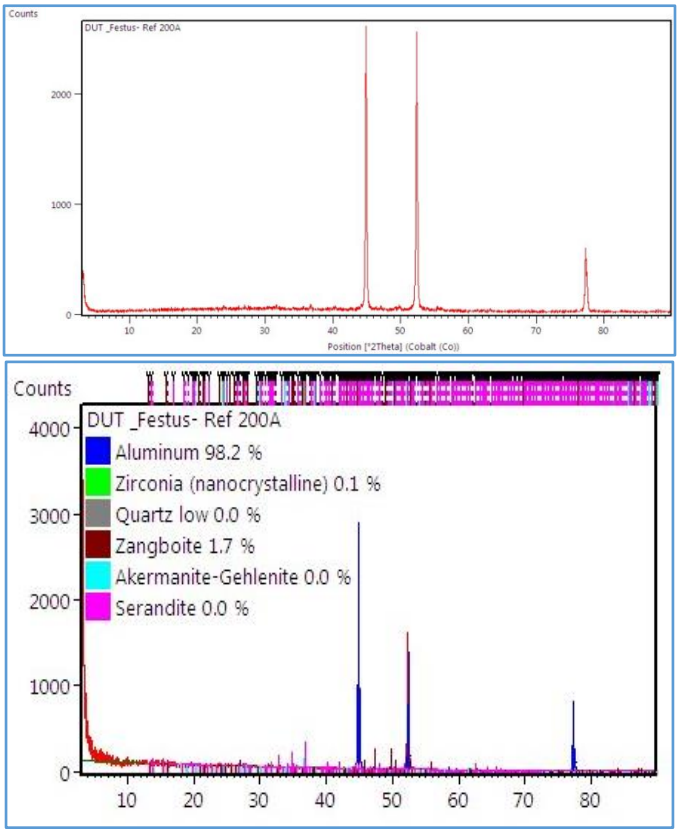

(i)

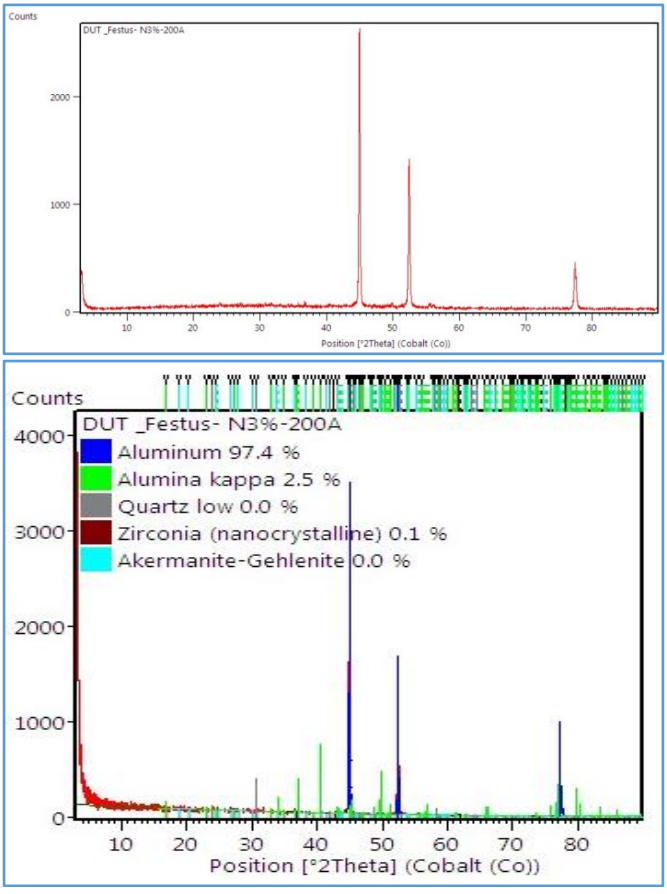

(ii)

Figure 5-12: XRD results (i) Reference Samples, and (ii) Samples with 3%wt *Nanofil 116*.

In contrast, at relatively higher nanoclay contents (*Figure 5-11(iii)*), micro-cracks originating from the grain-boundaries were observed to propagate outwards into the grains of the matrix. This phenomenon was increasingly observed as the nanoclay content was increased especially from 3% upwards.

Prevalence of the observed micro-cracks was considered to suggest insitu formation of brittle phases of a ceramic nature during sintering. In fact, it was established that thermally instigated reactions amongst chemical elements in the nanoclays and matrix resulted into formation of minerals of ceramic nature as seen in *Figure 5-12*. Despite the XRD graphs seemingly looking the same, a comparison of the chemical composition of the two samples showed a decline in the percentage proportion of Aluminium (Al) in favour of increased presence of ceramic compounds such as Alumina (Al_2O_3). This may be attributed to the presence of Aluminium in both the matrix and nanoclays, coupled with incremental introduction of organic elements through the nanoclay.

The variation in composition can further be seen in the crystallinity of the samples whereby the sample with 3%wt nanoclay shows a relatively higher number of secondary peaks than the reference sample. This was represented by a relative shift to the formation of *Alumina* and *Akermanite* in preference to *Serandite*. Besides the peaks being shorter in the reference sample, the d-spacing is also generally reduced across all data points. This may be reflective of the observed nanoclay's grain-refinement effect on the matrix as discussed in *Chapter 5*.

At increased %wt content of *Nanofil 116*, it may expected that the relative quantity of magnesium in the AMC became higher than the 0.1 – 1% recommended for the favourable break-up of the surface oxide layer through the development of a $MgAl_2O_4$ phase [229]. In this context of increased presence of magnesium, the inferior phase would not completely dissolve in solid solution, thereby staying as a complex at the grain boundaries resulting to

embrittlement of the AMC [230]. This phenomenon was evident during microscopy analysis as exemplified in highlighted zones (dotted zones) in *Figure 5-13* whereby the spinel phase was probably the bluish shaded particles at the grain-boundaries. Further TEM analysis is therefore recommended.

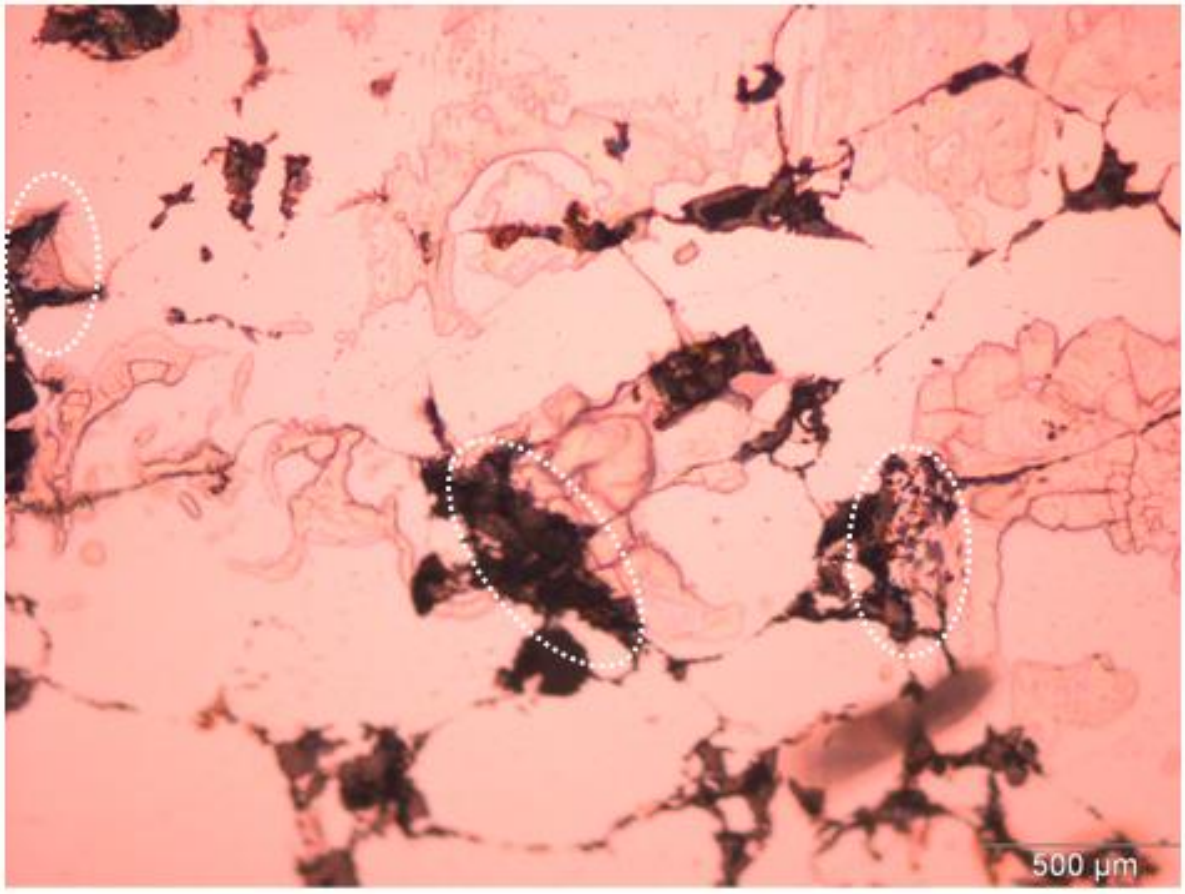

Figure 5-13: Microscopy Image of sample with 3**%**wt *Nanofil 116*.

Figure 5-14 shows an SEM image for a 160 Bars sample containing 12.5%wt *Nanofil 116* and on which an EDX analysis was conducted. Besides positive identification of metallic elements such as aluminium and copper, it was evident that there were sufficient and varied non-metallic and semi-metallic elements that typically anchor the formation of ceramic compounds. These compounds were validated using XRD analysis, confirming presence of a diverse range of minerals such as akermanite, serandite, zirconia (nanocrystalline), zangboite, almandine, magnesite, quartz, and Al-Cu spinels. These minerals were in addition to the formation and

relatively high presence of khatyrkite (Al_2Cu) that may be associated with the relatively higher solubility of copper in aluminium.

It was further observed that the micro-cracks also tended to originate at sites having a relatively high content of copper. With reference to *Figure 5-14, Spectrum 138* marks the centre of a

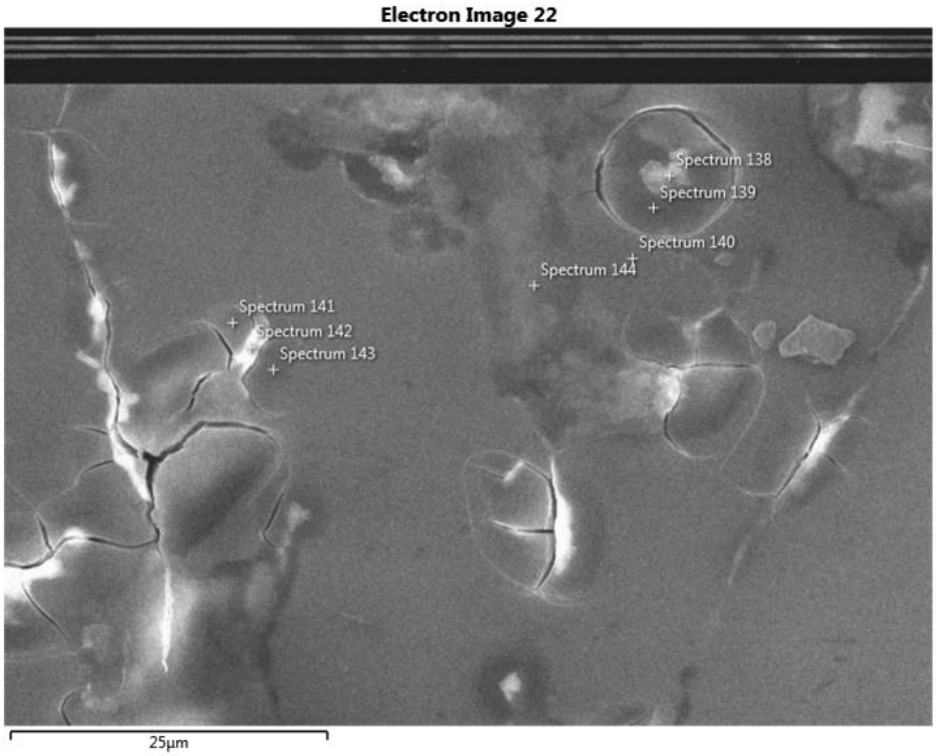

Element	Wt%	Wt% Sigma
C	6.59	0.36
O	50.45	
Na	1.79	0.08
Al	32.58	0.27
Si	1.00	0.05
S	0.16	0.03
Ca	0.20	0.03
Cu	7.22	0.16
Total:	100.00	

Spectrum138

Element	Wt%	Wt% Sigma
C	2.81	0.20
O	48.94	
Na	0.58	0.03
Al	45.54	0.20
Si	0.21	0.02
Ca	0.07	0.02
Cu	1.84	0.07
Total:	100.00	

Spectrum 139

Element	Wt%	Wt% Sigma
C	1.62	0.14
O	48.25	
Al	49.12	0.15
Cu	1.01	0.04
Total:	100.00	

Spectrum 140

Element	Wt%	Wt% Sigma
C	4.08	0.24
O	49.79	
Na	0.81	0.04
Al	40.58	0.21
Si	1.49	0.04
Ca	0.14	0.02
Cu	3.11	0.08
Total:	100.00	

Spectrum 141

Element	Wt%	Wt% Sigma
C	6.02	0.25
O	47.66	
Al	22.16	0.14
Si	6.54	0.07
Ca	0.10	0.02
Cu	17.52	0.16
Total:	100.00	

Spectrum 142

Element	Wt%	Wt% Sigma
C	3.48	0.22
O	49.64	
Na	0.47	0.04
Al	43.37	0.21
Si	0.98	0.03
Ca	0.06	0.02
Cu	1.99	0.07
Total:	100.00	

Spectrum 143

Element	Wt%	Wt% Sigma
C	3.90	0.52
O	49.91	
F	1.86	0.15
Na	2.49	0.07
Mg	3.80	0.07
Al	19.34	0.22
Si	15.95	0.19
K	0.18	0.03
Ca	0.35	0.03
Fe	1.28	0.06
Cu	0.93	0.07
Total:	100.00	

Spectrum 144

Figure 5-14: SEM Image and spectra for 160 Bars sample with 12.5%wt *Nanofil 116*.

circular micro-crack, with a 7.22 %wt Cu, which decreases with the shift to *Spectrum 139* (1.84%Cu) and *Spectrum 140* (1.01%Cu). A similar correlation was observed in *Spectrum 142* (17.52%Cu) relative to the neighbouring *Spectrum 141* (3.11%) and *Spectrum 143* (1.99%Cu). In both cases, it was clear that these micro-cracks were within the grains as opposed to being aligned with the conventional grain boundaries. Since there was no significant variation in content of the other major elements across the both sets of spectra, it can be argued that the evident localized origination of micro-cracks around copper can directly or indirectly be linked to the differences in coefficient of thermal expansion of copper relative to the bordering elements and/or ceramic compounds.

5.7 Summary

Nanofil 116-AMCs specimens were successfully sintered despite minor delubrication concerns. Stress concentrations can contribute to deformation of specimens when sintering in the supersolidus temperature regime. The deformation may induce exudation. Despite increased porosity at 5%wt content of *Nanofil 116*, the transition to globular microstructure yields a gain in densification. Porosity decreased with the green compaction pressure. This was attributed to increased cumulative surface area of contact for conductive heat transfer as a result of cold-welding induced during green compaction. At high nanoclay content, the pores became scarcely distributed but larger in size.

Beside the nanoclay having a resultant filler effect on the AMCs at as low as 1%wt content, increase in nanoclay content did improve the heat transfer dynamics and induced granular collapse or disintegration, thereby playing a significant role in densification. Precipitates were observed both at the grain boundaries and within the grains. These precipitates increased with increase in content of *Nanofil 116*, with the precipitates becoming fewer in distribution but larger in size as the nanoclay content was increased especially beyond 3%wt content.

CHAPTER 6:

NANOFIL 116 – AMCs: Thermal Properties

6.0 Introduction

In the introduction to the current study, it was hypothesized that improvement of thermal properties of the material for automotive engine blocks, cylinder-heads, and associated components can increase the engine's operating temperatures, potentially yielding improved operational efficiency, lower fuel consumption, and lower carbon foot-print on the environment. This chapter is dedicated to the reporting of experimental results and discussion of the thermal behaviour of *Nanofil 116*-AMCs as assessed using physical inspection, DSC-TGA, optical microscopy, SEM, thermal conductivity, specific heat capacity, thermal diffusivity, thermal expansion percentages, coefficients of thermal expansion, and modelling.

6.1 Thermal Behaviour of AMCs

6.1.1 Thermal behaviour of sintered reference specimens

For ease of reference, samples were labelled in a standardized manner as "*Matrix – Alloy - Nanoclay %wt Content - Nanoclay's Name - Green Compaction Pressure - Sintering Profile Settings - Sample Number*", e.g. *Al-2712-0-REF-160-A-1.001* refers to sample number 1 of AMB-2712 alloy matrix with 0%wt content of Nanoclay (i.e. Reference specimens), previously subjected to 160 Bar green compaction pressure, and processed using *Set "A" run* sintering profile-settings. Similarly, *Al-2712-3-Nanofil 116-240-A-2.001* refers to sample number 2 of AMB-2712 alloy matrix with 3%wt content of *Nanofil 116*, previously compacted to 240 Bars, and processed using *Set-"A"-run* sintering profile-settings.

Figure 6-1 shows results for *Set-"A"-run* reference specimens while *Figure 6-2* shows an expanded view of the boxed region in *Figure 6-1*. In similarity to the as-received aluminium powder, the melting in the sintered Reference sample starts at approximately 512^0C and ends

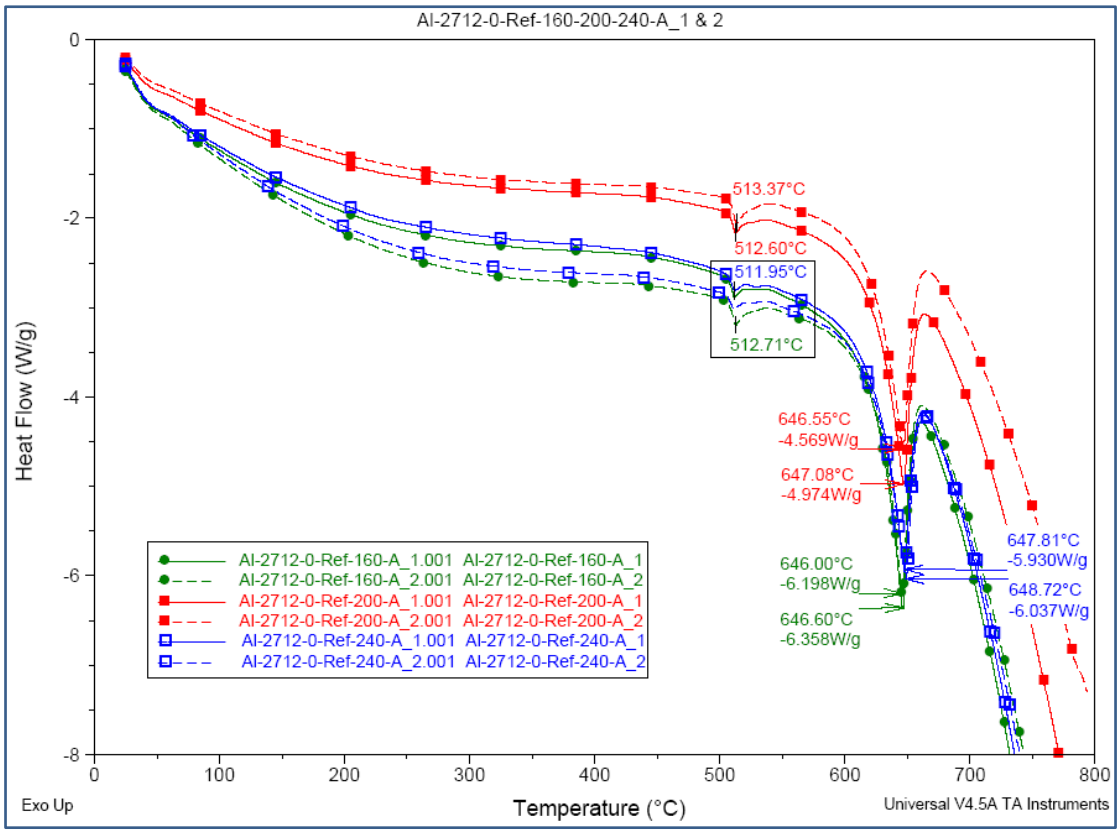

Figure 6-1: Heat flow results for *Set-"A"-run* reference samples as a function of Green Compaction Pressure.

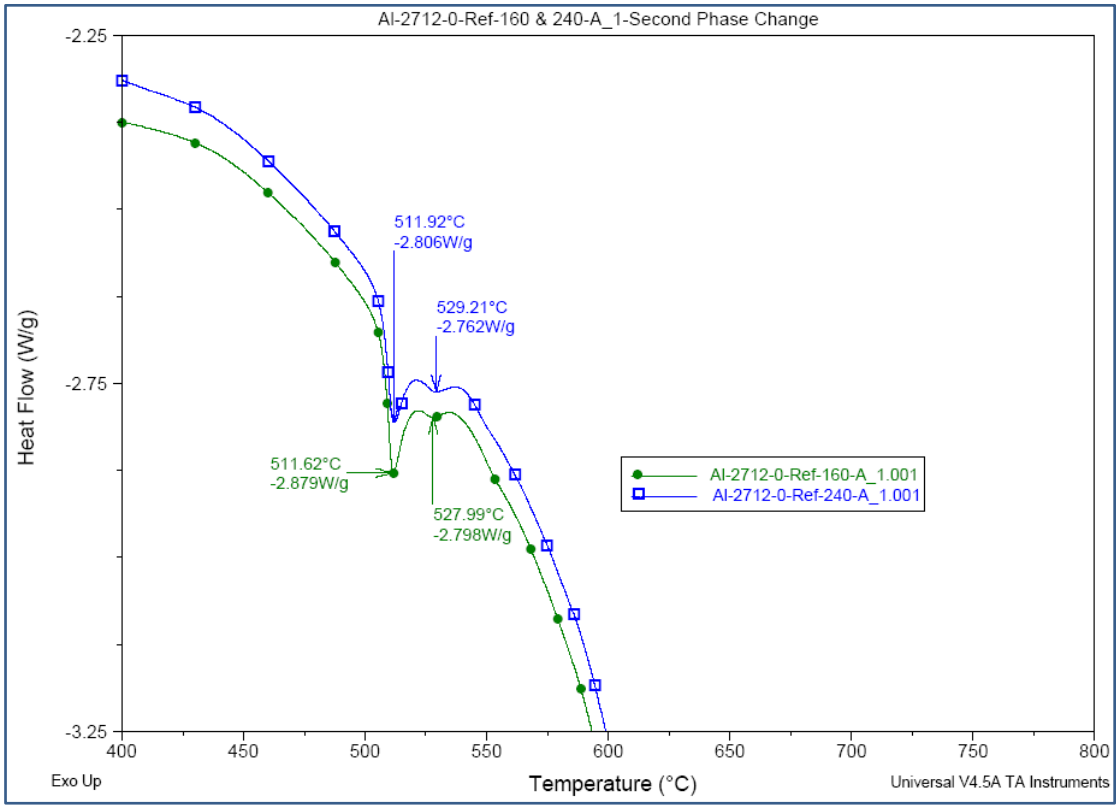

Figure 6-2: Second phase change under *Set-"A"-run* processing settings.

at around 646^0C. Based on a typical binary-phase-diagram for Al-Cu alloy, the phase change at 646^0C closely corresponded to the 648^0C and represents transition from supersolidus to liquidous phase.

It would be reasonable to expect thermal behaviour of specimens to exhibit some degree of proportionality to the green compaction pressure. However, samples from the 200 Bars specimen generally depicted superior heat flows relative to the 160 and 240 Bars specimens and thereby implying a relatively higher entropy. As alluded to earlier on, this behaviour may be related to the systems' quest to attain equilibrium in entropy representing a balance between pressure, density, and temperature according to the second law of thermodynamics [243], which dictates that the entropy of an isolated system not in equilibrium will tend to increase over time, approaching a maximum value at equilibrium [245].

It is hereby contended that the aforementioned anomaly may typically be related to, and deemed consistent with, the anomalous behaviour reported on Al-Cu composites by K. Yamaguchi et al [51]. For the same reference green compaction pressures and volume fractions, they observed that the sintered density of Al-Cu composites became smaller than that of the green compact. At a comparative level, this was unlike their observation with Cu-Fe composites where the density of sintered parts was observed to increase with sintering temperature and volume fraction of Copper powders. In their study, this anomaly was attributed to relative increase in volume of the samples. An effort to explain the anomaly is herein given in the section preceding conclusions, i.e. in the form a heat-transfer-matrix model.

6.1.2 Effect of *Nanofil 116* on Phase changes

Figure 6-3 shows thermal behaviour results for nanoclay-infused-specimens previously compacted at 160 Bars. These results were consistent for both tested samples, showing improved thermal properties over the reference samples. It was also observed that the Nanoclay

delayed the melting temperature by almost 7^0C at 8%wt content. This corresponds to a 34% reduction in heat flow, with the maximum reduction of 40% being recorded for the specimen induced with 12.5%wt content of *Nanofil 116*. On the same note, it was interesting to notice that 1%wt content of the nanoclay raised the melting temperature by 6.6^0C as well as reduced the heat flow by 25%, the greatest incremental impact with reference to the other %wt contents of the nanoclay.

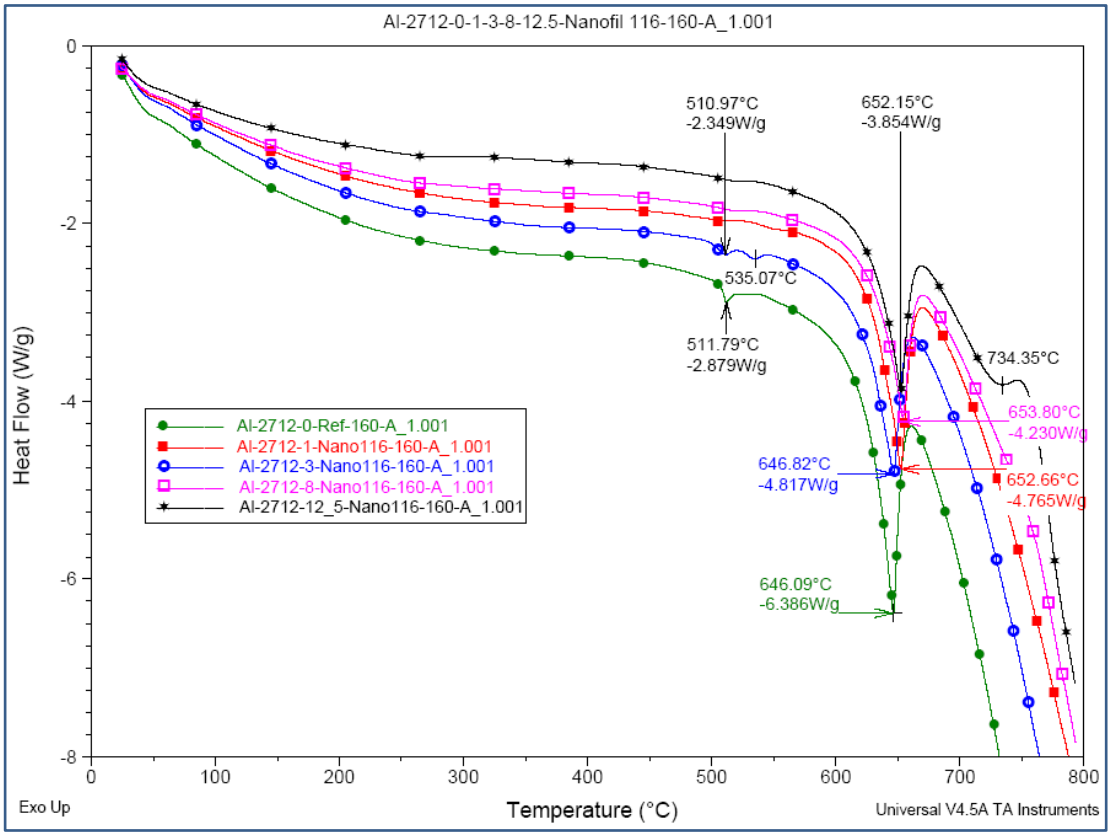

Figure 6-3: Thermal properties of 160 Bars specimen with varying %wt *Nanofil 116*.

Of significance was the observation that the thermal properties improved with increase in %wt content of *Nanofil 116* except for the 3%wt specimen which showed inferior thermal properties than its counterpart having 1%wt specimen at 160 Bars compaction pressure. However, this was not the case with the 200 and 240 Bars specimens, which showed a consistent trend of improvement of the properties with increase in nanoclay content as shown in *Figure 6-4*. Further, it was observed that the first two endothermic peaks (e.g. at ~ 512^0C and ~ 535^0C)

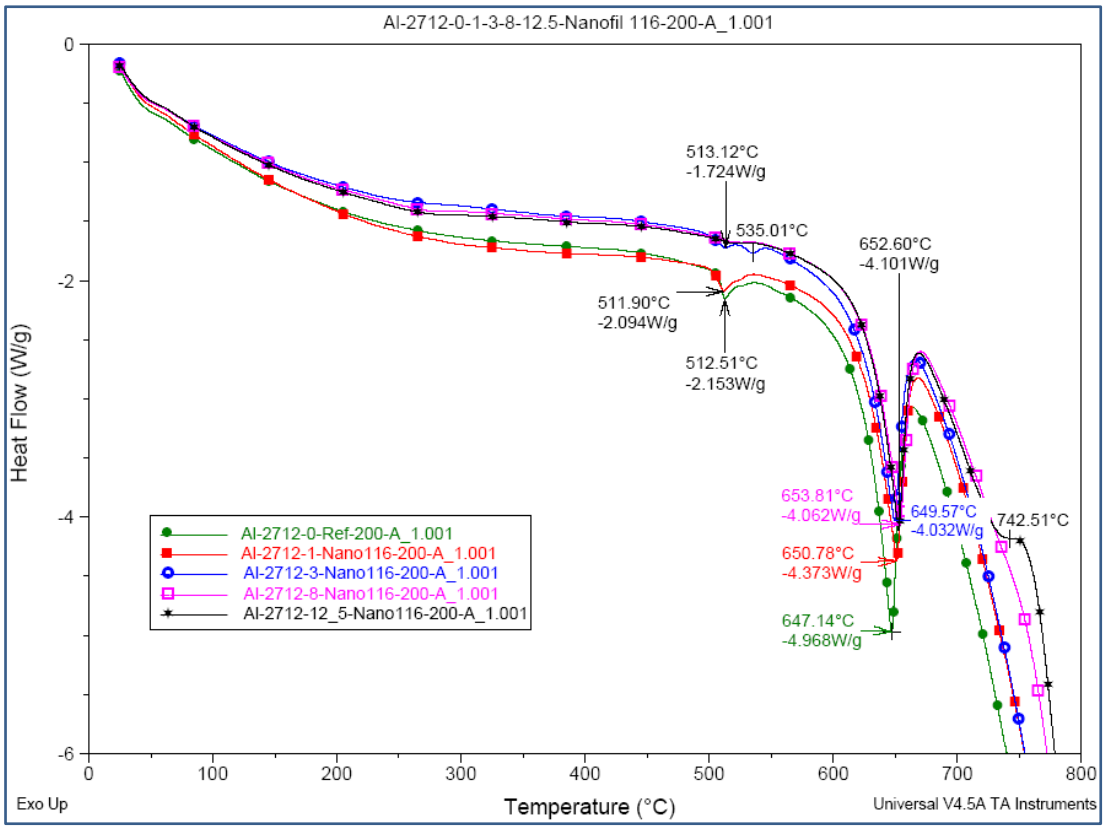

(i)

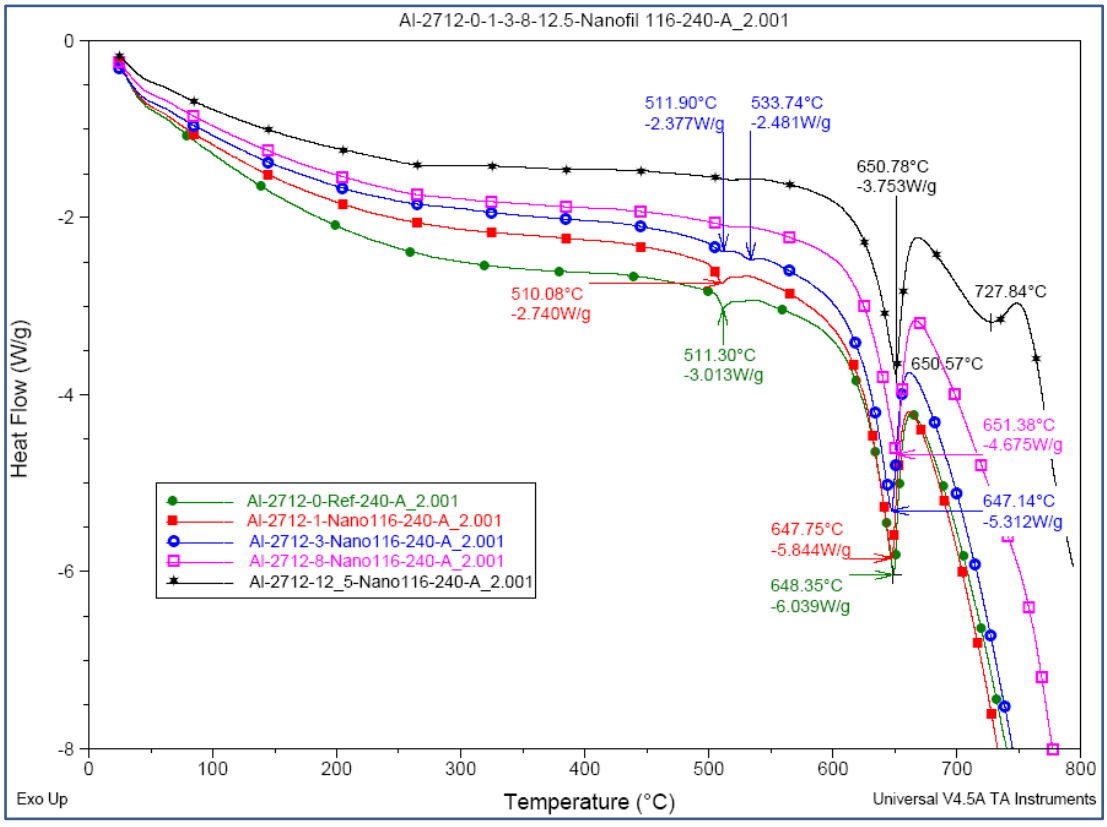

(ii)

Figure 6-4: Thermal behaviour properties of (i) 200 Bars, and (ii) 240 Bars specimen.

were typically augmented at 3%wt content of the nanoclay, after which they significantly diminished as the nanoclay content was increased. This observation was similarly evident in the 200 and 240 Bars specimens with a variation of approximately 2^0C in the 511-535^{0}C range as shown in *Figure 6-4(i)* and *(ii)* respectively. This phenomenon potentially indicates that the new AMC may be expected to have improved high-temperature mechanical properties as a result of modifying the heat-transfer-matrix.

In addition to compaction-induced residual stresses being attributed to the first two phase changes, it is envisaged that these phase changes also partly related to an element or combination of elements present in the matrix and/or the nanoclay. The contemplated elements or their chemical combinations thereof are Si, Al, and O. This view is based on two observations.

Firstly, the second phase change in the specimen infused with 3%wt-nanoclay is only additional to the typical phase change observed in both the reference samples (*Figures 6-1 and 6-2*) and 1%wt-nanoclay samples. This second phase change was relatively not fully developed in these latter sets of samples (i.e. references & 1%wt samples) possibly due to the relatively lower quantity of the second-phase's definitive elements or their chemical combinations thereof.

Secondly, it was evident from *Figure 6-4* that both of these pronounced phase-changes were evidently absent in the 8% and 12.5%wt specimens, yet the second phase change seemed to become more augmented or articulate as the %wt-nanoclay increased from 0 to 3%. This potentially implies (1) incremental thermal-chemical effect of an element or combination of elements contained in the *Nanofil 116*, (2) heat flow inhibition as the %wt nanoclay content increases, thereby creating increasingly dispersed sites for heat dissipation, and/or (3) induction of thermal-barrier-behaviour into the AMC at the interfaces of the nanoclay and adjacent / surrounding media. In effect, these nanoclay-occupied sites would undergo delayed phase

change either alongside the matrix or after the matrix has melted depending on relative quantity. This was evident in *Figures 6-5(i), (ii)* and (iii) that show the phase change signatures before, during, and after the melting of the matrix respectively in the order of %wt content of nanoclay. This evidence is irrespective of the green compaction pressure.

It was also noticeable that as the clay content increased beyond 1%, the 160 Bars specimen exhibited relatively superior thermal properties than the 200 and 240 Bars specimens. It was further evident that, for these specimens with increased nanoclay content, the 240 Bars specimen consistently exhibited better thermal behaviour than the 200 Bars specimen. It should also be noted here that, irrespective of the green compaction pressure, the melting temperatures for samples with 8%wt and 12.5%wt of *Nanofil 116* were above the liquidous temperature of 650^0C with reference to the Al-Cu binary-phase diagram [218, 219]. In as much as the conditions under which the diagram was obtained could have been different from the current study's experimental conditions, this observation as based on comparative analysis does significantly fortify the contention of the nanoclay serving as an intergranular thermal-barrier-medium and/or heat dissipation sites in the AMC.

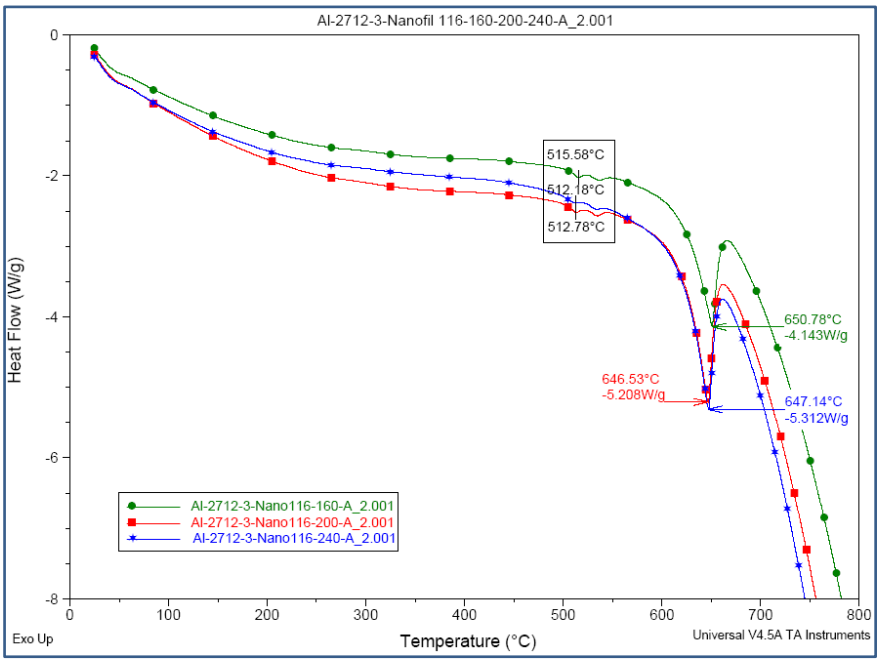

Figure 6-5 (i)

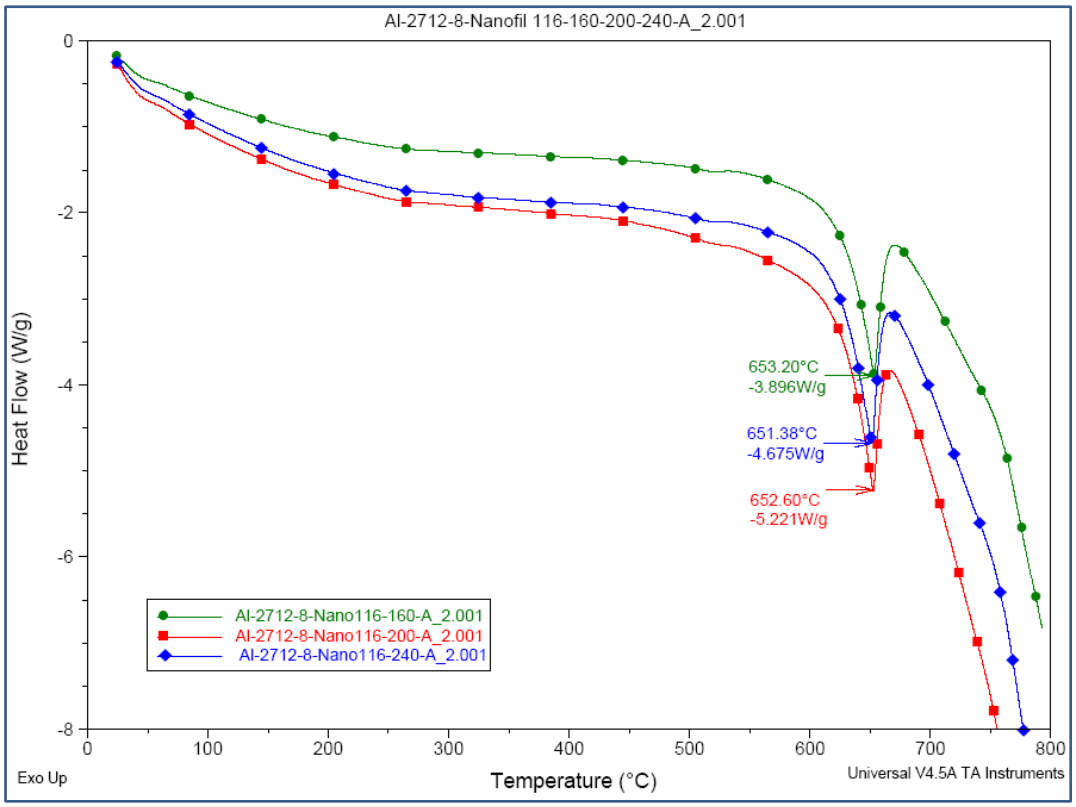

(ii)

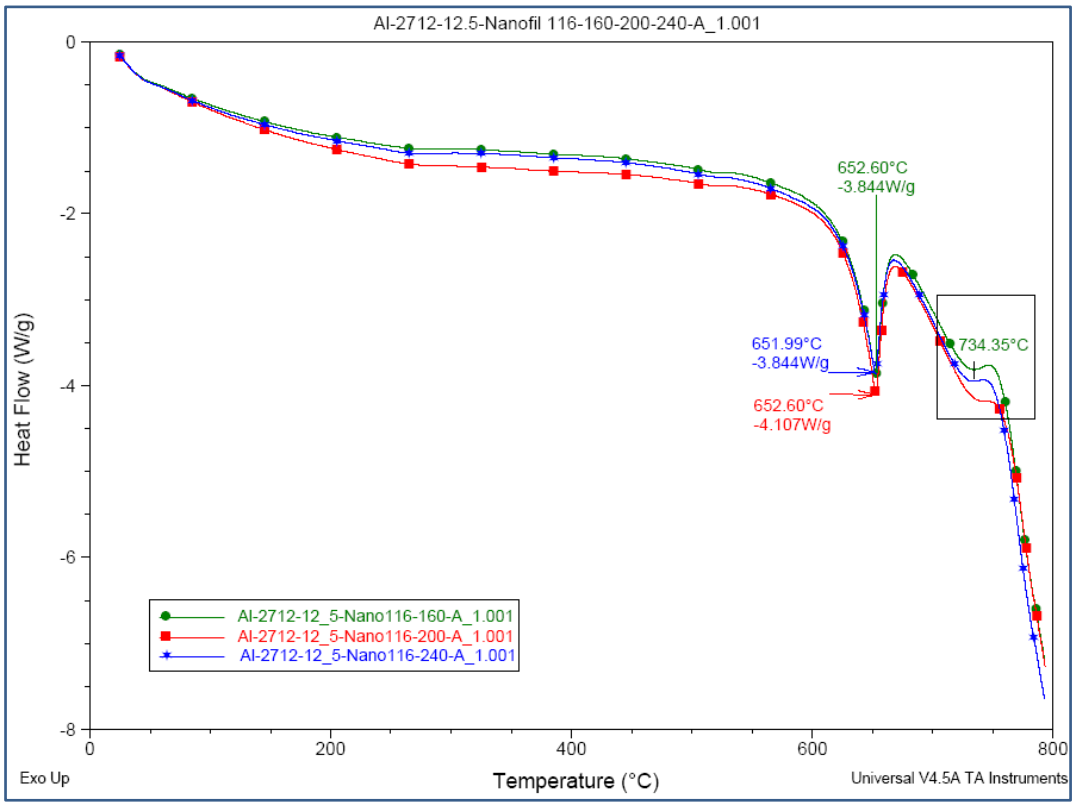

(iii)

Figure 6-5: Phase changes at (i) 3%, (ii) 8%, and (iii) 12.5%wt *Nanofil 116* content.

The afore-going observations can be attributed to the role and chemical nature of *Nanofil 116*, not forgetting the interaction with the constituents of the matrix. In as much as the alloying elements (and potentially the nanoclay elements) are perceived to be in homogenous solution with no individual properties, we cannot ignore their intrinsic elemental differences and individualized effects on properties of the bulk material. On that note, and with reference to the AMB-2712 Al-*Nanofil 116* composite, *Figure 6-6* shows a simplistic Venn diagram representation of three primary sets of conceptualized interfacial virtual boundaries. Three primary interfaces are identifiable: (A) Interface between *Nanofil 116* and Aluminium matrix, (B) Interface between Aluminium matrix and any of the alloying elements, and (C) Interface between *Nanofil 116* and any of the alloying elements. The system becomes more complex as we consider multidirectional heat flow states, interactions between any two of the alloying elements, and the interfacial boundaries represented by X in the Venn diagram.

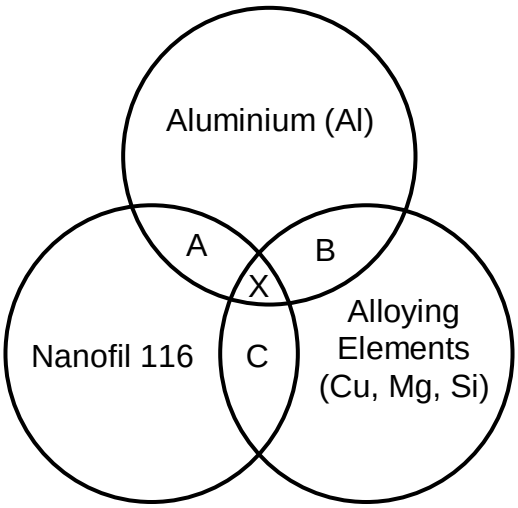

Figure 6-6: Virtual interfacial interactions in AMB-2712-*Nanofil 116* Composite.

The interfaces represented by A, B, and C affects the effective heat transfer at both macro- and micro-scopic levels due to the inherent diversity of heat transfer dynamics. It is envisaged that the factors that determine or influence these dynamics include, but are not limited to: (1) the size of particles and their distributions (size of interactive surface area) [6, 53, 59, 230], (2)

orientation of the surface area [43], (3) presence of voids / cracks / cavities / pores (void dynamics) [79], (4) localized chemical reactions [100, 203], (5) crystalline and morphological packing of constituent particles [59], (6) thermal-treatment residual stresses [81], (7) thermally induced stresses due to difference in thermal conductivity of adjacent materials [80-84], (8) temperature gradient across the interface [81], and (9) thermal properties of the interfacial medium [43, 71-75]. These factors are generally interconnected, for instance from analytical geometry, it can be shown that reduction in spherical particle's size increases the specific surface area as well as the angle of curvature. Similarly from geometry, different granular lattice structure such as Body-Centred-Cubic (BCC), Face-Centred-Cubic (FCC) and Simple Cubic yields different volume fractions and bulk densities. Therefore, optimizations of the interfaces at A, B, and C do present a significant potential in thermal engineering of composites.

It is hereby proposed that, at relatively high %-weight-content, the nanoclay dominates the heat-flow-matrix with reasonable resilience to variations in green-compaction-pressures. This phenomenon may be attributable to two possibilities: (i) The increased presence of nanoclay particles possibly inhibits the conductive heat propagation across the interfacial and inter-granular boundaries at microscopic level, and (ii) due to the increased presence, the nanoclay serves as a filler content in the unoccupied inter-granular spacing, thereby resulting into relatively increased heat-retention or serving as sites for heat disposal.

Chances of obtaining and optimizing interfaces such as represented by zone *X* in *Figure 6-6* are relatively limited because of production feasibility issues and the typically low %wt content of alloying elements as well as *Nanofil 116*. Additionally, the effect of processing conditions such as the green compaction pressure and %wt. content of lubricant / binder do have knock-on effect(s) on other factors such as the porosity, inter-particle residual stresses, and bulk hoop stresses [51, 53, 62].

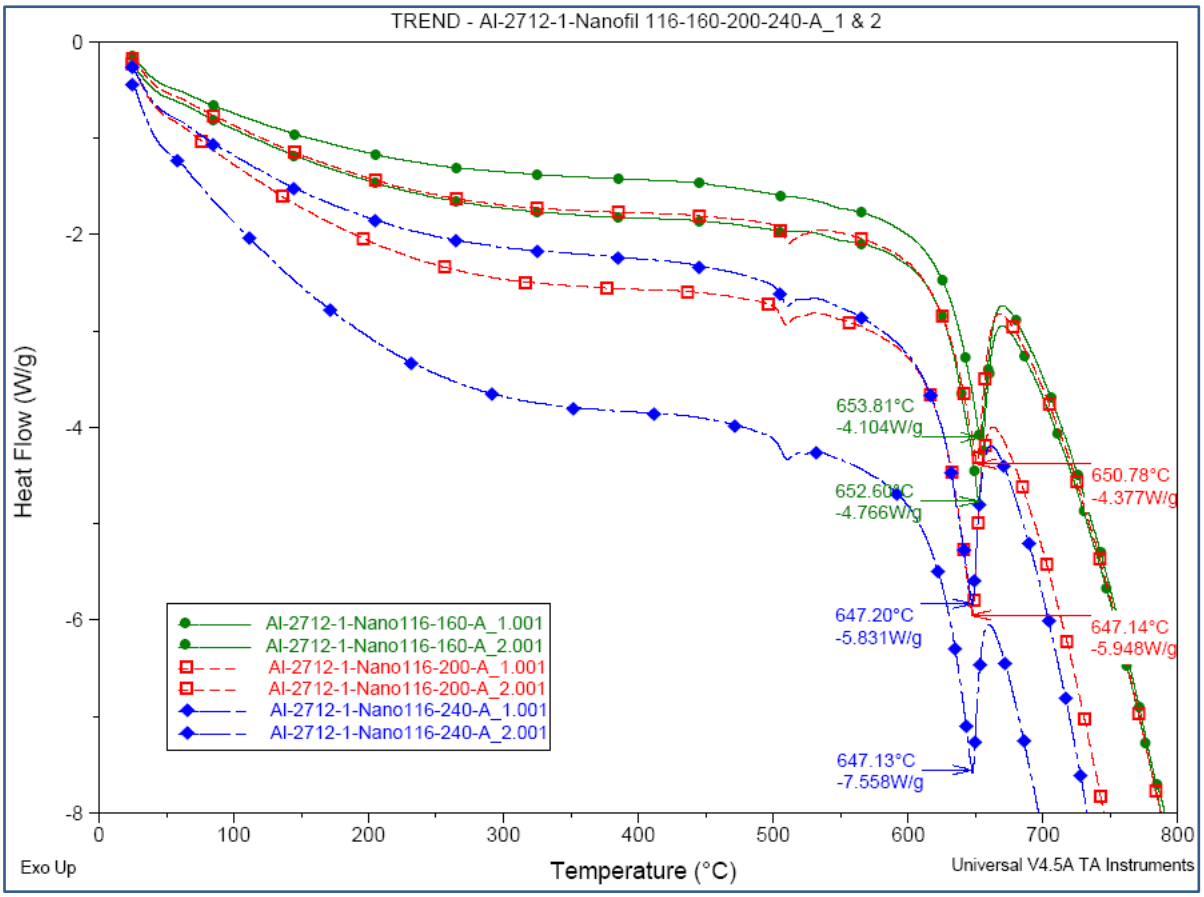

Figure 6-7: Trend of green compaction pressure on thermal behaviour of 1%wt-*Nanofil 116* samples.

The synergistic effects of these and other contributory factors, such as the method of integrating nanoclays into the matrix and the subsequent thermal processing, could yield some empirical variances in results. In order to counteract potential misjudgement based on variances in results from sample to sample, graphs mapping significant behavioural trends were extracted. For example, *Figure 6-7(i)* shows a trend of the effect of green compaction pressure on specimens infused with 1%wt content of *Nanofil 116*. From this trend, it was observed that, for 1%wt content and regardless of the sample's original location on the sintered specimen, thermal behaviour was proportionally related to the green compaction pressure with the 160 Bars specimen showing the best thermal behavioural tendencies. This observation is affirmed by the comparative microstructures as shown in *Figure 5-4* in the preceding chapter.

It should be noted here that the trend depicted by 1%wt-Nanoclay specimens was in contrast to the trend represented by the effect of green compaction pressure on thermal behaviour of reference specimens as was shown in *Figure 6-1*. In the reference samples' case, the 240 Bars specimen consistently depicted better thermal behaviour than the 160 Bars specimens, while the 200 Bars specimen had the best overall thermal behaviour. This performance shift from reference samples to nanoclay-infused samples was best observed with the 3%wt content samples as shown in *Figure 6-8* whereby the widest disparity in results was noticed with respect to 200 Bars samples. The disparity for this pair of 3%wt samples reflected approximately 23% difference in heat flow as the composite entered the liquidous phase. This corresponds to a 3^0C difference in melting temperature between the two samples at this phase change. This transition and maximum disparity coincided with the changes noticed from a *single* to clearly defined *double* phase-changes before reaching the melting temperature.

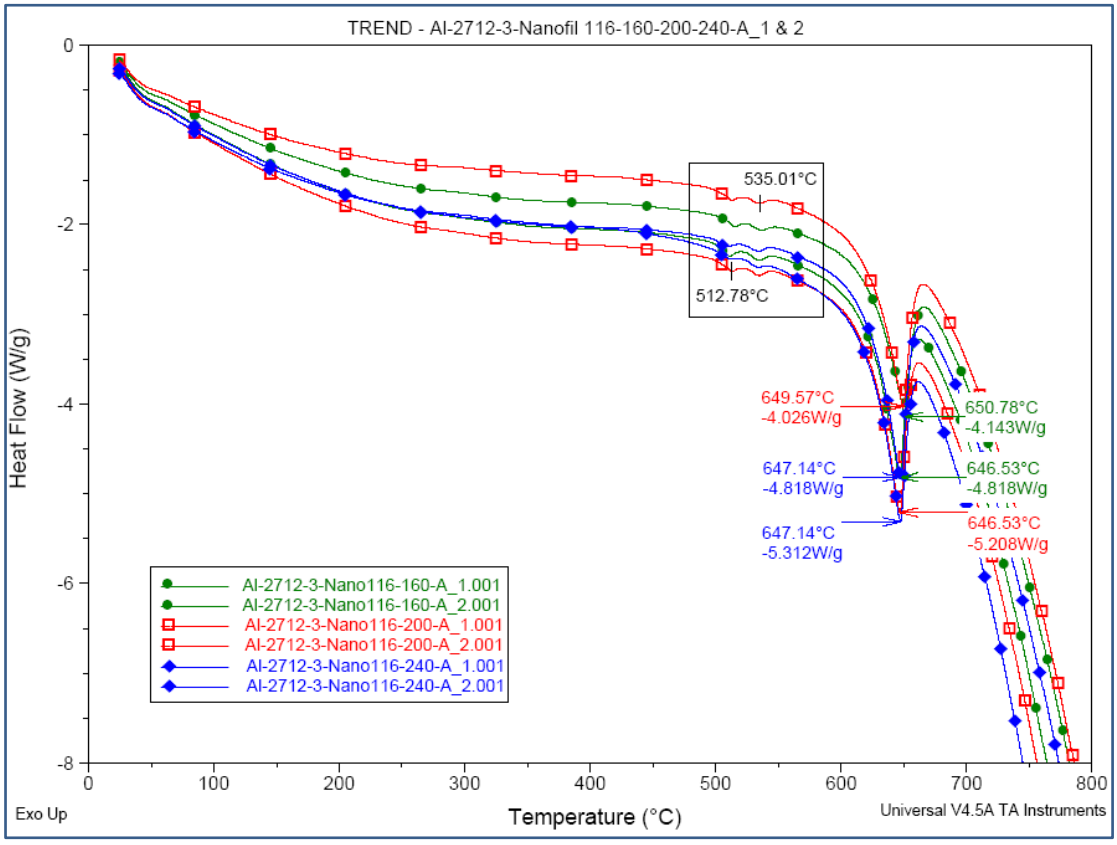

Figure 6-8: Trend of the effect of green compaction pressure on thermal behaviour of 3%wt-*Nanofil 116* samples.

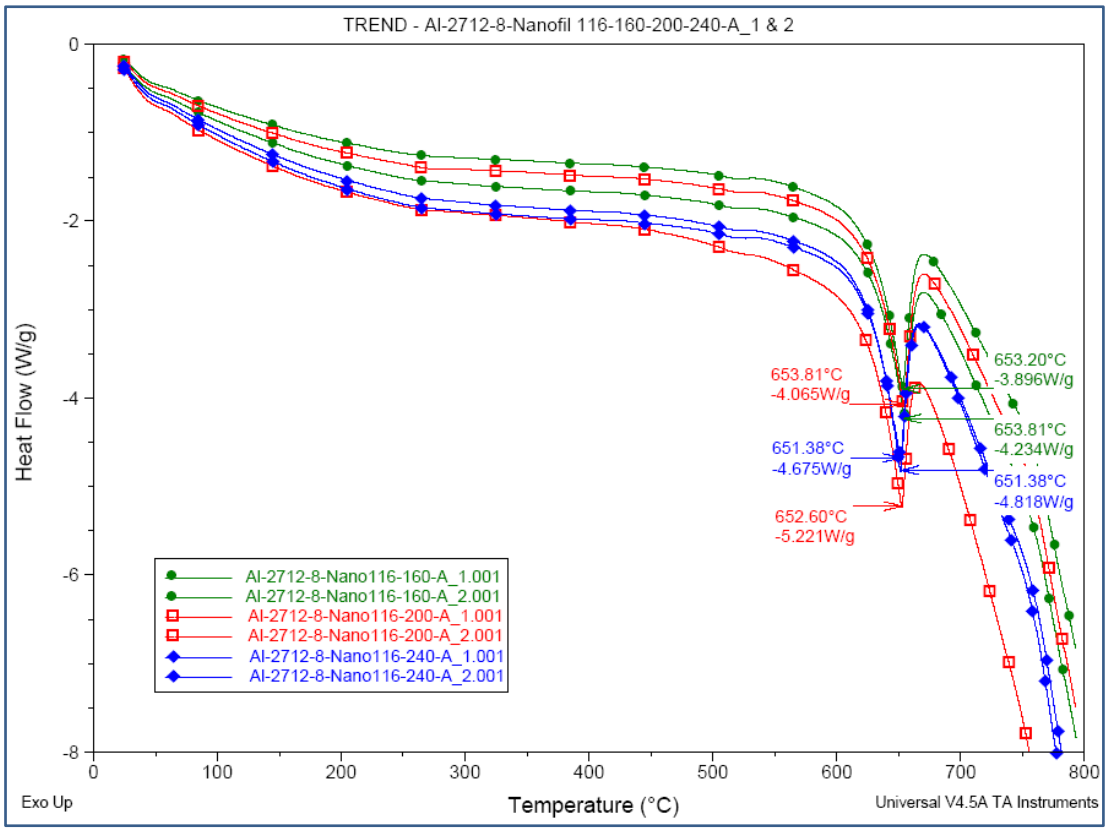

(i)

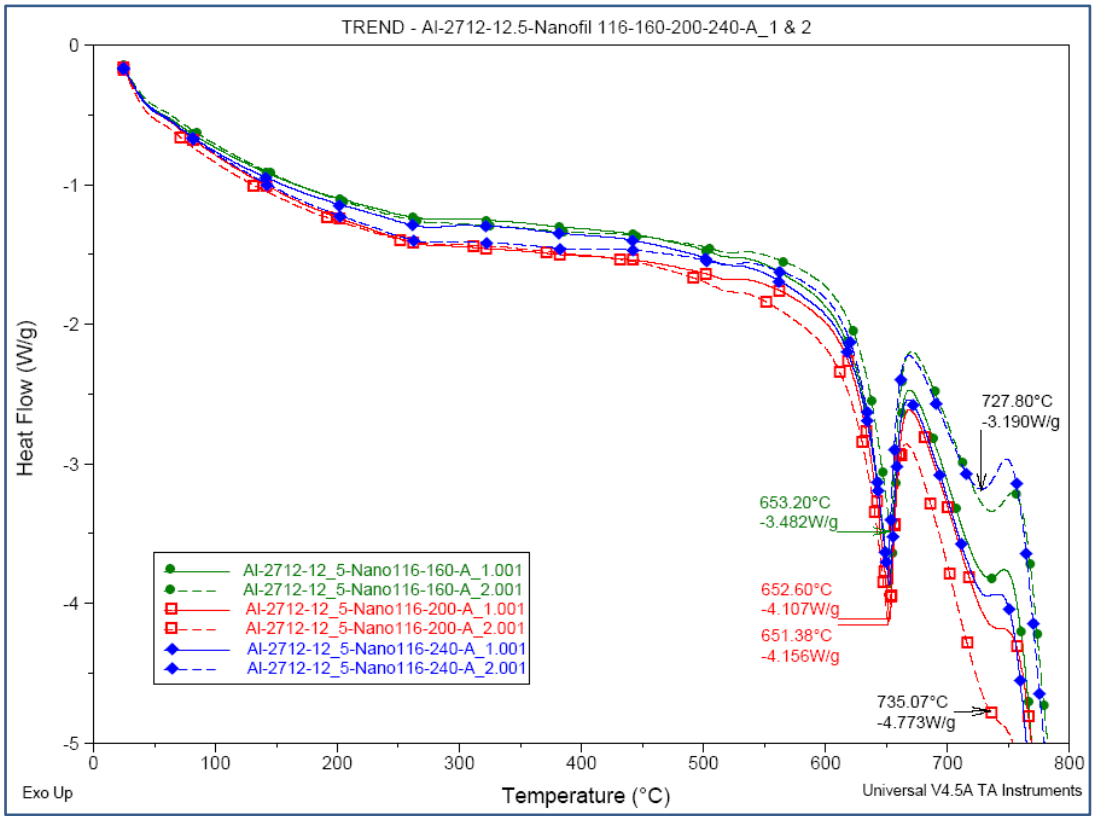

(ii)

Figure 6-9: Trend of the effect of green compaction pressure on thermal behaviour of: (i) 8%wt, and (ii) 12.5% *Nanofil 116* samples.

The transition is further evident to gradually progress in the graphs for 8% and 12.5%wt samples shown in *Figure 6-9(i)* and *(ii)* respectively. It was noted that, as the nanoclay content increased from 8%wt to 12.5%wt, thermal properties of the 200 Bars samples deteriorated relative to the 160 and 240 Bars samples. The corresponding heat flow disparity for 200 Bars samples with 8%wt *Nanofil 116* was 22% while the melting temperature difference was approximately 1^0C. This interpreted to a 1% drop in sample-to-sample heat flow disparity and 2^0C temperature difference with reference to the 3%wt-nanoclay samples.

From both *Figures 6-9(i)* and *(ii)*, it was observed that the thermal performance of 160 Bars samples was consistently superior to that of the 240 Bars specimens. Disparity in the respective samples' thermal performance for both the 200 and 240 Bars samples was observed to be negligible at 12.5%wt. At this %wt content, the transitional progressive decline in thermal performance of the 200 Bars samples saw this composite comparatively ranking as the poorest candidate for thermal barrier applications. Nonetheless, corresponding disparity was minimal at approximately 1% and 1^0C in heat flow and melting temperatures respectively. This implies some level of stability in the system's entropy in terms of the combination of pressure, temperature and density according to the second law of thermodynamics [236]. The manifestation of changes in heat-transfer-matrix in response to variations in green-compaction-pressure and %wt content of nanoclay was consistently depicted by the microstructural changes as evident in *Table 5-4* in the preceding chapter.

6.1.3 Effect of *Nanofil 116* on control-weight

Results for weight variation as a function of temperature and green-compaction pressures gave an insight into operational stability of the Al-nanoclay material system. TGA curves in *Figure 6-10* shows the effect of green compaction pressure on weight variation as a function of temperature. The general trend was similar to that for thermal behaviour, whereby samples from the 200 Bars specimen showed better properties than those from the 160 and 240 Bars

specimens. It was similarly observed that the 160 Bars specimen consistently had relatively less percentage weight loss than the 240 Bars specimen. It further recorded the lowest weight loss disparity of 0.11%. These results reinstate the relative preference of using 160-Bar as the green-compaction pressure in lieu of 200 or 240 Bars.

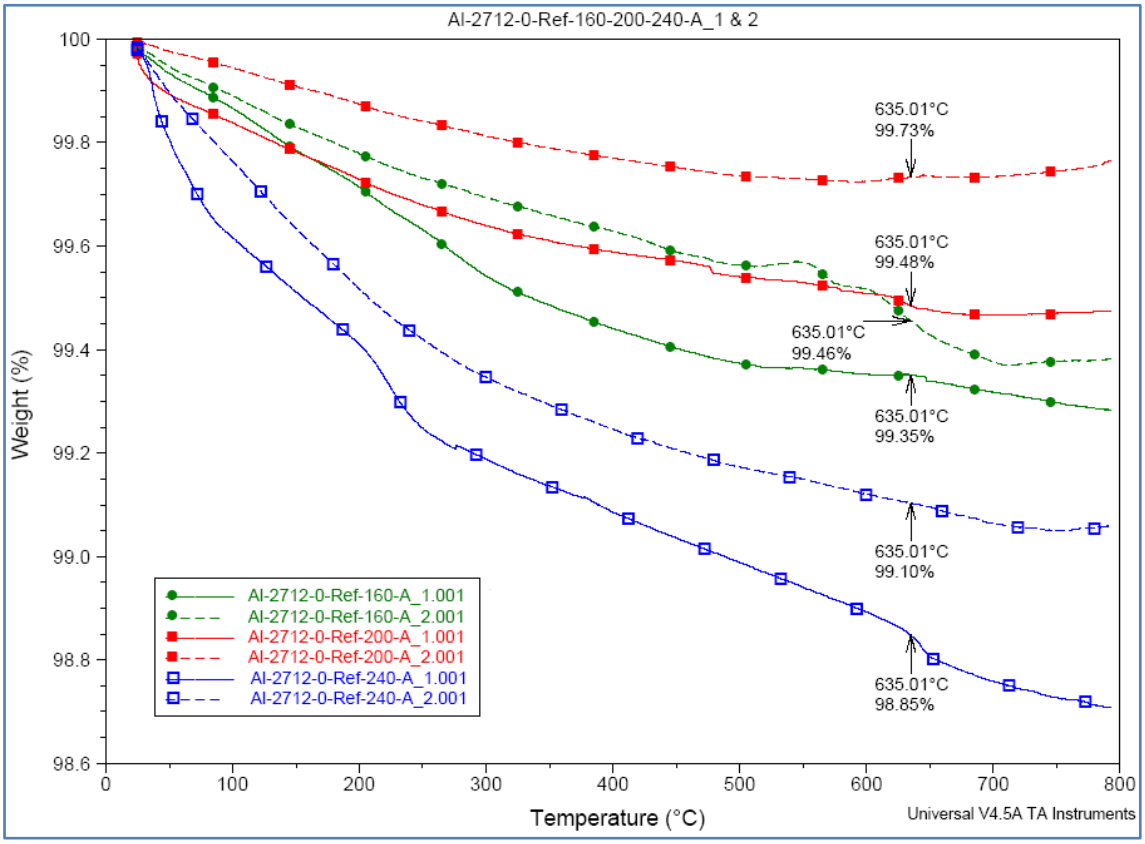

Figure 6-10: Effect of green compaction pressure and temperature on specimens sintered using *Set"-A"-run* profile settings.

Figure 6-11(i), (ii) and (iii) shows the effects of %wt content of *Nanofil 116* on the percentage weight loss in samples from specimens previously compacted to 160, 200, and 240 Bars and processed using *Set-"A"-run* profile settings. It was generally evident that the magnitude of percentage weight loss increased in the order of percentage content of *Nanofil 116* relative to the reference samples. This trend was attributed to proportionate loss of H_2O and OH as well as burn out of the organic elements contained in the nanoclay's chemical composition. It was further observed in *Figure 6-11(iii)* that, in addition to this general trend remaining true, the percentage weight loss in the 1%wt-nanoclay-content samples from 240 Bars specimen was

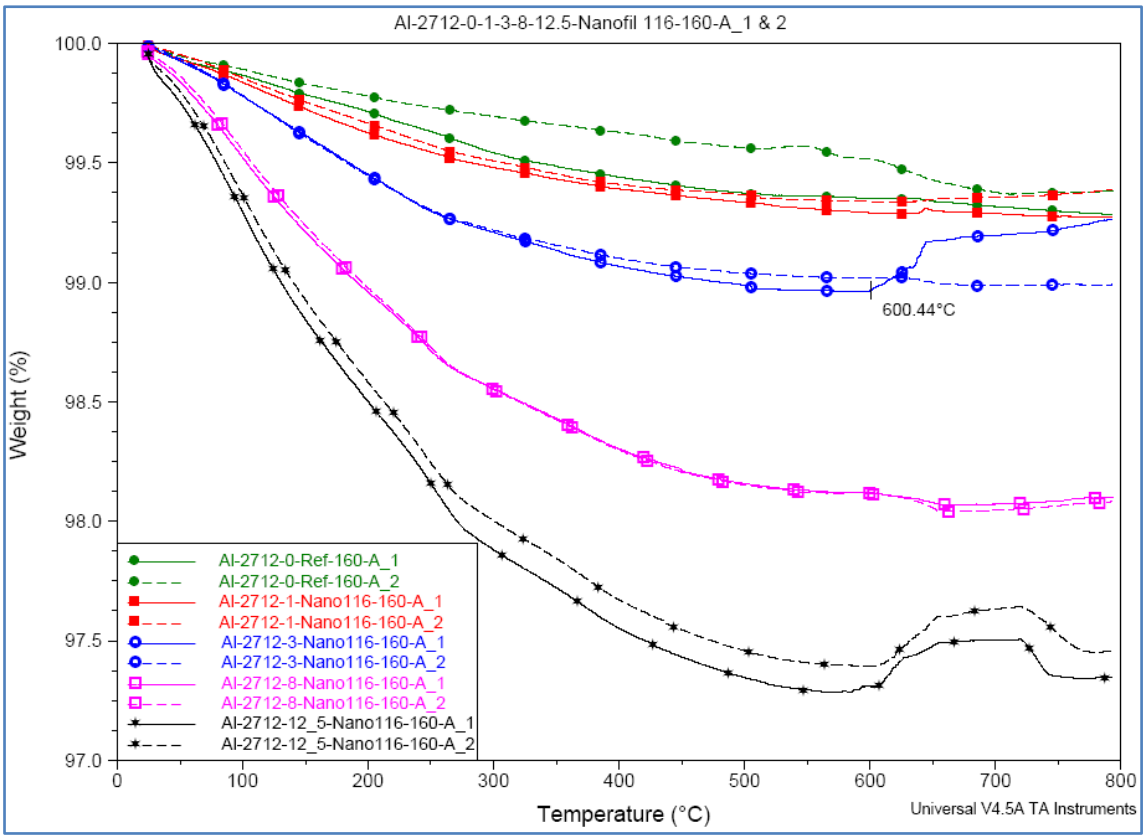

Figure 6-11 (i)

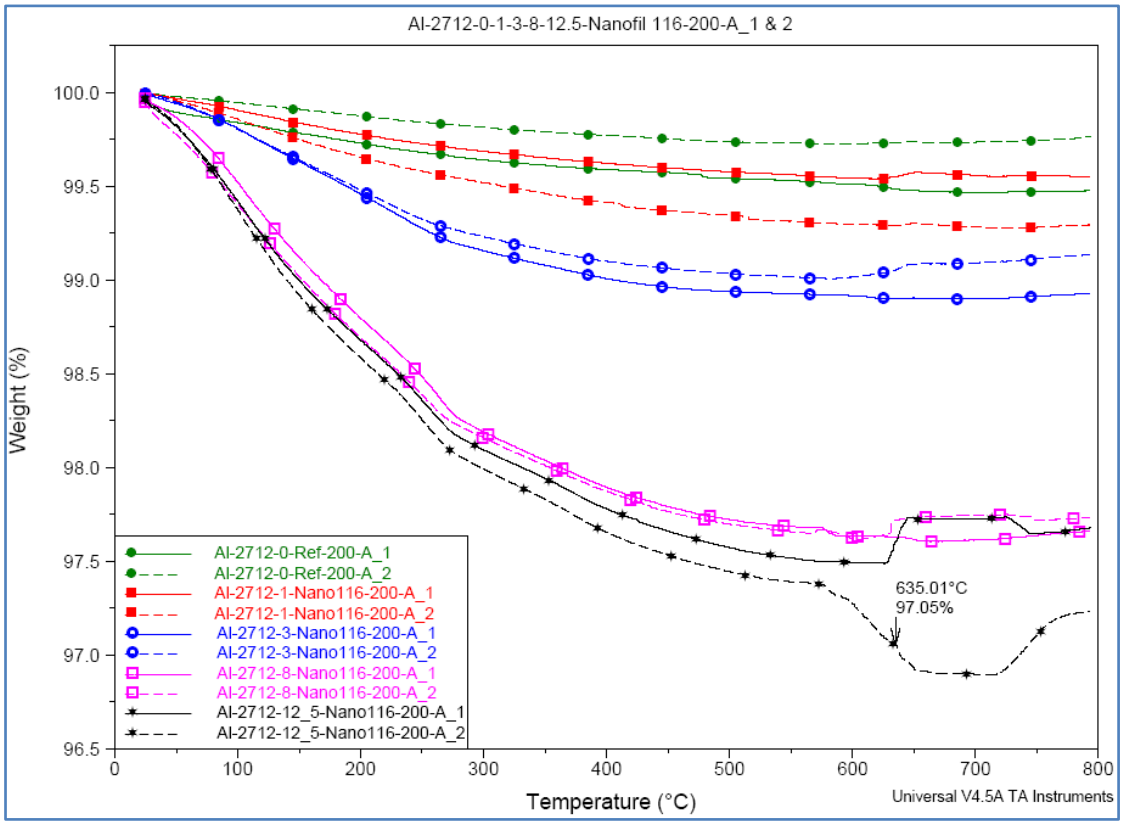

Figure 6-11 (ii)

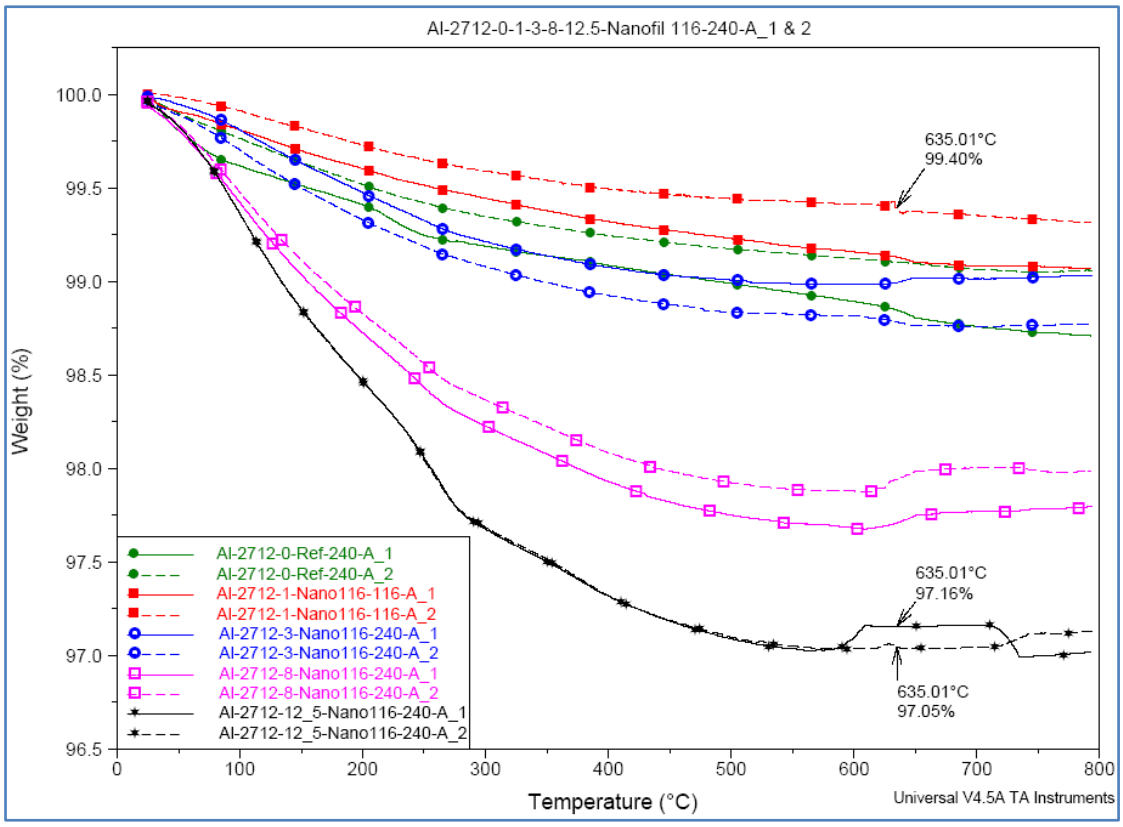

(iii)

Figure 6-11: Effects of %wt content of *Nanofil 116* on percentage weight loss in samples from (i) 160, (ii) 200, and (iii) 240 Bars specimens.

relatively less than that of reference samples. Proposed reason for this was that new compounds could have chemically been formed such that their *positive* marginal effect on bulk-weight (gain) was relatively higher than the *negative* effect of any burnt-out elements on bulk-weight (loss).

Table 6-1: Summary of effect of *Nanofil 116* on % wt loss at 635^0C.

	Ref. Samples			1% wt.			3% wt.			8% wt.			12.5% wt.			AV. Diff.
Compaction Pressure / Sample Ref. No.	1	2	Diff.	1	2	Diff.	1	2	Diff.	1	2	Diff.	1	2	Diff.	
160 Bars	0.65	0.54	0.11	0.71	0.66	0.05	0.94	0.99	0.05	1.91	1.91	0	2.56	2.49	0.07	0.06
200 Bars	0.52	0.27	0.25	0.45	0.71	0.26	1.10	0.95	0.15	2.37	2.28	0.09	2.39	2.95	0.56	0.26
240 Bars	1.15	0.90	0.25	0.87	0.60	0.27	1.01	1.22	0.21	2.29	2.06	0.23	2.84	2.95	0.11	0.21
Average Diff.			0.20			0.19			0.14			0.11			0.25	

Table 6-1 shows a summary of quantitative data extracted from the graphs at a reference temperature of 635^0C. Samples from 160 Bars specimen showed the least weight loss

irrespective of %wt content of *Nanofil 116*, with zero disparity between samples having 8%wt content. These samples also recorded the lowest average disparity in weight loss (0.06%). On basis of average difference in percentage weight loss between samples from the same specimen, it was generally evident that the disparity decreased gradually with increase in %wt content of nanoclay until the content reached 8%wt. Thereafter at 12.5%wt, the disparity was greater than even the reference samples. Therefore with respect to weight stability in bulk production, a composite having 8%wt *Nanofil 116*, compacted at 160 Bars, and processed using *Set-"A"-run* profile settings would be recommended.

6.2 Thermal properties indicators

6.2.1 Thermal conductivity, Specific heat, and Thermal diffusivity

Figure 6-12 shows results for thermal conductivity, specific heat and thermal diffusivity for the Reference, 1%wt and 3%wt nanoclay-infused samples of AMB-2712 alloy. Specimen with 1%wt *Nanofil 116* consistently recorded a higher thermal conductivity than both the reference and 3%wt *Nanofil 116* specimens. An approximate 7% and 9% improvement was noted at the 120^0C and 220^0C respectively with the material's conductivity stabilizing at 90 W/mK, which interpret to 22% improvement at 300^0C. Comparable thermal conductivity for pure aluminium is given as 250 W/mK at 225^0C. The observed decrease in conductivity between theoretical and the experimental values obtained from this study may partly be related to increased presence of Al_2O_3 content in the AMB-2712 powder [102]. However, there is room for improvement by changing the sintering atmosphere from argon to nitrogen whereby nitrogen has been associated with breaking down the oxide layer as discussed in *Chapter 9*.

Of significance was the observation that, unlike the reference specimen whose conductivity deteriorated after 220^0C, conductivity of the nanoclay-infused samples consistently increased beyond that temperature and showed signs of stabilizing at 300^0C. In the context of engine components such as the engine block and cylinder head, this would interpret to the material's

enhanced efficiency in conducting away heat from the combustion chambers to the engine's cooling system. These results were positively mirrored in the corresponding results for specific heat capacity of the specimens and further explain the observed delay in phase change as reflected by the comparative melting temperatures. Thermal conductivity results hereby confirm that increased presence of nanoclay particles does inhibit the conductive heat propagation across the interfacial and inter-granular boundaries at microscopic level. In the lower temperature regime up to 220^0C, thermal conductivity of the sample with 3%wt content of *Nanofil 116* was observed to be similar to that of the reference. This implies that the effect of nanoclay in deterring thermal conduction was similar to the cumulative effect of cracks and porosity that was observed in the reference samples.

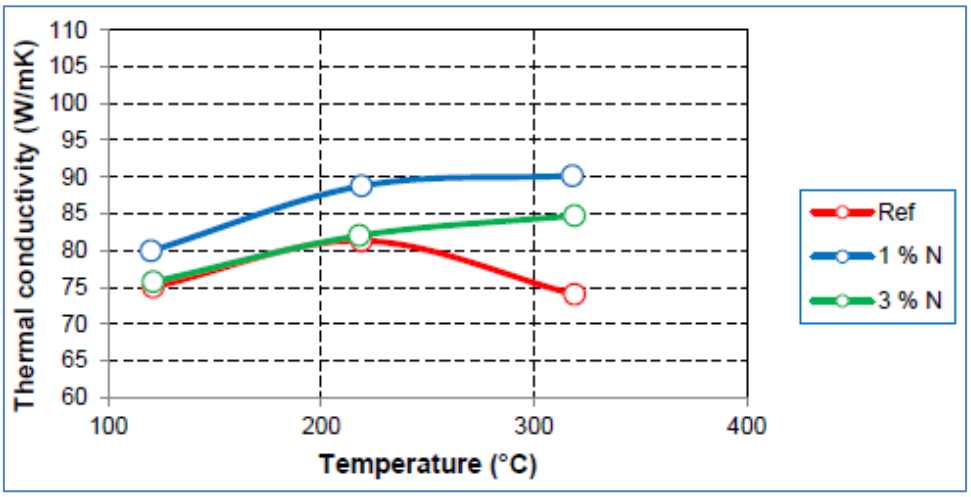

Figure 6-12 (i)

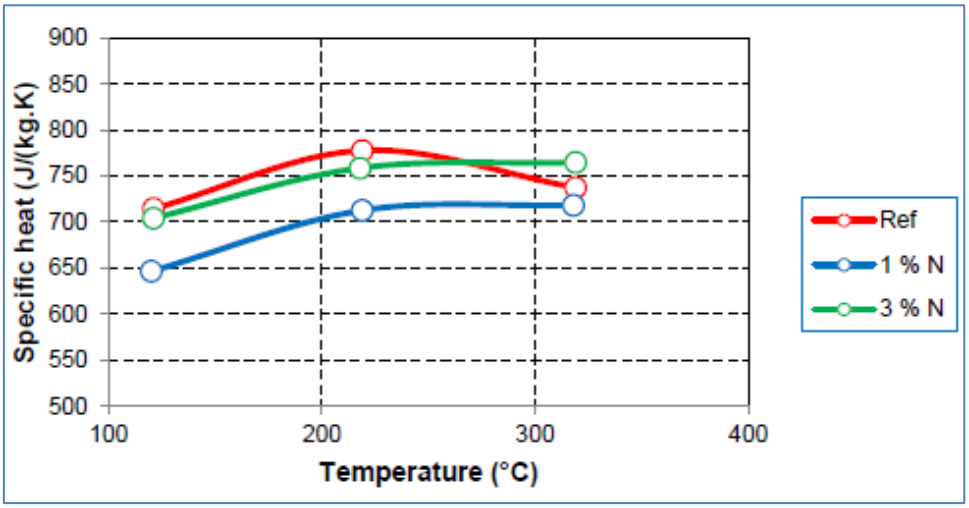

Figure 6-12 (ii)

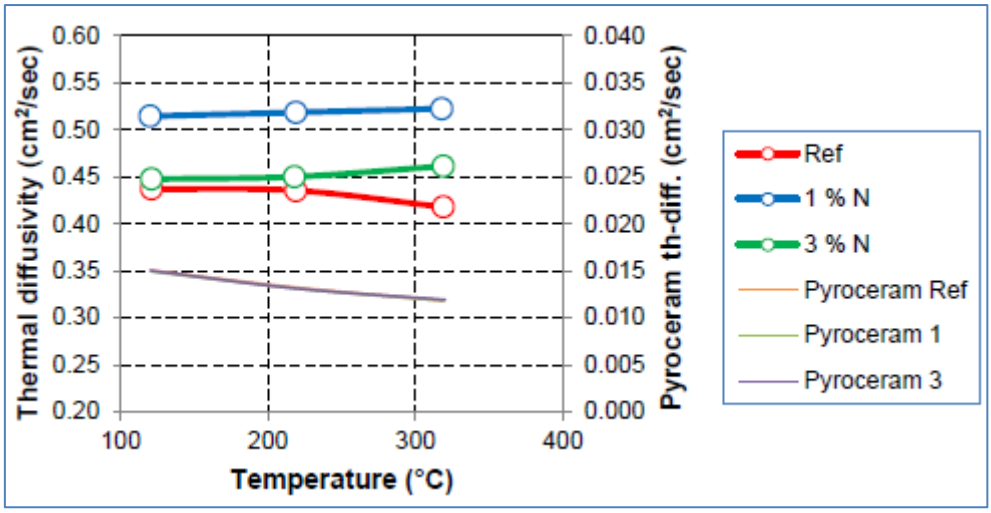

(iii)

Figure 6-12: Thermal Properties for ref, 1%wt, and 3%wt *Nanofil 116*-AMB-2712 Alloy: (i) Thermal conductivity, (ii) Specific Heat, and (iii) Thermal diffusivity.

Similarly, the specimen with 1%wt *Nanofil 116* recorded relatively higher thermal diffusivity than the Reference and 3%wt specimen in the test-temperature range. In comparison to reference specimen, the percentage improvement in thermal diffusivity by adding only 1%wt nanoclay was observed to vary almost exponentially with increase in temperature. Highest value recorded was 5.22 x 10^{-5} m^2/s at 300^0C. Even though there seemed to be little difference in the performance between the Reference and 3%wt specimens, the stability of thermal flux as reflected by the diffusivity graph is important especially as the temperature exceed 300^0C. In the context of the automotive engines for instance, the importance lie in the possibility that engines can then run at a relatively higher temperature while other peripheral systems such the heat exchangers deliver higher heat dissipation efficiencies.

The almost horizontal sections of the graphs for nanoclay-infused specimens in the 220 – 300^0C imply an improvement in thermal stability of the material, thereby interpreting to higher thermal resilience at the face of fluctuating weather conditions. In general, these results implicitly point at potentially superior thermal-mechanical properties as alluded to by the favourable effect of *Nanofil 116* on phase changes. However, the lower thermal conductivity

and other properties of 3%wt compared to the 1% wt specimen may have been caused by three factors. *Firstly*, both *Nanofil 116* and the AMB-2712 matrix have magnesium as one of their ingredients. Magnesium has been reported to enhance sinterability of aluminium in nitrogen atmosphere due to intermediate reactions between sublimated magnesium and nitrogen [123]. In argon atmosphere, this must not have been the case. Accordingly as the %wt content of nanoclay increased, so did the accumulative content of magnesium. Since elevated content of magnesium does not completely dissolve in solid solution, this inferior phase is reported to cause embrittlement in aluminium [60], which potentially resulted into the formation of observed microcracks. Such micro-cracks have on the other hand been shown to have a negative effect on conductive heat transfer [79]. Furthermore, alternative heat transfers modes such as radiation and convection across cracks do not help the situation either and can even be considered to be absent [79]. It should be reiterated here that Argon was used as a datum sintering atmosphere owing to its inert nature. This was meant to facilitate an initial analysis of the new AMCs without any reference to atmosphere-induced chemical reactions. Thereafter, the effect of sintering atmosphere was analysed as part of process optimization as detailed in *Chapter 9* (Processability of Nanoclays - AMCs).

Secondly, hydrogen gas may similarly have been released during dehydration and dehydroxylation [231, 232] process of the *Nanofil 116*, yet the gas is known to have negative effect on sinterability of Aluminium even when in small concentrations [123]. On the same note, the natural oxide typically formed on aluminium powder (about 100 x 10^{-10}m thick) is amorphous and contains adsorbed water [102]. Upon heating at high temperature, the oxide crystalizes first to $\eta(Al_2O_3)$, then to $X(Al_2O_3)$ and finally to the stable $\gamma(Al_2O_3)$. In the process, the adsorbed water reacts with the metal to form additional oxide and release hydrogen. This hydrogen may produce porosity at the grain boundaries and cracking or blistering. The higher the oxide content, the more the hydrogen get released and the more pronounced the embrittling

and defect deformation especially with cyclic heating and cooling. It has been indicated [102] that the vacuum treatment or high temperature sintering before complete compacting reduce hydrogen content and eliminates most if not all cracking. Small additions of aluminium fluoride are also said to reduce the effect of hydrogen [102].

Thirdly, Nanofil 116 contains SiO_2, which is known to react with Al with a resultant detrimental effect on the thermal properties of the material [246]. However, at 3%wt content of nanoclay, microstructural analysis revealed increased presence of pure silicon precipitates in addition to presence of other Si-based compounds including SiO_2. Despite silicon having a relatively higher thermal conductivity (149W/m.K) [247] as compared to SiO_2 (12 (|| c-axis), 6.8 (⊥ c-axis), 1.4 (am.) W/m·K) [248], its precipitation was noted to be less distributed but in larger-sized crystals compared to precipitation in the specimen with 1%wt nanoclay. These enlarged crystals would effectively interpret into a reduced surface area of thermal conductance. In addition, these crystals were mostly engulfed in the then increased quantity of secondary ceramic phases identified from the XRD results. End effect of these aspects would be to render the 3%wt specimen less conductive, with lower thermal diffusivity and higher specific heat capacity due to the resultant induced thermal-barrier-tendencies.

In comparison to the reference specimen, the combined effect of increased silicon content and nanoclays-filler effect in the 3%wt specimen must have outweighed the effect of microcracks, which were prevalent in both categories of specimens. Furthermore, it can be argued that the increased precipitation of silicon and the relatively increased secondary ceramic phase in 3%wt specimen did play a role in stabilizing the heat transfer within the specimen. This would explain the thermal stability in this specimen as demonstrated by the results particularly beyond 220^0C. With every increase in nanoclay content, the combined effect of these factors generally become more significant and thereby reflect on thermal performance of the nanoclay-infused AMCs.

6.2.2 Thermal expansion

Table 6-2 shows results for thermal expansion of the tested samples. At the same temperature readings, the reference samples were observed to expand more in the argon atmosphere than in air at lower test temperatures with the gap closing up as the temperature was increased towards 300^0C.

Table 6-2: Thermal Expansion Percentages and Coefficients.

REF IN ARGON			REF IN AIR		
Temperature (°C)	**Expansion (%)**	**Coefficient**	**Temperature (°C)**	**Expansion (%)**	**Coefficient**
24	0.000	-	24	0.000	-
100	0.127	16.7E-6	100	0.107	14.1E-6
300	0.635	23.0E-6	300	0.619	22.4E-6
500	1.152	24.2E-6	-	-	-
1 % N IN AIR			**3 % N IN AIR**		
Temperature (°C)	**Expansion (%)**	**Coefficient**	**Temperature (°C)**	**Expansion (%)**	**Coefficient**
23	0.000	-	24	0.000	-
100	0.108	14.0E-6	100	0.110	14.5E-6
300	0.635	22.9E-6	300	0.675	24.5E-6
-	-	-	-	-	-

Under similar test conditions and atmosphere, both the percentage thermal expansion and coefficient of thermal expansion increased with percentage nanoclay content. The relatively greater thermal expansion and coefficients for *Nanofil 116*-AMCs compared to Reference sample relate to the nanoclay's structure, i.e. *Nanofil 116* constitutes 99-100% Bentonite (*Appendix B-1*), a hydrated aluminium silicate whose major component is montmorillonite, which on the other hand belong to a group of silicate minerals known as dioctahedral smectites [231]. The structure of this material is formed from two tetrahedral sheets with Si(IV) as a central atom and one octahedral sheet containing Al(III), which can be substituted by Fe(III) and/or Mg(II). This kind of structure is said to exhibit cation exchange properties, swelling ability, plasticity, cohesion, compressibility, adsorptive properties and catalytic activity [231].

Nonetheless, the adverse disparity between thermal expansion of Reference and 1%wt specimens was 2.58% compared to 9.05% for the 3%wt specimen.

6.3 Heat-flow-matrix model

The evident anomaly observed between Al-**Cu** and **Cu**-Fe sets can largely be traced back to the correlation between heat-transfer on one hand, and the intrinsic properties of materials on the other. Variation of thermal conductivity of Aluminium at a reference temperature of 25, 125, and 225^{0}C works out to 2% with a maximum value of 255 W/m.^{0}C recorded at the 125^{0}C [42]. Over the same reference temperatures, thermal conductivity of Copper varies by only 0.75% with a maximum value of 401 W/m.^{0}C, whereas that of Iron varies by as much as 25% from 80 to 60 W/m.^{0}C at 25 and 225^{0}C respectively. This means that copper as an element is relatively more resilient to thermal gradients. Further mapping of the temperature-related variation of thermal conductivity over the reference temperatures indicate that the sensitivity to thermal gradients is dependent on quantitative measure of the materials' relative conductivities. For example, ranking in the order of increasing thermal conductivity for the current contextual materials at 25^{0}C would be Iron (80W/m.^{0}C), Aluminium (250W/m.^{0}C), and Copper (401W/m.^{0}C) respectively, which is similar to the ranking in order of increasing thermal resilience, i.e. Iron (25%), Aluminium (2%), and then Copper (0.75%) respectively.

Holding all other variables constant, the correlation of heat-transfer across the Al-Cu interface at particulate level can be modelled using electrical resistance concepts. Fourier determined that *Q/A*, the heat transfer per unit area (W/m^2) is proportional to the temperature gradient *dT/dx*, with the material's thermal conductivity (*k*) being the constant of proportionality [249].

$$Q/A = -k\,\frac{dT}{dx} \qquad (1)$$

Since thermal barrier or thermal resistance relates to the ratio of temperature difference, *dT*, to the heat transfer, *Q*, thermal resistance is analogous to Ohm's Law, in which the electrical

resistance is defined as the ratio of the voltage drop across a resistor to the current flow across the resistor [250].

$$\Delta V = IR \qquad or$$

$$R = \frac{\Delta V}{I} \ (Ohm's\ Law) \qquad (2)$$

Similarly,

$$\Delta T = (Q/A)\, R \qquad or$$

$$R = \frac{\Delta T}{(Q/A)} \ (On\ per\ unit\ area\ basis) \qquad (3)$$

Equation (3) can be rearranged to express conductive thermal resistance as [250]:

$$R_{cond.} = \frac{\Delta T}{(Q/A)} = \frac{L}{k} \qquad (4)$$

where L = thickness of the material.

Assuming a steady state heat transfer scenario, and further assuming for simplicity purposes that heat transfer is primarily one dimensional across the resistance element, the thermal interaction between two solids that have different thermal conductivity may be represented as shown in *Figure 6-13, where* k_i represents the thermal conductivity of solid material *i*, k_I represents the constitutive thermal conductivity of the interface between the two adjacent solids, and L_i represents the respective thicknesses of the segments.

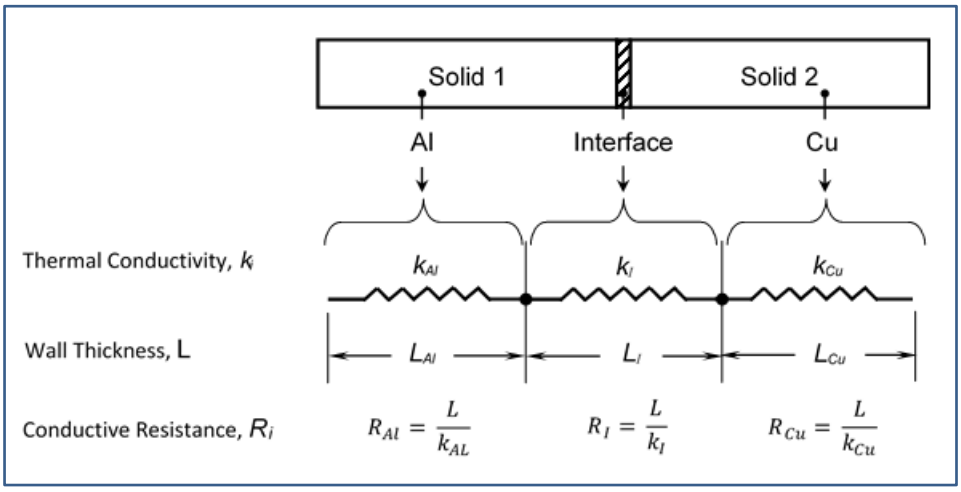

Figure 6-13: Example of binary thermal resistance model: Al-Cu.

The effective thermal conductive resistance for the series model becomes:

$$R_{cond.} = \frac{L}{k_{Al}} + \frac{L}{k_I} + \frac{L}{k_{Cu}} \qquad (5A)$$

Even though this model was based on heat flow per unit area, it was in agreement with the model proposed by DPH Hasselman et al [43] for flat plates dispersions perpendicularly oriented to heat flow. The latter model was based on volumetric analysis whereby the composite was considered to consist of a matrix with parallel plate dispersions with half-thickness, *a/2*, and with concentration *n* dispersions per unit volume. Taking K_d to be the thermal conductivity of dispersions imbedded in a matrix with thermal conductivity K_m, and further relating the volume fraction of dispersions, V_d, to the dispersion size and concentration *n* by $V_d = na$, the latter model for a two-component composite (i.e. binary interface) with perfect contact resistance was expressed as:

$$\frac{1}{K_{eff}} = \frac{V_d}{K_d} + \frac{V_m}{K_m} \qquad (5B)$$

Holding all other factors constant, this inverse proportionality between *R* and *k* as expressed in *Equations (4)* and (*5A*) simply affirms the fact that thermal barrier property (*R*) of a solid material becomes lower as its thermal conductance (*k*) increases. For a given value of *k*, and a unit ΔT for a material, decreasing the value of *R* consequently interprets to an increase in the quantity *Q/A*. For the exemplified binary-materials system, this means increased system's enthalpy with the potential knock-on effect of melting and / or densification of the system.

From this analogy and model as expressed in *Equation (5A)*, the interfacial interaction in a binary-materials system can be better appreciated with respect to heat transfer. Let *D* be difference between the respective *k* values for the two adjacent solids as we hold K_I and all other factors constant. If we substitute one of the materials with another material having a bigger *k* value, the effective *D* value becomes less and vice versa. Subsequently, the effective thermal resistance, $R_{cond.}$, becomes smaller and *Q/A* increases. Such is the scenario when comparing *Al-*

Cu and ***Cu***-*Fe* interaction having a *D* value of 145 W/m.^{0}C and 332 W/m.^{0}C respectively. Since *Al* has a higher *k* value compared to *Fe*, thermal interaction defined by *Equation (5A)* would yield higher effective thermal conductive resistance in the latter system and a relatively higher *Q/A* and entropy for any given temperature gradient. In general, the higher the *D* value for any binary-materials combination, the better the thermal barrier properties and this significantly explains the anomalous observations made by K. Yamaguchi et al [51].

From the afore-going perspective it would therefore be more sensible to use a 5XXX Al-Mg alloy or 6XXX Al-Mg-Si alloy for engineering applications where optimization of thermal barrier properties is of primary importance. Such is the case with some automotive engine components. This proposition is based on the fact that magnesium as an alloying element has 60% lower thermal conductivity. Additionally, magnesium has relatively lower density and enthalpies than copper [42, 69, 251, 252]. However, this could mean trading off Copper's relatively higher mechanical properties. The use of magnesium could also decrease the alloy's corrosion resistance [253] and ductility [60] and its relative content should therefore be closely monitored. With the targeted use of nanoclays for thermal-engineering purposes, it would therefore be recommendable to prioritize reliance on magnesium content from the nanoclay during formulation of nanoclay-infused AMCs rather than using a pre-alloyed matrix.

An alternative approach to improving thermal barrier properties of 2XXX Al-Cu alloy includes the lowering of the thermal conductivity of the interfacial boundary (k_I) without trading off the strength properties associated with Copper. This can be achieved by, as optimally as possible, strategically positioning a material with lower thermal conductivity at the interactive interface between constituent binary metallic elements. Preceding results relating to the use of nanoclays are testimonial to this concept.

6.4 Summary

Thermal behavioural properties in AMB-2712 alloy were not proportionate to the green compaction pressure. Samples from 200 Bars reference specimen showed superior thermal behaviour compared to the 160 and 240 Bars reference counterparts. The behaviour was observed to be consistent irrespective of the two sintering profile settings. This anomalous behaviour was explored from both a thermodynamic perspective and modelling of thermal conductivity of materials in analogy to electrical resistance according to Ohm's law.

To the contrary of reference samples, the thermal behaviour of Nanofil 116-AMCs was found be proportionate to the green compaction pressures with a trend favouring the lowest pressure of 160 Bars irrespective of the %wt content of nanoclay. It was further observed that thermal behaviour was significantly improved with increase in the %wt content of nanoclay, yielding as much as 25% improvement at 1%wt *Nanofil 116* and increasing the melting temperature by 6.6^0C. Thereafter the improvement was marginally incremental upto a maximum of 40% improvement in the thermal behaviour being achieved with the 12.5%wt samples and accompanied by 7^0C increase in melting temperature.

A second phase-change was observed closely succeeding the first phase-change. Since this second phase was evident in both the reference and Al-nanoclay sample, the change was associated with element(s) common to both the matrix and *Nanofil 116*, being Al, Si and O or their chemical combinations thereof. This phase seemed to shift with reference to the %wt content of nanoclay, thereby occurring before, during and after the melting temperature at the corresponding 3%, 8%, and 12.5%wt content of *Nanofil 116* respectively.

Based on %wt loss and disparity of results from one sample to another, weight loss results reinstate the supremacy of using 160-Bar as the most preferred green-compaction pressure. However, the percentage weight loss in 1%wt-nanoclay-content samples from the 240 Bars

specimen was relatively less than that of reference samples. Weight stability increased with %wt content of *Nanofil 116* upto 8%wt content. Nonetheless, magnitude of percentage weight loss increased with increase in weight content of nanoclay.

Specimen with 1%wt *Nanofil 116* consistently recorded a higher thermal conductivity than both the reference and 3%wt *Nanofil 116* specimens, showing an approximate 7% and 9% improvement at the 120^0C and 220^0C respectively. It was observed that, unlike the reference specimen whose conductivity deteriorated after 220^0C, conductivity of the nanoclay-infused samples consistently increased beyond that temperature and showed signs of stabilizing at 300^0C.

Corresponding results for specific heat capacity of the specimens reiterated the thermal conductivity and diffusivity results and further explained the observed delay in phase changes as reflected by increased melting temperatures. Thermal conductivity results confirmed that increased presence of nanoclay particles does inhibit the conductive heat propagation across the interfacial and inter-granular boundaries at microscopic level. In the lower temperature regime up to 220^0C, thermal conductivity of the sample with 3%wt content of *Nanofil 116* was observed to be similar to that of the reference. This was perceived to imply that the effect of nanoclay in deterring thermal conduction was similar to the cumulative effect of micro-cracks and porosity that was observed in the reference samples. However, the combined effect of increased silicon content and nanoclays-filler effect in the 3%wt specimen seemed to outweigh the effect of micro-cracks, which were prevalent in both categories of specimens. The increased precipitation of silicon and the relatively increased secondary ceramic phase in 3%wt specimen did play a role in stabilizing the heat transfer within the specimen. This would explain the thermal stability in this specimen (compared to reference samples) particularly beyond 220^0C.

Under similar test conditions and atmosphere, both the percentage thermal expansion and coefficient of thermal expansion increased with percentage nanoclay content. The relatively greater thermal expansion and coefficients for *Nanofil 116*-AMCs compared to Reference sample were attributed to the nanoclay's intrinsic structure.

Based on the aforegoing results for the datum "Set-A-Run" sintering profile settings, it is deemed befitting to conclude that the best AMC-System observed thus far in this study comprised of *AMB 2712 - 1%wt Nanofil 116 - 160 Bars*. This assertion is founded on:

(1) Thermal behaviour improved with increase in the %wt content of nanoclay. However, the greatest marginal improvement was observed at 1%wt nanoclay content, i.e. a 6.6% increase in melting temperature and 25% reduction in heatflow.

(2) Regardless of the nanoclay content, 160 bars (950 MPa) not only gave the best thermal behaviour as shown by *Figure 6-5 (i) – (iii)* but also gave the best weight-stability as shown by the minimal average difference of 0.06% in *Table 6-1*.

(3) Compared to the Reference and 3%wt nanoclay samples, the 1%wt nanoclay samples favourably dominated the thermal properties indicators including the thermal conductivity, specific heat capacity, thermal diffusivity, and thermal expansion.

CHAPTER 7:

NANOFIL 116 – AMCs: Mechanical Properties

7.0 Introduction

As mentioned in the research methodology and design chapter, three different batches were prepared under different settings and used for evaluation of different mechanical properties of the Nanoclay-AMCs. Despite the diversity in preparation procedures, the results were deemed sufficiently valid for comparative analysis based on the fact that every representative specimen in a batch was exposed to the same processing conditions as any other specimen in that batch and therefore duly comparable. The choice of a batch for a particular evaluation was based on suitability of the respective size to a target test method. The ensuing comparative analysis in this chapter was primarily based on the hardness and tensile testing methods of assessment.

7.1 Batch 1

7.1.1 Physical inspection

Physical inspection observations were as given in *Section 5.1* of *Chapter 5*.

7.1.2 Rockwell B Hardness

Figure 7-1 shows Rockwell B Hardness results from *Batch 1*. Specific data values were as given in *Table 7-1*. Three hardness test readings for the 12.5%wt sample were rejected as the tests initiated visible macro-cracks in the respective regions of measurement. Except for the 160 Bars specimens that showed a 6.33% decline in hardness compared to the corresponding reference specimen, the general trend showed a 1.72% and 2.48% increase in hardness for the 200 and 240 Bars specimens at 1%wt content of nanoclay. This initial increase in hardness may be attributed to the nanoclay's filler effect at the grain boundaries, regions which were previously characterized by porosity as depicted in *Figure 7-2*. It should be noted here that the

comparative observation shown thereof was consistent throughout all specimens and irrespective of green compaction pressures.

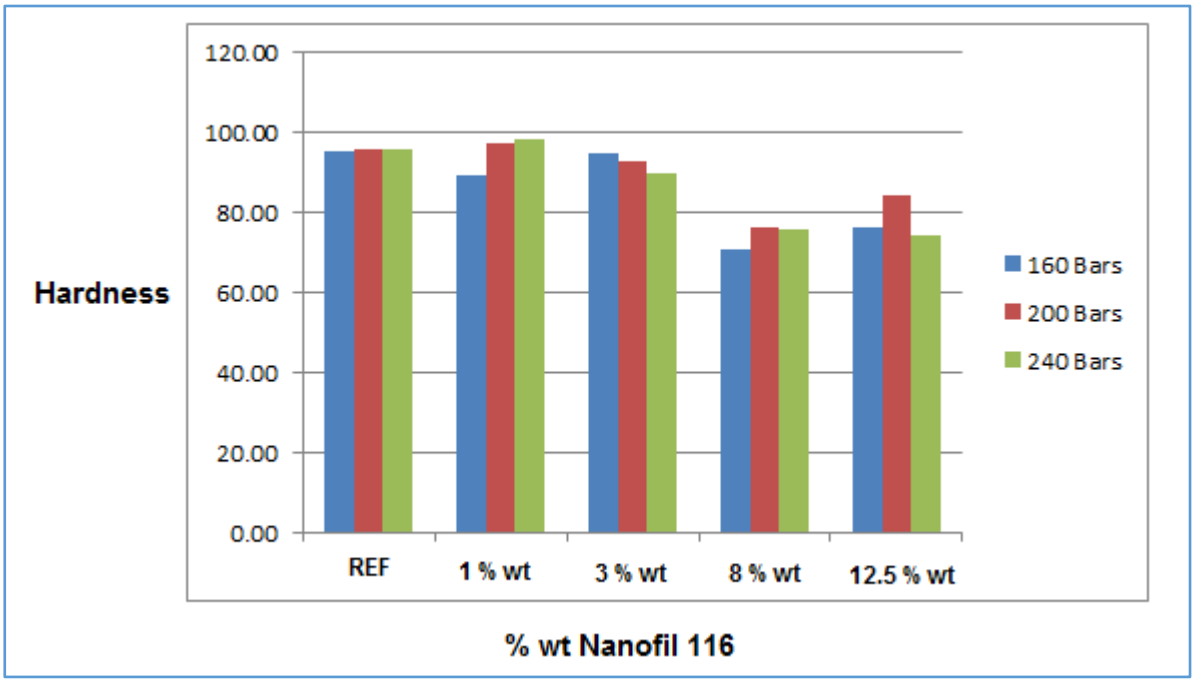

Figure 7-1: Rockwell B Hardness test results for Batch 1 specimens.

Table 7-1: Rockwell B Hardness Results for *Batch 1*.

AMB 2712 - ROCKWELL **B** HARDNESS RESULTS - REFERENCES

REFERENCE SAMPLES	Rockwell B Hardness Values										
	1	2	3	4	5	6	7	8	9	10	AVERAGE
REFERENCE Samples											
REF @ 160 Bars	93.50	89.00	90.75	98.50	98.00	97.25	99.25	95.50	95.75	98.50	**95.60**
REF @ 200 Bars	95.75	94.25	92.25	96.00	97.00	95.75	98.50	98.00	94.50	95.50	**95.75**
REF @ 240 Bars	93.00	93.25	96.50	99.00	97.00	96.00	97.25	94.50	97.25	95.75	**95.95**
1%wt Nanofil 116 Samples											
160 Bars	88.75	93.75	93.75	90.25	91.50	88.25	87.50	87.00	87.50	87.25	**89.55**
200 Bars	99.00	99.75	98.25	100.75	96.50	91.00	97.75	96.50	95.50	99.00	**97.40**
240 Bars	98.75	101.50	104.00	98.25	98.00	96.75	95.25	97.25	95.50	98.00	**98.33**
3%wt Nanofil 116 Samples											
160 Bars	88.25	93.75	94.50	96.25	97.00	97.00	95.25	96.00	96.00	96.25	**95.03**
200 Bars	86.25	94.75	95.00	96.50	94.00	93.25	91.75	93.25	91.50	91.50	**92.78**
240 Bars	88.75	90.75	90.25	91.25	92.00	88.75	90.75	86.00	90.75	88.00	**89.73**
8%wt Nanofil 116 Samples											
160 Bars	72.50	72.25	70.00	73.25	69.00	69.50	70.25	69.50	70.25	71.25	**70.78**
200 Bars	80.50	81.75	76.00	77.50	76.75	74.50	73.75	73.50	74.75	73.50	**76.25**
240 Bars	73.25	76.25	76.75	75.25	75.50	76.75	76.00	76.75	72.50	76.25	**75.53**
12.5%wt Nanofil 116 Samples											
160 Bars	83.50	81.50	76.50	77.25	75.25	72.00	78.75	76.75	70.25	70.25	**76.20**
200 Bars	74.75	83.00	83.25	75.25	90.00	90.00	88.25	89.75	82.25	89.50	**84.60**
240 Bars	78.00	74.25	76.00	75.75	73.25	72.75	71.50	N/A	N/A	N/A	**74.50**

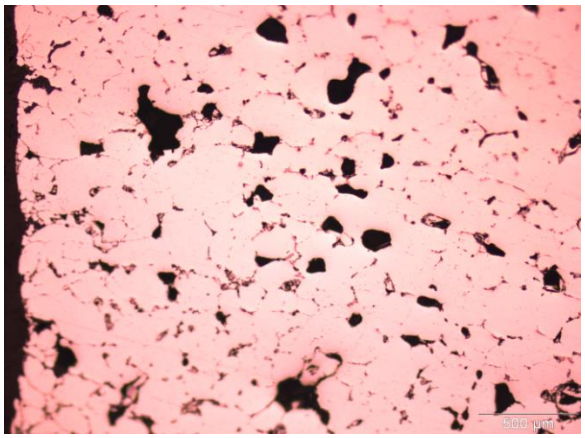

(i) 240 Bars Reference Sample

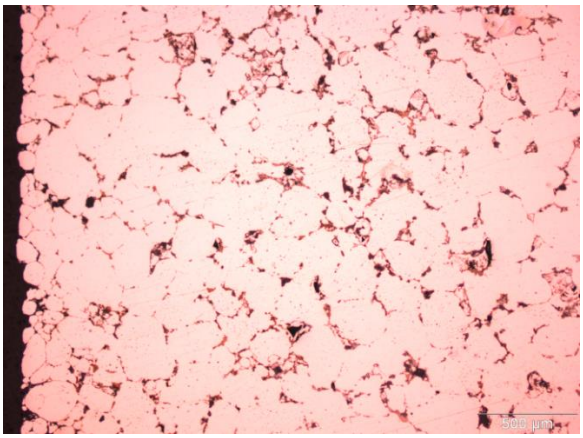

(ii) 240 Bars Sample @ 1%wt *Nanofil 116*

Figure 7-2: 500µm Images of microscopy samples viewed near the edge.

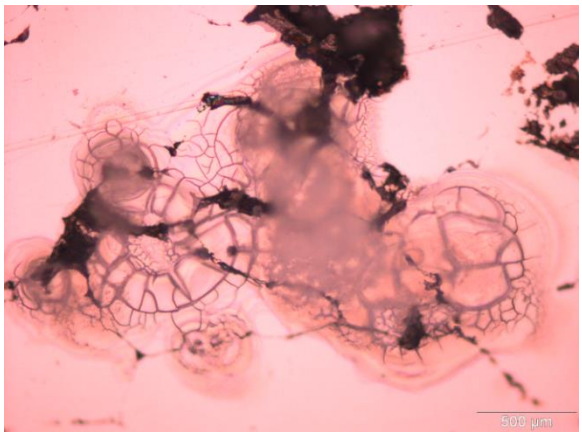

(i) 200 Bars Sample @ 3%wt *Nanofil 116*

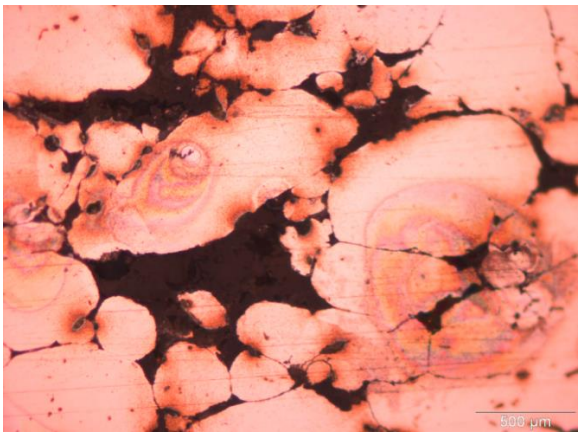

(ii) 200 Bars Sample @ 8%wt *Nanofil 116*

Figure 7-3: Examples of (i) Granular collapse, and (ii) Thermal stress concentrations.

The initial increase in hardness was observed to be followed by a consistent decline in hardness at 3% and 8% respectively. A maximum average hardness of 98.33 was recorded at 1%wt nanoclay content combined with a green compaction pressure 240 bars. The observed decline in hardness was attributed to the prevalent thermally induced granular collapse (*Figure 7-3(i)*) as a result of thermal stress concentrations (*Figure 7-3(ii)*) around the nanoclay-filled sites. However, a regain of some of the hardness was observed for some specimens at 12.5%wt content, being possibly related to: (i) high concentration of derived ceramic compounds that are typically both brittle and hard, hence inducing the reflected increase in hardness values,

and (ii) significant completion of the transition to globular microstructure as a result of the effect of the nanoclay's thermal induction of granular disintegration, i.e. since increased nanoclay content was observed to lower thermal conductivity of the AMCs, the nanoclay serves as a heat reservoir, thereby increasing thermal stress concentration around the grains leading to their breakdown into relatively smaller sizes.

In general, for the same sintering conditions and groups, the average group's hardness decreased with increase in %wt content of *Nanofil 116*. In comparison with the reference samples, this quantitatively interpreted to 0.7% and 3.4% decline in average group's hardness for the group with 1%wt and 3%wt nanoclay respectively. Corresponding decline for the group with 8%wt and 12.5% nanoclay was 22.5% and 18.1% respectively. This increased declines at higher nanoclay contents affirmatively correlates with the increased adverse and unreliable surface finish results for this latter groups of samples. From a structural perspective and despite the nanoclay serving as filler in the inter-granular spaces, it was considered that the dispersed nanoclay either constituted or contributed to formation of sites of relatively lower compressive strength, hence the reported decline in hardness with increase in the nanoclay's percentage weight content. One possibility is that despite any so formed ceramic compounds contributing to increase in hardness, the presence of microcracks had a deleterious effect on the resultant hardness.

7.2 Batch 2

7.2.1 Physical inspection

Physical inspection observations were as given in *Section 5.1* of *Chapter 5*.

7.2.2 Vickers hardness

Figure 7-4 shows Vickers Hardness results from *Batch 2* at a load of 2Kg. Specific data values were as given in *Table 7-2*. Specimen with 1%wt content of nanoclay showed a 25% increase

Table 7-2: Vickers hardness test results for *Batch 2*.

AMB-2712 Samples - Batch 2						
	HV2kg					
# Indent	Ref	1%N	2%N	3%N	4%N	5%N
1	52.2	59.2	59.7	48.6	35.7	48.7
2	39.4	59.8	37.8	44.4	36.3	39.2
3	41.4	62.2	52.3	38	42.7	47.7
4	33	49.3	60	65	41.8	57.2
5	46.4	62.7	43.1	54.4	39.7	53.7
6	40	41.9	46.4	47	43.5	57.4
7	39.5	54.3	53.6	48.9	43.5	43.3
8	47.2	39.5	40.5	37.4	35.5	42.1
9	39.4	50.3	63.9	37.5	47	47
10	48.7	54.9	53.4	44.3	47.8	48.1
Mean	42.72	53.41	51.07	46.55	41.35	48.44
Std dev	5.727866	8.120406	8.852627	8.565855993	4.461751	6.141697
Std error	1.81131	2.567898	2.799446	2.708761505	1.41093	1.942175

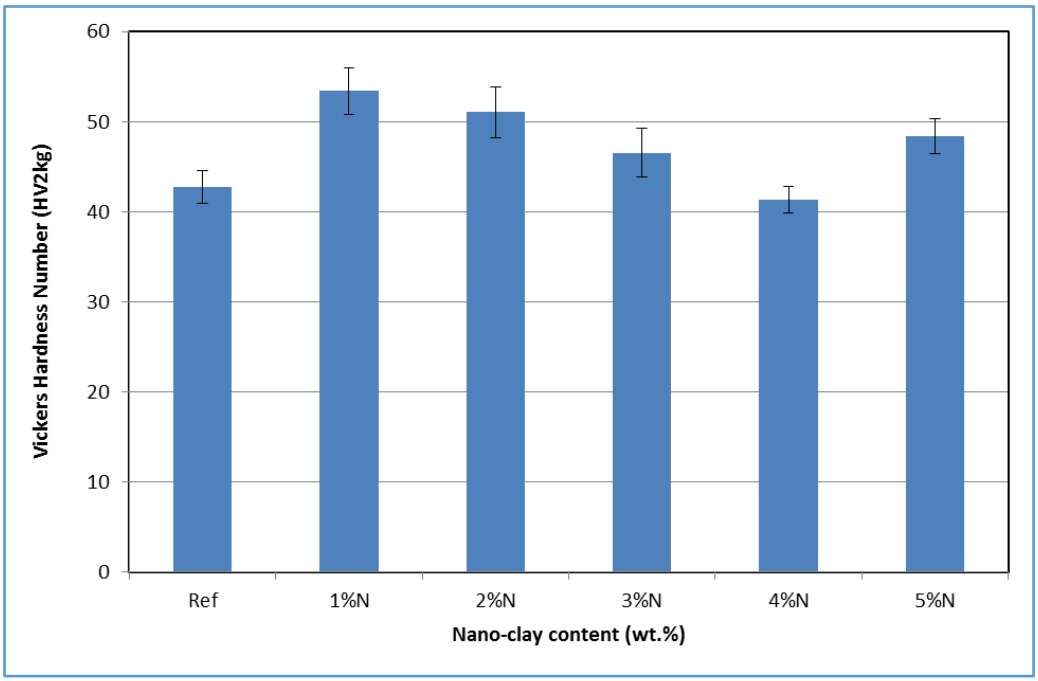

Figure 7-4: Vickers hardness results for *Batch 2*.

in hardness compared to the reference sample. The difference in percentage improvement in hardness between *Batch 1* and *Batch 2* was due to precipitation hardening in *Batch 2* specimens. Nonetheless, and despite the hardness scale being different, the results trend was the same

whereby an increase was realized by addition of 1%wt nanoclay, followed by a decrease in hardness values thereafter, and finally a gain in hardness at 5%wt content (12.5%wt in *Batch 1*). Possible causes of this trend were discussed in the preceding section.

7.3 Batch 3

7.3.1 Physical inspection

Figure 7-5 representatively shows sintered specimens from *Batch 3*. Due to their low green strength (46.5 MPa), some of the specimens from this batch broke even before sintering while others broken prematurely during testing. Specimens containing nanoclay showed signs of deformation after sintering. They were also observed to be asymmetrical. Since these physiological changes were universal across the nanoclay-infused specimens, comparative analysis was deemed still valid. The deformation was attributed to the effects of nanoclay on heat-transfer-matrix with respect to liquid-phase ratio during sintering. Relating to thermal conductivity results, the improved heat flow through the 1%wt content specimen would interpret into formation of a higher volume of liquid phase as compared to the reference sample, hence the visible gravity-induced sulking in these specimens.

Figure 7-5 (i) - Reference Specimens

Figure 7-5 (ii) 1%wt. *Nanofil 116* Specimens.

(iii) 3%wt *Nanofil 116* Specimens.

Figure 7-5: Sample of *Batch 3* sintered tensile test specimens showing: (i) Reference, (ii) 1%wt, and (iii) 3%wt *Nanofil 116* content.

However, at high nanoclay content, the thermal barrier effect dominates as reflected by relatively lower thermal conductivity. On the other hand, nanoclay-induced thermal stress concentrations cause localized thermal gradients, thereby causing delayed but gradually progressive sintering. This proposed pattern of events explains the non-uniform sintering of specimens containing 3%wt *Nanofil 116* as depicted by a combination of relatively rough and smooth patches of the specimen's surface.

7.3.2 Tensile test results

Table 7-3 shows the tensile test results for the successfully sintered and tested specimens from *Batch 3*. Despite the green compaction pressure being relatively low compared to the ASTM standard's stipulation, the ensuing relative analysis of the effect of *Nanofil 116* based on available experimental green compaction capacity holds relevance and validity as a preliminary foundation for further experimental investigation. Based on the maximum load values, it was observed that 1%wt nanoclay content improved the composite's maximum tensile loading capacity by 155% and a corresponding 150% improvement in tensile strain at fracture. The ultimate tensile strength is therefore 50% higher than the respective theoretical value for Aluminium of 110 MPa [254]. This phenomenon is hereby attributed to the filler effect of nanoclays and improved localized heat transfer at the grain-boundaries complementarily resulting to better granular fusion. The relative sintered densities and porosity results affirm the effectiveness of 1%wt nanoclay content in improving the heat-transfer-matrix, and hence the observed improved level of sintering, i.e. 1%wt nanoclay content showed the highest density (2.6165 g/cm^3), which interpreted to the lowest porosity of 3.09%, i.e. 96.91% densification.

At 2%wt content, the corresponding improvements on tensile loading capacity and strain at fracture are 86% and 67% respectively. In spite of this being a relatively better performance than the reference samples, this represents a significant decline in marginal effect of increasing

percentage weight content of nanoclay from 1% to 2%. This decline was persistently observed with further increase in content of nanoclay, whereby at 3%wt, the composites performance was worse than the reference samples and out-rightly infeasible at 4% and 5%wt contents.

Table 7-3: *Batch 3* Tensile Test results.

SAMPLE's PARTICULARS					TEST RESULTS		DERIVED RESULTS			
Sample ID.	**Sample No.**	**Mass**	**Width (W)**	**Thickness (t)**	***Maximum Load**	**Extension At Break**	**Sintered Density**	**Porosity**	**Ultimate Strength (σ_{ut})**	**Maximum Strain (ε)**
		(g)	(mm)	(mm)	(N)	mm	(g/cm^3)	(%)	(Mpa)	(mm/mm)
REF	1		5.9	5.4	1865	1.69	2.1708		58.54	0.07
	2		6.1	5.2	1549	1.57	2.2467		48.83	0.06
	3		5.9	5.4	1972	1.28	2.2659		61.90	0.05
Average			**6.0**	**5.3**	**1795**	**1.51**	**2.2278**	**19.12**	**56.42**	**0.06**
1%N	1		5.5	5.0	4040	3.21	2.6234		146.03	0.13
	2		5.5	5.1	4730	4.06	2.5339		168.35	0.16
	3		5.5	4.9	4960	3.96	2.6923		184.30	0.16
Average			**5.5**	**5.0**	**4577**	**3.74**	**2.6165**	**5.01**	**166.23**	**0.15**
2%N	1		5.5	5.1	3190	2.59	2.5690		113.93	0.10
	2		5.7	5.3	3290	2.34	2.4905		108.48	0.09
	3		5.7	5.2	3560	2.60	2.4449		120.06	0.10
Average			**5.6**	**5.2**	**3347**	**2.51**	**2.5015**	**9.19**	**114.16**	**0.10**
3%N	1		6.1	5.4	1020	0.42	2.2128		31.20	0.02
	2		6.1	5.4	1270	0.47	2.4239		38.02	0.02
	3		6.1	5.6	1110	0.39	2.4353		32.68	0.02
Average			**6.1**	**5.5**	**1133**	**0.43**	**2.3573**	**14.42**	**33.96**	**0.02**
4%N	1		6.2	5.5	N/A	N/A	2.2542		N/A	N/A
	2		6.2	5.3	N/A	N/A	2.2948		N/A	N/A
	3		6.1	5.5	N/A	N/A	2.3054		N/A	N/A
Average			**6.2**	**5.4**	**0**	**0.00**	**2.2848**	**17.06**	**0.00**	**0.00**
5%N	1		6.1	5.4	N/A	N/A	2.2225		N/A	N/A
	2		6.2	5.3	N/A	N/A	2.3288		N/A	N/A
	3		6.3	5.3	N/A	N/A	2.1968		N/A	N/A
Average			**6.2**	**5.3**	**0**	**0.00**	**2.2494**	**18.34**	**0.00**	**0.00**
KEY	*		Maximum Load after accounting for preload							
	N/A		Fractured during pre-load stage							

Samples in the latter two categories were observed to fracture fairly within the preloading phase of the test procedure with scarcely any recorded extension. This tendency was considered to represent an onset of brittleness or significant loss of the composite's ductility. The underlying transition was attributed to presence of micro-cracks and formation of brittle ceramic compounds.

This observation was further complimented by the observed variation in sintered density of the samples. Beyond 1%wt nanoclay content, the sintered density consistently declined. Samples with 1%wt nanoclay content recorded the highest density (2.6165 g/cm^3), which interpreted to the lowest porosity of 5.01%, i.e. approximately 95% densification.

7.4 Batch 4

7.4.1 Physical inspection

Figure 7-6 shows representative *Batch 4* samples as wire cut from successfully sintered specimens and machine-turned with reference to *ASTM E63-01* standards. Detailed discussion of this batch is given in *Chapter 9* on processability of Nanoclay-AMCs.

7.4.2 Tensile test results

All other factors being held constant, results showed that samples with 1%wt *Nanofil 116* had a 12% higher yield strength than the reference samples. This was accompanied by 3% and 1% increase in young's modulus and ultimate tensile strength respectively. The quantitative structural markers for these specimens were almost similar to those reported for *Batch 3* above. A detailed analysis and discussion is given in *Chapter 9* on processability.

Figure 7-6 (i) Reference Sample

(ii) 1%wt *Nanofil 116* Sample

(iii) 3%wt *Nanofil 116* Sample

Figure 7-6: Tensile test samples from *Batch 4* specimens.

7.5 Summary

The general trend showed an increase in hardness with increasing nanoclay content. This was attributed to resultant filler effect of the nanoclay. Effect of nanoclay beyond 3%wt content reduced the hardness due to thermal induction of granular collapse. A regain of hardness was observed at 12.5% and related to the microstructural evolution to dominantly globular microstructure as a result of induced localized thermal stress concentrations. Based on the maximum load values, it was observed that 1%wt nanoclay content improved the composite's maximum tensile loading capacity by 155% and a corresponding 150% improvement in tensile strain at fracture. Minimal difference was observed between results for *Batch 3* (processed in argon) and *Batch 4* (processed in Argon + Nitrogen atmosphere).

CHAPTER 8:

NANOFIL 116 – AMCs: Machinability Properties

8.0 Introduction

Different automotive engine components require machining to different surface finish tolerances. To meet the target needs, a variety of variables can be fine-tuned through processing techniques and selection of fortifying ingredients. In addition to environmental considerations of machining processes, machinability of a metal affects the costs dynamics of a production process with a knock-on effect on the absorption costing of the end product. It is imperative therefore, that machinability is considered as a pivotal factor in the design space. This chapter presents machinability results and discussion with respect to AMB-2712 Al-*Nanofil 116* composites processed using powder metallurgy. *Batch 1* was used for assessment of machinability properties. Variables included the green compaction pressure and percentage weight content of the nanoclay.

8.1 The reference samples

Figure 8-1 (i) shows result for the profilometer's reference master while *Figure 8-1 (ii)* shows representative results for surface finish obtained from machined reference samples from the specimens previously compacted to 160-, 200-, and 240-Bars.

(i)	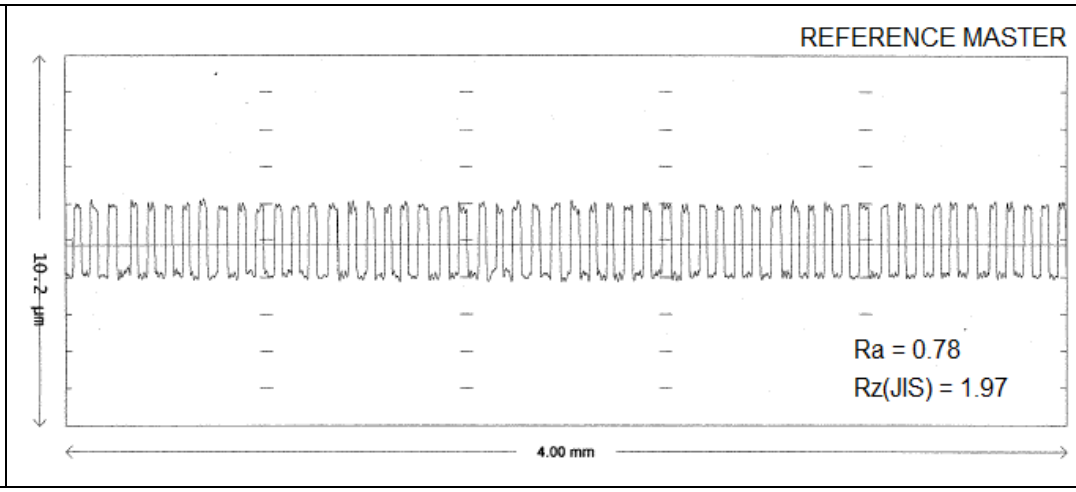

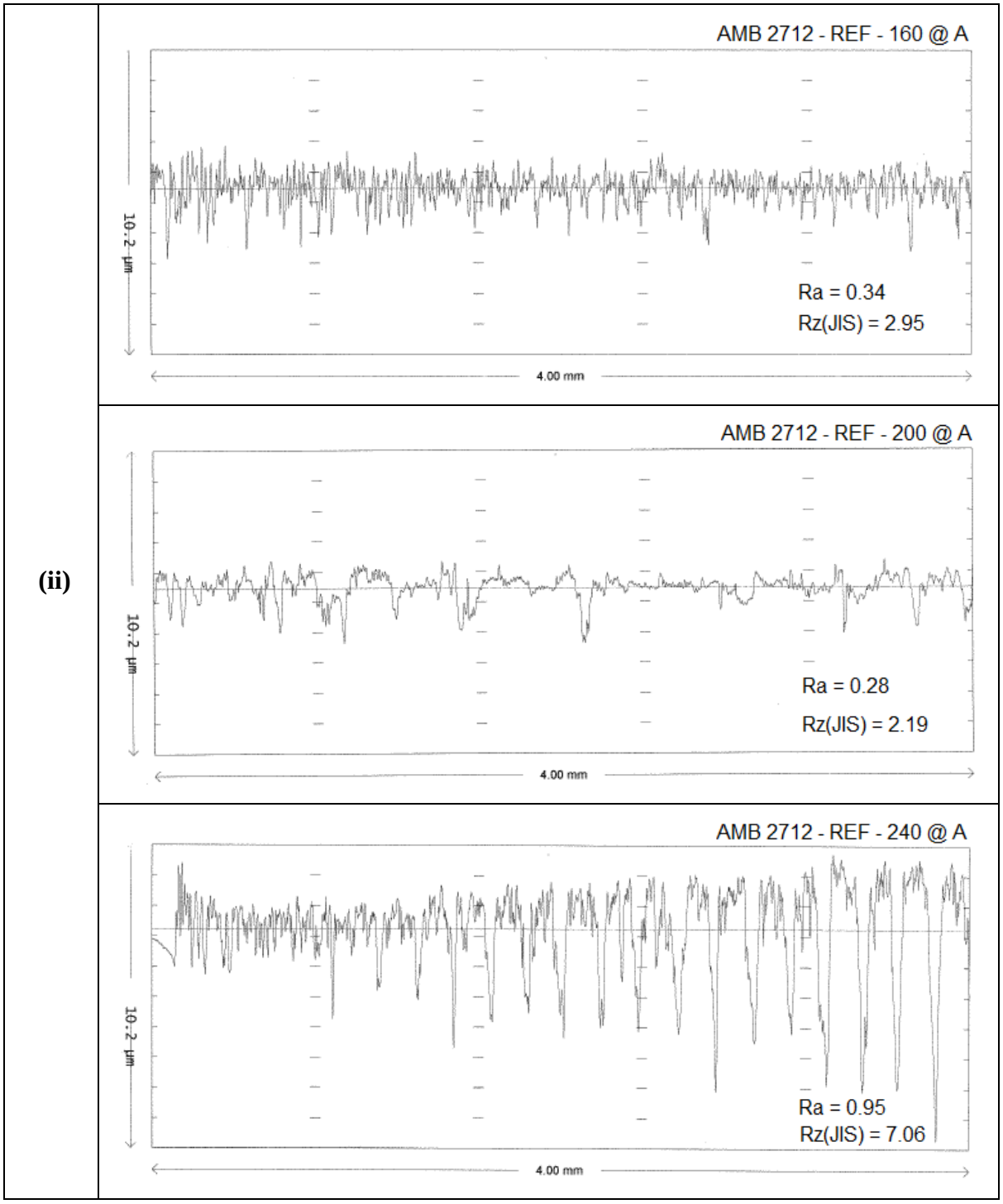

Figure 8-1: (i) Reference Master, and (ii) *Reference* samples from: 160, 200, and 240-Bar specimens.

8.2 Effects of *Nanofil 116* on machinability

Figure 8-2 shows sample results from the specimens infused with *Nanofil 116* and processed using *Set-"A"-run* sintering profile. Results indicated that as the *Nanofil-116* content increased

from 1 – 3%, the surface finish with reference to R_a improved by 14% from 1.60-to-1.38 microns. To the contrary, the quality seemed to deteriorate with reference to R_z increasing by 14% from 8.13-to-9.28 microns. This may be attributed to the filler effect of the nanoclay towards closing-up any pores progressively from the pore's walls inwards. In that manner, the R_a value as based on the reduced *surface area in the vertical plane* of the probe stands to decrease without necessarily having a corresponding decrease in the *depth* of the pore as accounted for by the R_z.

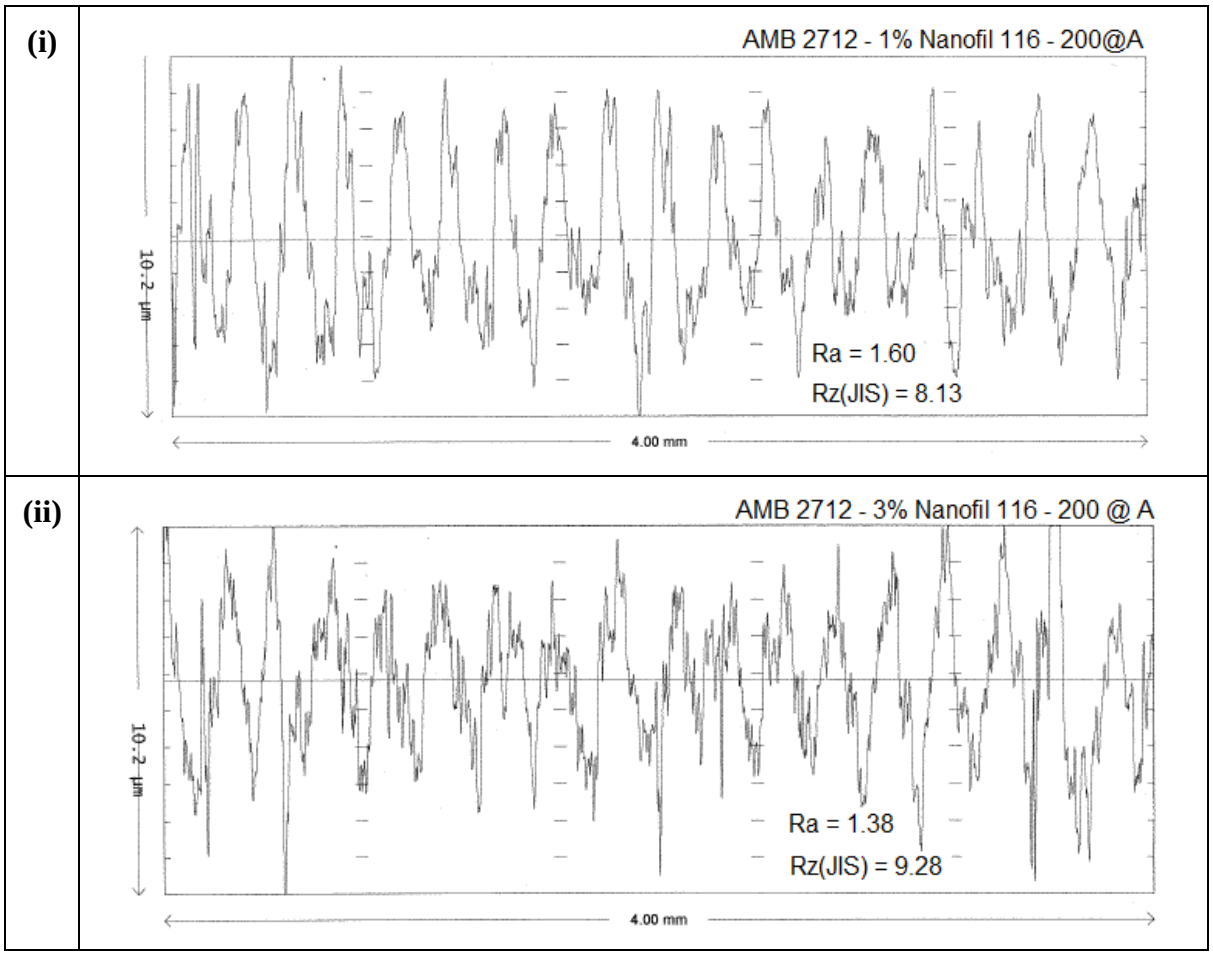

Figure 8-2: *Set-"A"-run*; 200-Bar specimens: (i) 1% wt, and (ii) 3% wt *Nanofil-116.*

Owing to substantial increase in the amplitudes recorded during preliminary readings of the surface finish for 8%- and 12.5%wt content samples, the vertical scale was adjusted from 10.2 microns to 20.3 microns. This observed increase in amplitudes was attributed to: (1) localized fracture mechanisms whereby the increased presence of brittle ceramic compounds as a result

of increased nanoclay content would tend to predominantly create rough fracture surfaces during the phenomenal shearing of chips off the specimen, and (2) despite the filler effect of nanoclay, pore sizes in the latter set were relatively fewer but bigger in size than those observed in the 1% & 3%wt set of samples. It is envisaged that this shift in pore-sizes was caused by bubbling of gases through the relatively large nanoclay sites. Corresponding sample results for the latter pair are shown in *Figure 8-3*.

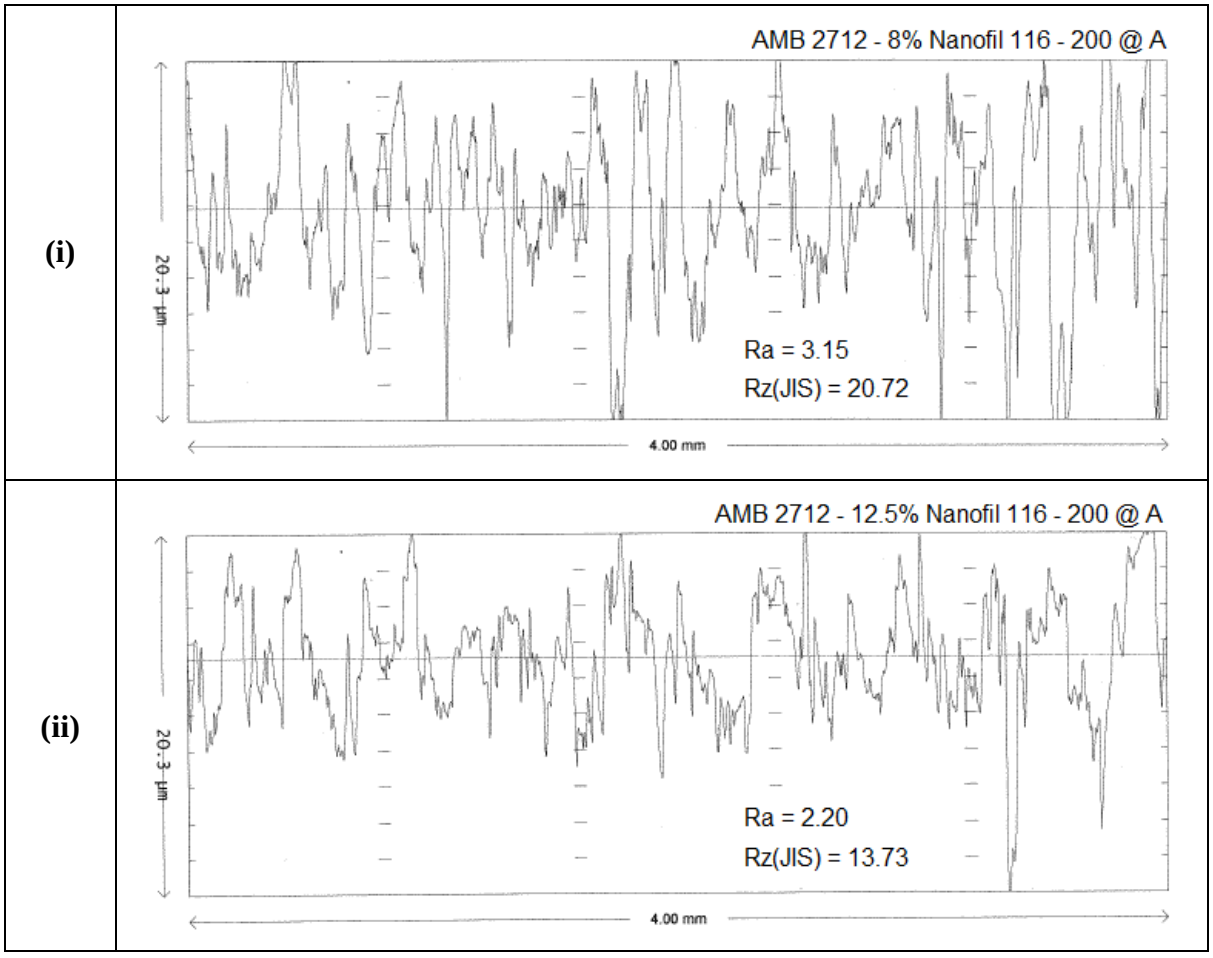

Figure 8-3: *Set-"A"-run*; 200-Bar specimens: (i) 8% wt, and (ii) 12.5% wt *Nanofil-116*.

This set of results showed that as the %wt. content of nanoclay increased from 8%wt. to 12.5%wt., the values of R_a and R_z improved from 3.15 – to – 2.20 microns and 20.72 – to – 13.73 microns, which interpreted to 30% and 34% improvement respectively. Notably, the order of magnitude of surface finish values for the first pair (1%wt and 3%wt) was relatively

lower than that of the second pair (8%wt and 12.5%wt). The leap from 3%wt to 8%wt was marked by a 128% and 123% adverse variation in R_a and R_z respectively.

For both sets of samples having the low and high %wt nanoclay content, the trend in results held true with respect to the graphical results as well as the results reflected in the quantified surface-finish values of both R_a and R_z, which declined in magnitude with increase in the compaction pressure. However, this trend was not consistent from one section of sample's surface to another. To mitigate the apparent variations, five readings were recorded and averaged in order to obtain a representative surface-finish-value for the sample. *Table 8-1* quantitatively presents a summary of the surface-finish values for both sets of *test samples*.

Reference samples previously subjected compacted to 200 bars of green compaction pressure consistently yielded the best machinability results in terms of both R_a and R_z. To the contrary, nanoclay-infused samples previously subject to the same pressure of 200 bars generally yielded the worse machinability results in terms of both R_a and R_z irrespective of the %wt content of nanoclay. This phenomenon was considered to infer to the laws of thermodynamics. Accordingly, a correlation must be existing amongst processing parameters such as green compaction pressure, heat transfer, and other factors towards establishing a thermodynamic equilibrium with a knock-on effect on the material's resultant properties such as the extent of particulate fusion, hardness, density, porosity, and structural strength. Inclusion of alloying and/or reinforcing material such as nanoclay simply amplifies an already existing complex dynamics.

With regard to the first pair of %wt nanoclay content, it was generally evident that for the same green-compaction pressure, increase in %wt content of *Nanofil-116* generally improved the surface finish. This was attributed to the effect of nanoclay acting as a filler and grain-refinement ingredient. Of the nanoclay-infused samples, best machinability results with

Table 8-1: Surface finish results for machined *Batch 1* samples.

NANOFIL 116 SAMPLES		Quantified Surface Finish values (μm)						STD. DEV.
		1	2	3	4	5	AVERAGE	
REF Samples								
REF @ 160 Bars	**Ra**	0.47	0.52	0.66	0.34	0.42	**0.48**	**0.11**
	Rz(JIS)	4.82	4.55	5.10	2.95	3.93	**4.27**	**0.77**
REF @ 200 Bars	**Ra**	0.28	0.51	0.55	0.36	0.41	**0.42**	**0.10**
	Rz(JIS)	2.19	3.14	3.54	3.66	3.27	**3.16**	**0.52**
REF @ 240 Bars	**Ra**	1.39	0.95	1.51	1.07	1.37	**1.26**	**0.21**
	Rz(JIS)	8.17	7.06	8.15	6.93	8.42	**7.75**	**0.62**
1%wt Nanofil 116 Samples								
160 Bars	**Ra**	1.50	1.63	1.41	1.68	1.56	**1.56**	**0.10**
	Rz(JIS)	10.70	9.74	9.65	12.29	11.19	**10.71**	**0.98**
200 Bars	**Ra**	1.84	1.69	1.75	1.76	1.69	**1.75**	**0.06**
	Rz(JIS)	9.48	8.77	9.50	8.88	9.77	**9.28**	**0.39**
240 Bars	**Ra**	1.40	1.09	1.33	1.38	1.23	**1.29**	**0.11**
	Rz(JIS)	8.22	9.96	8.15	10.71	8.08	**9.02**	**1.10**
3%wt Nanofil 116 Samples								
160 Bars	**Ra**	0.62	0.60	0.65	0.64	0.63	**0.63**	**0.02**
	Rz(JIS)	5.71	4.58	4.91	4.36	4.79	**4.87**	**0.46**
200 Bars	**Ra**	1.40	1.70	1.63	1.44	1.57	**1.55**	**0.11**
	Rz(JIS)	10.53	10.35	9.74	9.32	9.81	**9.95**	**0.44**
240 Bars	**Ra**	0.68	0.54	0.60	0.59	0.59	**0.60**	**0.05**
	Rz(JIS)	4.78	4.52	4.13	4.37	4.45	**4.45**	**0.21**
8%wt Nanofil 116 Samples								
160 Bars	**Ra**	1.38	Unreliably Inconsistent				**1.38**	
	Rz(JIS)	11.14					**11.14**	
200 Bars	**Ra**	1.78	Unreliably Inconsistent				**1.78**	
	Rz(JIS)	13.20					**13.20**	
240 Bars	**Ra**	1.72	1.71	1.30	1.69	1.49	**1.58**	**0.16**
	Rz(JIS)	13.14	13.31	9.89	12.21	12.74	**12.26**	**1.24**
12.5%wt Nanofil 116 Samples								
160 Bars	**Ra**	Unreliably Inconsistent						
	Rz(JIS)							
200 Bars	**Ra**	Unreliably Inconsistent						
	Rz(JIS)							
240 Bars	**Ra**	Unreliably Inconsistent						
	Rz(JIS)							

reference to both R_a and R_z were observed at 3%wt nanoclay content combined with a green compaction pressure of 240 Bars. In comparison to the corresponding reference sample, this

represented an improvement in machinability by 52% and 43% in terms of R_a and R_z respectively. This was interestingly a turning-point performance because the results for all other test samples were observed to be inferior to those of the corresponding reference samples irrespective %wt nanoclay content or green compaction pressure. After the 3%wt-cum-240 bars combination, the results for were observed to significantly deteriorate and unreliably inconsistent.

8.3 Topography of machined surfaces

The afore-going observations resonated reasonably with optical micrographs of the milled surfaces as presented in *Table 8-2*, whereby the surface texture topography was observed to significantly vary with %wt content of nanoclay. These sample micrographs consistently represent results across the population of samples and variety of regions across each sample's surface. In general, no significant topographical differences were discernible across samples based on variation of green compaction pressures, i.e. key determinant factor was the presence (or absence) of nanoclay and the relative %wt. content thereof.

Table 8-2: Effect of (i) Sintering profile and (ii) %wt of *Nanofil 116*.

	200 Bar	240 Bars
REF	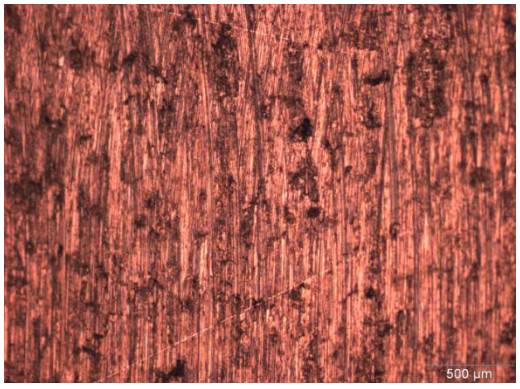	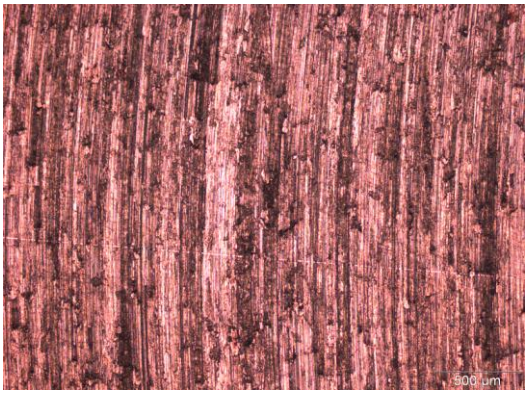
(i)		

1%N	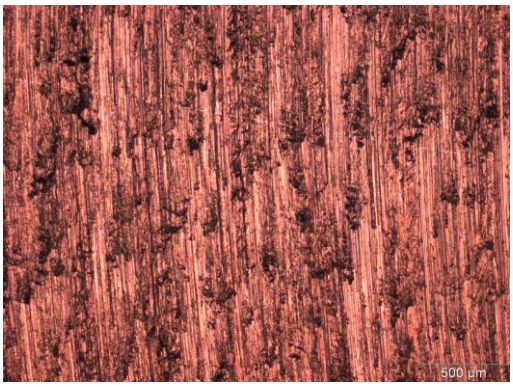	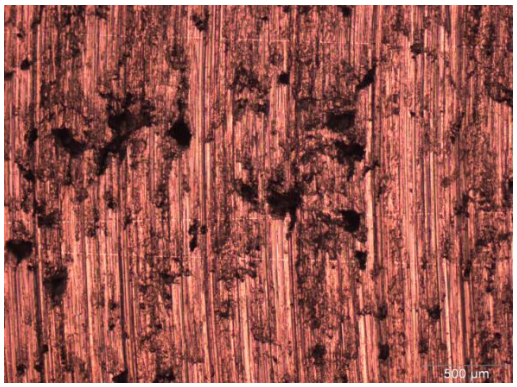
3%	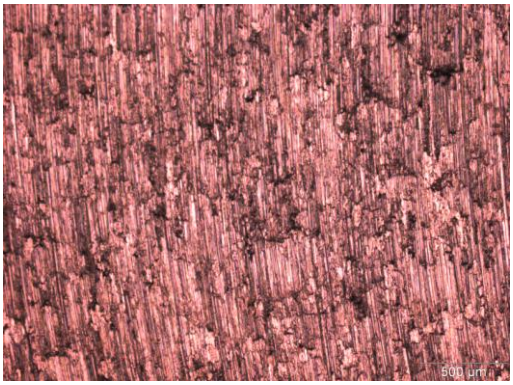	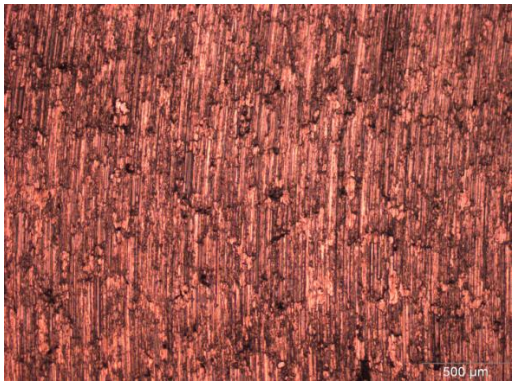
First %wt Pair		
8%	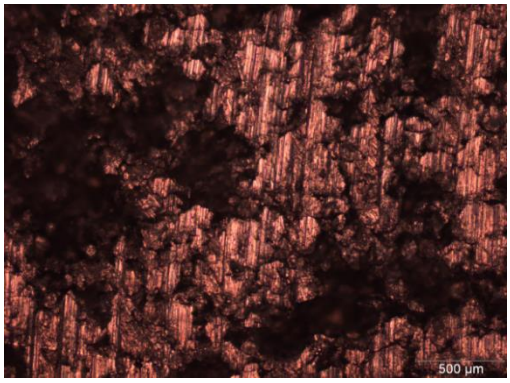	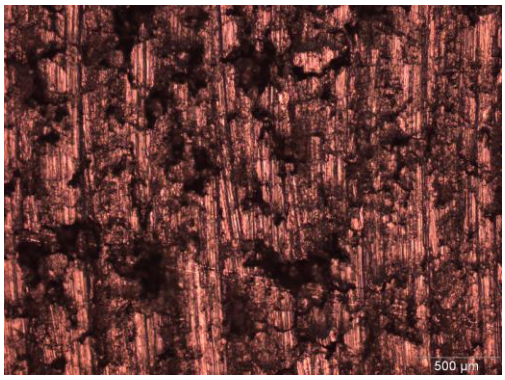
12.5 %	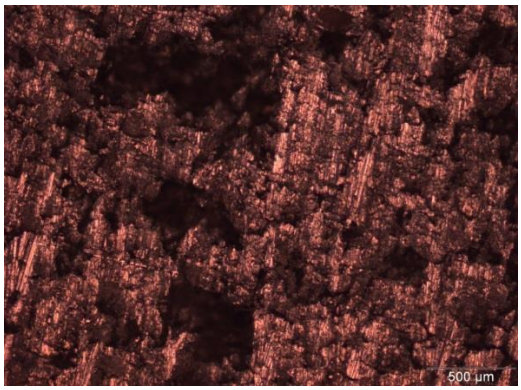	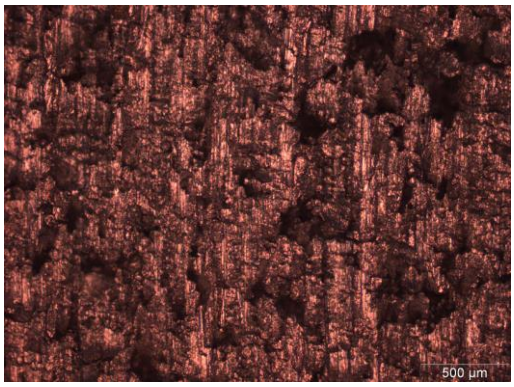
Second %wt Pair		
(ii)		

With reference to preceding microstructural analysis (*Chapter 5*), the first pair of nanoclay-infused samples showed that porosity was evidently reduced as the %wt content increased from 1% to 3%. This explain the relatively better surface finish in the latter sample. This phenomenon was associated with the filler effect of nanoclay on the composite. However, the second pair of samples showed that, as the clay content increased to 8% and 12.5%, the milled surfaces were dominated by vacant patches, which were not typical of the porosity observed from polished optical microscopy specimens. Three factors are hereby proposed as the possible causes of these patches: (a) granular and/or particulate erosion during milling, (b) weak granular and/or inter-particle fusion, and (c) The effect of micro-cracks.

8.3.1 Granular and/or particulate erosion

Factors that could contribute to the granular and/or particulate erosion phenomenon include: (i) Since milling is an interrupted cutting process, the impact loading as each tooth engages with the grains could be more than the structural strength of medium holding the grain(s) and/or particles in position, (ii) With increased nanoclay content, inter-particle boundaries evidently became relatively thicker in width and characterized with localized porosity, which would have the effect of weakening the structural support around the grain(s) and/or particles, and (iii) Due to inherent disparity in thermal properties of *Nanofil 116* and the matrix, samples with significant %wt content of nanoclay were characterised by localized thermal stresses that seemingly created structurally weaker zones eventually leading to defragmentation of the grains into relatively smaller ones.

8.3.2 Weak granular-fusion and/or inter-particle-fusion

Figure 8-4(i) shows the integrity of metallic grains being threatened by thermal stress within the grains as well as from the edges of the grains resulting into granular collapse or disintegration. Similarly, *Figure 8-4(ii)* shows connections at the grain boundaries being in the process of disruption resulting into stand-alone metallic grains surrounded by the dark phase

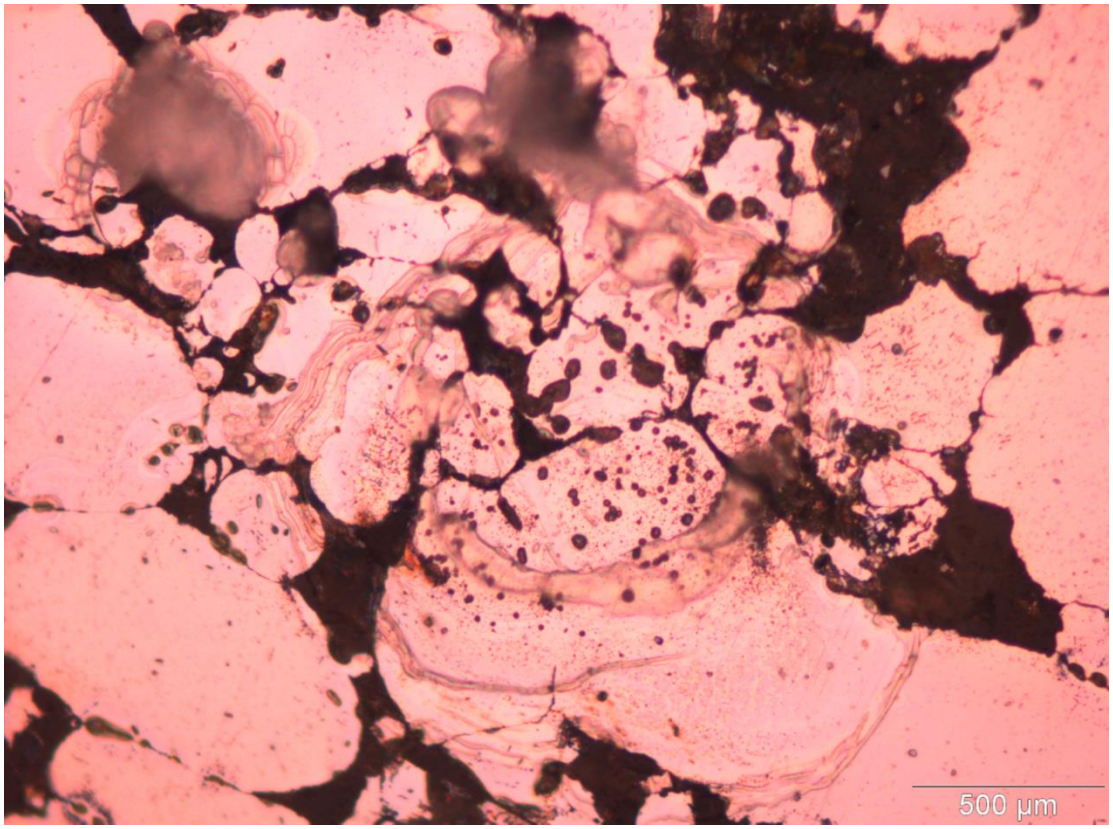

(i)

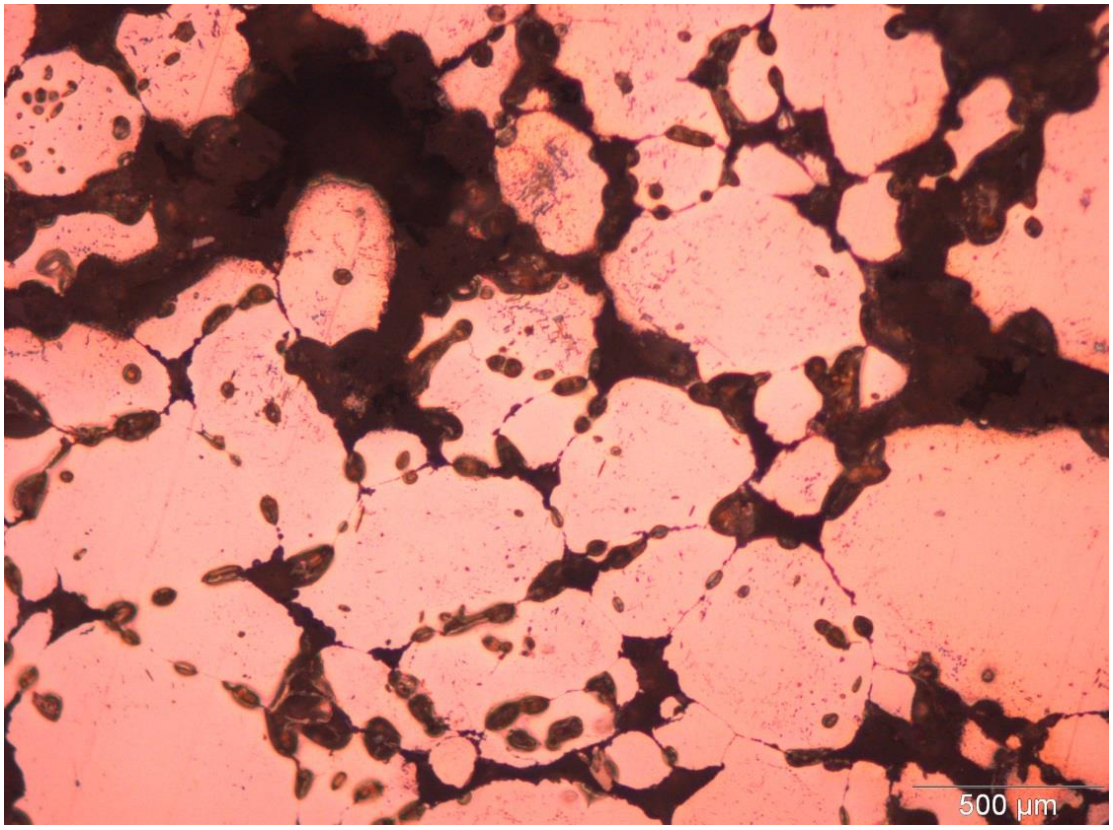

(ii)

Figure 8-4: Micrographs of 12.5%wt *Nanofil 116* samples showing metallic fusion under attack: (i) within grains, and (ii) at grain boundaries.

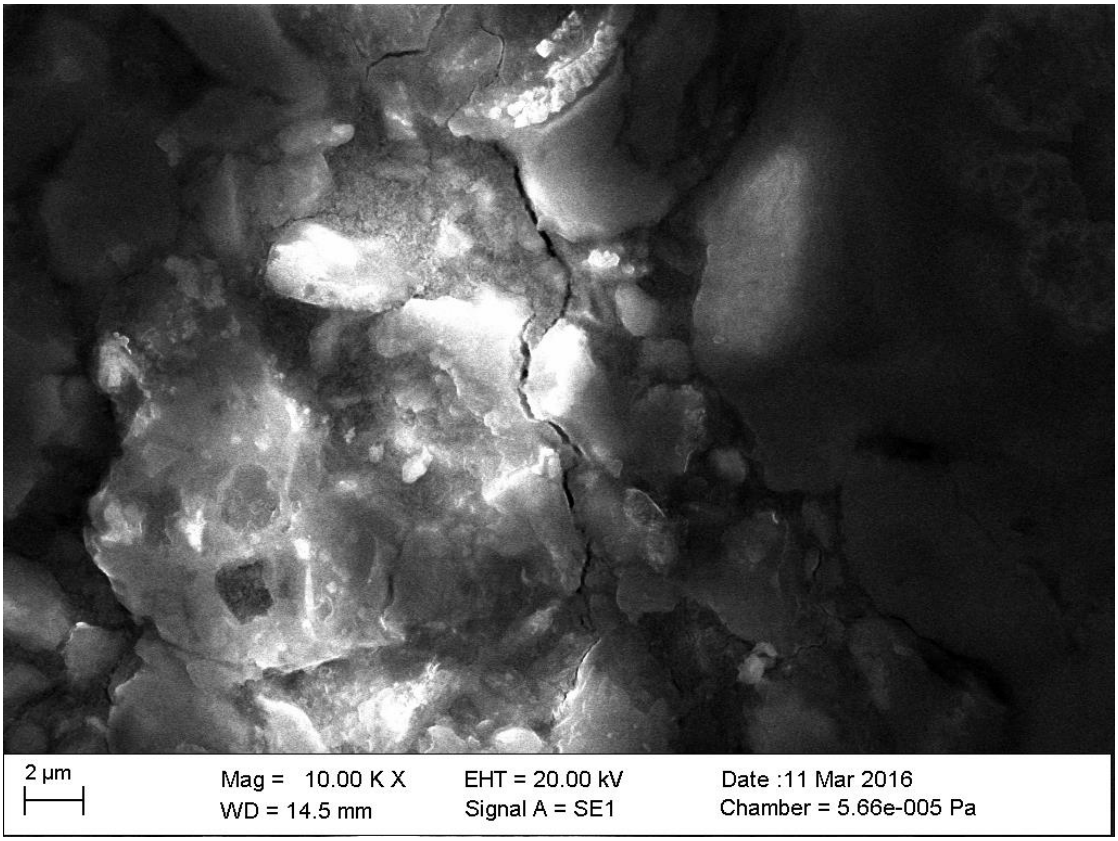

(i)

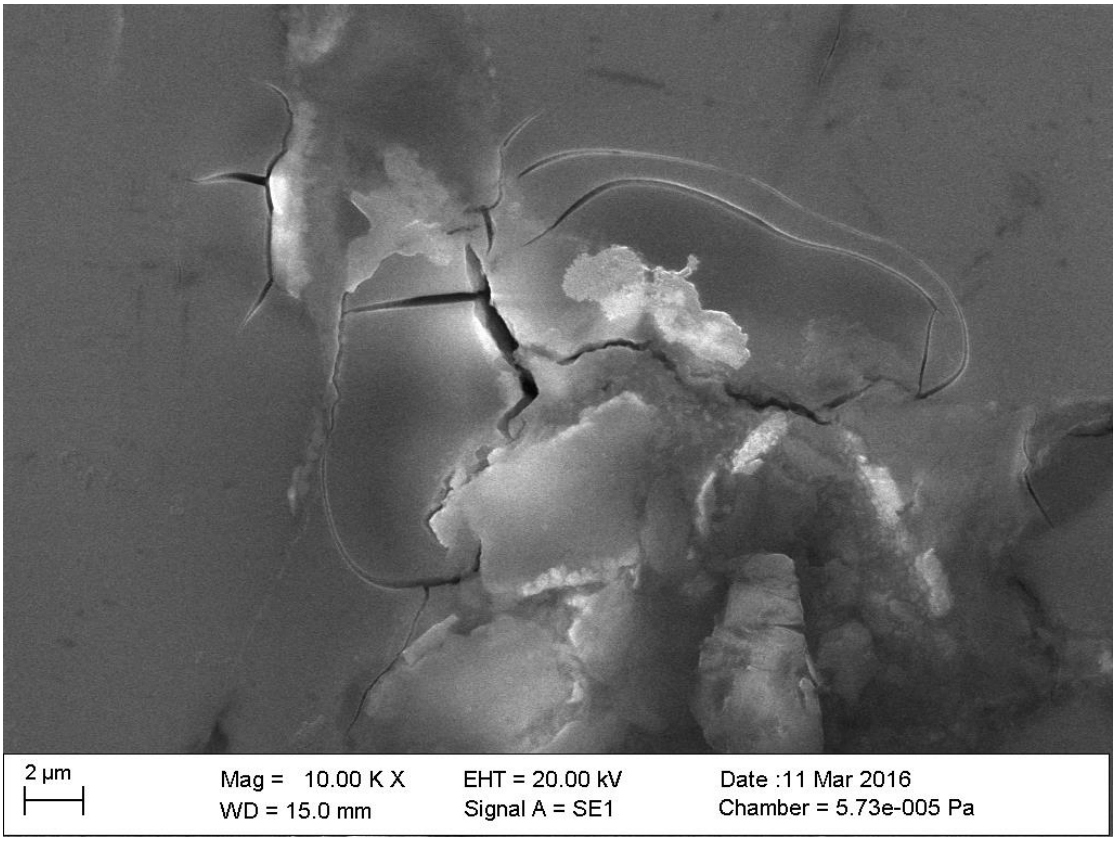

(ii)

Figure 8-5: SEM images showing micro-cracks in (i) 8%wt and (ii) 12.5%wt specimens.

that was relatively weaker due to presence of micro-cracks. Both micrographs were from specimens containing 12.5%wt *Nanofil 116* and previously compacted to 160 Bars.

8.3.3 The effects of micro-cracks.

In *Chapter 5*, the presence of micro-cracks in the non-metallic phase was validated and discussed. The effect of such discontinuities in the material would be to weaken the material structural integrity at both microstructural and bulk level. *Figure 8-5* shows more exemplary SEM images of cracks that may cause significant structural weaknesses.

8.3 Summary

As the *Nanofil-116* content increased from 1 – 3%, the surface finish in terms of R_a improved by 14%. To the contrary, the quality seemed to deteriorate with reference to R_z increasing by 14%. Nevertheless, it was generally evident that for the same green-compaction pressure and sintering settings, increase in %wt content of *Nanofil-116* generally improved the surface finish. Best machinability results in terms of both R_a and R_z were observed at 3%wt nanoclay content combined with a green compaction pressure of 240 Bars.

Milled surface topography was observed to vary both at the grain boundaries and within the grains. This phenomenon depicted preference of the relatively fine grain-structure in favour of the course grain-structure. Porosity was evidently reduced as the %wt content increased from 1% to 3% resulting to a relatively better surface finish in the latter sample. However, the milled surfaces of samples with 8% and 12.5%wt were dominated by vacant patches deemed to be possibly caused by granular and/or particle erosion during milling and incomplete fusion.

As for the 1%wt nanoclay content, average hardness increased with the green compaction pressures just like in the reference samples, whereas the average hardness decreased with green compaction pressure in the 3%wt content samples. Maximum hardness was recorded at 1%wt nanoclay content combined with a green compaction pressure 240 bars. For the same sintering

conditions, the average batch hardness generally decreased with increase in %wt content of *Nanofil 116*.

Preference between 1%wt and 3%wt would entail a trade-off between machinability and hardness. Further reference to thermal-mechanical properties may be necessary depending on the design context. It is hereby recommended that these results be bench-marked against the industrial norms for acceptable surface finishes and hardness depending on contextual design requirements for the end-user applications.

CHAPTER 9:

PROCESSABILITY OF NANOCLAYS-AMCs

9.0 Introduction

The final properties of an engineered material are reflective of the sum-total effects of the respective material's signature processing parameters and techniques. For instance, materials processed through powder metallurgy are known to exhibit different properties as compared to those prepared through casting processes. Furthermore, the parameters used during the powder metallurgy processing do significantly affect the properties of material thus made. These parameters include the physical and chemical nature of stock powders used, relative quantities of the ingredients, green compaction parameters (such as the pressure, compaction temperature, and lubricant), and the sintering conditions (temperature profile and atmosphere).

This chapter documents results from the experimental investigation of processability of *Nanofil 116*-AMCs with a focus on the effect of variables such the quantity of *Nanofil 116* relative to AMB-2712, green compaction pressure, sintering profile and sintering atmosphere. Properties of the resultant specimen AMCs were benchmarked against a reference sample of the matrix prepared using a datum set of sintering conditions and atmosphere as detailed in the research methodology chapter. Effort was made to investigate only one variable at every iterative evaluation of the significant parameters. Reference results used for comparative analysis include the physical examination of processed samples, sintered density, DSC-TGA, hardness, tensile properties, and microstructural analysis.

9.1 *Nanofil 116* versus *Cloisite* Ca^{++}*DEV*

Table 9-1 shows surface finish results for *Cloisite* Ca^{++}*DEV*-AMCs. For ease of reference, the comparable average and standard deviation values for samples with *Nanofil 116* have been integrated to *Table 9-1* in the last two columns. Full results for the *Nanofil 116*-AMCs were as

furnished in preceding chapter on machinability (*Table 8-1*). *Figure 9-1* shows sampled comparable machinability results for AMCs with 1%wt of *Nanofil 116* and *Cloisite Ca^{++}DEV*. For each of the nanoclays, these results reflect the effect of green compaction pressures.

Table 9-1: Surface finish results for samples containing *Cloisite Ca^{++}DEV*.

CLOISITE Ca++DEV SAMPLES		Quantified Surface Finish values (μm)						STD. DEV.	NANOFIL 116 SAMPLES	
		1	2	3	4	5	AVERAGE		AVERAGE	STD. DEV
REF Samples										
REF @ 160 Bars	**Ra**	0,47	0,52	0,66	0,34	0,42	**0,48**	**0,11**		
	Rz(JIS)	4,82	4,55	5,10	2,95	3,93	**4,27**	**0,77**		
REF @ 200 Bars	**Ra**	0,28	0,51	0,55	0,36	0,41	**0,42**	**0,10**		
	Rz(JIS)	2,19	3,14	3,54	3,66	3,27	**3,16**	**0,52**		
REF @ 240 Bars	**Ra**	1,39	0,95	1,51	1,07	1,37	**1,26**	**0,21**		
	Rz(JIS)	8,17	7,06	8,15	6,93	8,42	**7,75**	**0,62**		
1%wt Cloisite Ca++ Samples										
160 Bars	**Ra**	1,69	1,79	1,60	1,58	1,36	**1,60**	**0,14**	**1,56**	**0,10**
	Rz(JIS)	8,66	8,95	8,36	8,56	7,61	**8,43**	**0,45**	**10,71**	**0,98**
200 Bars	**Ra**	1,73	1,52	1,79	1,52	1,76	**1,66**	**0,12**	**1,75**	**0,06**
	Rz(JIS)	8,25	8,35	9,43	8,34	9,07	**8,69**	**0,47**	**9,28**	**0,39**
240 Bars	**Ra**	1,42	1,65	1,28	1,58	1,52	**1,49**	**0,13**	**1,29**	**0,11**
	Rz(JIS)	8,11	9,56	8,23	9,05	8,91	**8,77**	**0,54**	**9,02**	**1,10**
3%wt Nanofil 116 Samples										
160 Bars	**Ra**	Visibly unacceptable surface finish							**0,63**	**0,02**
	Rz(JIS)								**4,87**	**0,46**
200 Bars	**Ra**	2,64	2,02	1,64	2,08	2,27	**2,13**	**0,33**	**1,55**	**0,11**
	Rz(JIS)	23,42	13,81	12,49	18,33	17,87	**17,18**	**3,85**	**9,95**	**0,44**
240 Bars	**Ra**	Visibly unacceptable surface finish							**0,60**	**0,05**
	Rz(JIS)								**4,45**	**0,21**
									At 240 Bars	
8%wt Nanofil 116 Samples		Visibly unaccpetable surface finish					**X**	**X**	**1,58**	**0,16**
									12,26	**1,24**
12.5%wt Nanofil 116 Samples		Visibly unacceptable surface finish					**X**	**X**	**X**	**X**

With reference to the results for *Nanofil 116*, Ra showed declining results (from 1.65-to-1.75 microns) as green pressure switched from 160 to 200 bars and then improved (from 1.75 – 1.25 microns) as pressure changed from 200 to 260 bars. On the other hand, Rz consistently improved from 10.71-to-9.02 microns as the green compaction pressure increased through 160 – 200 – 240 bars. For the compaction pressures considered, best results for both Ra and Rz were obtained at 240 bars.

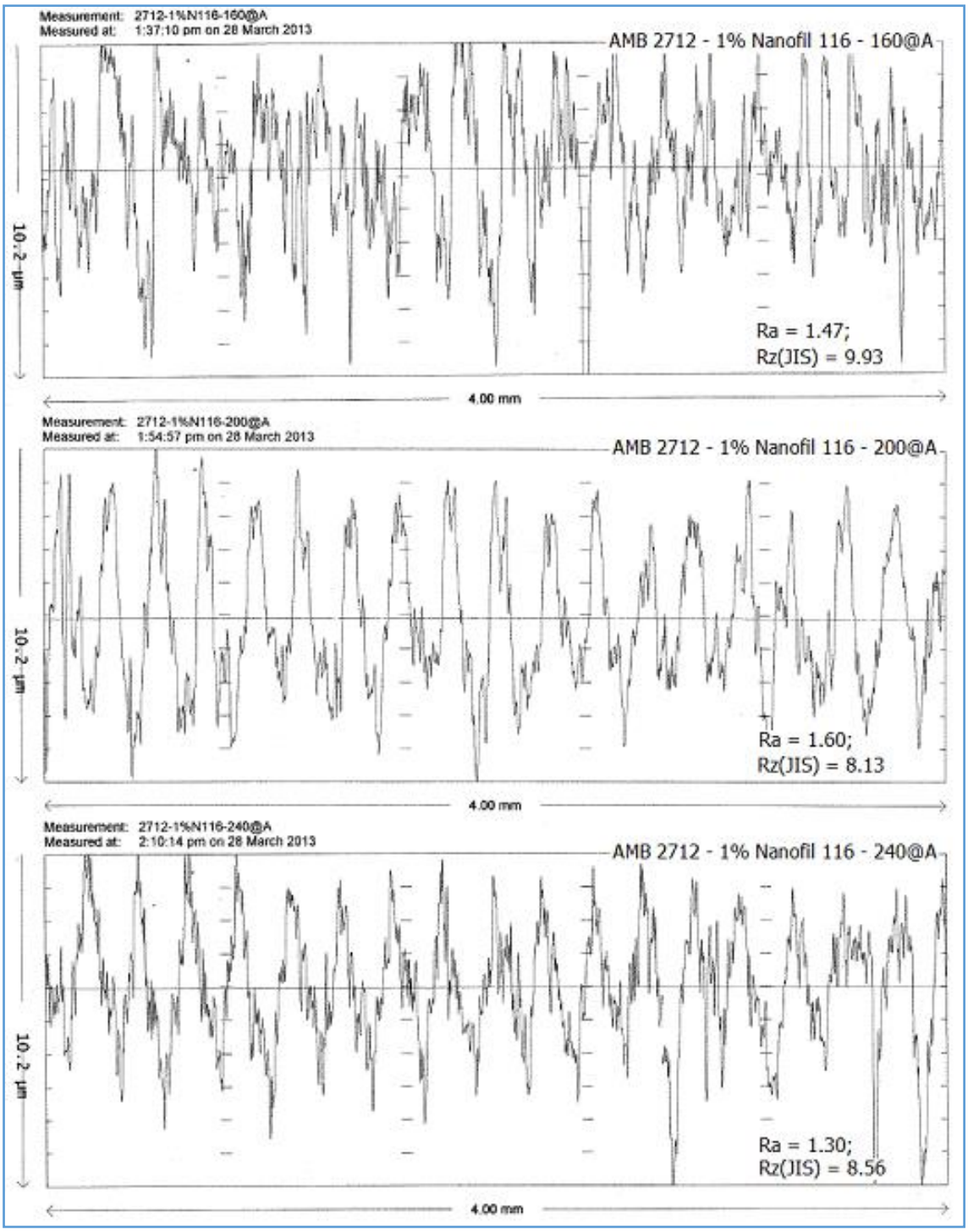

Figure 9-1(i): Sample machinability results for AMCs with 1%wt of *Nanofil 116*.

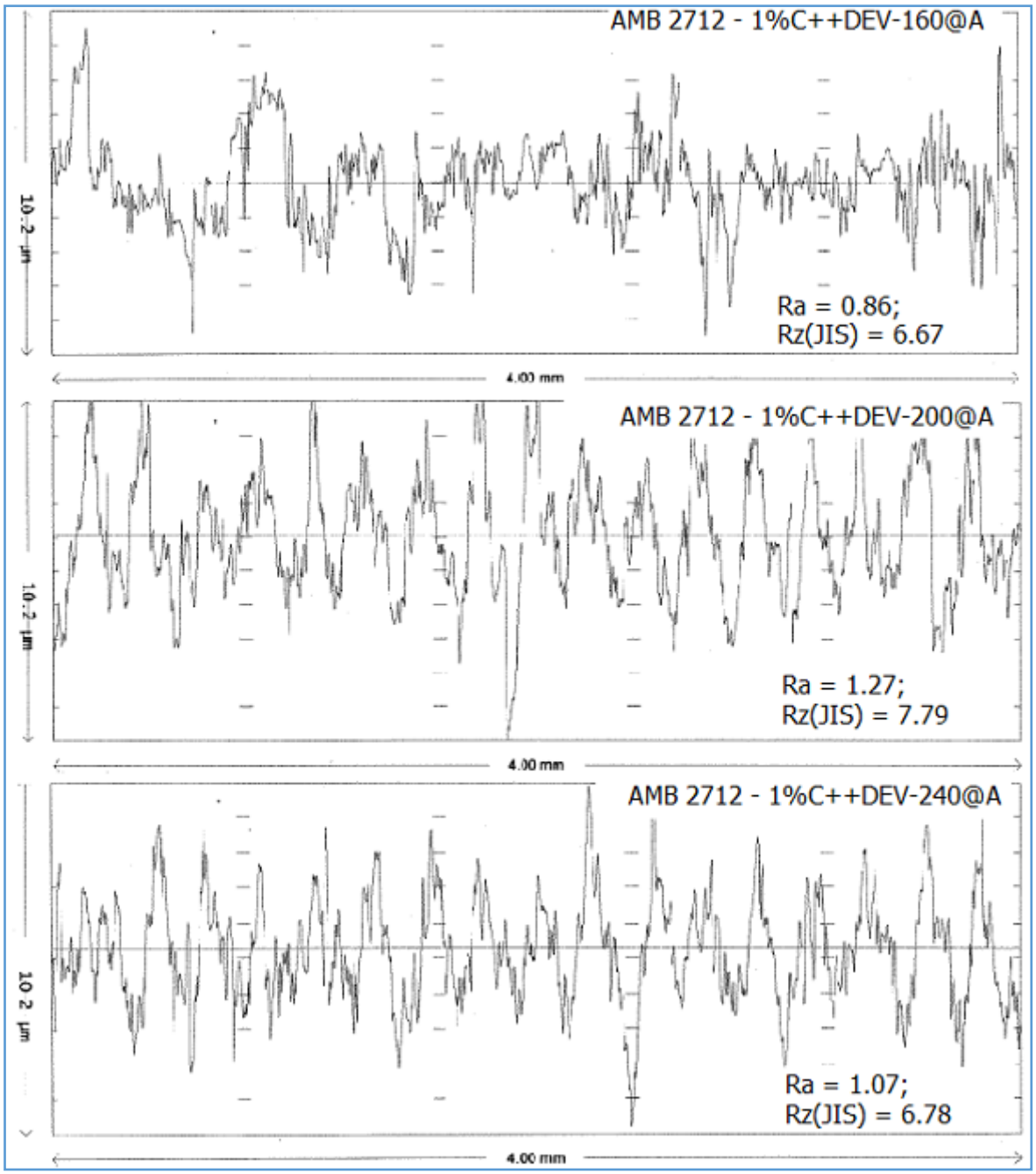

Figure 9-1(ii): Sample machinability results for AMCs with 1%wt of *Cloisite* Ca^{++} *DEV*.

Corresponding results for the samples with 1%wt *Cloisite Ca++DEV* indicated that both R_a and R_z declined as the pressure increased from 160 – 200 bars and then increased as the pressure increased from 200 – 240 bars. Best results according to R_a were obtained at 160 bars while Rz showed best results at 240 bars. Comparatively for 1%wt, same green compaction pressure, and datum sintering conditions, *Cloisite Ca++DEV* consistently posted better results than *Nanofil 116*.

As noted in the preceding chapter on machinability, increasing the %wt content of *Nanofil 116* from 1% to 3% generally improved the machinability results in terms of both Ra and Rz values irrespective of the green compaction pressure with an exception of Rz for 200 bars specimen (seemingly an outlier). To the contrary, comparable results for samples with 3%wt *Cloisite* Ca^{++}*DEV* and above were observed to be unreliably inconsistent due to exaggerated surface profile amplitudes (R_z), thereby necessitating the raising of scale from 10.2µm to 50.2µm on Y-axis as shown in *Figure 9-2*. *Nanofil 116* was noted to still give surface finish readings even at 8%wt content at the same reference compaction pressures, though at taken at amplitudes set at the scale of 20.3µm.

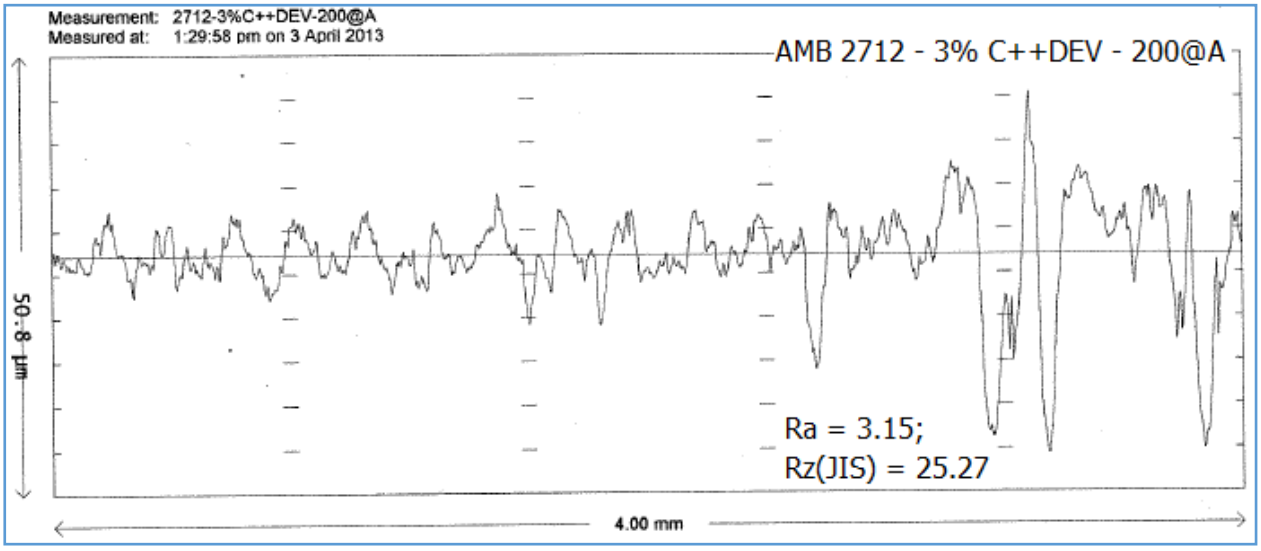

Figure 9-2: Machinability results for sample with 3%wt *Cloisite* Ca^{++}*DEV*.

Since the main difference between these nanoclays is in the quantity of quartz, it is hereby proposed that the poor performance of *Cloisite* Ca^{++}*DEV* above 1% wt content as reflected by especially high R_z values is most likely associated with formation of Si-based compounds with a knock-on-effect of embrittlement of the AMCs, bigger grains as a result of enhanced heat-transfer matrix, and therefore bigger holes being left after granular erosion during the machining process. This contention is in agreement with the observed deterioration of results for AMCs with *Nanofil 116* at much higher %wt contents, which would imply potential

existence of a threshold capacity of SiO_2 for the AMB-2712 and other aluminium alloys. Further investigation in this line may be helpful.

9.2 *Trial-Run* versus Set-*"A"-Run* (datum) sintering profile

For ease of reference, *Figure 9-3* represents these two sintering profiles under evaluation.

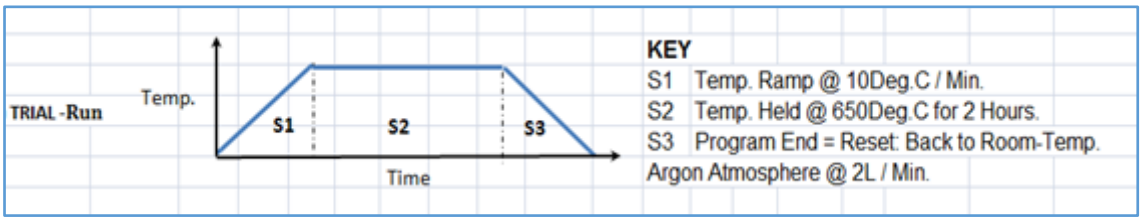

(i) General Reference *Trial-Run* profile

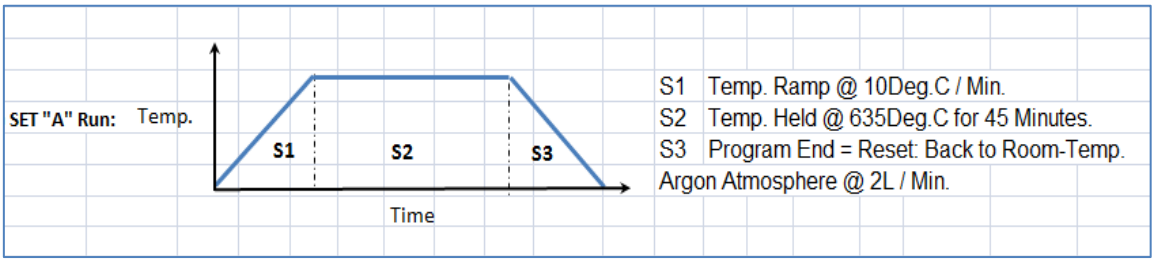

(ii) Datum Reference *Set-"A"-Run* profile.

Figure 9-3: Reference sintering profiles.

9.2.1 Physical Observations

Figure 9-4 (i), (ii), and *(iii)* show the top-, side-, and bottom-view of samples from the *Trial-run*, respectively. With reference to *Figure 9-4*, two observations were imminent. The *First Observation* relates to the cratering visible on the top surface (as highlighted in dotted white line in *Figure 9-4 (i)*). This indicates that there was physical mass transfer, which potentially implies some level of densification. The distortion can be assessed in terms of relative changes in both the diameter and height of the specimens. This phenomenon was evident when observing samples from the side-view images whereby the initial cylindrical profile was clearly

(i)			
	160 Bars	200 Bars	240 Bars
(ii)			
	160 Bars	200 Bars	240 Bars
(iii)	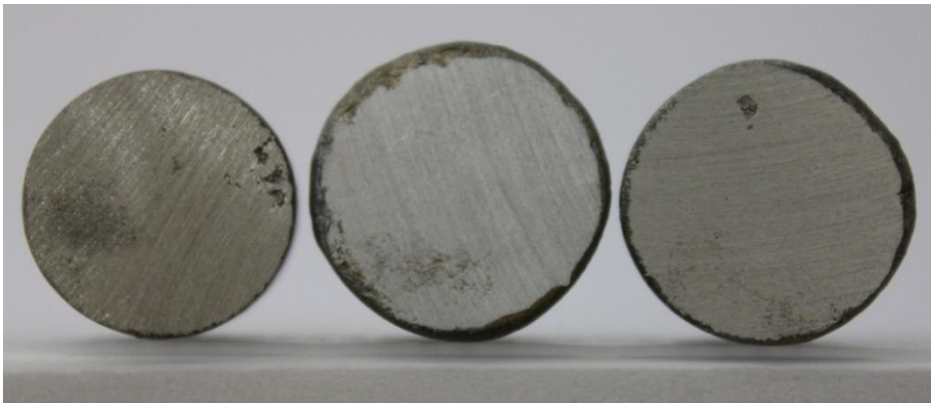		
	160 Bars	200 Bars	240 Bars

Figure 9-4: Trials Samples: (i) Top view, (ii) Side view, and (iii) Bottom view.

distorted especially the bulged base in the case of the 200 Bars and 240 Bars specimens. A quantitative measure of the distortion could potentially verify the proposed densification. Nonetheless, reference to both the top-view and side-view, which shows the surface area and depth of the cratering-patch respectively, was deemed to be a reasonable reflection of the extent

of mass transfer as well as the resultant effect of heat-transfer dynamics. This concept can be explored from two perspectives, viz, cratering and distortion.

A: Cratering

It was notable from the top-views that the cratering was not aligned to the central axis of the specimens' cylindrical profile. However, with reference to all the three specimens, exterior-boundaries of the craters were significantly aligned to the outer cylindrical wall or circumferential profile of the specimens while the interior-boundaries were curvilinear and depicting a somewhat similar but sequential progression. With reference to the dotted white lines in *Figure 9-4 (i)*, notice the acute-angled horn-like profiles as the interior boundaries cease being aligned to the circumferential profile. Similarly notice the wavy interior boundary: in the 160 Bars specimen, one wave is evident while in the 200 Bars specimen there are two waves. In the 240 Bars specimen, the second wave to the right seemed to have progressively disappeared and that zone was relatively the deepest.

Assuming that the heat energy was evenly distributed around the specimens, the observed profile and positioning of craters at the top surface of the specimen infers to three potential primary heat-transfer dynamics: *Firstly*, alignment of the crater's exterior boundary to the circumferential boundary of the cylindrical specimen suggests that heat transfer must had progressed from the exterior surface of the specimen towards the central axis, i.e. highest temperature located at the surface. This potentially caused localized melting (de-nucleation) of particles on the outermost surface with the resultant effect of progressive radial distribution of that thermal energy to the neighbouring particles. Ideally, this de-nucleation would arguably commence evenly throughout the surface area of the sample. Even though care was take in positioning the specimens inside the sintering furnace with approximately the same spacing from each other and from end-walls, the fact remains that they were all sitting inside a sintering boat made of a refractory ceramic material (Zirconia).

Besides the contact-interface between the boat's floor and the base of specimens, the thermodynamic interfaces represented by the space between the specimens' cylindrical wall and the boat's side-walls (≈ 1 mm), the space between specimens and end-walls (≈ 4.5 mm), and the space between any two adjacent specimens (≈ 4.5 mm) were all different. On the same note, the specimens' top-surfaces were exposed to the furnace's open space. As a result, the varied heat transfer dynamics across each interface and/or space cannot be expected to be the same. Accordingly the de-nucleation must have started at such a point or zone on the cylindrical surface that the temperature was differentially the highest, and then gradually conductively spread inwards to the neighbouring particles.

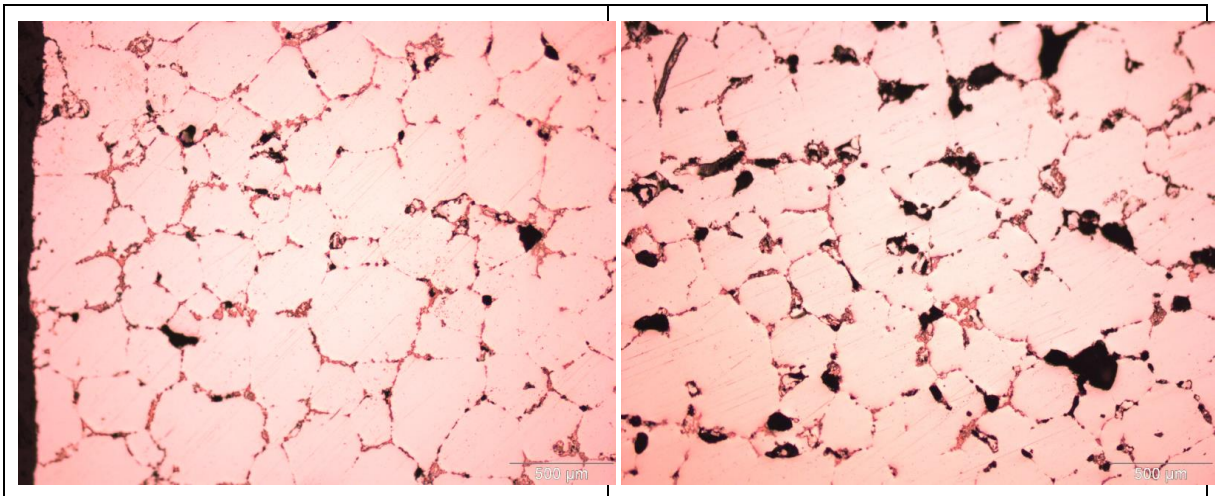

(i)	(ii)

Figure 9-5: Microstructure of 160 Bars specimen sintered under *Trial-Run* settings and viewed at: (i) Edge of Cylindrical wall, and (ii) Central Axis.

In support of this contention, *Figure 9-5* (i) and (ii) shows the microstructure of trial specimen previously compacted at 160 Bars and viewed at the mid-section of the edge of cylindrical wall and at the central axis, respectively. Both images were taken in the mid-zone along the height of the specimens. Image (i) depicts a relatively greater level of inter-particle fusion compared to image (ii) which is characterized by a visibly higher level of porosity. This observation was consistent across all the *Trial-run* specimens irrespective of the green compaction pressure.

However, this contrast was not easily discernible from the specimens processed under *Set-"A"-run* specimens due to relatively higher levels of porosity as seen in the corresponding images in *Figure 9-6 (i)* and *(ii)* for 160 Bars specimen.

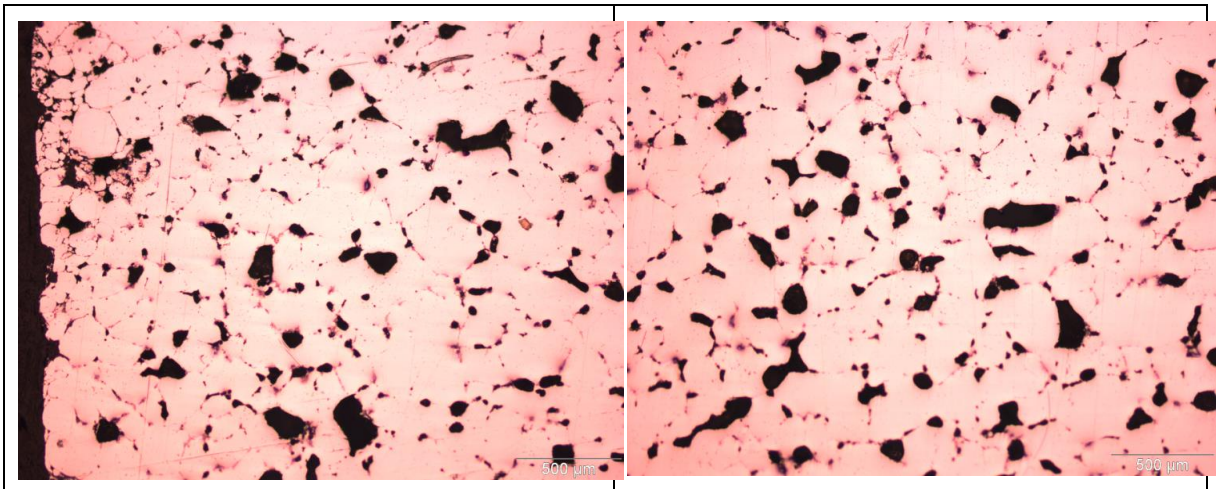

(i) Edge	(ii) Central

Figure 9-6: Microstructure of 160 Bars specimen sintered under *Set-"A"-run* settings and viewed at: (i) Edge of Cylindrical wall, and (ii) Central Axis.

Secondly, since there was relatively nothing in close proximity to the top-surfaces, heat transfer from the furnace through the specimens' top-surfaces must have been relatively higher compared to the specimens' cylindrical walls and bases that were bordering refractory material of the sintering boat's walls and floor, respectively. This partly explains the cratering being on the specimens' top-surfaces.

Thirdly, the role of gravity at macroscopic level, especially in a semi-solid phase cannot be ignored. Assuming an evenly distributed capillary pressure at a solid-liquid interface and holding all other factors constant, a grain surrounded by a liquid phase would tend to flow downwards due to gravitational pull.

These three mechanisms imply the specimen's highest possible temperature to have been at a point or zone located at the right-angled corner between a specimen's top surface and cylindrical wall. These mechanisms synergistically partly explain the signature profile and

depth of craters, and the resultant bulging at the base of specimens. Secondary contributory factors may include the geometry of specimens, which may typically affect the distribution of inter-particle thermal stresses as well as thermally-induced bulk hoop stresses.

B: Distortion

The relative proportion of solid- and liquid-phase in the specimens most likely affected the extent of distortion. With reference to Al-Cu binary phase diagram [218, 219], the cause for this distortion was most likely the fact that, at 650^0C, the particulate matrix was already exiting the supersolidus liquid phase sintering temperature range, thereby entering into the liquidous phase. As much as this has some inference to the distortion, the fact that the three specimens had been subjected to the same temperature profile would dictate their having the same extent of distortion. Since this was not the case, an insight into the processing variables would be helpful, hence the *Second Observation*.

Based on the noted relative cratering and distortion, and the fact that their composition and sintering parameters were the same, it was evident that the green compaction pressures had a significant effect on the final sintered product. With reference to the three sets of images in *Figure 9-4*, the greatest physical profile distortion was depicted by the specimen previously compacted at 200 Bar, while the least distortion was evident on the 160 Bar specimen. Since all the three specimens were sintered in the same space in one run for the same duration of time, it is hereby contended that the variation in the degree of distortion may partly be attributable to the dependence of heat-flow-matrix on the degree of particulate agglomeration and/or compaction, i.e. the green density.

Figure 9-7 shows the side view of Reference specimens as compared to specimens having varying contents of *Cloisite* Ca^{++}*DEV*. The features were similar to those observed in the case of specimens having varying contents of *Nanofil 116* except that no physically discernible

REF			
	160 Bars	200 Bars	240 Bars
1%C			
	160 Bars	200 Bars	240 Bars
3%C			
	160 Bars	200 Bars	240 Bars
8%C			
	160 Bars	200 Bars	240 Bars
12.5%C			
	160 Bars	200 Bars	240 Bars

Figure 9-7: Side view of *Set "A" Run* specimens showing effect of *Cloisite* Ca^{++}*DEV*.

cracks were observed in all the *Nanofil 116* specimens irrespective of the nanoclay's contents. The cause(s) of cracking observed in specimens containing 8%wt. *Cloisite* Ca^{++}*DEV* and yet not observed in the specimens containing a relatively higher content (12.5%wt.) of the same nanoclay is still not understood.

9.2.2 DSC-TGA Results

9.2.2.1 Implications on thermal behaviour

Figure 9-8 shows heat flow profiles for the randomly selected *Trial-run* samples 1 and 2 respectively as a function of green compaction pressure. The results were consistent for both of the samples, indicating that heat-flow was partly a function of green compaction pressure. It was evident that the correlation between heat-flow and green compaction was not a proportionate one. Samples from specimen previously compacted to 200 Bars showed a relatively higher order of heat flow than the 160 and 240 Bars specimens. In fact, results for the 200 Bars specimens seemed to be generative of heat energy unlike the 160 Bars and 240 Bars sample which represent typical endothermic processes. This observation was consistent with the level of geometrical distortion and cratering of the 200 Bars specimen.

Disregarding the samples' reference numbers, the 160 Bars samples generally showed better thermal behaviour than the 240 Bars specimens. There was better consistency in results for the 160 Bars specimen, depicting a common temperature of 514^0C at the first phase change, and a melting temperature of 645^0C with a variation of 0.6^0C for the two samples. This interpreted to a 6.7% disparity in heat flows for the two samples. Corresponding heat flow disparity between the two respective samples was 73% and 11% for the 200 and 240 Bars specimens, respectively. With reference to the second law of thermodynamics and holding all other factors constant, the implications of this superior heat flow rate would be an increase in localized entropy at both macroscopic and microscopic level per unit time [243, 245]. This partly explains the relatively greater distortion sustained by the 200 Bar specimens compared to 160 and 240 Bars specimens.

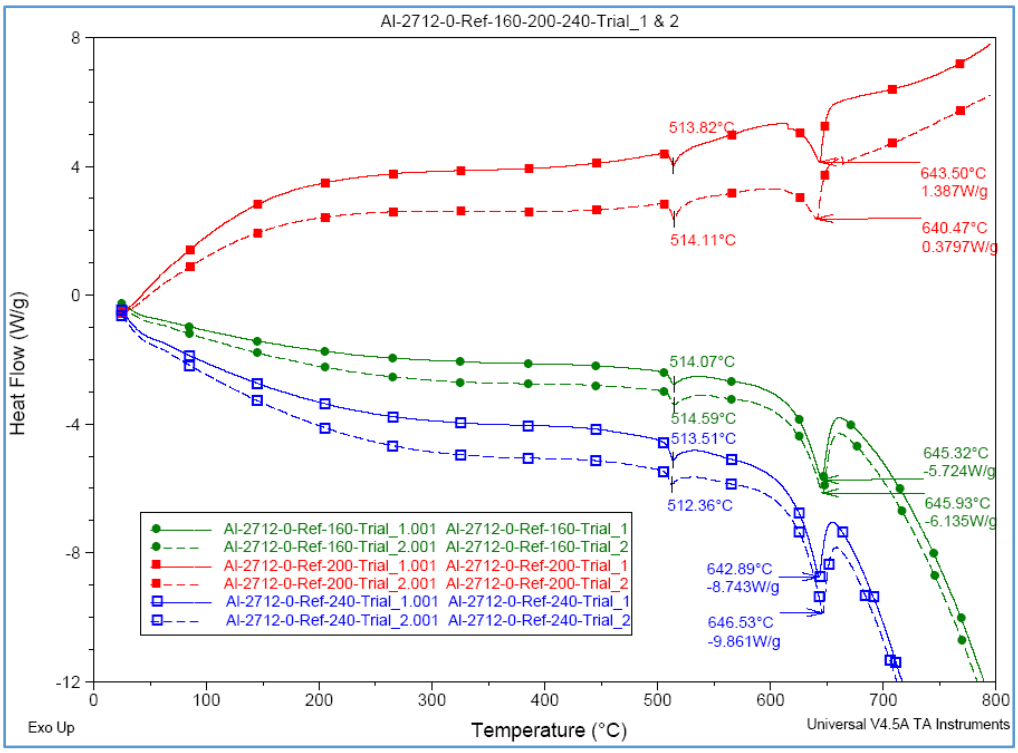

Figure 9-8: Heat flow results for *Trial-run* reference samples as a function of Green Compaction Pressure.

In general, the average melting temperatures seemed to increase with the increase in green compaction pressure, i.e. 646.3^0C at 160 Bars, 646.8^0C at 200 Bars, and 648.3^0C at 240 Bars; an overall increase of 2^0C. This trend is fully supported by the microstructure of the specimens as shown in *Figure 9-9 (i) – (iii)*. From these images however, it cannot be determined what proportion of the reduced porosity may be attributed to the effect of green compaction pressure on inter-particle voids on one hand, and the effect of improved heat flow on the other.

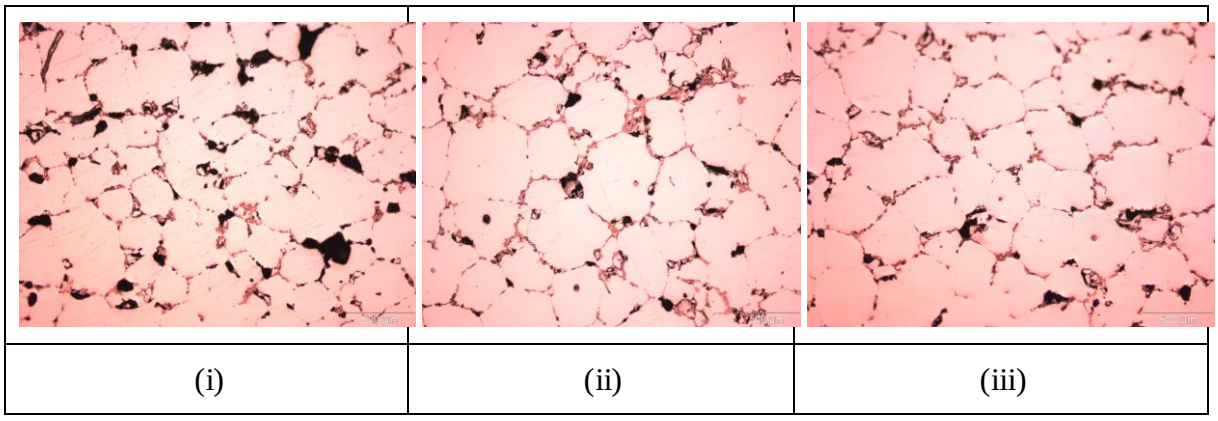

Figure 9-9: Microstructure at central Axis for *Trial-run* specimens previously compacted at: (i) 160 Bars, (ii) 200 Bars, and (iii) 240 Bars.

Of the three green compaction pressures experimented with, it was observed that the 160 and 240 Bars specimens generally produced consistent heat flow patterns irrespective of the sintering profile settings (*Trial-run* or *Set-"A"-run*). *Figures 9-10 (i), (ii)* and *(iii)* shows comparative results for samples from the 160, 200, and 240 Bars specimens respectively as processed using the two sintering profiles. With focus on the melting temperature zone, *Table 9-2* shows a summary of performance indicators from the three graphs. The % disparity in heat flow between the respective pair of samples is calculated on basis of absolute values while the difference in melting temperatures is as determined at the peak representing transition to liquidous phase.

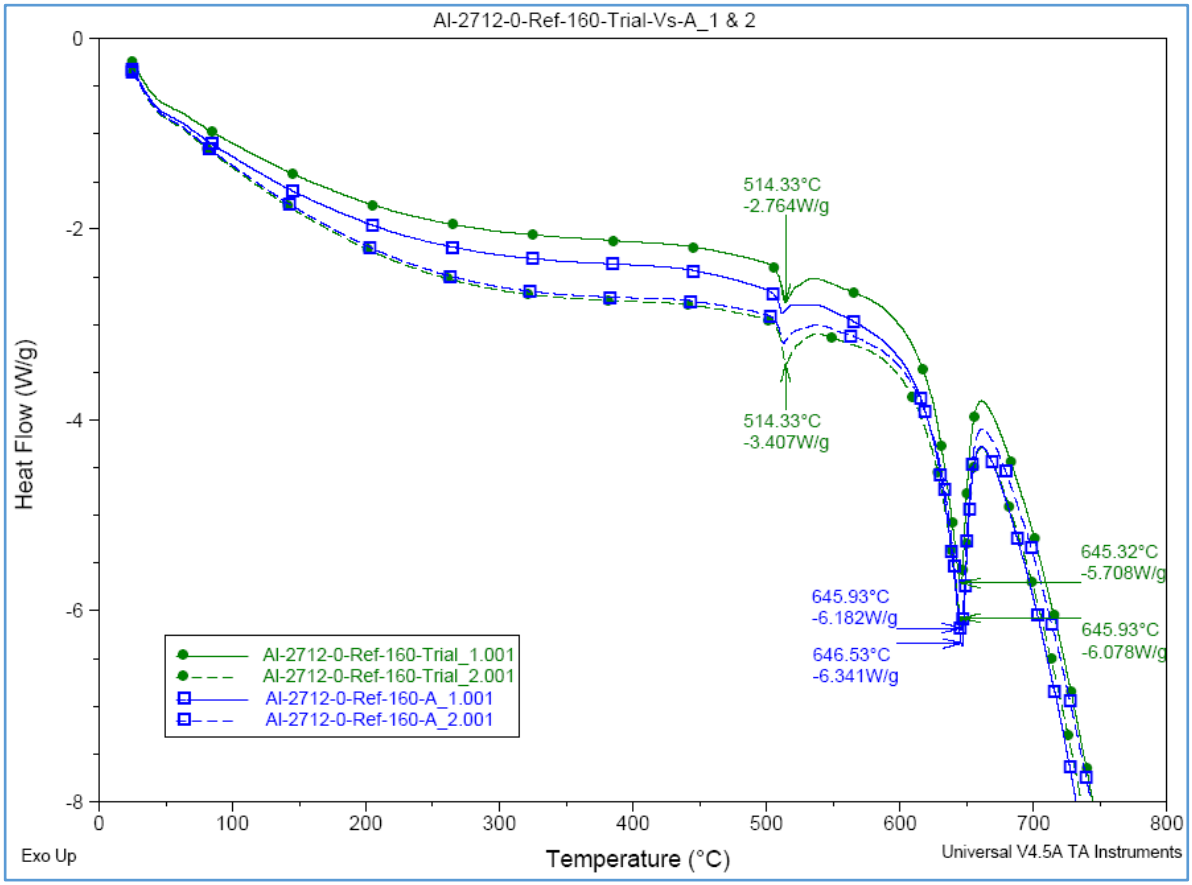

Figure 9-10: (i)

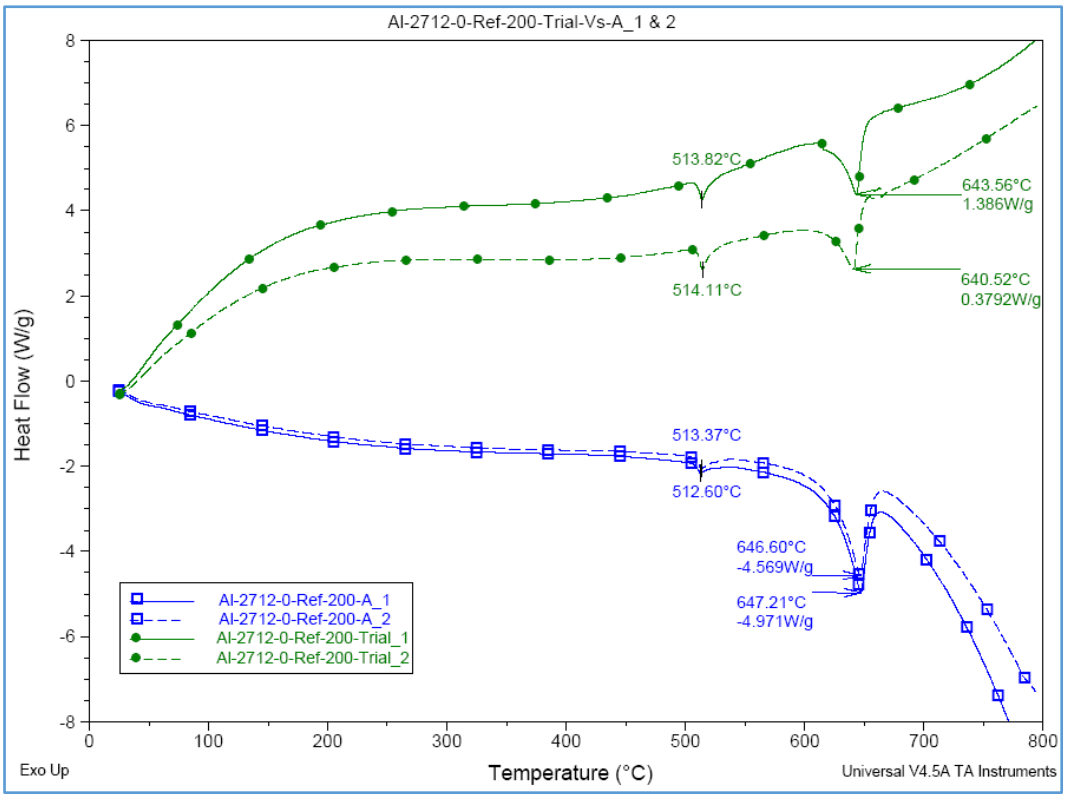

(ii)

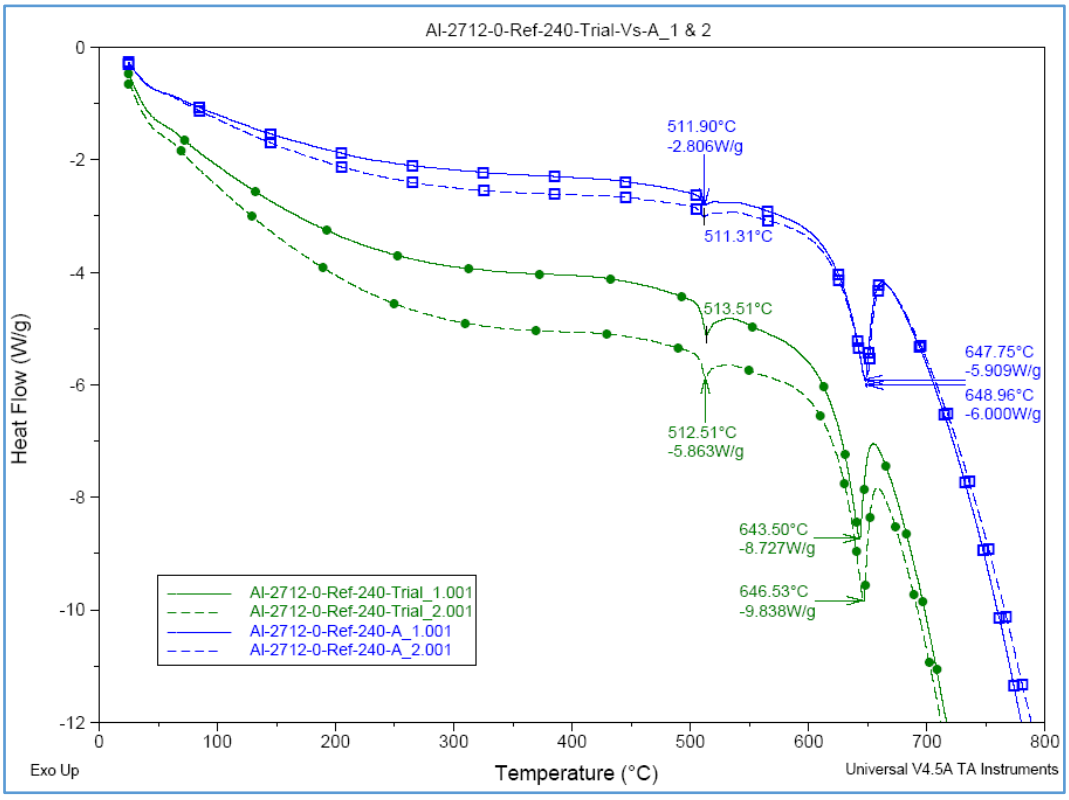

(iii)

Figure 9-10: Effect of sintering profiles on thermal behaviour of specimens previously subjected to: (i) 160, (ii) 200, and (iii) 240 Bars of compaction pressure.

Table 9-2: Summary of key performance indicators for Graphs in *Figure 9-10: (i) – (iii)*.

	Trial-Run		Set-"A"-Run		Average	
Green Compaction Pressure	% Heat-Flow Disparity	Diff. in Melting Temp. (^{0}C)	% Heat-Flow Disparity	Diff. in Melting Temp. (^{0}C)	% Heat-Flow Disparity	Diff. in Melting Temp. (^{0}C)
160 bars	6.1	0.6	2.5	0.6	**4.3**	**0.6**
200 Bars	72.6	3.0	8.0	0.6	**40.3**	**1.8**
240 Bars	11.3	3.0	1.5	1.2	**6.4**	**2.1**
Average	**33.8**	**2.2**	**4.0**	**0.8**		

Two observations were prominent in terms of sintering process parameters and the green compaction pressure. *Firstly*, on average heat flow basis, *Trial-run* settings showed 5.7% better thermal barrier properties on the 160-Bar specimen than the *Set-"A"-run* settings. However, this represents a disparity of 6.1% between the *Trial-run* samples compared to a 2.5% disparity between *Set-"A"-run* samples. This behaviour was similarly observed with samples from the 200 Bars specimens that showed a disparity of 72.6% and 8% for the Trial-run and Set-"A"-run samples respectively. In contrast to this trend, the 240 Bars specimens showed 35.8% better thermal barrier properties in the *Set-"A"-run* samples than the *Trial-run* samples. The corresponding disparity between the respective pair of samples' heat-flows was 1.5% and 11.3% respectively. It can therefore be deduced that the *Trial-run* set of processing parameters exhibit a relatively greater sensitivity (hence less thermal stability) to variations in the green compaction pressure in comparison to *Set-"A"-run* processing parameters.

Secondly, it was also observed that, for the same green compaction pressure, there was disparity / sensitivity in thermal barrier properties in response to variation in sintering profile settings. On average, the 240 Bars samples showed 86.7% improvement in thermal stability when sintered under *Set-"A"-run* settings compared to those sintered under *Trial-run* settings. Corresponding improvement for samples from the 160 Bars specimens was 59%. It may

therefore be argued that the observed reversal of thermal barrier performance between the 160 and 240 Bars sets of samples was as a result of the alluded favourable insensitivity of *Set-"A"-run* processing parameters to variations in green compaction pressure.

In general, it was evident from the graphs and summarized results that *Set-"A"-run* sintering profile settings were more reliable in terms of less disparity in results across the varying green compaction pressures. It was also observed that the 160 Bars specimen recorded the least average disparity in results as the sintering profile settings were switched between *Trial-run* and *Set-"A"-run* settings. In a manufacturing scenario, this low disparity would interpret to a better consistency in the quality of production outputs as well as less vulnerability to process controls.

9.2.2.2 Implications on control-weight

Results for weight variation as a function of temperature, green-compaction pressures, and the sintering process settings gave an insight into operational stability of the *Nanofil 116*-AMCs material system. *Figure 9-11 (i)* and *(ii)* shows the effect of sintering process settings on weight variation as a function of temperature and green compaction pressure. It was not clearly understood as to what could have caused the consistent sudden percentage weight loss in samples from the 200 Bars *Trial-run* specimen at 615^0C and 663^0C. The general trend was similar to that for heat flow, whereby samples from the 200 Bars specimen showed higher values than those from the 160 and 240 Bars specimens. However, the disparity of results between the two test samples for 200 Bars specimen was also adversely the largest at 1.36%. It was similarly observed that the 160 Bars specimen consistently had relatively less percentage weight loss than the 240 Bars specimen irrespective of the sintering profile settings.

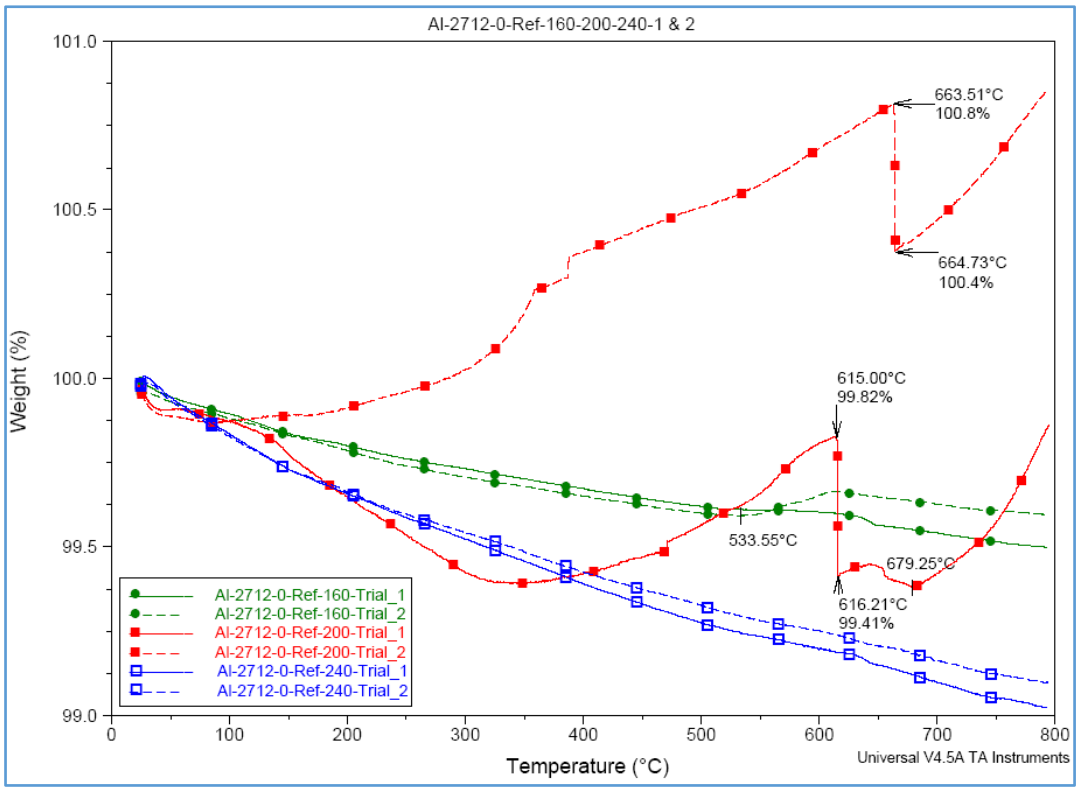

(i)

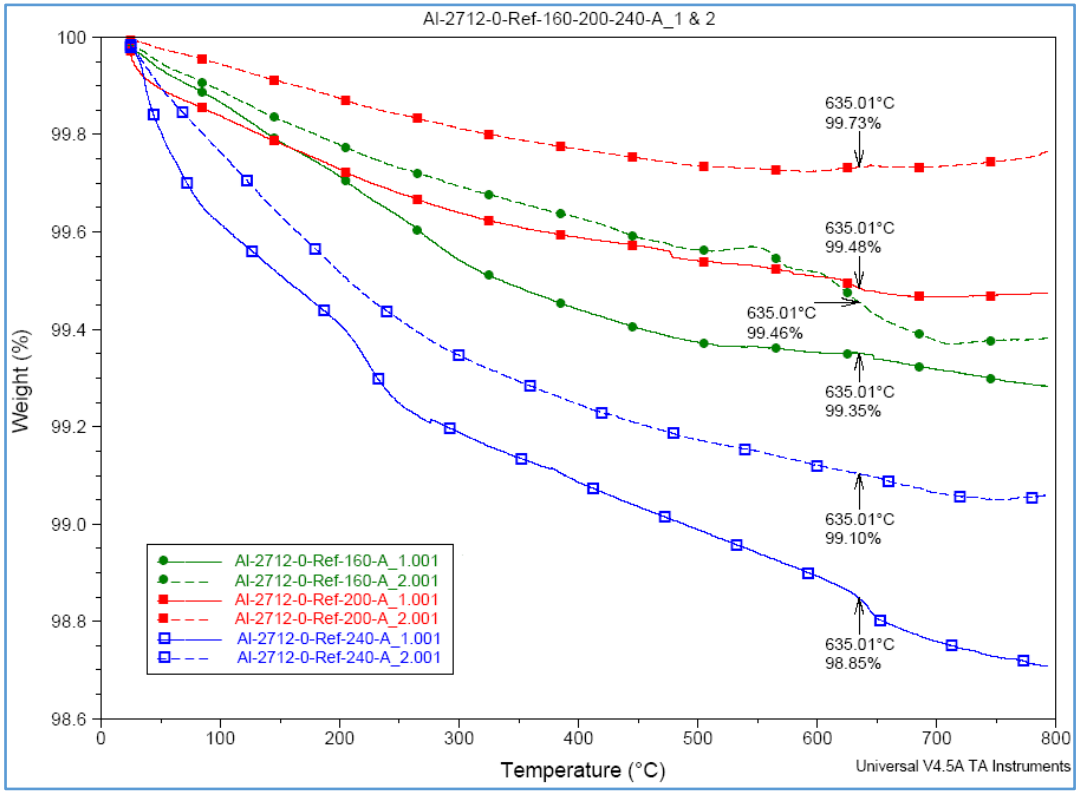

(ii)

Figure 9-11: Effect of green compaction pressure and temperature on specimens sintered using: (i) Trial-run, and (ii) Set"-A"-run profile settings.

A summary of quantitative data from these graphs is shown in *Table 9-3* with reference to properties recorded at 635^0C. It can be seen that the least variation in percentage weight loss between the tested pair of samples for each specimen was observed in *Trial-run* specimens with a negligible difference of 0.01%, i.e. 0.05% and 0.06% weight loss for the 240 and 160 Bars respectively. With the *Set-"A"-run* specimens, samples from the 160 Bars specimens showed the least disparity in weight loss, while samples from the 200 and 240 Bars specimens equally showed more than twice as much disparity in percentage weight loss. These results reinstate the supremacy of using 160-Bar as the preferred green-compaction pressure. Nonetheless, this is subject to evaluation of the effects of nanoclays addition into the portfolio of variables.

Table 9-3: Percentage Weight Loss (%) at 635^0C.

	Trial-Run Samples			Set-"A"-run Samples		
Compaction Pressure / Sample Ref. No.	1	2	Diff.	1	2	Diff.
160 Bars	0.41	0.35	0.06	0.65	0.54	0.11
200 Bars	0.56	-0.8	1.36	0.52	0.27	0.25
240 Bars	0.83	0.78	0.05	1.15	0.90	0.25

9.2.3 Machinability

Table 9-4: Surface finish results for *Trial-Run* and *Set-"A"-Run* reference samples.

REFERENCE SAMPLES		Quantified Surface Finish values (µm)						STD. DEV.
		1	2	3	4	5	AVERAGE	
Trial-Run REF Samples								
REF @ 160 Bars	**Ra**	0,81	0,89	0,80	0,76	0,83	**0,82**	**0,04**
	Rz (JIS)	6,73	6,48	4,81	5,26	5,34	**5,72**	**0,86**
REF @ 200 Bars	**Ra**	0,85	0,86	0,75	0,82	0,73	**0,80**	**0,05**
	Rz (JIS)	6,59	6,34	5,29	6,67	5,90	**6,16**	**0,51**
REF @ 240 Bars	**Ra**	1,22	1,47	1,42	1,45	1,47	**1,41**	**0,09**
	Rz (JIS)	8,27	9,02	8,44	9,76	8,86	**8,87**	**0,52**
Set-"A"-Run REF Samples								
REF @ 160 Bars	**Ra**	0,47	0,52	0,66	0,34	0,42	**0,48**	**0,11**
	Rz(JIS)	4,82	4,55	5,10	2,95	3,93	**4,27**	**0,77**
REF @ 200 Bars	**Ra**	0,28	0,51	0,55	0,36	0,41	**0,42**	**0,10**
	Rz(JIS)	2,19	3,14	3,54	3,66	3,27	**3,16**	**0,52**
REF @ 240 Bars	**Ra**	1,39	0,95	1,51	1,07	1,37	**1,26**	**0,21**
	Rz(JIS)	8,17	7,06	8,15	6,93	8,42	**7,75**	**0,62**

Table 9-4 shows the surface finish results for Trial Run and Set-"A"-Run reference samples, while *Figure 9-12* shows samples of the machinability test results as printed out. It was observed that as Set-"A"-Run specimens generally posted better surface finish results that the Trial Run specimens irrespective of the green compaction pressure.

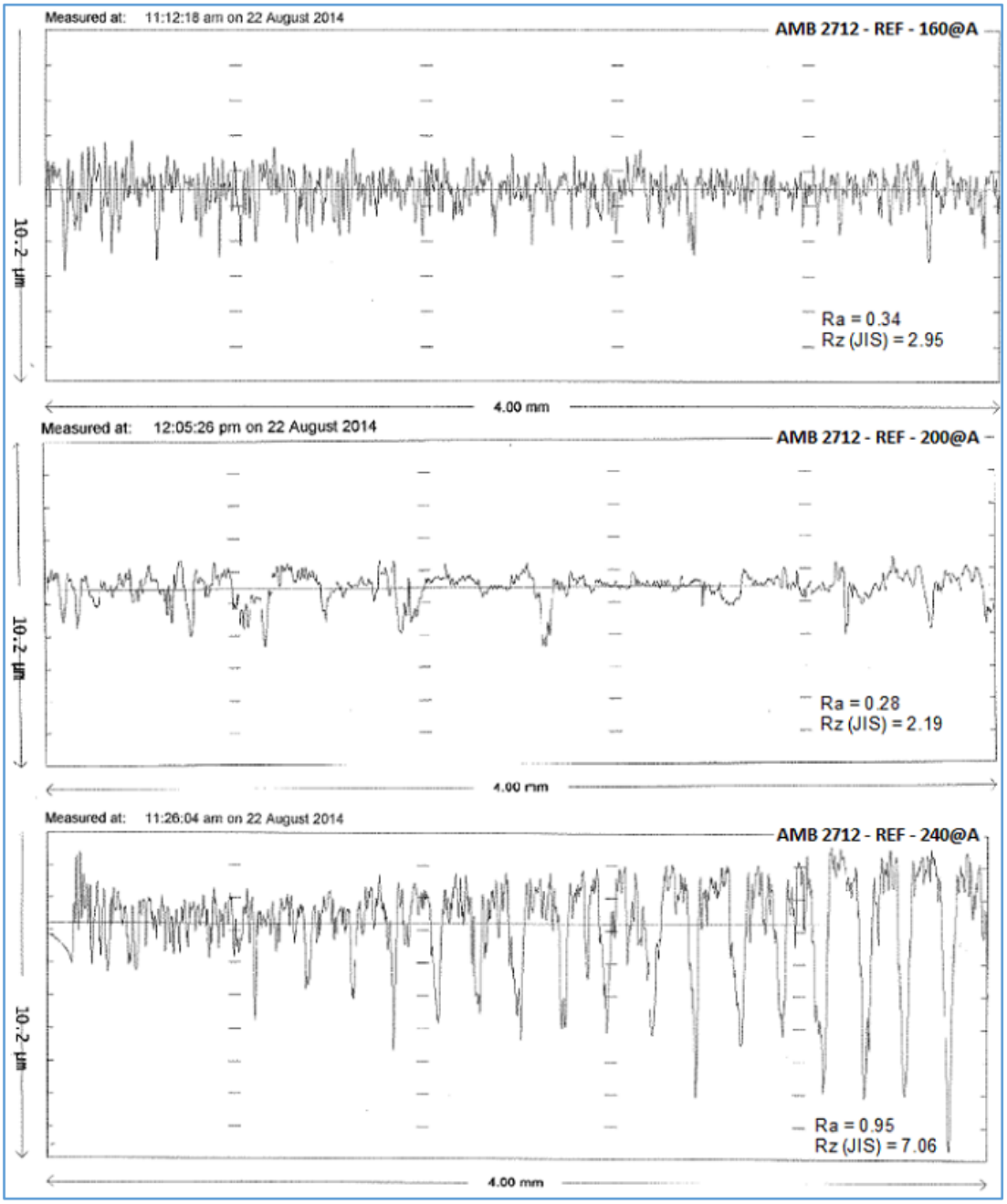

Figure 9-12 (i)

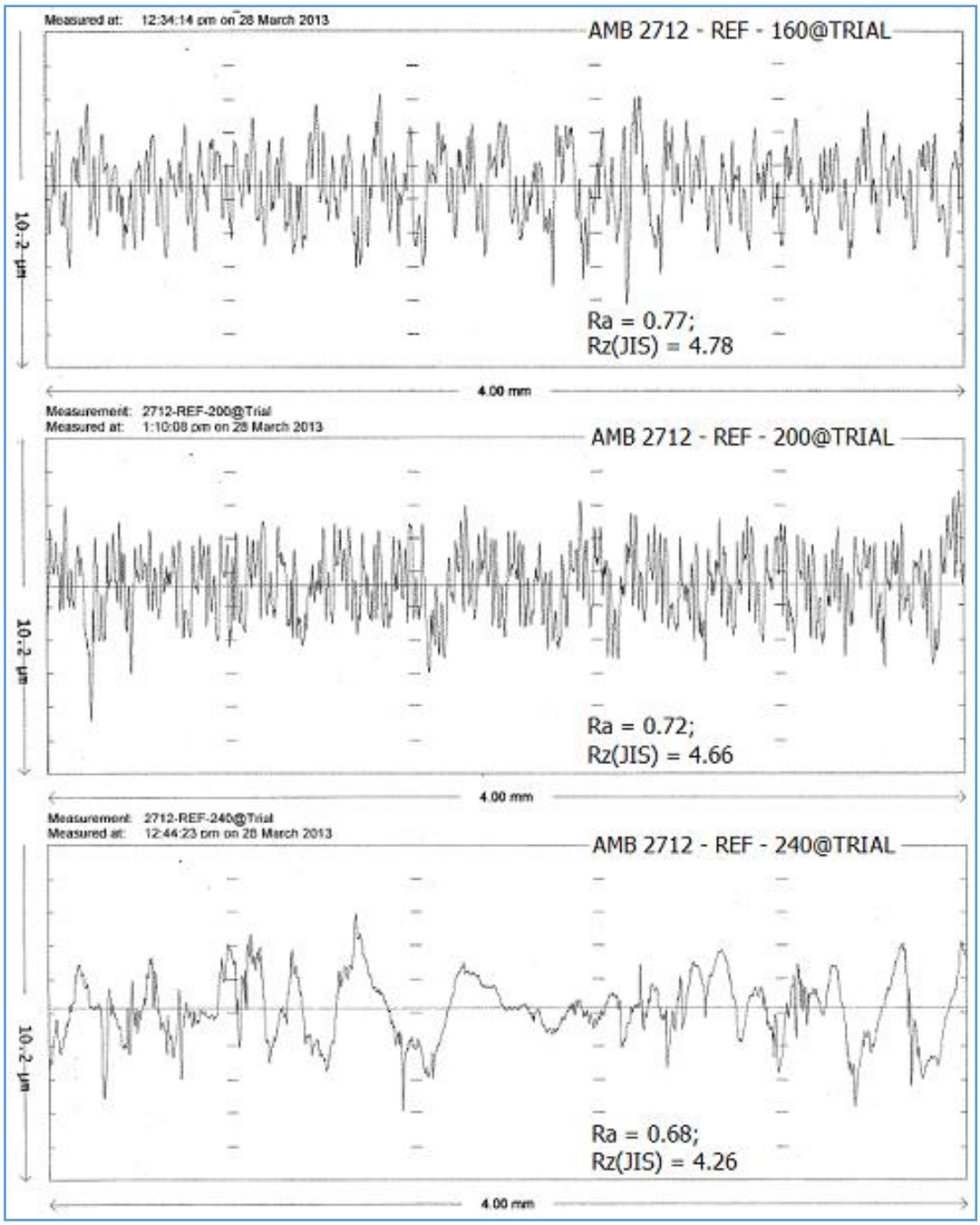

(ii)

Figure 9-12: Sample machinability results for *Trial-Run* samples.

9.3 Optimization of processing parameters

9.3.1 Overview

Table 9-5 shows the different sintering temperature profiles and atmospheres that were experimented with and their corresponding specimens. The series of iterative sintering attempts were motivated by a line of thought trailing a sequence of inquisitive queries that then directed

selection of parameters for the succeeding sintering attempt. Since the datum sintering profile (*Set-"A"-Run* in argon atmosphere) had resulted into sufficiently sintered specimens, the chosen starting point for the iterative process encompassed using the same temperature profile but with nitrogen as the sintering atmosphere. For ease of reference, the datum conditions are shown here as *Step 0*.

Table 9-5: Sintering conditions optimization process.

<table>
<tr><th>STEP</th><th>SINTERING PROFILE & NOTATION</th><th>LINE OF THOUGHT & ACTIONS</th></tr>
<tr><td rowspan="2">0</td><td colspan="2"> 

<table>
<tr><th>Sintering Process Profiles</th><th>S1</th><th>S2</th><th>S3</th><th>Sintering Atmosphere</th></tr>
<tr><td>Set "A" Run</td><td>10⁰ C /Min.</td><td>635⁰C x 45 Minutes</td><td>Prog. End to Room Temp.</td><td>Argon @ 2L/Minute</td></tr>
</table></td></tr>
<tr><td>Results: Batch 1
 
Top View
 
Side View</td><td>Query:
What impact would the sintering atmosphere and holding time have on these Nanofil 116-AMCs?

Action:
Varied the sintering atmosphere to Nitrogen and increased the holding time to 2 hours, i.e. Set-"AA"-Run profile.</td></tr>
</table>

	Results: **Batch 2**  	**Secondary Querry:** Does size matter?
1	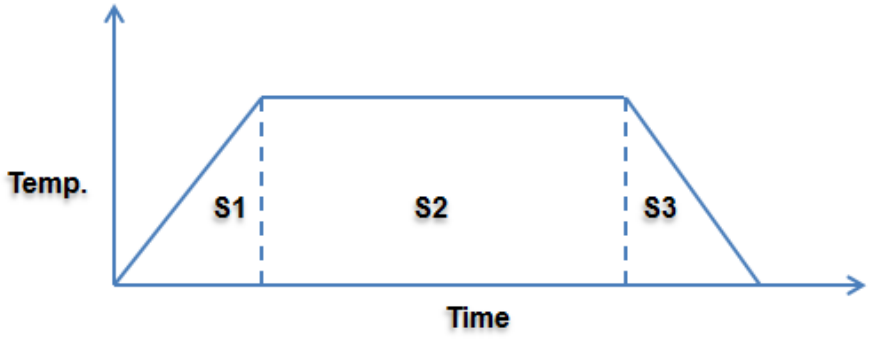 **Sintering Process Profiles** | **S1** | **S2** | **S3** | **Sintering Atmosphere** Set "AA" Run | 10^0 C /Min. | 635^0C x 2 Hours | Prog. End to Room Temp. | Nitrogen @ 2L/Minute	
	RESULTS  	**Notes:** Specimen looked physically alright, but after sectioning, it showed signs of incompletely fused particles as depicted by fractured surfaces and ease of breakage by bare hands. Rough gliding of specimen led to disintegration of the ground part into powder. **Further Characterization: YES**
	NEXT STAGE	**Query:** What impact would increasing the green compaction pressure have on the problem of incomplete fusion of particles?

		Action: Tried sintering samples compacted to 525 bars while maintaining the sintering profile Set-"AA"-Run and Nitrogen atmosphere at 2L/minute.
	RESULTS  REF @525 Bars @AA @Nitrogen	**Notes:** Specimens looked physically alright and significantly sintered. No cracks were observed. Upper diameter of both specimens looked slightly smaller than the bottom diameter, thereby making the originally cylindrical walls look tapered. Additionally, the entire top surface of both specimens showed slight, though evenly distributed, sulking from the edges to the central axis. This was perceived to be reflective of some sort of densification dynamics. **Further Characterization: YES**
	 1%wt @525 Bars @AA @Nitrogen	**Notes:** Physically, the specimens looked almost alright, significantly sintered, and cracked near the upper end of cylindrical wall. Geometry was intact. Different shades of colour were observed on both specimens. At the onset, the cracking was associated to the effect(s) of *Nanofil-116* on the AMC at chemical level and/or as a result of its impact on the heat-flow-matrix. **Further Characterization: YES**
	 2%wt @525 Bars @AA @Nitrogen	**Notes:** Specimens significantly cracked but still seemingly sintered.

<table>
<tr>
<td></td>
<td> 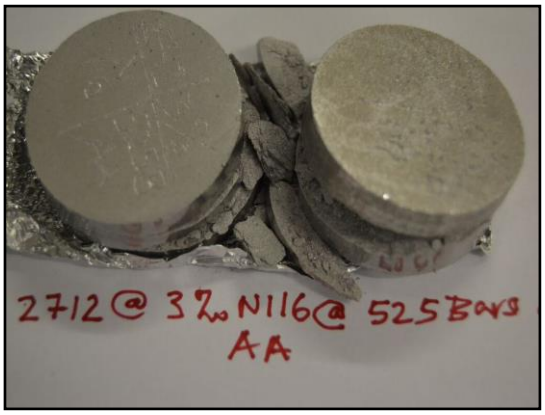

3%wt
@ 525 Bars
@ AA
@ Nitrogen</td>
<td>Notes:
Specimens looked heavily cracked and not sintered. Their sintering cycle was stopped after about 1 hour as the furnace-tube's exit cover opened up by default. This was attributed to observed clogging of the exit-over's hole by what seemed to be accumulated remains on acrawax as a result of delubrication.</td>
</tr>
<tr>
<td></td>
<td rowspan="2">NEXT STAGE</td>
<td>Query:
What impact would lowering the green compaction pressure have on the problem of observed cracking?</td>
</tr>
<tr>
<td></td>
<td>Action:
Tried sintering samples compacted to 350 bars while maintaining the sintering profile Set-"AA"-Run and Nitrogen atmosphere at 2L/minute.</td>
</tr>
<tr>
<td></td>
<td> 

REF
@ 350 Bars
@ AA
@ Nitrogen</td>
<td>Notes:
Specimen looked physically alright, significantly sintered, and having different shades of colour. No cracks were observed. These colours were suspected to be reflective of different stages of the delubrication process of the specimen, with black shades representing fully burnt out acrawax binder while the transition of shades from black to lighter tones being reflective of the specimen's temperature gradient and hence the direction of effective delubrication.</td>
</tr>
</table>

Notes:

The specimen looked physically alright, significantly sintered, having uniform colour distribution, but seemingly cracked at the bottom end of the cylindrical wall. The absence colours compared to the reference sample was attributed to possible higher thermal conductivity through the specimen, thereby resulting in effective delubrication.

Further Characterization: YES

NEXT STAGE

Query:

What impact would a delubrication stage and lower heating rate have on the persistently observed cracking and/or sinterability of the Nanoclay-AMCs?

Action:

Tried sintering samples compacted to 350 bars using a new sintering profile Set-"AB"-Run (lower heating rate from 10^0C to 5^0C) and Nitrogen atmosphere at 2L/minute.

3

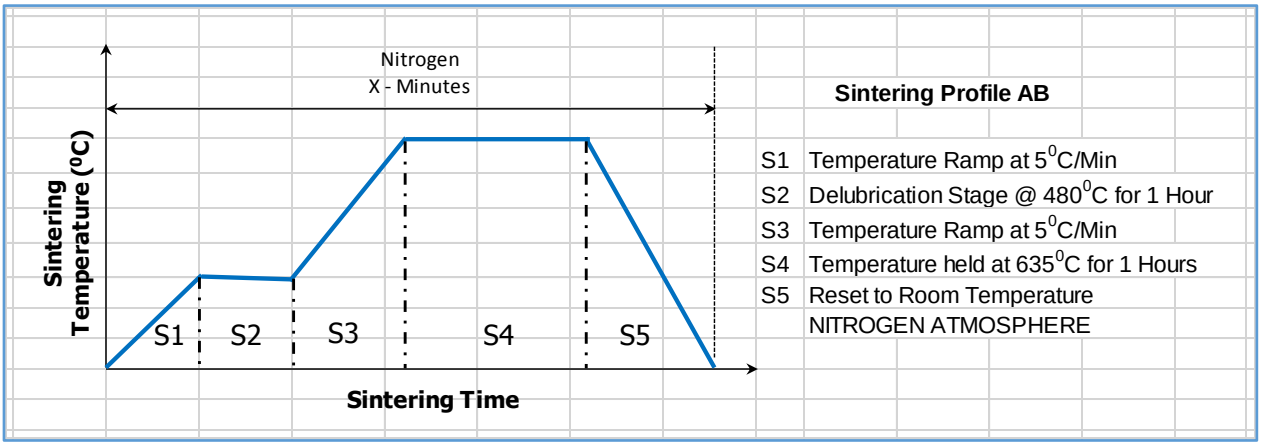

RESULTS

Notes:

The specimen looked physically alright, significantly sintered, but having varying shades of colour. As in previous specimens, the variation in colour shades was attributed to heat-flow-gradient and efficiency of the delubrication process. For the

	 1%wt @ 350 Bars @ AB @ Nitrogen	first time, no cracks were observed in the Nanoclay-AMCs specimens.
	NEXT STEP	**Query:** What would be the impact of a delubrication stage and further lowering the heating rate from 5^0C to 2^0C?
		Action: Tried sintering samples compacted to 350 bars using sintering profile Set-"AC"-Run and Nitrogen atmosphere at 2L/minute.
4	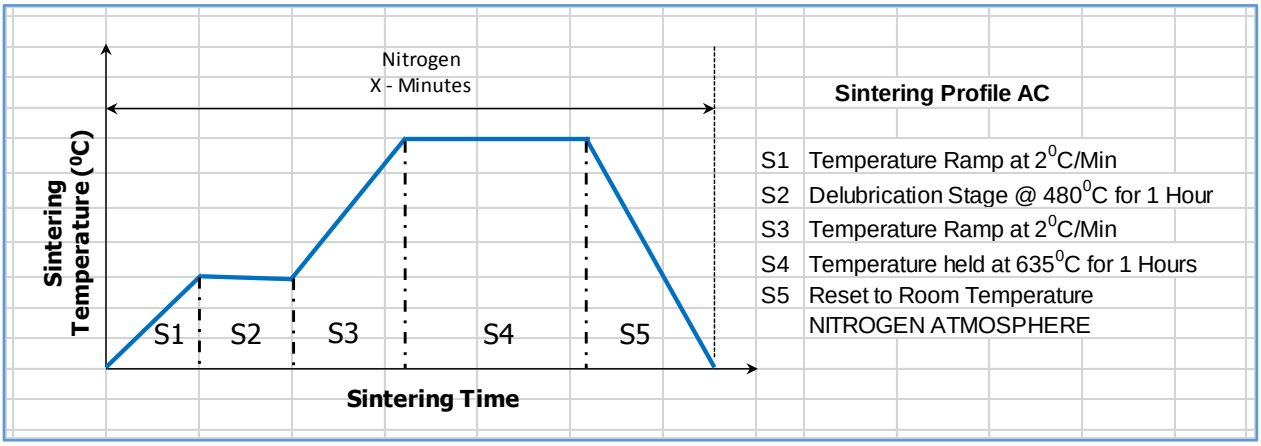	
	RESULTS 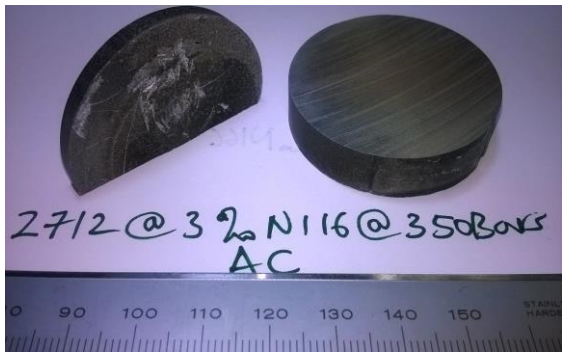 3% wt @ 350 Bars @ AC @ Nitrogen	**Notes:** Sample physically seemed satisfactorily sintered with no cracks. However, both flat surfaces were bulged. After sectioning, an internal open space like a bubble was observed. **Further Characterization: YES**
	NEXT STEP	**Query:**

		What would be the impact of maintaining the delubrication stage and heating rate of 2^0C but increasing the duration of holding temperature from 1 hour to 2 hours and switching from Argon to N_2?
		Action: Tried sintering samples compacted to 350 bars using sintering profile Set-"AD"-Run and Argon + Nitrogen atmosphere at 2L/minute.
5	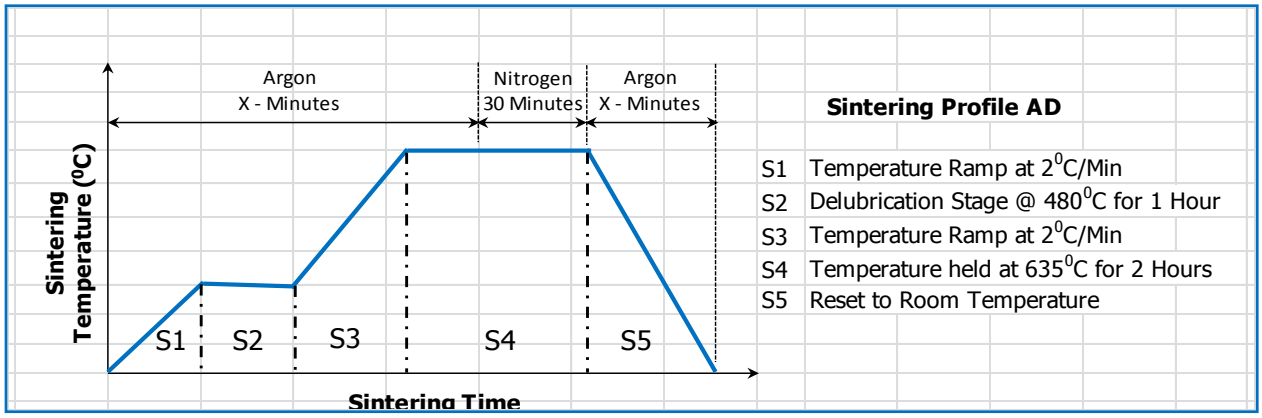	
	RESULTS 	**Notes:** Sample physically seemed satisfactorily sintered with no cracks. **Further Characterization: YES**
	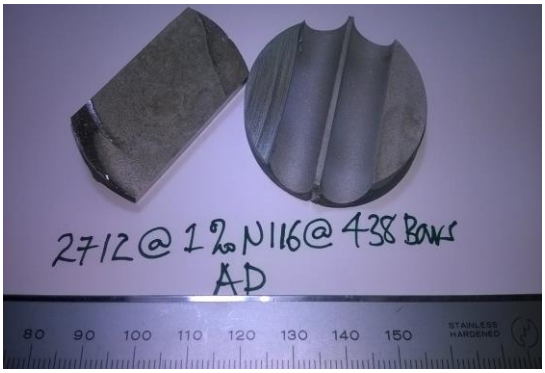	**Notes:** Sample physically seemed satisfactorily sintered with no cracks. **Further Characterization: YES**

	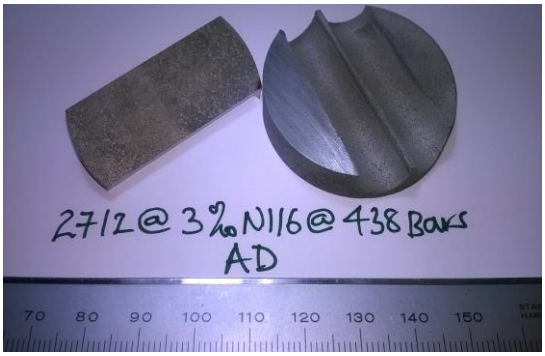 3% wt @ 438 Bars @ AD @ Ar + N_2	**Notes:** Sample physically seemed satisfactorily sintered with no cracks. **Further Characterization: YES**
	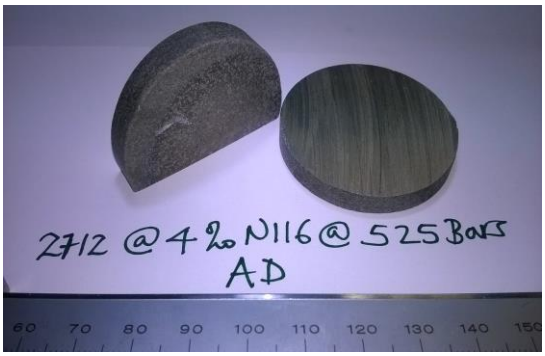 4% wt @ 525 Bars @ AD @ Ar + N_2	**Notes:** Sample physically seemed satisfactorily sintered with no cracks. **Further Characterization: YES**
	 5% wt @ 525 Bars @ AD @ Ar + N_2	**Notes:** Sample physically seemed satisfactorily sintered with no cracks. **Further Characterization: YES**
	 10% wt @ 525 Bars @ AD @ Ar + N_2	**Notes:** Sample physically seemed satisfactorily sintered with no cracks. **Further Characterization: YES**
	Provisional Conclusion Sintering profile and atmosphere deemed sufficiently optimized as reference for future research work / interests.	**Future Work Queries:** What may be the effect of mechanical alloying of *Nanofil 116* – AMB-2712 via Ball Milling?

Table 9-6 shows a summary of specimens that were sampled for further characterization in terms of sintered density, optical micrographs, SEM–cum–EDX analysis, DSC-TGA, hardness, and/or tensile testing. Specimens that had no physically noticeable defects are highlighted in bold.

Table 9-6: Summary matrix of specimens sampled for further investigation based on physical inspection.

Composition →	REFERENCE	1%	2%	3%	4%	5%	10%
Pressure ↓							
160 Bars *(157 MPa)*	✔ AA						
350 Bars *(344 MPa)*		✔ AA		✔ AC			
438 Bars *(431 MPa)*	✔ **AD**	✔ **AD**		✔ **AD**			
525 Bars *(516 MPa)*	✔ **AA**	✔ AA			✔ **AD**	✔ AD	✔ **AD**

9.3.2 Sintered Density

Table 9-7 shows the respective sintered density of selected specimens. Results for Set-"A"-Run specimens are also provided here for purposes of ease of reference. Similarly, specimens that had no physically noticeable defects are highlighted in bold. The green compaction pressure as further shown in brackets (in MPa) was calculated based on the respective die's diameter. Of interest was the consistency of profile AD as applied to REF, 1% and 3% that had been subjected 438 bars of green compaction pressure. Of these three, the 1%wt nanoclay sample showed an almost 100 % densification at 2.50% porosity (i.e. 2.6856 g/cm^3). This represents a significant optimization of the processing parameters.

Table 9-7: Sintered densities of sampled specimens.

Composition →		REF	1%	2%	3%	4%	5%	8%	10%	12.5%
Pressure ↓										
PART 1 – Reference Samples										
Trial Run	160 Bars *(950 MPa)*	✔ 2.5168								
	200 Bars *(1187 MPa)*	✔ 2.5471								
	240 Bars *(1425 MPa)*	✔ 2.5444								
Set- "A"-Run	160 Bars *(950 MPa)*	✔ **A** 2.4812	✔ **A**		✔ **A**			✔ **A**		✔ **A**
	200 Bars *(1187 MPa)*	✔ **A** 2.4841	✔ **A** 2.4656		✔ **A** 2.3605			✔ **A** 2.4577		✔ **A** 2.3201
	240 Bars *(1425 MPa)*	✔ **A** 2.4818	✔ **A**		✔ **A**			✔ **A**		✔ **A**
16.5 Bars *(550 MPa)*		✔ **A**	✔ **A**	✔ **A**	✔ **A**	✔ **A**	✔ **A**			
PART 2 – Processability Samples										
160 Bars *(157 MPa)*		✔ AA 2.5196								
350 Bars *(344 MPa)*			✔ AA 2.7095		✔ AC 2.4211					
438 Bars *(431 MPa)*		✔ **AD** 2.6211	✔ **AD** 2.6856		✔ **AD** 2.4321					
525 Bars *(516 MPa)*		✔ **AA** 2.6586	✔ AA 2.7113			✔ **AD** 2.4229	✔ AD 2.3420		✔ **AD** 2.3962	

Densification of sintered samples can be closely associated with liquid phase formation in the sample. On the other hand, liquid formation on heating of an atomized alloy particle has been claimed to involve the reverse of solidification whereby liquid nucleates at the sites that solidified last during atomization [61]. It has been suggested that particle formation during atomization is far from an equilibrium solidification event and accordingly, liquids might form at temperatures 50^0C lower than indicated by the phase diagrams. The liquid phase is reported to have three possible locations during sintering [61]: (1) at the inter-particle necks, along the grain boundaries inside the particle, and (3) at pockets located inside the grains. In the same work, it was suggested that the liquid located at the inter-particle necks provides the capillary force for densification, while liquid located in the grain boundaries lubricates grain-sliding densification. From quenched micrographs, the necks appeared to form early but densification was delayed by the particle rigidity. It is further suggested that the liquid that forms inside the grains plays no discernible role in densification [61].

9.3.2.1 Effect of Green compaction pressure

As for the Trial-Run reference samples, mean sintered density for the batch was 2.5361 with a standard deviation of 0.0137. For the Set-"A"-Run samples, mean sintered density was 2.4824 with a standard deviation of 0.0012. Trial Run samples generally posted a higher density that the Set-"A"-Run samples. This was associated with the observed physical deformation which represented some level of densification. Nonetheless, the Set-"A"-Run sintering profile can be said to be more stable than the Trial Run profile based on a significantly lower standard deviation.

For both batches of reference samples, the highest sintered density was observed for samples from specimens previously compacted to 200 bars. Since the only difference between the two batches was the sintering profile, this peaking was deemed to be independent of the sintering profile. The peaking at 200 bars compared to the 160 and 240 bars was therefore considered to

infer to the tendency of every system to thermodynamically equilibrate by self-regulating the temperature, pressure and volume. Nonetheless, it was noted that in both reference batches, the sintered density was below that of pure aluminium (2.7 g/cm^3).

The observed low standard deviation about the mean density especially in the case of Set-"A"-Run samples reiterates the understanding that the sintered density is resilient to green compaction pressures as proposed by [62] and rather much more dependent on the sintering conditions. On the other hand, the 2% difference in mean densities for the two reference batches points to possible effects of (1) sintering profiles and/or (2) sintering atmosphere on the heat-transfer-matrix.

9.3.2.2 Effect of sintering atmosphere

It has already been noted that green compaction pressure has limited effect (if any) on the sintered density. From the references column of *Table 9-7*, it is notable that the *Trial-Run*, *Set-"A"-Run* and *Set-"AA"-Run* sintering profiles were observed to post different sintered densities for specimens previously compacted to 160 bars. However, the latter of these three samples had been noted to exhibit signs of incomplete fusion as evident in *Table 9-5*. This aspect may have had an adverse effect on the sintered density. Despite this incomplete fusion, *Set-"AA"-Run* sample interestingly still posted better sintered density than the corresponding datum *Set-"A"-Run* sample. Since both samples had been subjected to the same sintering profile, the underlying 1.55% improvement in density (from 2.4812 to 2.5196 g/cm^3) must had resulted from the effect of sintering atmosphere, i.e. a favourable effect of nitrogen as compared to argon atmosphere.

This observation is further complemented by the observed improved sintered density of all comparable samples in PART 2 of the *Table 9-7* relative to those in PART 1 of the same table irrespective of the green compaction pressures. In agreement to this observation, sintering

under argon and hydrogen have elsewhere been observed to lead to lower sintered density and swelling behaviour [121]. This has been attributed to the insolubility of argon in liquid aluminium with a resultant inhibiting effect upon densification. However, sintering in argon has been noted to be effective only at high green density and when magnesium is present [121].

On the same note, hydrogen has been observed to result in lesser liquid formation in aluminium alloys, thereby preventing shrinkage. Hydrogen is furthermore said to have a higher solubility in liquid aluminium [121, 220] to the effect of degrading the wetting behaviour and thereby retarding pore filling [255]. It has been suggested that a concentration of 5 vol.% hydrogen in the mixture should be considered as a critical level, above which no sintering shrinkage occurs [123]. However, it is positively reported that shrinkage observed in the lower hydrogen content atmospheres suggested that hydrogen does not concentrate preferentially on the Al surface and its amount was not high enough to hinder totally the reaction between nitrogen and Al, thereby producing shrinkage. Nevertheless, even a small amount of hydrogen in the sintering atmosphere lowers the rate of AlN formation, which results both in a longer shrinkage incubation time and a lower shrinkage when compared with the hydrogen free atmosphere [123]. This potentially explains why the sintered density in the current study decreased with increase in nanoclay contents above 1% regardless of the green compaction pressure. The detrimental effect of hydrogen on the sintering response of aluminium still needs further investigation.

In contrast to the argon and hydrogen atmospheres, sintering in nitrogen has been reported to induce a weight gain, the formation of AlN, and densification [121]. The presence of AlN phase is elsewhere reported to alter surface wetting characteristics and in turn enhance rearrangement and densification in sintered aluminium alloys [220]. The favourable effect of nitrogen as a sintering atmosphere has been associated with chemical reactions involving the breakdown of

Al_2O_3 with the resultant effect of enhancing sinterability [121, 220, 229, 256-258]. Scaffer [256] noted that the thickness of the oxide (5 – 15nm) is dependent on the temperature at which it formed and the atmosphere in which it is stored, particularly the humidity. This researcher pointed out that although the oxide cannot be removed under conventional sintering atmospheres, it may be disrupted by sintering in the presence of magnesium. The researcher further reiterated previous researchers' comments that magnesia has lower free energy of formation than alumina and magnesium metal can partially reduce alumina to form spinel, $MgAl_2O_4$. Reaction of Mg with Al_2O_3 film is accordingly claimed to rupture the oxide during sintering, thereby exposing the underlying metal and facilitate sintering and less than 0.2% Mg is all that is required [229, 256]. A proposed possible reaction for the formation of spinel is shown below, which is a partial reduction reaction [229]:

$$3Mg + 4Al_2O_3 \leftrightarrow 3MgAl_2O_4 + 2Al \qquad (1)$$

This reaction is reportedly observed at bonding interfaces in metal matrix composites and in studies of the oxidation behaviour of Al-Mg alloys [229]. Because of the relative changes in free energy, the aforegoing reaction is favoured at low magnesium levels. At concentrations between 4 and 8% Mg in Al-Mg based composites, complete reduction is favoured and linked to the equilibrium activity of Mg [229]:

$$3Mg + Al_2O_3 \leftrightarrow 3MgO + 2Al \qquad (2)$$

Since nanoclays under study have been observed to quantitatively increase the amount of magnesium in the AMCs, the resultant effect would be to favour the reaction in *Equation 2* with little or no formation of AlN. This further explains the observed lower sintered density of samples containing relatively higher %wt content of nanoclays regardless of the green compaction pressure and / or sintering profile.

The presence of spinel in Al-Mg powder alloys has been considered to indicate that local Mg concentration may have been low when the oxide rupture occurred [229]. In contrast, MgO

should occur if the reaction proceeded via direct contact with Mg particles or with the Al-Mg eutectic liquid. However, it was noted that no evidence for MgO was found, thereby suggesting that the oxide was not reduced through contact with the eutectic liquid. It was further argued that it would be unnecessary for the magnesium to be in contact with the exterior of the powder particles for there is no reason why the oxide could not be reduced from within. In any case, some direct contact would be established during compaction. Accordingly, magnesium could diffuse through the aluminium and along the aluminium-oxide interface from the contact points and react at the metal-oxide interface, not at the oxide-vapour interface. In this way, only a limited quantity of magnesium is required as observed experimentally and further facilitates reaction in the solid state at temperatures below the eutectic temperature [229]. Besides the related shrinkage due to nitrogen atmosphere, this underlying bare requirement of low magnesium content and sub-eutectic temperature for the reduction equation potentially explains further why the 160 bars reference specimen as processed in nitrogen atmosphere showed better sintered-density than the one sintered in argon atmosphere despite signs of incomplete fusion.

Magnesium has been noted to be transported in aluminium alloys in vapour form [121, 229]. Since this has been observed to occur in both argon and nitrogen atmospheres, the formation of Mg_3N_2 was ruled out as a prerequisite for vapour transport and thus for sintering, thereby demanding an alternative explanation for the effect of the nitrogen atmosphere. This is further supported by the understanding that magnesium has a higher vapour pressure than magnesium nitride, which suggests that the formation of nitride phase may not be necessary for vapour transport to occur [121]. It was accordingly reported that nitrogen can reduce the oxide and form aluminium nitride by the reaction below:

$$2Al_2O_3 + 2N_2 \rightarrow 4AlN + 3O_2 \qquad (3)$$

provided that the partial pressure of oxygen is below a critical value Pc given by:

$$P_C = \left[P_{N_2} \frac{\alpha_{Al_2O_3}}{\alpha_{AlN}^2} e^{\left(\frac{-\Delta G^0}{RT}\right)} \right]^{2/3} \quad (4)$$

where P_{N_2} - is the partial pressure of nitrogen,

$\alpha_{Al_2O_3}$ and α_{AlN}^2 - are the activities of oxide,

R - is the gas constant,

T - is the temperature, and

ΔG^0 - is the change in free energy for the reaction.

In their study, Schaffer and Hall hypothesized that the oxide layer grows as the temperature increases [121]. Understandably, this would have a knock-on effect of decreasing the oxygen partial pressure in the gas as it travels into the pore network. The fresh gas impinging on the surface of the compact would have a high oxygen partial pressure. However, deep in the pore network, where the gas flow rate is much lower than on the surface, the oxygen may be consumed by the aluminium faster than it can be replenished by the incoming gas. The local partial pressure of oxygen would then fall. In essence, the aluminium acts as a self-getter. This self-gettering phenomenon would be operative only deep inside the pore network because it is only there that the oxygen is not replenished fast enough. This suggests that the sample surface would not sinter because it is always exposed to oxygen in the fresh gas, but the same surface layers act as a getter for the core [121].

Supposing the self-getter hypothesis is correct, the question arose as to how this effects sintering in nitrogen and not in other inert atmospheres bearing in mind that self-gettering also occurs in argon and vacuum [121]. It was then proposed that thermal expansion may cause the oxide layer to fracture. Where oxygen would be present, these fractures would readily heal. However, the oxide would not heal when the oxide is reduced by self-gettering. Under N_2, the exposed metal would readily react according to [121]:

$$2Al + N_2 \rightarrow 2AlN \quad (5)$$

which is an exothermic reaction. This would cause an increase in the local temperature, which may induce local melting, thereby aiding sintering.

The possibility that self-gettering reduces the oxygen partial pressure to below *Pc* was also proposed [121]. In that case, reduction of the oxide by reaction in *Equation 3* would occur, thereby exposing fresh metal. Reduction of the oxide would not happen under argon and sintering would not be enhanced. It was emphasized that in either case, AlN should be apparent in samples sintered in nitrogen. Inspection of optical micrographs suggested that the quantity of the nitride decreases as the compaction pressure increases (the green porosity decreases). The N_2 was envisaged to be ineffective at high green density because the pore network would be closed and permeability would be low. Magnesium would then be required and argon could be used. The critical factor is the reduction in the oxygen partial pressure through self-gettering by aluminium and the formation of AlN [121].

After experimenting with different sintering atmospheres (argon, vacuum, nitrogen, nitrogen/hydrogen, and nitrogen/argon), Pieczonka et al [123] observed that only nitrogen caused a detectable shrinkage of aluminium samples during sintering. Addition of hydrogen even in small amounts to nitrogen was observed to be detrimental because it strongly decreased the sintering shrinkage. Addition of argon to nitrogen was also observed to reduce shrinkage, but only at much higher contents than hydrogen. They further reported that shrinkage may be quickly interrupted by a change of the atmosphere during sintering. Their results indicated that the sintering shrinkage was associated with nitride formation while an increase in the oxygen content was simultaneously observed. Therefore, the assumption of a possible Al_2O_3 reduction by nitrogen [121] was deemed questionable. They argued that the proposed reduction of the Al_2O_3 by gaseous nitrogen at low oxygen pressures [121] is not a condition for the nitride formation. They further argued that a direct reduction of Al_2O_3 by gaseous nitrogen seems

unlikely because magnesium, even in small amounts present in Al powder, concentrates on the surface of powder particles and enhances sintering by local reduction of Al_2O_3 prior to the incorporation of nitrogen according to the following two equations [123]:

$$3Mg + 4Al_2O_3 \rightarrow 3Al_2MgO_4 + 2Al \qquad (6)$$

and then

$$2Al + N_2 \rightarrow 2AlN$$

They suggested that the higher nitride content in the interior should be explained by the constant thickness of the oxide layer, while the growing oxide layers at the surface of the specimen hinder the nitrogen diffusion. Accordingly, there is still a lack of understanding about the details of nitride formation and its positive influence on the sintering behaviour. Nonetheless, strength results indicated that stronger bonds between Al-particles are produced in nitrogen atmosphere [123].

It is worthwhile noting that in this particular study, besides the effects of sintering atmosphere, 1%wt Cloisite C++DEV posted better results than 1%wt Nanofil 116. Since the respective samples were processed under similar conditions, it is also possible that the relatively higher content of quartz (or lower content of Bentonite) in the latter nanoclay might have affected the oxides formation and thereby resulting in, or contributing to the observed phenomena.

9.3.2.3 Effect of sintering profile

Effect of this variable can be deciphered from the samples with 1%wt *Nanofil 116* content as shown in *Table 9-7*. Of the three samples, the samples processed under Set-"AA"-Run sintering conditions (350 and 525 bars) were observed to have a similar sintered density just above 2.7g/cm^3. To the contrary, sample from the specimen previously compacted to an intermediate green pressure of 438 bars posted a relatively lower sintered density. Since the effect of variation in green compaction pressure has been found to be irrelevant, the only significant difference between this sample and the other two was the sintering profile whereby the 438

bars specimen as processed using Set-"AD"-Run sintering profile. This reduction in sintered density is attributable to the effect of switching of sintering atmosphere from argon to nitrogen (for 30 minutes) as observed by Pieczonka et al [123].

9.3.2.4 Effect of Nanofil 116 content

For the sampled specimens, the sintered density was observed to peak up at the 1%wt nanoclay content. This peaking represented a 2.5% and 2.0% improvement from the reference sintered density for the samples from specimens previously compacted to 438 and 525 bars respectively. Beyond 1%wt *Nanofil 116* content, the sintered density decreased significantly. For instance at 3%wt content, the density for specimens previously compacted to 438 bars decreased by 10%. This decrease corresponds well with a common 12% decrease in sintered density for samples from the specimens previously compacted to 350 and 525 bars as nanoclay content increased from 1% to 3 and 4% respectively. This indicates a strong dominance of the effect of nanoclay content on the AMCs compared to the sintering conditions. As alluded to earlier on, this significant drop in density at nanoclay contents higher than 1% is potentially linked to the evolution of hydrogen gas (from the nanoclay) with its associated detrimental effects being manifested in the form of physically discernible cracks. This contention is further supported by the observation that reduction of the heating rate to from 10^0C – to – 5^0C – to – 3^0C and finally to 2^0C as represented by Set-"AD"-Run sufficiently mitigated the cracking problem. With reference to the 1%wt samples, it is suspected that the slow heating rate afforded by Set-"AD"-Run profile did effectively provide room for gradual evolution of the hydrogen gas before being adversely entrapped within the interstitial locations / sites as liquid formed at the particles contact points.

It was interesting to notice that the peak sintered density was observed in 1%wt nanoclay content samples from specimens previously compacted to 350 and 525 bars as processed using *Set-"AA"-Run* sintering profile and nitrogen atmosphere, i.e. 2.7095 and 2.7113 g/cm^3

respectively. It is evident that that this peaking must have been related to the effect of nitrogen on densification of the specimens irrespective of the green compaction pressure. However, noting that both of these two samples had visible physical defects, the need for fine-tuning the sintering profile and atmosphere is obvious. Such moderation is represented by the sample from specimens previously compacted to 438 bars and sintered using Set-"AD"-Run conditions, i.e. 2.6856 g/cm^3, which represents 99.5% of the theoretical density of aluminium.

9.3.3 Mechanical Properties

9.3.3.1 Tensile Testing Results

As an excerpt from *Table 9-7*, matrix for specimens that were subjected to tensile testing is as shown in *Table 9-8*. All other follow-up tests and analysis were based on these three specimens. The respective numbers (1 to 12) indicated below the samples labels are simply for tagging purposes only with respect to analysis of the results.

Table 9-8: Sampled specimens subjected to tensile testing.

Composition →	REFERENCE	1%	2%	3%	4%	5%	10%
Pressure ↓							
160 Bars *(157 MPa)*	✔ AA						
350 Bars *(344 MPa)*		✔ AA		✔ AC			
438 Bars *(431 MPa)*	✔ **AD** **1, 2, 3, 4**	✔ **AD** **6, 7, 8**		✔ **AD** **11 & 12**			
525 Bars *(516 MPa)*	✔ **AA**	✔ AA			✔ **AD**	✔ AD	✔ **AD**

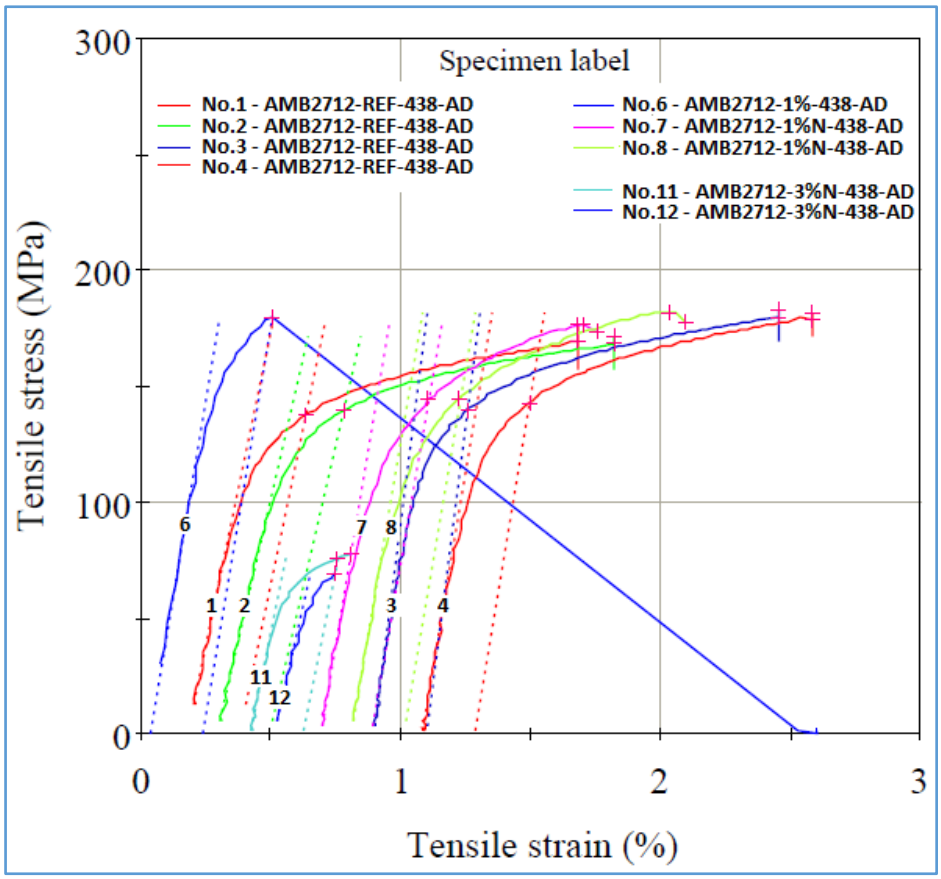

Figure 9-13: Tensile testing results for samples successfully sintered, machined and tested.

Figure 9-13 shows the graphical representation of the tensile testing result for the selected samples while *Table 9-9* quantitatively shows the same results. Every of the Ref, 1%wt, and 3%wt categories had four satisfactorily sintered specimens for the machining phase of samples preparation. The first few samples that were machined broke during the process of turning the gauge section to the specified Ø2.5mm, in particular samples No. 5, 9, and 10. For further reference, the respective images of these samples are provided in *Table 9-10* alongside corresponding images for the successfully machined and tested samples. Based on the preliminary failure during machining phase, a decision was made to deviate from the provisions of *ASTM E63-01* standards by machining the gauge lengths to a minimum diameter of 5mm instead of the specified Ø2.5 mm. Since stress is a relative measure, it was considered that this modification would not affect the signature properties of the AMCs as evaluated using the modified samples. This aspect is evident from results for the one sample that was successfully

machined to Ø3 mm, i.e. sample No. 6, which posted results similar to those of its batch members irrespective of the difference in diameter at the gauge length.

Table 9-9: Tensile test results for *Set-"AD"-Run* samples.

TAG No.	SPECIMEN LABEL	Area $(mm)^2$	Tensile Stress at Yield (0.2% Off-set) (MPa)	Young's Modulus (Gpa)	UTS (MPa)	Elongation (%)
1	AMB 2712 - REF - 438 Bars - AD - 1	19,24	137,02	54,40	176,35	4,75
2	AMB 2712 - REF - 438 Bars - AD - 2	19,24	139,02	48,90	171,58	3,63
3	AMB 2712 - REF - 438 Bars - AD - 3	28,37	139,13	89,00	182,59	3,77
4	AMB 2712 - REF - 438 Bars - AD - 4	28,46	142,58	67,40	181,59	3,00
	Average		***139,44***	***64,93***	***178,03***	***3,79***
	Std. Dev.		*2,00*	*15,44*	*4,41*	*0,63*
5	**AMB 2712 - 1%N - 438 Bars - AA - 0**	**0**	**0,00**	**0,00**	**0,00**	**0,00**
6	AMB 2712 - 1%N - 438 Bars - AD - 1	4,91	179,61	66,90	179,63	1,43
7	AMB 2712 - 1%N - 438 Bars - AD - 2	28,27	143,83	66,30	176,43	2,23
8	AMB 2712 - 1%N - 438 Bars - AD - 3	28,27	144,23	67,20	181,86	1,77
	Average		***155,89***	***66,80***	***179,31***	***1,81***
	Std. Dev		*16,77*	*0,37*	*2,23*	*0,33*
9	**AMB 2712 - 3%N - 438 Bars - AD - 0**	**0**	**0,00**	**0,00**	**0,00**	**0,00**
10	**AMB 2712 - 3%N - 438 Bars - AD - 0**	**0**	**0,00**	**0,00**	**0,00**	**0,00**
11	AMB 2712 - 3%N - 438 Bars - AD - 1	27,99	75,60	56,20	77,06	1,31
12	AMB 2712 - 3%N - 438 Bars - AD - 2	19,17	0,00	49,30	68,99	1,15
	Average		***75,60***	***52,75***	***73,03***	***1,23***
	Std. Dev.		----	*3,40*	*4,04*	*0,08*

All other factors being held constant, results as furnished in *Table 9-9* show that samples with 1%wt *Nanofil 116* had a 12% higher yield strength than the reference samples. This was accompanied by 3% and 1% increase in young's modulus and ultimate tensile strength respectively. However, an adverse reduction in ductility was noted as reflected by a corresponding reduction in % elongation of the samples (about 52%). The observed young's modulus (66.80 GPa) for samples containing 1%wt *Nanofil 116* was found to be in the range reported elsewhere [108] for AMB-2712 (68 GPa). However, the respective percentage elongation for samples in current study was twice the value reported therein (0.9%), while their corresponding yield stress (355 MPa) was almost twice of the value obtained in this study. The underlying differences may be expected bearing in that the AMB-2712 reported on had been subjected to T6 heat treatment.

The observed reduction in ductility was related partly to the embrittlement associated with increased content of magnesium [211] since both the AMB-2712 matrix and *Nanofil 116* contained magnesium. Despite the content of aluminium not exceeding 5.5% in current wrought alloys e.g. in 5xxx series, magnesium has a solid solubility 17.4% in aluminium and precipitates preferentially at grain boundaries as a highly anodic phase (Mg_5Al_3 or Mg_5Al_8), which produces susceptibility to intergranular cracking and stress corrosion [87]. However, properly fabricated wrought alloys containing upto 5% have been observed to be stable under normal usage. In general, the addition of magnesium markedly increases the strength of aluminium without unduly decreasing the ductility [87].

Silicon is yet another element that deserves further investigation because of its presence both in the AMB-2712 matrix and *Nanofil 116*. The maximum solubility of silicon in aluminium has been reported to be 1.65%wt [244]. Besides being known to improve the fluidity of aluminium, silicon is said to have a favourable effect of lowering the melting temperature [169, 259], an aspect that is particularly relevant to the development of Nanoclay-AMCs system. However, Kalhapure, M.G. and Dighe, P.M [168] investigated the effect of silicon on aluminium alloys at contents of between 5 – 14% and found that it has a tendency of reducing ductility while increasing the hardness, tensile yield stress, and the ultimate tensile strength. Other researchers that experimented with 1.5 – 6% wt content of silicon [169] have observed similar effects.

In wrought alloys, silicon has been used with magnesium at levels up to 1.5% to produce Mg_2Si in the 6xxx series of heat-treatable alloys [87]. It is further indicated that additions of 0.5 – 4.0% silicon reduces the cracking tendency of aluminium-copper-magnesium alloys. Even though the addition of any amounts of magnesium to any silicon-containing alloy will render it heat-treatable, it has been cautioned that the addition of excess magnesium over that required

to form Mg_2Si sharply reduces the solid solubility of this compound. It has further been advised that silicon can be modified through the addition of sodium in eutectic and hypoeutectic alloys and by addition of phosphorus in hypereutectic alloys [87, 260]. The fact that silicon crystals were observed to precipitate and actually become bigger in size with increase in nanoclay content infers to the silicon thresh-hold being exceeded.

From another perspective, the presence of silicon in the form of silica may potentially affect the dynamics of solid solubility of silicon into aluminium. For instance in an experiment that was conducted in the heat treatment temperature range of 350-560^{0}C, SiO_2 was considered to effectively prevent the solubility of silicon into aluminium in argon atmosphere [261]**.** As both *Nanofil 116* and *Cloisite Ca^{++}DEV* have approximately 1% and 3%wt quartz respectively, this may be linked to the observed relatively poor sinterability of AMCs especially having more than 1%wt content of *Cloisite Ca^{++}DEV*. On the other hand, since the samples with 1%wt content of *Cloisite Ca^{++}DEV* generally posted better machinability results, it is possible that the relatively higher content of SiO_2 favourably improved the heat-flow-matrix (through effecting a better microstructure), thereby outweighing the adverse hindrance of diffusion of the silicon that was already present in the matrix.

It is envisaged that the objective of balancing the relative %wt of magnesium and silicon in the AMB-2712 alloy (and similar alloys) can be achieved by exploring the possibility of making the AMB-2712 alloy using *Nanofil 116* or *Cloisite Ca^{++}DEV* as the sole source of the required magnesium and silicon content for the alloy. Through that route, the adverse effects of excess contents may be mitigated while still optimizing performance of this Nanoclay-AMCs system.

Images in *Table 9-10* show that the sample tagged No. 3 seemingly fractured out of the gauge length. This is confirmed by the recorded maximum load for the specimen. Exclusion of this sample from the batch would interpret to an average yield stress of 56.90 MPa with a standard

Table 9-10: Images of faulty* as well as successfully machined-and-tested samples.

TAG No.	TENSILE TEST SAMPLE'S IMAGE
1	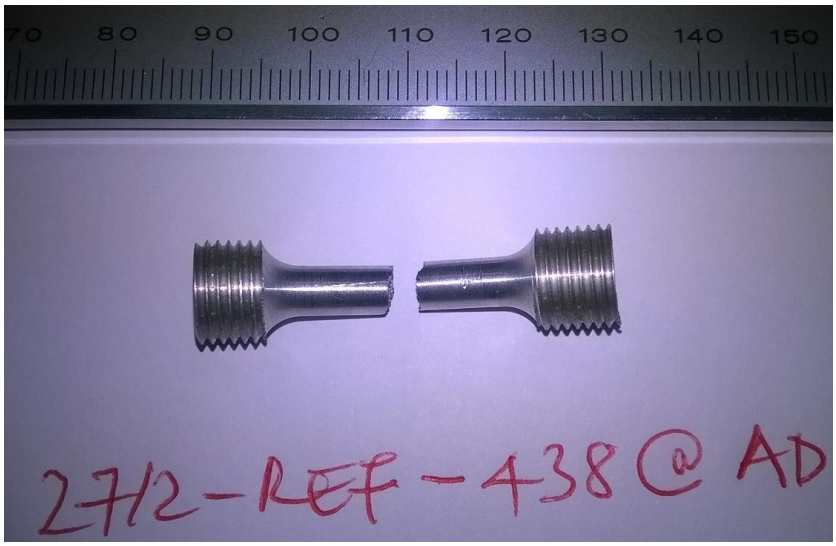
2	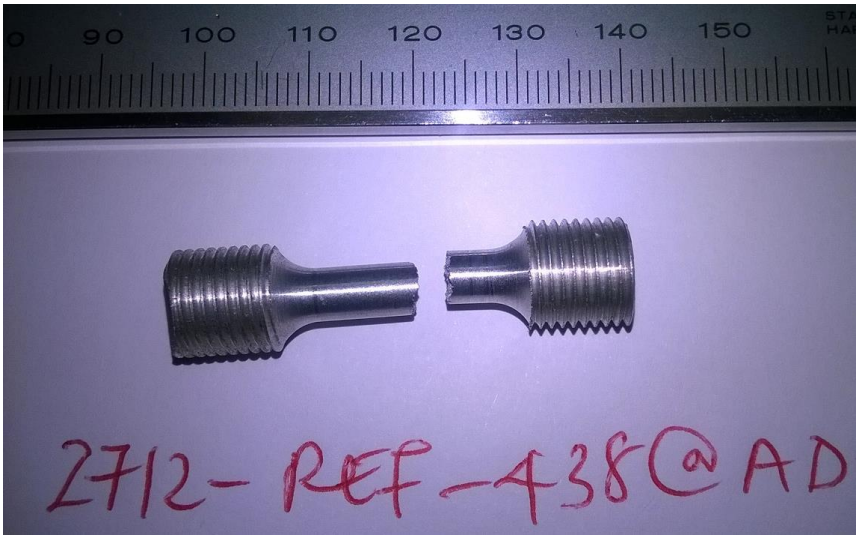
3	

4	 100 110 120 130 140 150 2712-REF-438@AD
5*	 80 90 100 110 120 130 140 150 2712-12N-438@AD
6	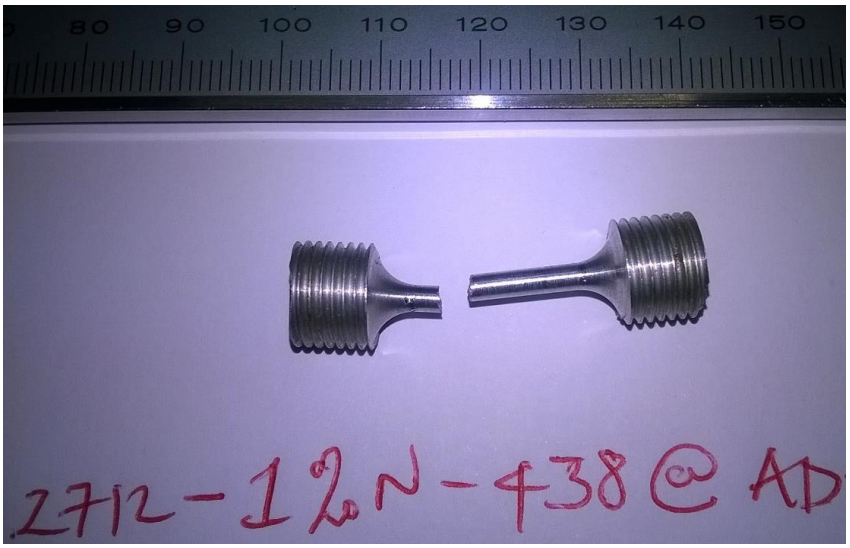 80 90 100 110 120 130 140 150 2712-12N-438@AD

7	 110 120 130 140 150 STAINLESS HARDENED 2712-12N-438@AD
8	 100 110 120 130 140 150 STAINLESS HARDENED 2712-12N-438@AD
9*	 70 80 90 100 110 120 130 140 2712-32N-438@AD

10*	
11	
12	

* Faulty specimens identified during machining process.

deviation of 13.44 MPa. Reported effect of *Nanofil 116* would then switch from 12 to 17% increase relative to the reference samples. Disregarding the differences in green compaction pressure, results for Set-"AD"-Run samples with 1%wt *Nanofil 116* represented an 8% improvement with respect to UTS compared to the datum Set-"A"-Run samples with 1%wt *Nanofil 116*.

Interestingly, corresponding results for reference samples showed an improvement of 215%. This reinforces the observed favourable effect of introducing nitrogen into the sintering atmosphere of AMB-2712 matrix and similar aluminium alloys containing magnesium, leaving the nanoclay's marginal effect at only 3%. At the on-set, this seemingly deleterious effect of nitrogen on the effectiveness of nanoclay as previously observed under argon-atmosphere-only is most likely attributable to two aspects: (1) presence of an ingredient that was in the *Nanofil 116* but not in the matrix, e.g. the incumbent effect of evolution of hydrogen gas, and/or (2) the introduction of silicon and/or magnesium element(s) beyond the threshold for optimal integrity of the matrix. This phenomenon requires further investigation.

9.3.3.2 Hardness test results

Table 9-11: Vickers hardness test for optimized specimens.

AMB2712-438Bar-AA			
	HV2kg		
# Indent	Ref	1%N	3%N
1	77.7	78.1	34.5
2	79.2	74.8	36.7
3	72.3	75.3	37.6
4	76.4	74.4	34.7
5	78.9	75.8	41.1
Mean	76.9	75.68	36.92
Std dev	2.799107	1.451551	2.68179
Std error	1.251799	0.649153	1.199333

Table 9-11 shows the Vickers hardness results for optimized specimens, i.e. previously compacted to 438 Bars and processed using *Set-"AD"-Run* sintering profile in argon and nitrogen atmosphere. Hardness value decreased with addition of nanoclay, with the hardness for 3%wt specimens being less than half that of the reference specimen.

9.3.4 Microstructural analysis

REF	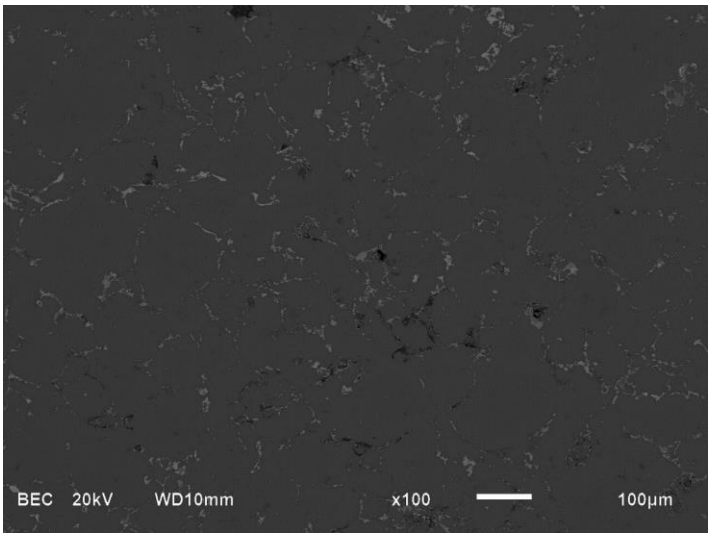
1%N	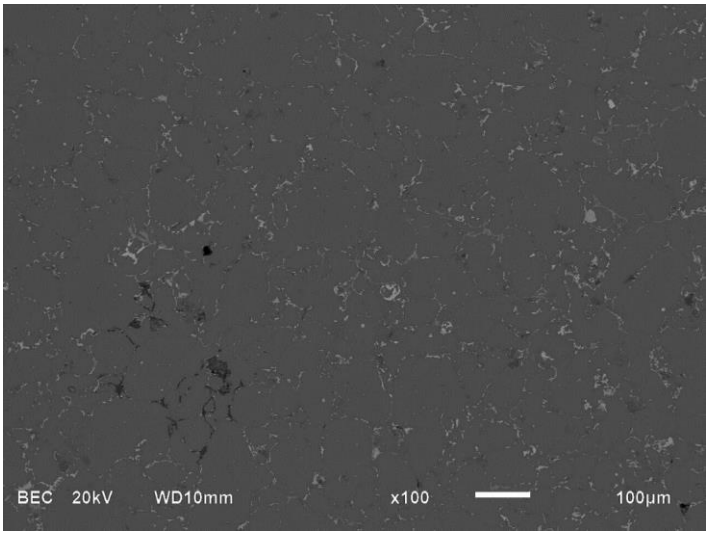
3%N	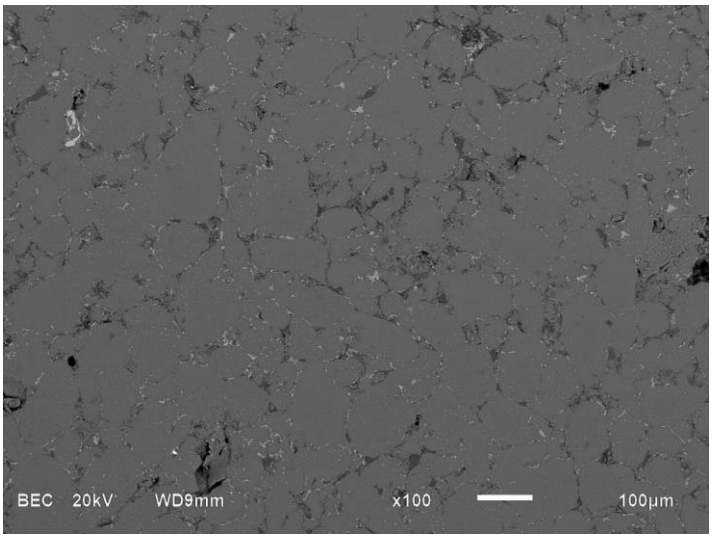

Figure 9-14: Microstructures of sampled sites showing complete fusion.

Figure 9-14 shows microstructures of the sampled sites showing that the specimens were fully sintered. Low or no porosity was observed. Traces of the dark phase as observed in previous specimens sintered in argon can also been seen here even at this magnification of 100 times. This dark phase, confirmed to be Mg_2Si, as well as other phases were better observed at a higher magnification as shown in *Table 9-12*. In similarity to previous specimens, figures in *Table 9-12* demonstrates at a higher magnification the trend of increasing distribution of precipitates with increase in the nanoclay content especially within the grains. The dark phase can be seen to have served a significant role of filling-up the interstitial spaces and/or pores.

At an even higher magnification, the dynamics of micro-cracks were visible in the dark phase as shown in *Table 9-13*. Notably, the phase was observed to have micro-cracks only when in large quantity at a particular site. Evidence for this is shown in figures given in *Figure 9-15* where micro-cracks can be noticed in image (i) and not in image (ii), yet these images were both from the same reference sample and at the same magnification.

The behaviour demonstrated in *Figure 9-15* validate the observation made earlier that the micro-cracks reflect a disparity in thermal properties between the dark phase and its surrounding phases. Furthermore, it can be noticed that the cracks appear mostly in the interior region of the dark phase as pointed out at A. This serves as an indication that the region cooled down last compared to the surrounding aluminium phase. The observation also alludes to the dark phase having refractory properties. The cracking observed at point B confirms this aspect because the crack is at the interphase with copper, a material with higher thermal conductivity than aluminium [42].

Table 9-12: Microstructures of sampled sites showing distribution of precipitates.

REF	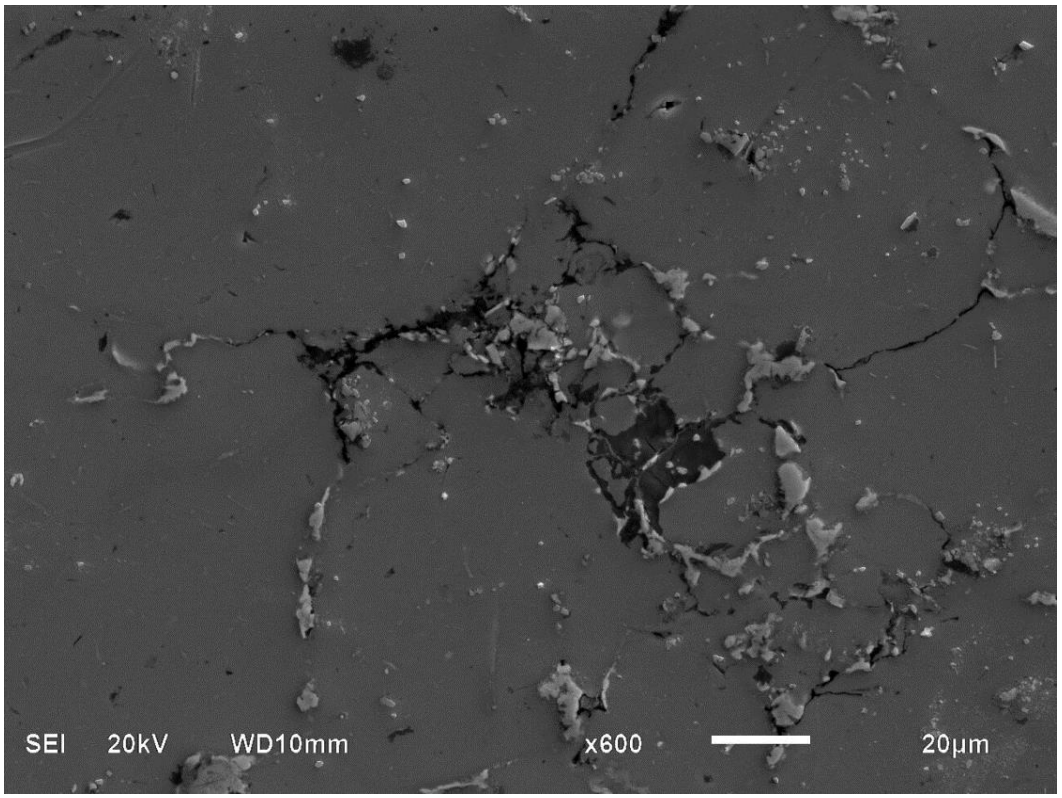
1%N	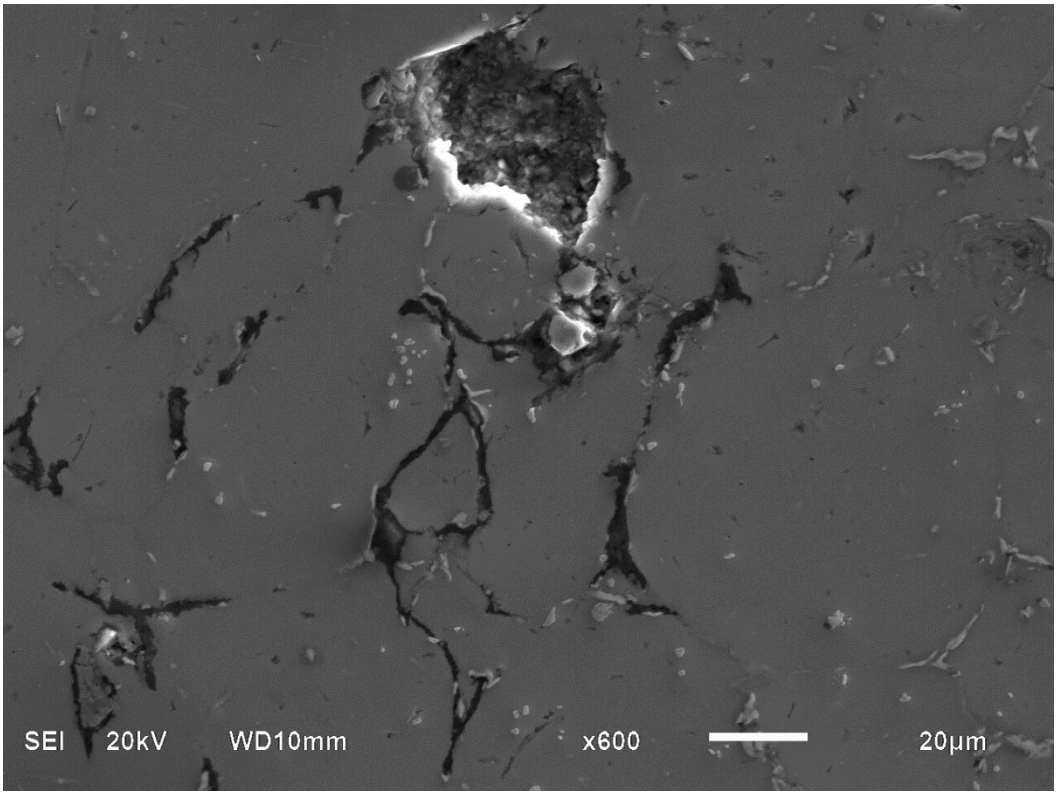

3%N	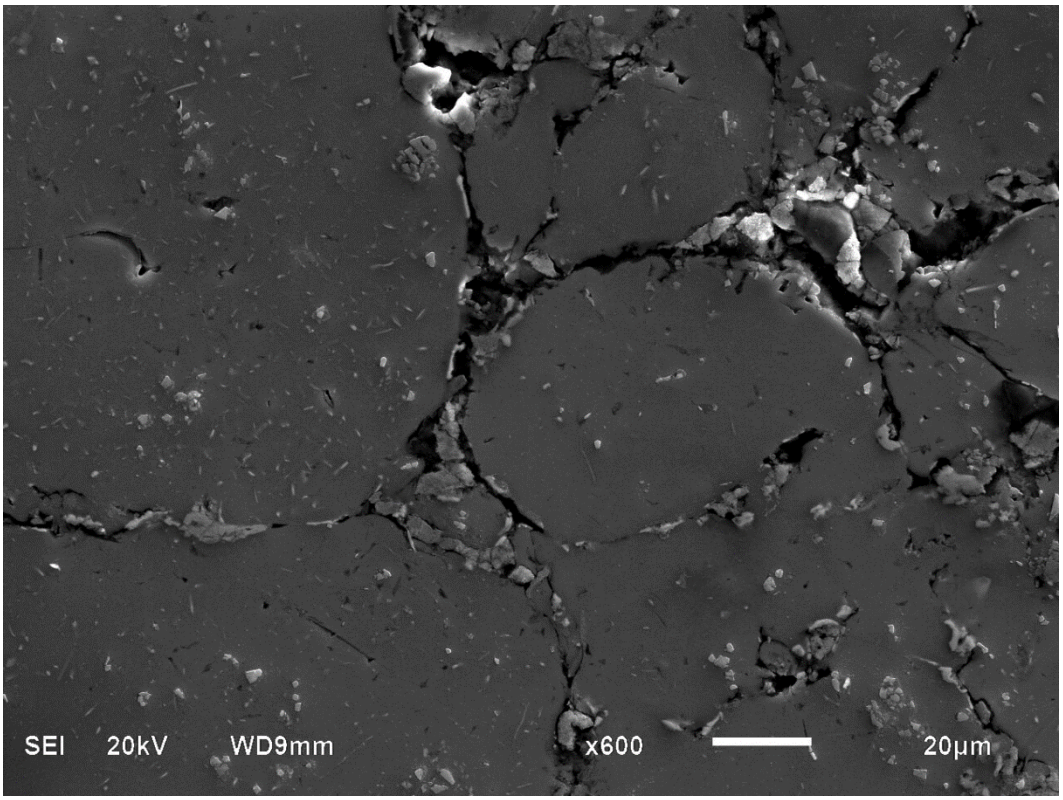

Table 9-13: Microstructures of sampled sites showing micro-cracks dynamics.

REF	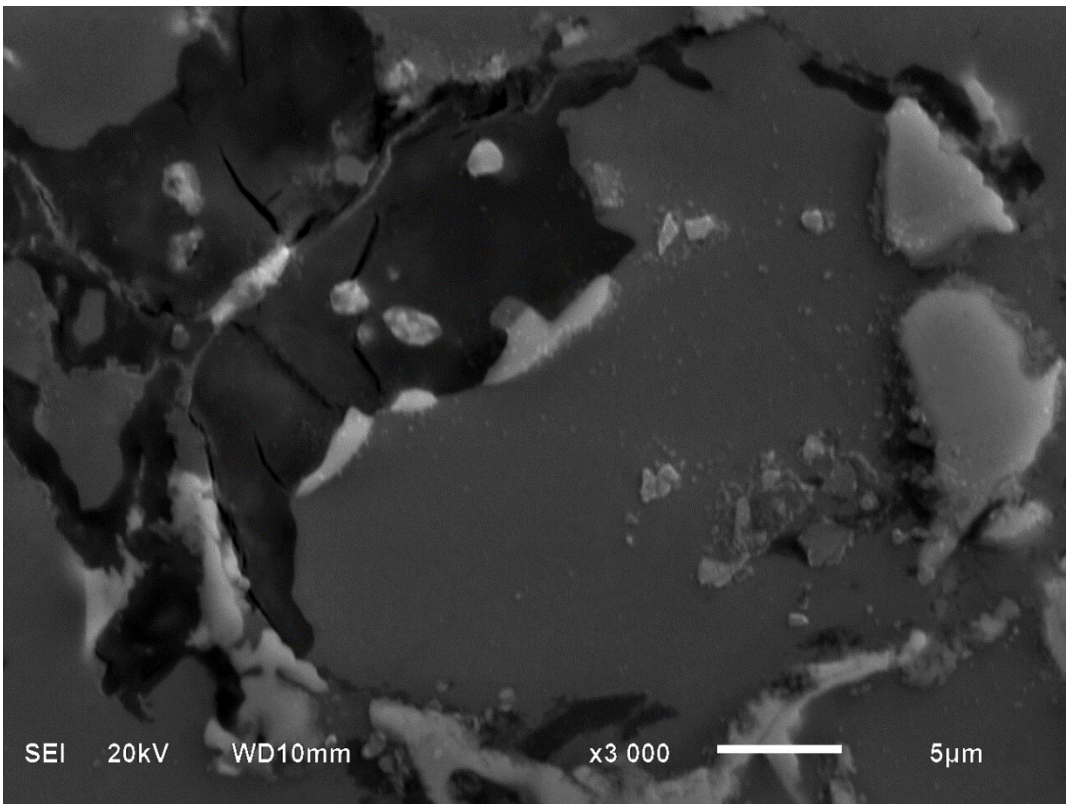

1%N	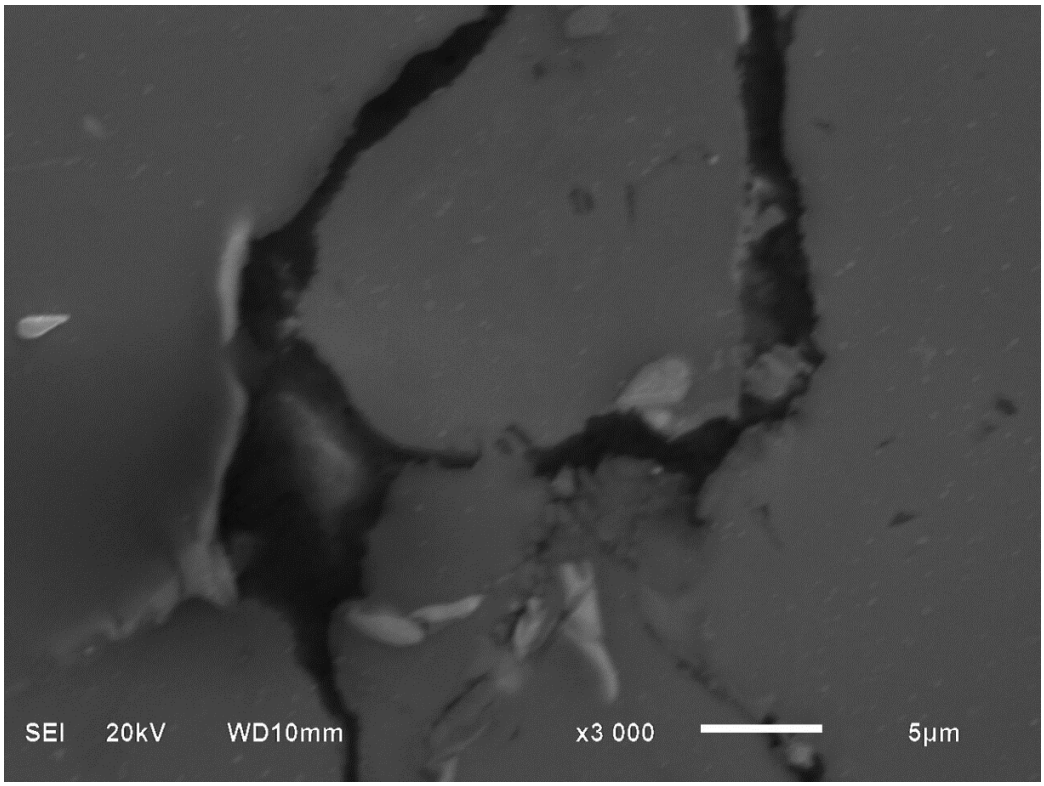
3%N	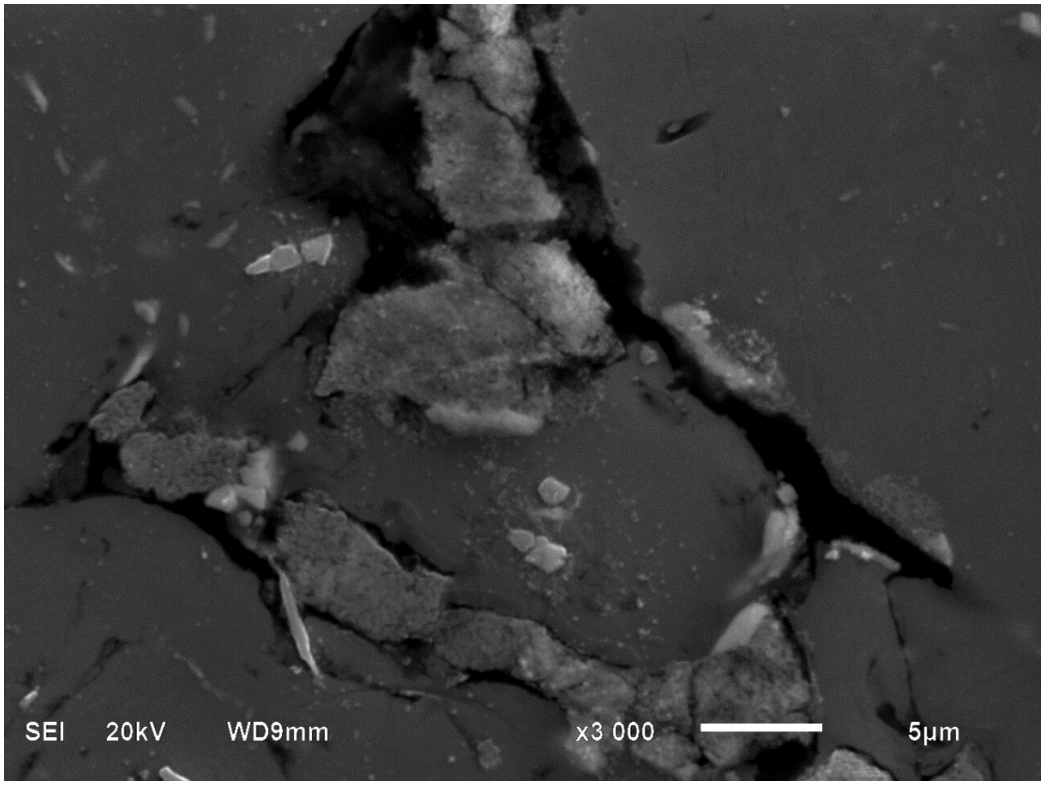

Additionally from *Figure 9-15*, it can also be observed that the interface between the dark phase and aluminium was seamless as pointed out at point C of *Figure 9-15(i)*. This serves as an indication of good wettability between the two phases.

REF	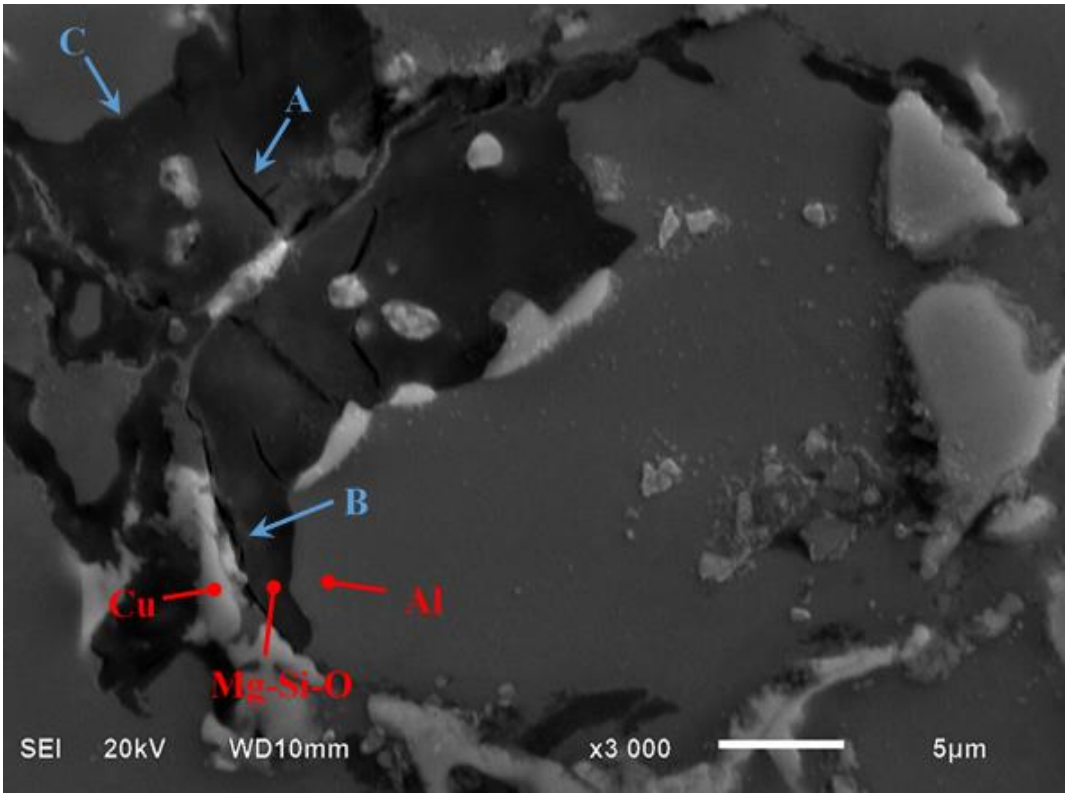 (i)
REF	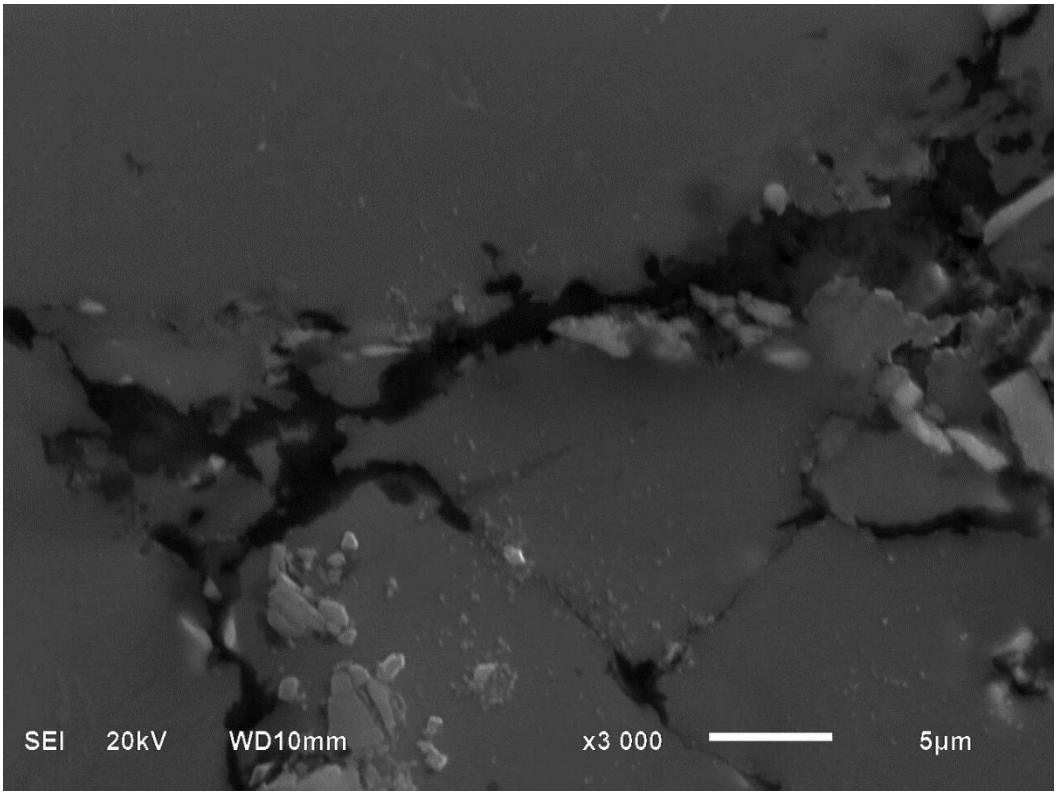 (ii)

Figure 9-15: Microstructures of sampled sites showing presence of micro-cracks in (i) and absence of micro-cracks in (ii).

9.3.5 EDX Analysis

Figures 9-16 to *Figure 9-24* show elemental compositions of selected sites as determined using EDX spectra overlays. Three site were considered for each of the specimens.

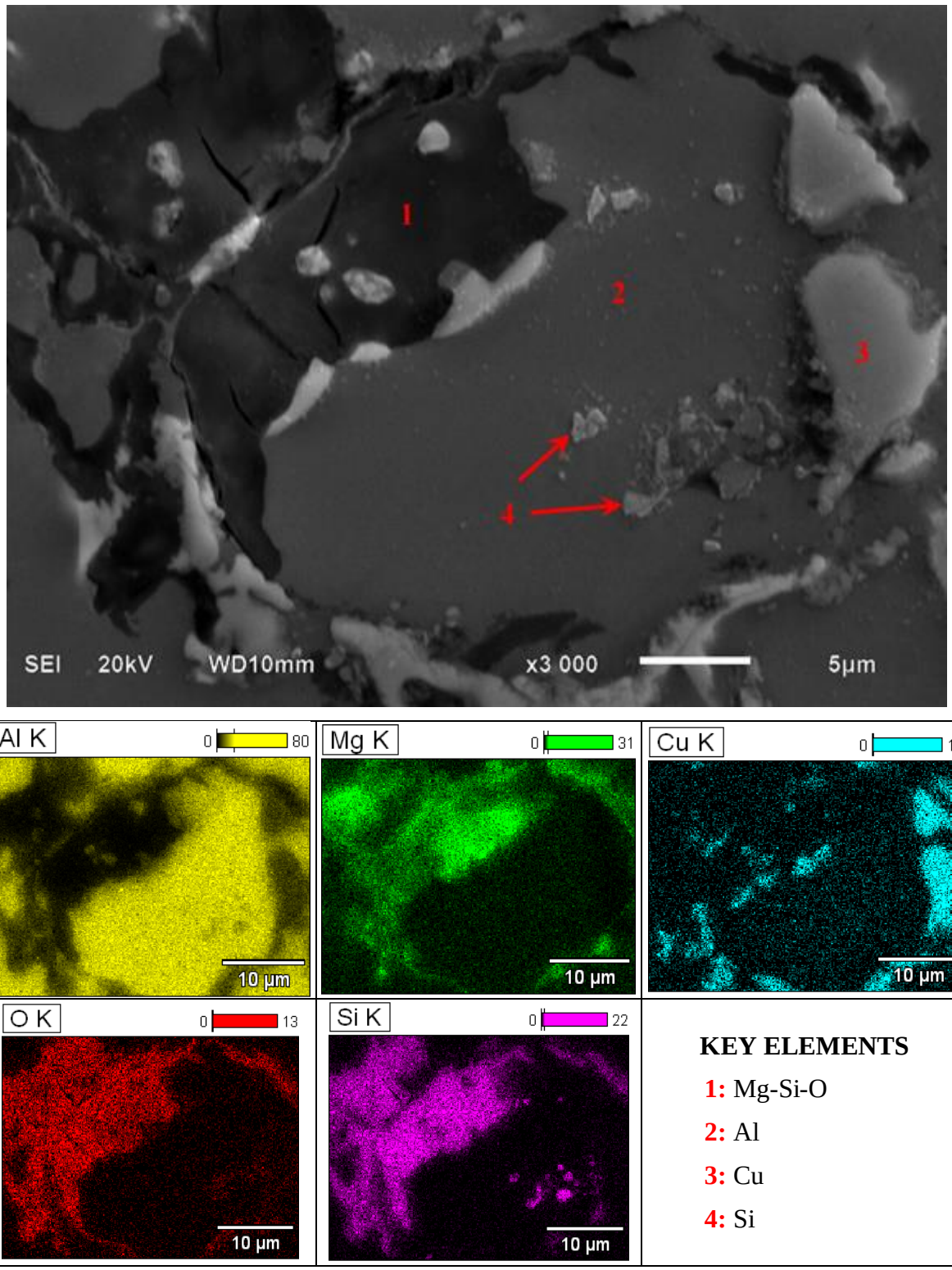

Figure 9-16: Reference Sample(438 Bars-REF-AD): **LOCATION 1**.

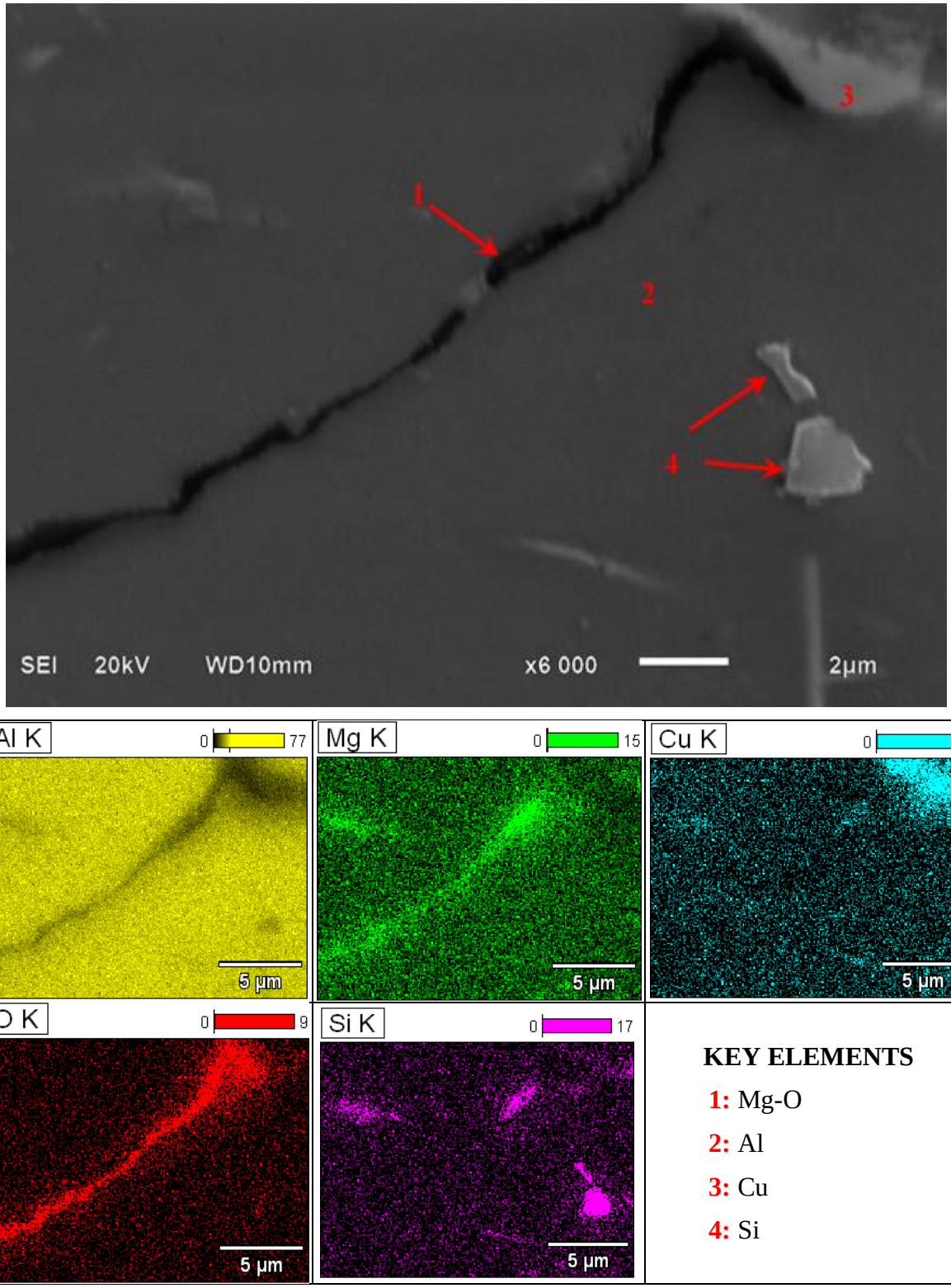

Figure 9-17: Reference Sample (438 Bars-REF-AD): **LOCATION 2**.

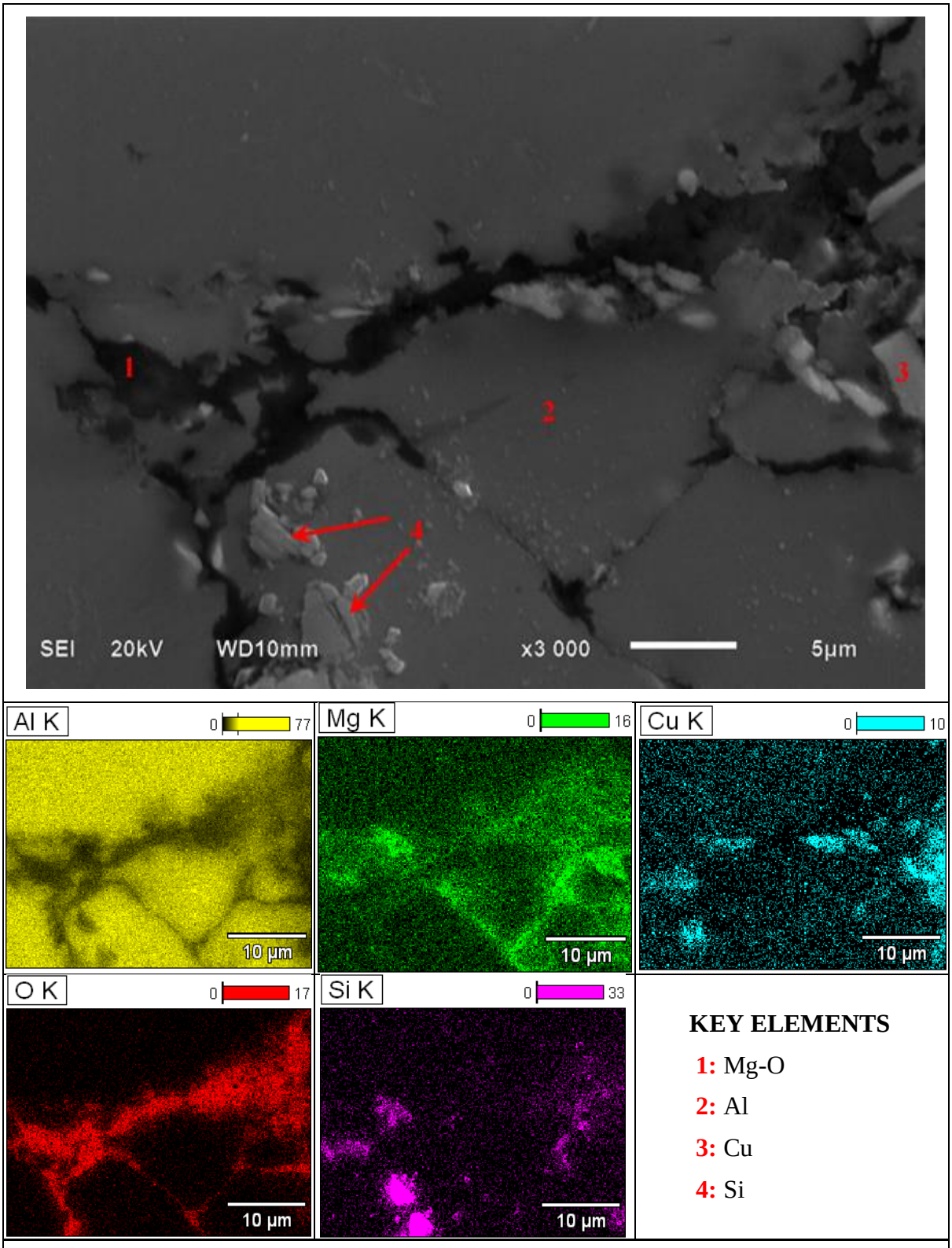

Figure 9-18: Reference Sample (438 Bars-REF-AD): **LOCATION 3**.

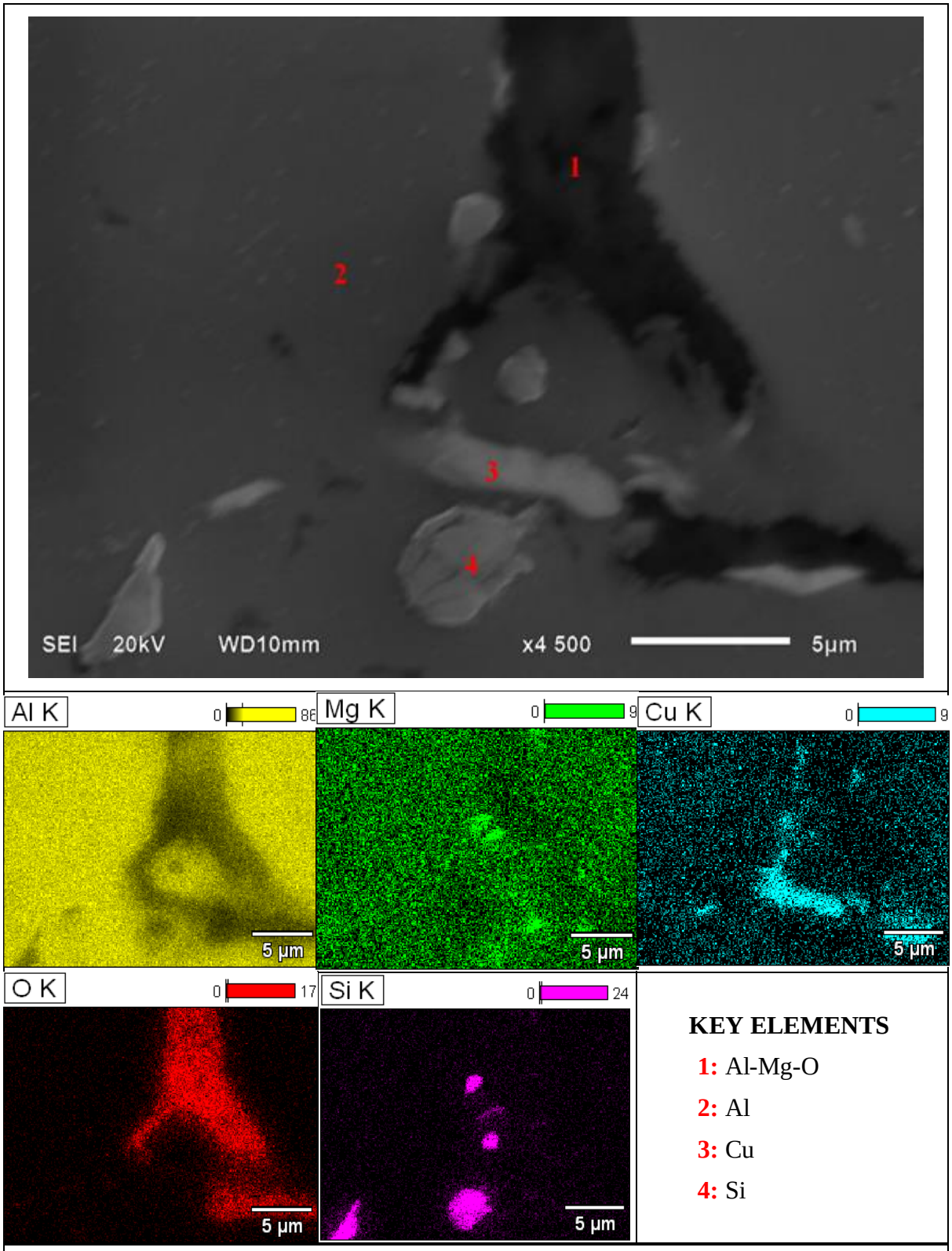

Figure 9-19: 1%wt Nanofil 116 Sample (438 Bars @ AD)**: LOCATION 1**

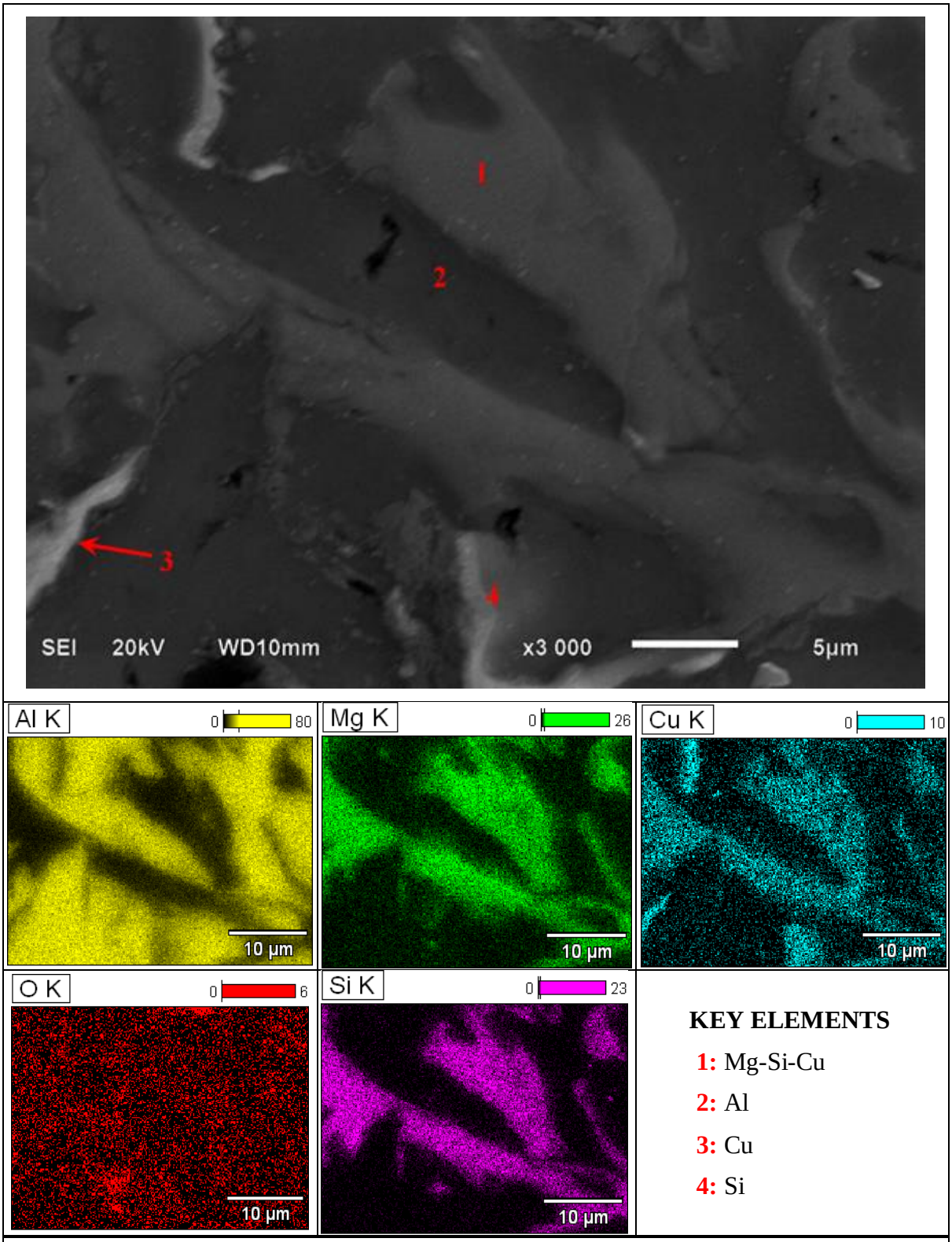

Figure 9-20: 1%wt Nanofil 116 Sample (438 Bars @ AD)**: LOCATION 2**

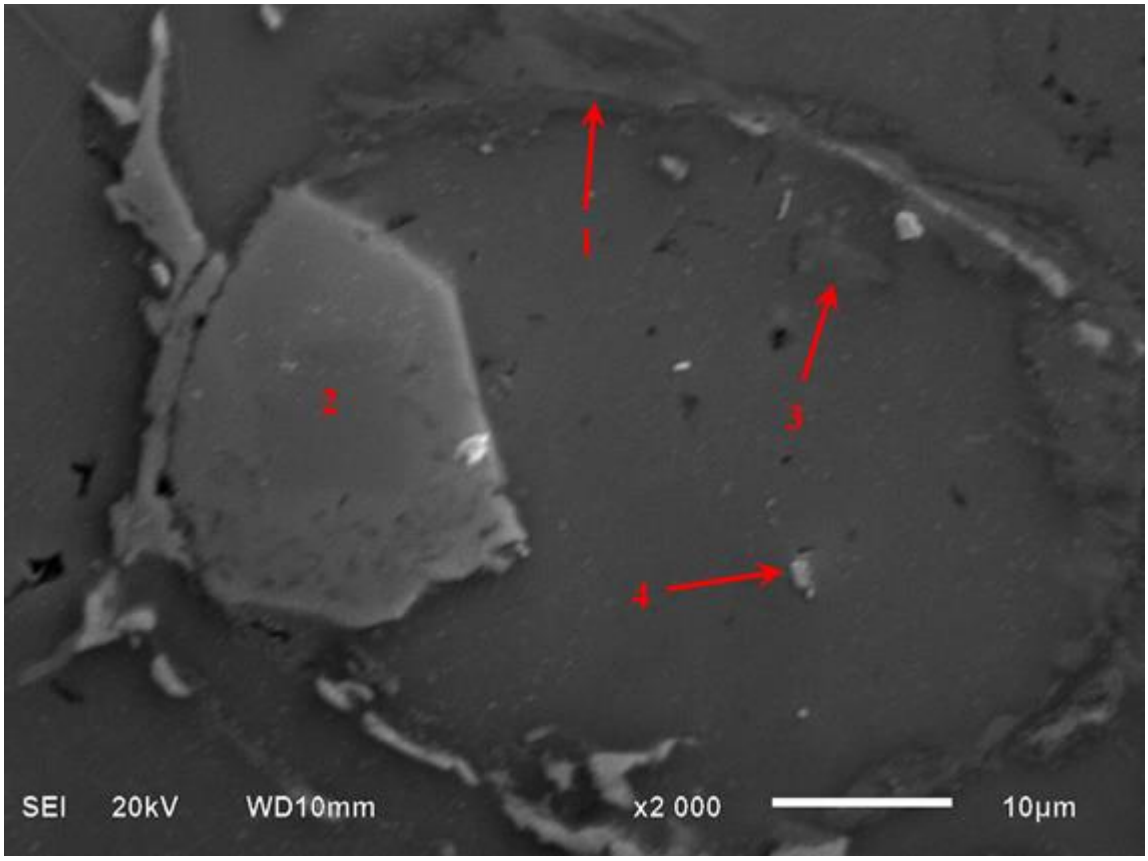

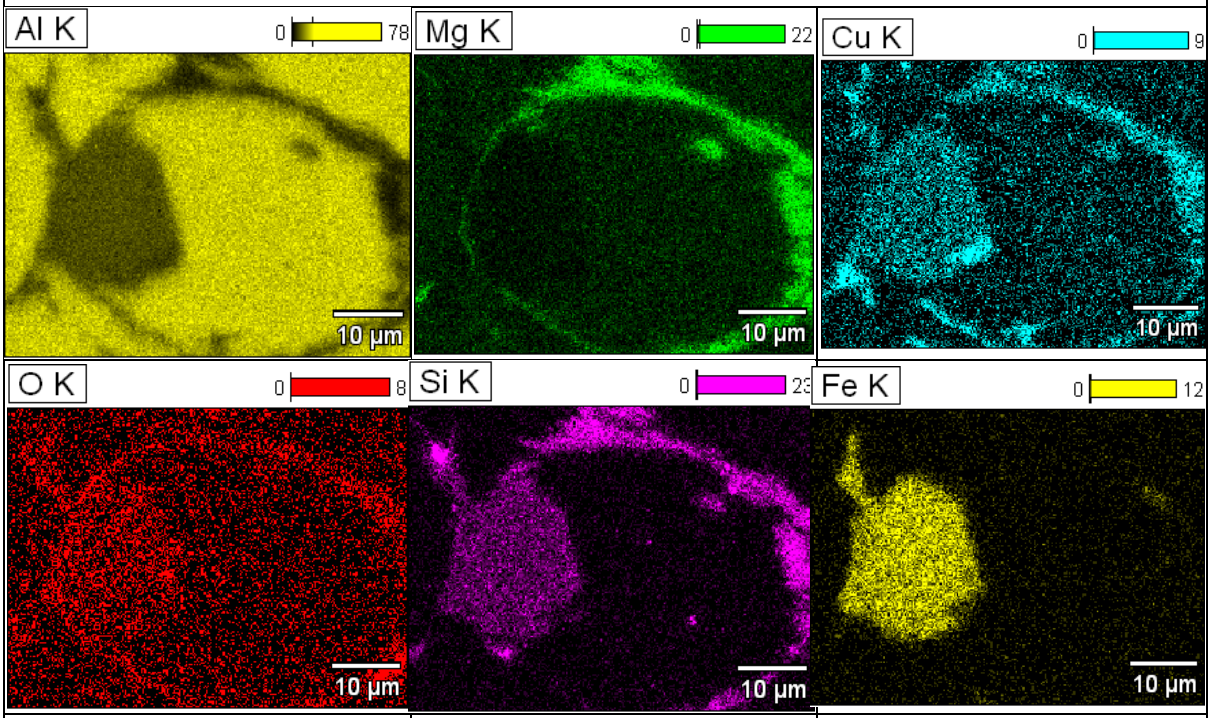

KEY ELEMENTS	**1:** Mg-Si-Cu-O **2:** Fe-Si-Cu-O	**3:** Mg-Si-Cu **4:** Si

Figure 9-21: 1%wt Nanofil 116 Sample (438 Bars @ AD)**: LOCATION 3**

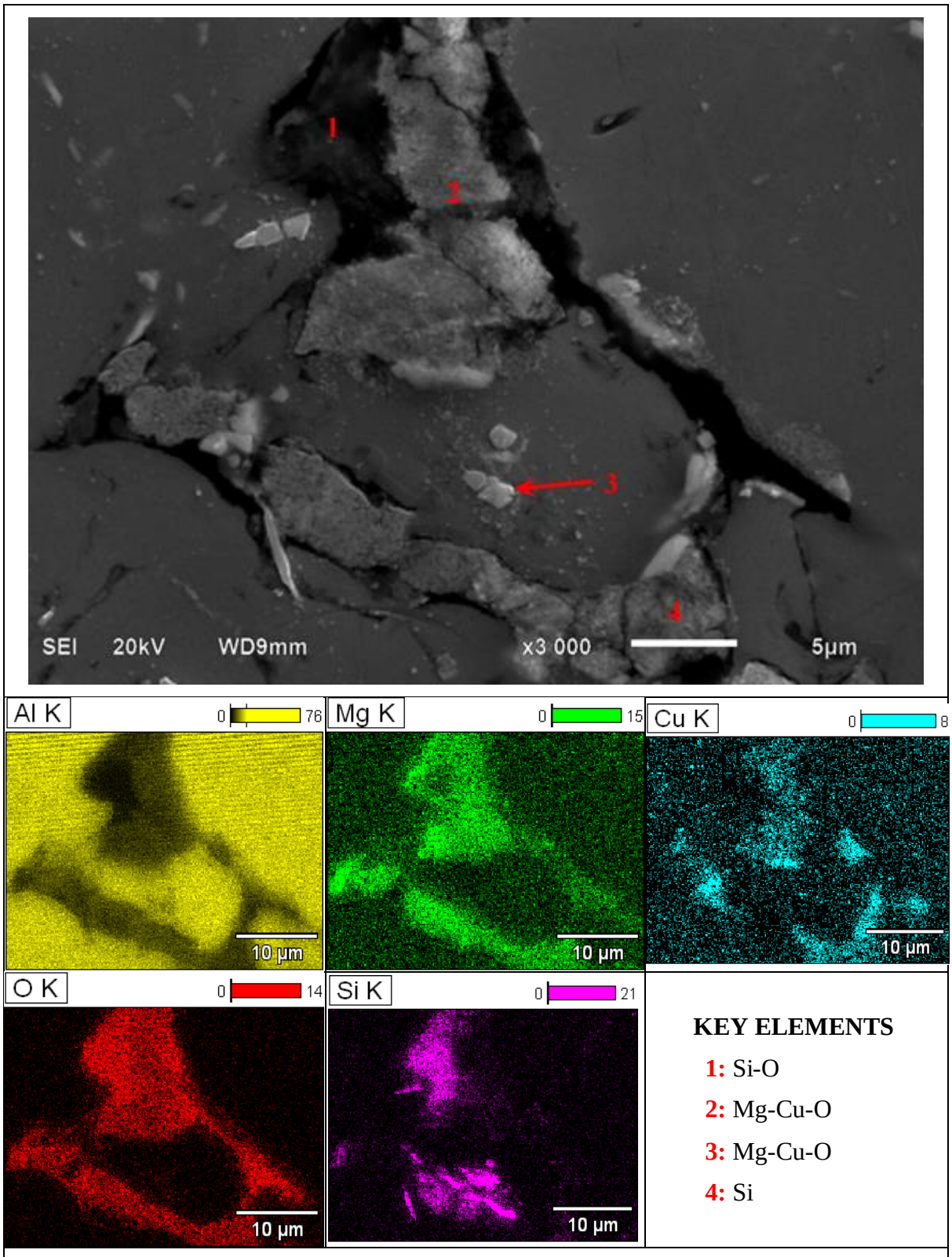

Figure 9-22: 3%wt Nanofil 116 Sample (438 Bars @ AD)**: LOCATION 1**

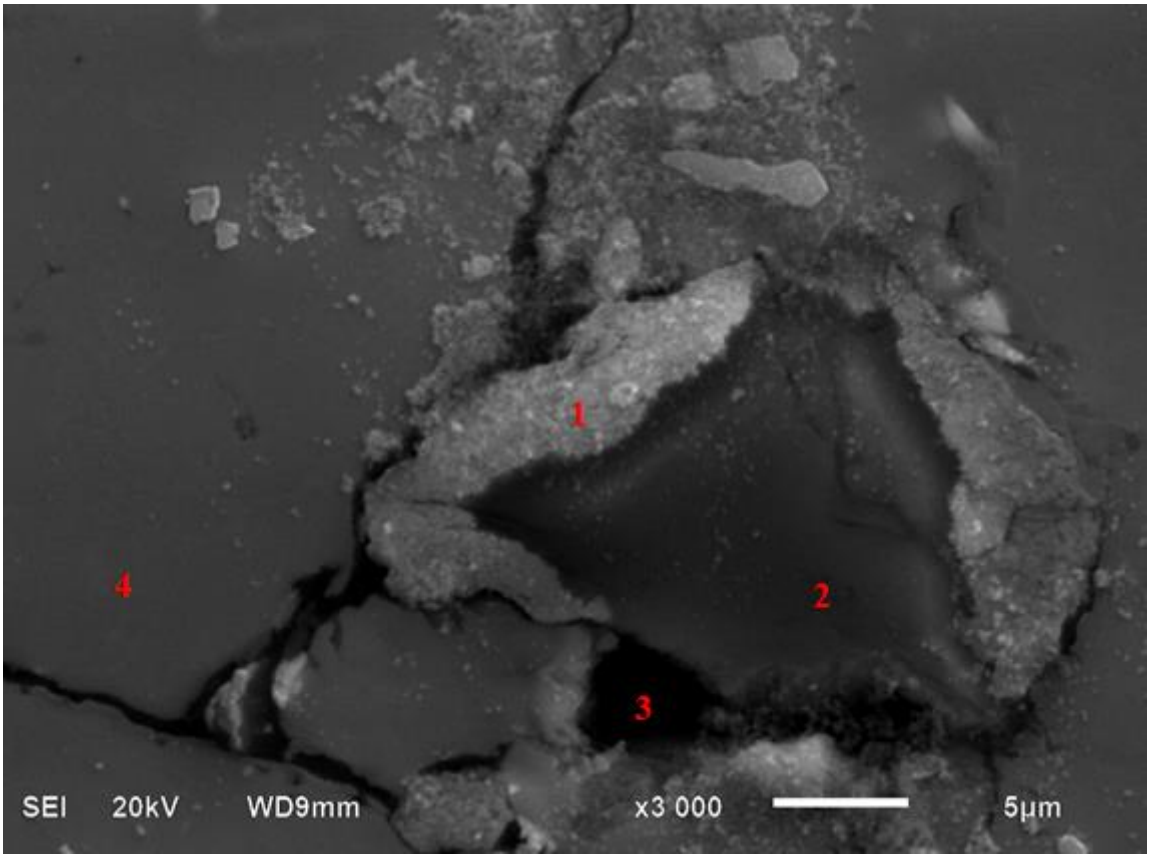

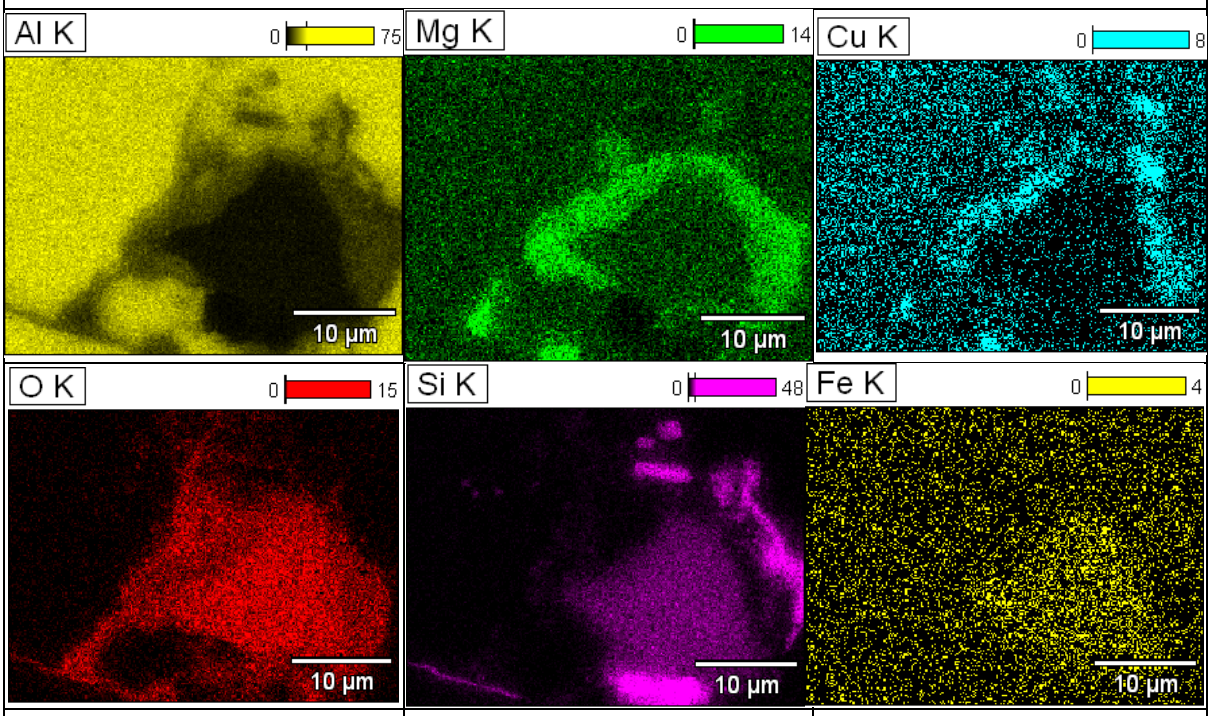

KEY ELEMENTS	**1:** Mg-Cu-O **2:** Fe-Si-O	**3:** Si-O **4:** Al

Figure 9-23: 3%wt Nanofil 116 Sample (438 Bars @ AD)**: LOCATION 2**

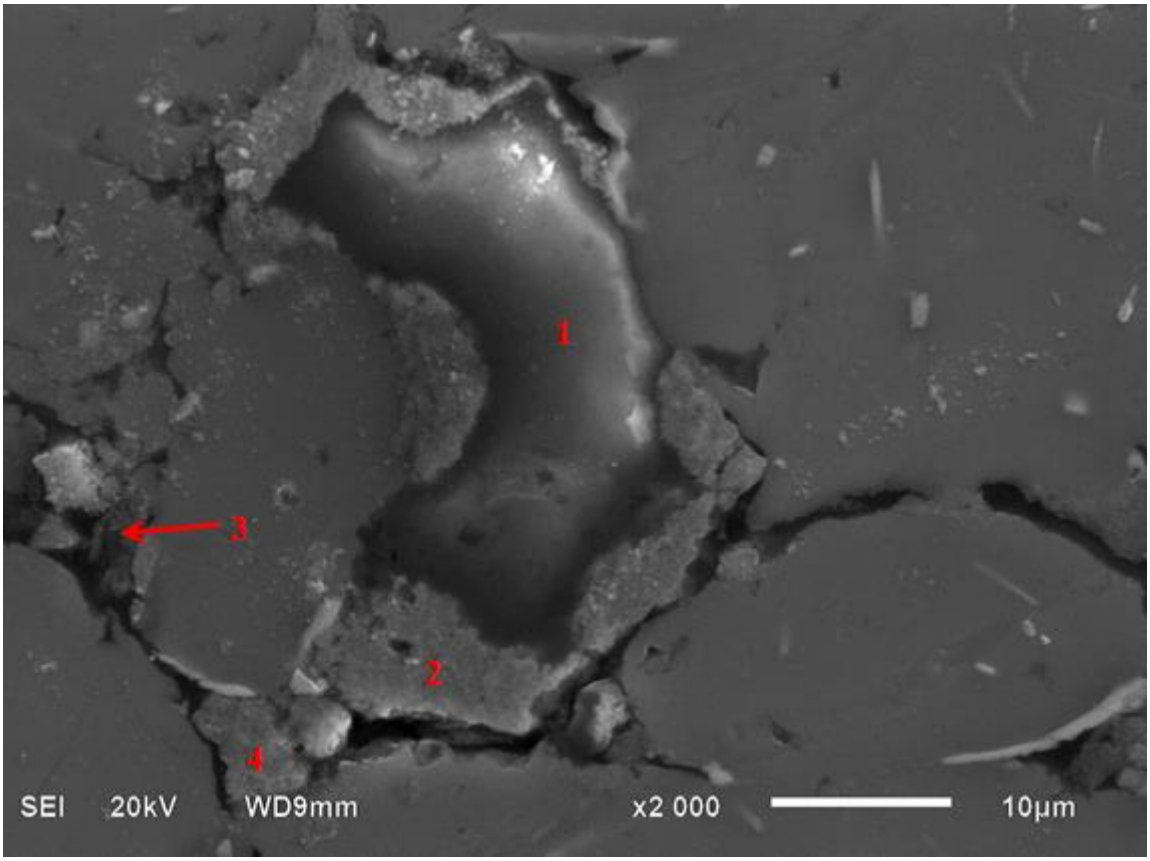

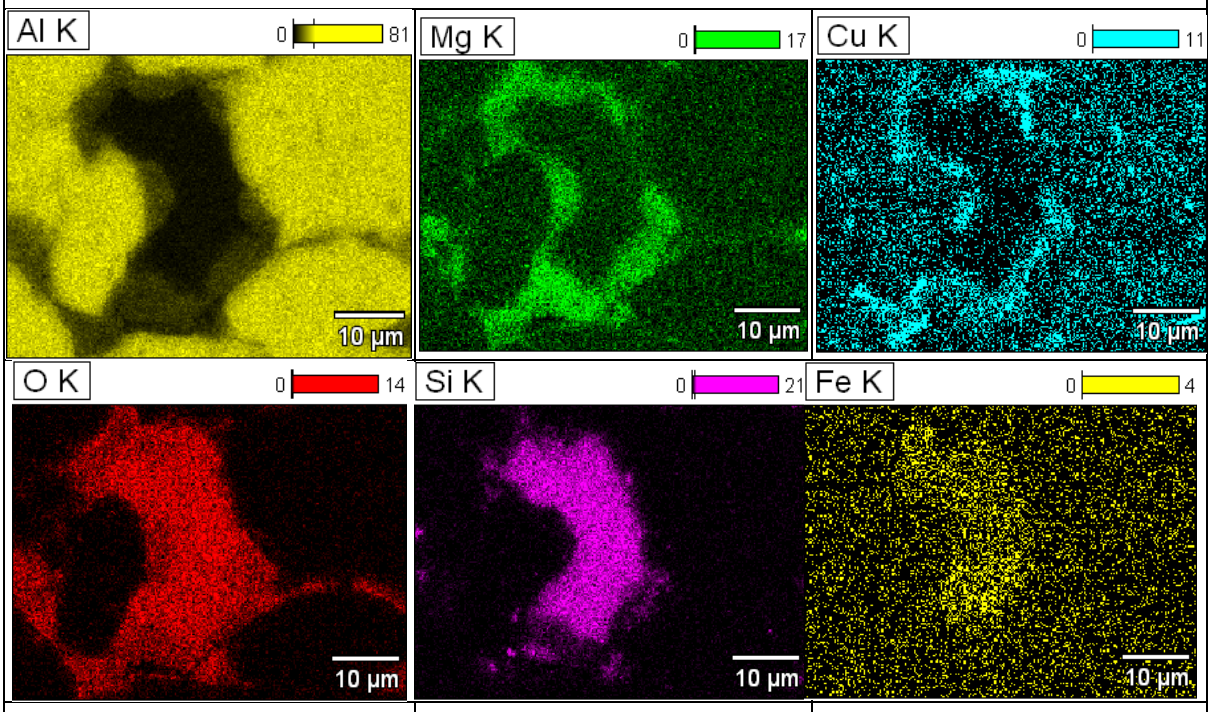

KEY ELEMENTS	**1:** Fe-Si-O **2:** Mg-Cu-O	**3:** Mg-O **4:** Mg-Cu-O

Figure 9-24: 3%wt Nanofil 116 Sample (438 Bars @ AD)**: LOCATION 3**

Even though the dark phase was observed to be having varying compositions as demonstrated, the phase was predominantly composed of Mg-O and Si-O. It was further observed that at 3%wt content *Nanofil 116*, Si-O was being formed preferentially compared to Mg-O. Possible factors contributing to this trend include: (1) This trend could suggest that, even though silicon could also be playing a role in breaking the Al_2O_3 layer, magnesium could be more active than silicon in facilitating that process through the nitridation process, (2) Since the heat of vaporization of magnesium (128kJ/mol.) [262] is equivalent to one third of the heat of vaporization of silicon (383 kJ/mol.) [247], it means that magnesium could easily be swept away from potential deposition sites as porosity increases due to higher contents of nanoclay, and (3) with 1%wt to 3%wt content of quartz in their formulation, the nanoclays already have a relatively higher content of silicon as compared to magnesium content. However, this advantage is minimized by virtue of the matrix alloy having higher magnesium content than silicon. With increased nanoclay contents, silicon is bound to be more than magnesium and thereby possibly over-shadow the effects of magnesium.

9.4 Summary

The Nanoclay-AMCs system can feasibly be processed. Key parameters include, amongst others, the choice of nanoclay, the relative composition and percentage weight content of nanoclay clay as compared to the matrix, the sintering profile and atmosphere, and the green compaction pressure. Use of nitrogen on its own as a sintering atmosphere yielded specimens with macro-cracks. The use of argon and introduction of nitrogen towards the end of the sintering stage is therefore recommended. Low contents of *Nanofil 116* and *Cloisite* Ca^{++}*DEV* are recommended in favour of high contents. Further modifications and/or advancement may improve the feasibility and favourable effectiveness of higher nanoclay contents and should be explored. TEM analysis may also give additional insights into the phases and interphase present in this Nanoclay-AMCs system.

CHAPTER 10:

CONCLUSIONS

10.0 Introduction

The objective of this study was to explore the efficacy of using nanoclays as a low-cost nanophased reinforcement system for aluminium and/or its alloys. In the study, an experimental approach was adopted. The study called for an understanding of the intrinsic nature of both the aluminium and/or its alloys on one hand and nannoclays on the other. Based on that understanding, potential processing technologies were identified, with powder metallurgy eventually emerging as the most preferred route of processing. Performance evaluation criteria revolved around comparative analysis with respect to the nanoclays effects on, among other aspects, the thermal, mechanical, machinability, and processability of the nanoclay-aluminium metal matrix composites. The experimental comparative study has successfully been completed with favourable results.

10.1 Materials analysis

Based on DSC TGA analysis, the nanoclays used in this study (*Nanofil 116* and *Cloisite* Ca^{++}*DEV*) were found to be functionally active upto a temperature of 650^0C, inclusive of a 200^0C temperature-window during which thermally-instigated chemical-reactions and/or transformations may be considered to occur. It was on basis of this temperature-dependent-stability of nanoclays that powder metallurgy or its variants was determined to be the most feasible processing route, i.e. the possibility of processing nanoclay-AMCs at temperatures below the liquidus temperature of the matrix.

TEM micrographs of plain AMB-2712 powder and *Nanofil 116* powder, respectively showed that both powders comprised of smooth-edged particles that seem to be predominantly agglomerated. The smooth edges for AMB-2712 alloy particles were attributed to the

associated gas atomization processing of the powder from molten stock. The agglomeration phenomenon is consistent with the behaviour of powders constituting very small particle sizes as validated by particle size analysis. Due to the adverse effect of agglomeration on the sinterability of powdered materials, a suitable method of eliminating such agglomerations would be appreciated. In that line of thought, ball-milling is hereby recommended.

10.2 Processing and characterization of Nanoclay-AMCs

10.2.1 Green compaction and sintering

High green compaction pressures were observed to hinder the delubrication process. Improvements in the sinterability of the AMCs were made by way of reducing the temperature-ramping-rate (from 10^0C/min. to 2^0C/min.) as well as providing a dedicated delubrication stage in the heating curve before the sintering stage. Favourable effect on densification was observed on specimen sintered in nitrogen atmosphere. However, these specimens were observed to be prone to cracking during the sintering process especially at high nanoclay contents. To avoid this macro-cracking trend, the specimens were sintered in argon and only exposed to nitrogen for a limited duration of time. I this way, the benefits densification benefits associated with nitridation were realized while mitigating the problem of macro-cracking. Under the processing conditions used in this study, nanoclay contents of 1%wt posted the better results than the reference samples across all evaluation platforms.

Supersolidus liquid phase sintering (SLPS) was observed to be sensitive to temperature and time variables, therefore calling for close regulation of the two, especially in the light of thermal behaviour modifications observed from the integration of nanoclays. Non-uniform load distribution during sintering was observed to infer into uneven stress distribution that possibly led to exudation in relatively thin members. Results from this study serve as a foundation for further explorations, developments, and process optimization efforts for the relatively new-found family of Nanoclay-AMCs.

10.2.2 Properties of Nanoclay AMCs

Structurally, nanoclay-aluminium composites displayed superior performance in terms of load bearing capacity and percentages elongation to fracture. Experimental results from the study showed that, with as low as 1% weight-content of nanoclay, the mechanical properties of the aluminium alloy used in the study were improved by more than 150% in terms of both the loading-bearing capacity and percentage elongation before fracture. Hardness of the material also increased with addition of 1%wt. content. Beyond this content, poor hardness results were observed and attributed to the effect of nanoclay of the material's thermodynamics. However, some regain of hardness was observed at nanoclay contents of above 5%wt and deemed to occur only after completion of a thermally instigated microstructural evolution, a process that was observed to be dependent on the percentage weight content of nanoclay.

From a heat transfer perspective, 1%wt nanoclay was observed to show a favourable 6.6^0C increase in the alloy's melting temperature. This was also affirmed by significant improvements in the alloy's thermal properties as reflected by a higher thermal conductivity, higher thermal diffusivity, lower specific heat capacity and small effect on thermal expansion / coefficient of thermal expansion. It was further demonstrated that the heat flow dynamics in composites can be modelled in a manner that links the observed thermal behaviour to the intrinsic properties of constituent chemical elements or compounds. In general, the superior performances of Nanoclay-AMCs underscore the suitability of nanoclays as a candidate reinforcement system in the making of novel AMCs for automotive engine applications where thermal management is a key design objective.

With reference to specimens containing 1%wt and 3%wt *Nanofil 116*, it was generally evident that for the same green-compaction pressure, increase in %wt content of *Nanofil-116* generally improved the surface finish. This was attributed to the effect of nanoclay acting as a filler and

also inducing some grain-refinement. In comparison to reference samples, topographical analysis of the machined surfaces showed no significant differences across this set of samples with low nanoclay content. However, surface finish results for samples with higher range of nanoclay contents (8%wt and 12.5%) were adversely affected, showing some grain-size vacant patches that had not been observed during microstructural analysis. These patches were considered to be as a result of (a) granular and/or particulate erosion during milling, (b) weak granular and/or inter-particle fusion, and (c) The effect of micro-cracks.

Microstructural analysis revealed significant precipitation of copper and silicon. Increasing the nanoclay content resulted into silicon precipitating as pure silicon crystals both at the grain boundaries and within the grains. This invariably points to the possibility that, since nanoclays such as those used in this study had chemical elements commonly used in commercial alloys, the nanoclays can actually be used in the formulation of some conventional alloys at elemental powder level. This in essence opens a new door to a new generation of low-cost nanophased AMCs.

10.3 Merits of the Proposed Nanoclay-AMCs

In summary, there are several merits of the proposed Nanofil 116 or Cloisite C++DEV Nanoclay-Al-Alloy-System especially with relevance to overcoming the limitations associated with currently available composites such as the ceramic, carbon fibre, carbon nanotube, fly ash, and even other nanoclay-based reinforced metal (Al) matrix composites. These merits include:

(1) Unlike other currently available nanoclays, Nanofil 116 and Cloisite C++DEV have significantly higher thresh-hold processing temperature that is close to the melting / processing temperature of Aluminium.

(2) Unlike most of the other reinforcement systems already tried on Aluminium, the proposed Nanoclays are relatively more economical and abundantly available as a natural resource in the earth's crust.

(3) The chemical elements in the proposed Nanoclays are significantly similar to those often found in currently existing aluminium alloys, especially Al, Si, and Mg. This study has proven that these elements as present in the proposed Nanoclays are chemically compatible with those in the Aluminium matrix. The proposed Nanoclays can thus be effectively used as substitute natural sources of these alloying elements.

(4) The current study has demonstrated that as minimal a quantity as 1%wt of the proposed Nanoclays is required to significantly improve ALL the studied properties of Aluminium and/or its Alloys including mechanical, machinability, and thermal properties.

(5) Unlike most of the existing competing reinforcement systems, the proposed Nanoclays are naturally available at nano-scale, thereby requiring no extra costs of processing from *micro*- to *nano*-scale towards realising the inherent advantages.

10.4 Future works

In addition to further investigating the effect of other commonly used process-optimization techniques, it is envisaged that exploring the following opportunities would be interesting.

(i) Ball-milling:

This has the potential to completely or significantly eliminate the challenge of particulate agglomeration and also induce mechanical welding of the nanoclays onto the matrix. It is anticipated that this will yield improved structural properties of the as-sintered specimens and also lower the required sintering temperature.

(ii) Heat treatment:

The precipitation observed was through natural aging. It would be interesting to tap into the full measure of benefits associated with heat-treatment of 2xxx series of aluminium alloys.

(iii) Processing route:

According to the supplier of AMB-2712 alloy powder that was used in this study as the matrix,

the powder was a blended powder except that copper was added to the blend as a proprietary copper / aluminium concentrated alloy powder. It would be interesting to explore the possibility of using a carrier ingredient into the formulation, e.g. integrate the nanoclays into a low-melting-point material such as tin before introducing it into the matrix.

(iv) Processing technology:

Amongst the known powder metallurgy avenues known to date, it would be interesting to use the spark plasma sintering technology, thereby tapping into its relatively lower sintering temperatures and shorter sintering times. This might potentially eliminate or minimize the observed grains disintegration resulting for the inherent thermal incubation when high nanoclay contents are used.

(v) Alternative formulation:

As a direct follow-up on the findings from this study, explore development of new formulation or blend of 2xxx series aluminium alloy using elemental powders of aluminium, copper, and nanoclay(s), where the latter powder serves as the sole source of magnesium and silicon.

- The possibilities are unlimited -

REFERENCES

1. Aalco. *Aluminium - specifications, properties, classifications, and classes, supplier data by Aalco*. 2005 [cited 2016 October 29, 2016]; Available from: http://www.azom.com/article.aspx?ArticleID=2863.
2. RUSAL, U. *How aluminium market works*. 2016 [cited 2016 5 November]; Available from: http://aluminiumleader.com/economics/how_aluminium_market_works/
3. AFSA. *Transport sector*. 2016 5/11/2016]; Available from: http://www.afsa.org.za/MarketSectors/Transport/tabid/139/Default.aspx.
4. Wikipedia-Contributors. *Metal matrix composite*. 14/09/2009 [cited 2009 14 September]; Available from: http://en.wikipedia.org/wiki/Metal_matrix_composite.
5. Kainer, K.U., *Basics of metal matrix composites*, in *Custom-made Materials for Automotive and Aerospace Engineering*, K.U. Kainer, Editor. 2006, Wiley-VCH: Weinheim, Chichester. p. 54.
6. Seleznev, M.L., et al., *Effect of Composition, Particle Size, and Heat Treatment on the Mechanical Properties of Al-4.5 wt.% Cu Based Alumina Particulate Reinforced Composites*. 1998, SAE International.
7. Maruyama, B., *Discontinuously reinforced aluminum: Current status and future direction.* JOM, 1999. **51**(11): p. 59-61.
8. Warner, A.E.M., J.A.E. Bell, and T.F. Stephenson, *Opportunities for new graphitic aluminium metal matrix composite.* Materials Science and Technology, 1998. **14**(9-10): p. 843-850.
9. Kaczmar, J., K. Pietrzak, and W. Włosiński, *The production and application of metal matrix composite materials.* Journal of Materials Processing Technology, 2000. **106**(1): p. 58-67.
10. Allison, J.E. and G.S. Cole, *Metal-matrix composites in the automotive industry: opportunities and challenges.* JOM Journal of the Minerals, Metals and Materials Society, 1993. **45**(1): p. 19-24.
11. Cole, G. and A. Sherman, *Light weight materials for automotive applications.* Materials characterization, 1995. **35**(1): p. 3-9.
12. Mayyas, A., et al., *Design for sustainability in automotive industry: A comprehensive review.* Renewable and Sustainable Energy Reviews, 2012. **16**(4): p. 1845-1862.
13. Institute, T.I.A. *Lightweight*. 2012 [cited 2016 4 November]; Available from: http://transport.world-aluminium.org/benefits/lightweight.html.
14. Aluminium, D. *Aluminium advantages: Efficiency*. 2016 [cited 2016 5 November]; Available from: http://www.drivealuminum.org/aluminum-advantages/efficiency/.
15. SBS. *Factbox: Carbon taxes around the world*. 2013; Available from: http://www.sbs.com.au/news/article/2013/10/29/factbox-carbon-taxes-around-world.
16. Institute, T.I.A. *Safe*. 2012 [cited 2016 4 November]; Available from: http://transport.world-aluminium.org/benefits/safe.html.
17. Institute, T.I.A. *Versatile*. 2012 [cited 2016 4 November]; Available from: http://transport.world-aluminium.org/benefits/versatile.html.
18. Padmavathi, C. and A. Upadhyaya, *Sintering Behaviour and Mechanical Properties of Al–Cu–Mg–Si–Sn Aluminum Alloy.* Transactions of the Indian Institute of Metals, 2011. **64**(4): p. 345-357.
19. Pandey, A., K. Kendig, and D. Miracle, *Development of a New Discontinuously Reinforced Aluminum for Space Applications.* Affordable Metal-Matrix Composites for High Performance Applications II, 2002: p. 35-45.
20. Zheng, Q., B. Wu, and R.G. Reddy, *In-Situ Processing of Al Alloy Composites.* Advanced Engineering Materials, 2003. **5**(3): p. 167-172.
21. Miracle, D.B., *Aeronautical applications of metal-matrix composites*, in *ASM handbook, Composites*, S.L. Donaldson, Editor. 2001, ASM International, Materials Park. p. 1043–1049.
22. Wood, J.V., et al., *Casting and mechanical properties of a reactively cast Al-TiB2 alloy.* Cast Metals, 1995. **8**(1): p. 57-64.

23. Cornie, J., *Advanced Pressure Infiltration Casting Technology Produces Near-Absolute Net-Shape Metal Matrix Composite Components Cost Competitively.* Materials Technology, 1995. **10**(3-4): p. 43-48.
24. Taleghani, M.J., E.R. Navas, and J.M. Torralba, *Microstructural and mechanical characterisation of 7075 aluminium alloy consolidated from a premixed powder by cold compaction and hot extrusion.* Materials & Design, 2014. **55**: p. 674-682.
25. Birol, Y. and O. Ilgaz, *Effect of cast and extruded stock on grain structure of EN AW 6082 alloy forgings.* Materials Science and Technology, 2014. **30**(7): p. 860-866.
26. Sjölander, E. and S. Seifeddine, *The heat treatment of Al–Si–Cu–Mg casting alloys.* Journal of Materials Processing Technology, 2010. **210**(10): p. 1249-1259.
27. Zhang, L.-J., et al., *High strength and good ductility at elevated temperature of nano-SiCp/Al2014 composites fabricated by semi-solid stir casting combined with hot extrusion.* Materials Science and Engineering: A, 2015. **626**: p. 338-341.
28. Zhang, P., et al., *Improved tensile properties of a new aluminum alloy for high pressure die casting.* Materials Science and Engineering: A, 2016. **651**: p. 376-390.
29. Ghasali, E., et al., *Vanadium carbide reinforced aluminum matrix composite prepared by conventional, microwave and spark plasma sintering.* Journal of Alloys and Compounds, 2016. **688, Part A**: p. 527-533.
30. Institute, T.I.A. *Cost effective*. 2012 [cited 2016 4 November]; Available from: http://transport.world-aluminium.org/benefits/cost-effective.html.
31. Institute, T.I.A. *Recyclable*. 2012 [cited 2016 4 November]; Available from: http://transport.world-aluminium.org/en/benefits/recyclable.html.
32. Institute, T.I.A. *Durable*. 2012 [cited 2016 4 November]; Available from: http://transport.world-aluminium.org/en/benefits/durable.html.
33. Institute, T.I.A. *Stylish*. 2012 [cited 2016 4 November]; Available from: http://transport.world-aluminium.org/en/benefits/stylish.html.
34. Bhandare, R.G. and P.M. Sonawane, *Preparation of Aluminium Matrix Composite by using Stir Casting Method & it's Characterization.* International Journal of Current Engineering and Technology ISSN, 2014: p. 2277-4106.
35. Surappa, M., *Aluminium matrix composites: Challenges and opportunities.* Sadhana, 2003. **28**(1-2): p. 319-334.
36. Kainer, K.U., *Metal matrix composites: custom-made materials for automotive and aerospace engineering*. 2006: John Wiley & Sons.
37. Wikipedia-Contributors. *Conservation of energy*. [cited 2017 27 July]; Available from: https://en.wikipedia.org/wiki/Conservation_of_energy.
38. Popely, R. *Should I worry about how hot my engine is running?* . [cited 2016 1 October]; Available from: https://www.cars.com/articles/should-i-worry-about-how-hot-my-engine-is-running-1420680334271/.
39. Wikipedia-Contributors. *Internal combustion engine cooling.* [cited 2017 7 June]; Available from: https://en.wikipedia.org/wiki/Internal_combustion_engine_cooling.
40. Davis, M. *What Is The Optimum Engine Oil Temperature?* . August 29, 2013.
41. Uddin, F., *Clays, nanoclays, and montmorillonite minerals.* Metallurgical and Materials Transactions A, 2008. **39**(12): p. 2804-2814.
42. *Thermal conductivity of some common materials and gases*. [cited 2017 17 July]; Available from: http://www.engineeringtool.box/thermal-conductivity-d_429.html.
43. Hasselman, D. and L.F. Johnson, *Effective thermal conductivity of composites with interfacial thermal barrier resistance.* Journal of Composite Materials, 1987. **21**(6): p. 508-515.
44. Khalaj, M.-J., et al., *Study of physical and mechanical properties of polypropylene nanocomposites for food packaging application: Nano-clay modified with iron nanoparticles.* Trends in Food Science & Technology, 2016. **51**: p. 41-48.

45. Mohan, T.P., J. Kuriakose, and K. Kanny, *Effect of nanoclay reinforcement on structure, thermal and mechanical properties of natural rubber–styrene butadine rubber (NR–SBR).* Journal of Industrial and Engineering Chemistry, 2011. **17**(2): p. 264-270.
46. Thabet, A., Y. Mobarak, and M. Bakry, *A review of nano-fillers effects on industrial polymers and their characteristics.* J. Eng. Sci, 2011. **39**: p. 377-403.
47. Khosravi, H. and R. Eslami-Farsani, *Enhanced mechanical properties of unidirectional basalt fiber/epoxy composites using silane-modified Na+-montmorillonite nanoclay.* Polymer Testing, 2016. **55**: p. 135-142.
48. GKN. *Materials*. [cited 2015 14 August]; Available from: http://engineershandbook.com/materials/index.htm.
49. *General physical properties*. [cited 2015 14 August]; Available from: http://engineershandbook.com/Materials/physical.htm.
50. Padmavathi, C. and A. Upadhyaya, *Densification, microstructure and properties of supersolidus liquid phase sintered 6711 Al-SiC metal matrix composites.* Science of Sintering, 2010. **42**(3): p. 363-382.
51. Yamaguchi, K., N. Takakura, and S. Imatani, *Compaction and sintering characteristics of composite metal powders.* Journal of Materials Processing Technology, 1997. **63**(1-3): p. 364-369.
52. Müller, S., et al. *Metal Matrix Composites: Properties of Sintered P/M Aluminium Composites*. in *European Congress and Exhibition on Powder Metallurgy. European PM Conference Proceedings*. 2011. The European Powder Metallurgy Association.
53. Zeng, R.J., B. Rand, and 曾人杰, *Particle size distribution, powder agglomerates and their effects on sinterability of ultrafine alumina powders.* Journal of Material Science Technology, 2000. **16**(4): p. 393 – 396.
54. Forrester, J.S., et al., *Effect of mechanical milling on the sintering behaviour of alumina.* Journal of Australian Ceramic Society, 2008. **44**(1): p. 47-52.
55. Iwaoka, T. and M. Nakamura, *Effect of Compaction Temperature on Sinterability of Magnesium and Aluminum Powder Mixtures by Warm Compaction Method.* MATERIALS TRANSACTIONS, 2011. **52**(5): p. 943-947.
56. Chua, A.S. and D.P. Bishop, *Effects of compaction technique on processing response of aluminium PM alloys.* Canadian Metallurgical Quarterly, 2014. **53**(4): p. 407-415.
57. Kapylou, A.V., et al., *Effect of compacting pressure, powder degassing and thermobaric treatment on densification and properties of nanocrystalline titanium nitride.* Processing and Application of Ceramics, 2009. **3**(3): p. 161-166.
58. Ghosh, A. and S. Chatterjee, *Effect of Al2O3 Content and Process Variables on Structure and Properties of Al-Al2O3 Compacts.* Journal of Minerals and Materials Characterization and Engineering, 2014. **2**: p. 121-128.
59. Ma, J. and L.C. Lim, *Effect of particle size distribution on sintering of agglomerate-free submicron alumina powder compacts.* Journal of the European Ceramic Society, 2002. **22**(13): p. 2197-2208.
60. Gokce, A. and F. Findik, *Mechanical and physical properties of sintered aluminum powders.* Journal of achievements in materials and manufacturing engineering, 2008. **30**(2): p. 157-164.
61. German, R.M., *Supersolidus liquid-phase sintering of prealloyed powders.* Metallurgical and Materials transactions A, 1997. **28**(7): p. 1553-1567.
62. Lefebvre, L.-P., Y. Thomas, and B. White, *Effects of lubricants and compacting pressure on the processability and properties of aluminum P/M parts.* Journal of light metals, 2002. **2**(4): p. 239-246.
63. Inada, S., T. Kimura, and T. Yamaguchi, *Effect of green compact structure on the sintering of alumina.* Ceramics International, 1990. **16**(6): p. 369-373.

64. *Thermal Properties*. [cited 2015 14 August]; Available from: http://engineeringhandbook.com/Materials/thermal.htm.
65. *Mechanical properties*. [cited 2015 14 August]; Available from: http://engineershandbook.com/Materials/mechanical.htm.
66. Suetin, D.V., I.R. Shein, and A.L. Ivanovskii, *Structural, elastic and electronic properties and formation energies for hexagonal (W0.5Al0.5)C in comparison with binary carbides WC and Al4C3 from first-principles calculations.* Physica B: Condensed Matter, 2008. **403**(17): p. 2654-2661.
67. Broekaert, S., et al., *Heat transfer in premixed spark ignition engines part I: Identification of the factors influencing heat transfer.* Energy, 2016. **116**: p. 380-391.
68. De Cuyper, T., et al., *Heat transfer in premixed spark ignition engines part II: Systematic analysis of the heat transfer phenomena.* Energy, 2016. **116**: p. 851-860.
69. *Copper*. [cited 2015 14 August]; Available from: http://engineershandbook.com/Materials/copper.htm
70. Miracle, D.B., *Metal matrix composites for space systems: current uses and future opportunities.* Affordable Metal-Matrix Composites for High Performance Applications II, 2001: p. 1-22.
71. Cheng, S. and R. Vachon, *The prediction of the thermal conductivity of two and three phase solid heterogeneous mixtures.* International Journal of Heat and Mass Transfer, 1969. **12**(3): p. 249-264.
72. Budiansky, B., *Thermal and thermoelastic properties of isotropic composites.* Journal of composite Materials, 1970. **4**(3): p. 286-295.
73. Crane, R. and R. Vachon, *A prediction of the bounds on the effective thermal conductivity of granular materials.* International Journal of Heat and Mass Transfer, 1977. **20**(7): p. 711-723.
74. Nomura, S. and T.-W. Chou, *Bounds of effective thermal conductivity of short-fiber composites.* Journal of Composite Materials, 1980. **14**(2): p. 120-129.
75. Hatta, H. and M. Taya, *Thermal conductivity of coated filler composites.* Journal of applied physics, 1986. **59**(6): p. 1851-1860.
76. Powell, B.R., et al., *Effect of Thermal Expansion Mismatch on the Thermal Diffusivity of Glass-Ni Composites.* Journal of the American Ceramic Society, 1980. **63**(9-10): p. 581-586.
77. Hasselman, D., et al., *Heat conduction characteristics of a carbon-fibre-reinforced lithia-alumino-silicate glass-ceramic.* Journal of materials science, 1987. **22**(2): p. 701-709.
78. Willis, J., *Bounds and self-consistent estimates for the overall properties of anisotropic composites.* Journal of the Mechanics and Physics of Solids, 1977. **25**(3): p. 185-202.
79. Hasselman, D.P.H., *Effect of cracks on thermal conductivity.* Journal of Composite Materials, 1978. **12**: p. 403-407.
80. Lepeshkin, A., *Investigations of thermal barrier coatings for turbine parts*. 2012: INTECH Open Access Publisher.
81. Christensen, A., E.A. Asche, and E.A. Carter, *Atomic-level properties of thermal barrier coatings: Characterization of metal-ceramic interfaces*. 2001, DTIC Document.
82. Padture, N.P., M. Gell, and E.H. Jordan, *Thermal barrier coatings for gas-turbine engine applications.* Science, 2002. **296**(5566): p. 280-284.
83. Toriz, F., A. Thakker, and S. Gupta, *Flight service evaluation of thermal barrier coatings by physical vapor deposition at 5200 H.* Surface and coatings technology, 1989. **39**: p. 161-172.
84. Wortman, D., B. Nagaraj, and E. Duderstadt, *Thermal barrier coatings for gas turbine use.* Materials Science and Engineering: A, 1989. **120**: p. 433-440.
85. Ugarteche, C.V., et al., *Effect of Microstructure on the Thermal Properties of Sintered Iron-copper Composites.* Materials Research, 2015. **18**: p. 1176-1182.
86. *Wrought Aluminium Alloys*. [cited 2015 14 August]; Available from: http://engineershandbook.com/Materials/wrought_aluminium_alloys.htm.

87. Davis, J.R. and A.S. Handbook, *Aluminium and aluminium alloys. 1993.* Materials Park, Ohio ASM International.
88. Rauta, V., C. Cingi, and J. Orkas, *Effect of Annealing and Metallurgical Treatments on Thermal Conductivity of Aluminium Alloys.* International Journal of Metalcasting, 2016. **10**(2): p. 157-171.
89. Lumley, R.N., et al., *The role of alloy composition and T7 heat treatment in enhancing thermal conductivity of aluminum high pressure diecastings.* Metallurgical and Materials Transactions A, 2013. **44**(2): p. 1074-1086.
90. *Straightening Aluminium Cylinder Heads*. [cited 2015 14 August]; Available from: http://www.acl.co.nz/wp-content/uploads/19-Straightening-Aluminium-Cylinder-Heads.pdf.
91. Garat, M. and G. Laslaz, *Improved aluminum alloys for common rail diesel cylinder heads.* AFS Transactions, 2007. **115**: p. 89-96.
92. Daud, M., et al., *Graphene/layered double hydroxides nanocomposites: A review of recent progress in synthesis and applications.* Carbon, 2016. **104**: p. 241-252.
93. Zhao, J., et al., *Grain Refinement Efficiency in Commercial-Purity Aluminum Influenced by the Addition of Al-4Ti Master Alloys with Varying TiAl3 Particles.* Materials, 2016. **9**(11): p. 869.
94. Torralba, J.M., C.E. da Costa, and F. Velasco, *P/M aluminum matrix composites: an overview.* Journal of Materials Processing Technology, 2003. **133**(1–2): p. 203-206.
95. Grayson, G.N., G.B. Schaffer, and J.R. Griffiths, *Observations of oxide films on fatigue fracture surfaces of a sintered 2xxx series aluminium alloy.* Materials Science and Engineering: A, 2007. **454–455**: p. 99-103.
96. Bishop, D.P., et al., *Powder metallurgy processing of 2xxx and 7xxx series aluminium alloys.* Canadian Metallurgical Quarterly, 2011. **50**(3): p. 246-252.
97. Rohatgi, P.K., D. Weiss, and N. Gupta, *Applications of fly ash in synthesizing low-cost MMCs for automotive and other applications.* JOM, 2006. **58**(11): p. 71-76.
98. Guo, R.Q., P.K. Rohatgi, and D. Nath, *Preparation of aluminium-fly ash particulate composite by powder metallurgy technique.* Journal of Materials Science, 1997. **32**(15): p. 3971-3974.
99. Basumallick, A. and S. Ghosh, *Processing of in situ aluminium matrix composites by micropyretic reactive sintering.* Materials and manufacturing processes, 2007. **22**(6): p. 692-695.
100. Yan, M., et al., *Secondary phases and interfaces in a nitrogen-atmosphere sintered Al alloy: Transmission electron microscopy evidence for the formation of AlN during liquid phase sintering.* Acta Materialia, 2010. **58**(17): p. 5667-5674.
101. Mwamba, I. and L. Chown, *The use of titanium hydride in blending and mechanical alloying of Ti-Al alloys.* Journal of the Southern African Institute of Mining and Metallurgy, 2011. **111**(3): p. 159-165.
102. *Sintered aluminium powder (SAP)*. [cited 2017 19 January]; Available from: http://www.totalmateria.com/Article76.htm.
103. Sumida, M., *Recent Advances in New Magnesium Alloy Design by Alloying.* Recent Patents on Materials Science, 2011. **4**(2): p. 94-105.
104. Rawal, S.P., *Metal-matrix composites for space applications.* JOM Journal of the Minerals, Metals and Materials Society, 2001. **53**(4): p. 14-17.
105. Bayraktar, E. and D. Katundi, *Development of a new aluminium matrix composite reinforced with iron oxide (Fe3O4).* Journal of achievements in materials and manufacturing engineering, 2010. **38**(1): p. 7-14.
106. BATE, M.L.Z.Z., *Effect of heat treatment on the microstructure and mechanical properties of piston alloys.* Materiali in tehnologije, 2013. **47**(5): p. 585-591.
107. *Ceramics Process Systems*. 14/09/2009]; Available from: www.alsic.com.
108. Dudhmande, A., et al., *Sintering and properties of new P/M aluminium alloys and composites.* Proc. of Euro PM2005, EPMA in Prague, Shrewsbury: EPMA, 2005: p. 293-298.

109. Santanach, J.G., et al., *Spark plasma sintering of alumina: Study of parameters, formal sintering analysis and hypotheses on the mechanism (s) involved in densification and grain growth.* Acta Materialia, 2011. **59**(4): p. 1400-1408.
110. Manohar, H., et al., *Effect of Heat Treatment on Damping Properties of Nanoclay Particulate Reinforced MMCs.* International Journal of Recent Technologies and Engineering (IJRTE), 2012. **1**(1): p. 38-42.
111. Manohar, H., N. Chikkanna, and B.U. Maheswar Gowd, *Effect of addition of nanoclay on Wear behaviour of Al/nanoclay metal matrix composites.* International Journal of Science Research, 2013. **1**(4): p. 363-369.
112. Manohar, H., N. Chikkanna, and B.U.M. Gowd, *Effect of Addition of Nanoclay on Machinability of Al/Nanoclay Metal Matrix Composites.* International Journal of Engineering Research and Applications (IJERA), 2012. **2**(5): p. 1360-1370.
113. Visser, D., *A Comparison of Manufacturing Technologies in the Connecting Rod Industry.* Submission to FIERF 06-06, 2008. **8**.
114. Sala, G., *Technology-driven design of MMC squeeze cast connecting-rods.* Science and Technology of Advanced Materials, 2002. **3**(1): p. 45-57.
115. Kevorkijan, V., *AZ80 and ZC71/SiC/12p closed die forgings for automotive applications: technical and economic assessment of possible mass production.* Materials science and technology, 2003. **19**(10): p. 1386-1390.
116. Ivanchev, L., et al., *Rheo-processing of semi-solid metal alloys: a new technology for manufacturing automotive and aerospace components.* South African Journal of Science, 2008. **104**(7-8): p. 257-259.
117. Shen, Z., et al., *Spark plasma sintering of alumina.* Journal of the American Ceramic Society, 2002. **85**(8): p. 1921-1927.
118. Liu, D., et al., *Spark plasma sintering of nanostructured aluminum: Influence of tooling material on microstructure.* Metallurgical and Materials Transactions A, 2013. **44**(4): p. 1908-1916.
119. Tokita, M. *Mechanism of spark plasma sintering*. in *Proceeding of NEDO International Symposium on Functionally Graded Materials*. 1999. Japan.
120. Suárez, M., et al., *Challenges and opportunities for spark plasma sintering: a key technology for a new generation of materials*. 2013: INTECH Open Access Publisher.
121. Schaffer, G. and B. Hall, *The influence of the atmosphere on the sintering of aluminum.* Metallurgical and Materials Transactions A, 2002. **33**(10): p. 3279-3284.
122. Arik, H., *Effect of mechanical alloying process on mechanical properties of α-Si3N4 reinforced aluminum-based composite materials.* Materials & Design, 2008. **29**(9): p. 1856-1861.
123. Pieczonka, T., et al., *Dimensional behaviour of aluminium sintered in different atmospheres.* Materials Science and Engineering: A, 2008. **478**(1): p. 251-256.
124. Johar, B., et al. *Effect of Sintering Environment to the Physical Properties of Al/Calcined Dolomite Composite*. in *Proceeding of 1st International Conference on Sustainable Materials (ICoSM2007)*. 2007.
125. Engineers-Edge-LLC. *Aluminium tempers, specifications and designations*. [cited 2017 19 January]; Available from: http://www.engineersedge.com/aluminum_tempers.htm.
126. Groover, M.P., *Fundamentals of modern manufacturing: materials, processes, and systems*. 3rd ed. 2007, Hoboken, N.J: J. Wiley & Sons.
127. Xu, K., et al., *An experimental investigation of micro-machinability of aluminum alloy 2024 using Ti (C 7 N 3)-based cermet micro end-mill tools.* Journal of Materials Processing Technology, 2016. **235**: p. 13-27.
128. Behera, R. and G. Sutradhar, *Machinability of LM6/SiCp metal matrix composites with tungsten carbide cutting tool inserts.* ARPN journal of Engineering and Applied Sciences, 2012. **7**(2): p. 216-221.

129. Gonçalves, R.A. and M.B. da Silva, *Influence of Copper Content on 6351 Aluminum Alloy Machinability.* Procedia Manufacturing, 2015. **1**: p. 683-695.
130. Zhang, Q., et al., *Studies on machinability of Al/Sip+ SiCp composite materials.* Journal of materials science, 2007. **42**(14): p. 5845-5850.
131. Prakash, J.U., T. Moorthy, and J.M. Peter, *Experimental investigations on machinability of aluminium alloy (A413)/Flyash/B4C hybrid composites using wire EDM.* Procedia Engineering, 2013. **64**: p. 1344-1353.
132. Songmene, V., et al., *Machining and machinability of aluminum alloys*, in *aluminium alloys, theory and applications*. 2011, InTech.
133. Wikipedia-Contributors. *Machinability*. [cited 2012 5 September]; Available from: http://en.wikipedia.org/wiki/machinability.
134. Zhang, Q., *Mechanical Behavior of Cu/Al multilayers fabricated by Accumulative Roll-Bonding (ARB) processing*. 2013: University of Nevada, Reno.
135. Senthil, P., T. Selvaraj, and K. Sivaprasad, *Influence of turning parameters on the machinability of homogenized Al–Cu/TiB2 in situ metal matrix composites.* The International Journal of Advanced Manufacturing Technology, 2013. **67**(5-8): p. 1589-1596.
136. Manna, A. and B. Bhattacharayya, *Influence of machining parameters on the machinability of particulate reinforced Al/SiC–MMC.* The International Journal of Advanced Manufacturing Technology, 2005. **25**(9): p. 850-856.
137. Rathod, P., S. Aravindan, and V. Rao, *Performance evaluation of novel micro-textured tools in improving the machinability of aluminum alloy (Al 6063).* Procedia Technology, 2016. **23**: p. 296-303.
138. Roy, P., et al., *Machinability study of pure aluminium and Al–12% Si alloys against uncoated and coated carbide inserts.* International Journal of Refractory Metals and Hard Materials, 2009. **27**(3): p. 535-544.
139. Chattopadhyay, A., et al., *Wettability and machinability study of pure aluminium towards uncoated and coated carbide cutting tool inserts.* Surface and Coatings Technology, 2009. **203**(8): p. 941-951.
140. Muthukrishnan, N., M. Murugan, and K.P. Rao, *An investigation on the machinability of Al-SiC metal matrix composites using pcd inserts.* The International Journal of Advanced Manufacturing Technology, 2008. **38**(5): p. 447-454.
141. Guru, P., S. Panigrahi, and G.J. Ram, *Enhancing strength, ductility and machinability of a Al–Si cast alloy by friction stir processing.* Journal of Manufacturing Processes, 2015. **18**: p. 67-74.
142. Demir, H. and S. Gündüz, *The effects of aging on machinability of 6061 aluminium alloy.* Materials & Design, 2009. **30**(5): p. 1480-1483.
143. Altınkök, N., *Investigation of mechanical and machinability properties of Al2O3/SiCp reinforced Al-based composite fabricated by stir cast technique.* Journal of Porous Materials, 2015. **22**(6): p. 1643-1654.
144. Rohatgi, P. and B. Schultz, *Lightweight metal matrix nanocomposites–stretching the boundaries of metals.* Material Matters, 2007. **2**(4): p. 16-20.
145. Behera, R., et al., *Study on Machinability of Aluminium Silicon Carbide Metal Matrix Composites.* Journal of Minerals & Materials Characterization & Engineering, 2011. **10**(10): p. 923-939.
146. Garg, H.K., et al., *Hybrid Metal Matrix Composites and further improvement in their machinability-A Review.* International Journal of Latest Research in Science and Technology, 2012. **1**(1): p. 36-44.
147. Olovsjö, S., et al., *Methodology for evaluating effects of material characteristics on machinability—theory and statistics-based modelling applied on Alloy 718.* The International Journal of Advanced Manufacturing Technology, 2012. **59**(1): p. 55-66.

148. Atuanya, C., A. Ibhadode, and I. Dagwa, *Effects of breadfruit seed hull ash on the microstructures and properties of Al–Si–Fe alloy/breadfruit seed hull ash particulate composites.* Results in Physics, 2012. **2**: p. 142-149.
149. Casati, R. and M. Vedani, *Metal matrix composites reinforced by nano-particles—a review.* Metals, 2014. **4**(1): p. 65-83.
150. Yilmaz, G., *The effects of temperature on the characteristics of kaolinite and bentonite.* Scientific Research and Essays, 2011. **6**(9): p. 1928-1939.
151. Sritharan, T. and H. Li, *Influence of titanium to boron ratio on the ability to grain refine aluminium-silicon alloys.* Journal of Materials Processing Technology, 1997. **63**(1-3): p. 585-589.
152. Kaiser, M., et al., *Effect of Grain Refinement Through Minor Additions of Scandium and Zirconium on the Machinability of Al–Mg Alloys.* Journal of The Institution of Engineers (India): Series D, 2013. **94**(1): p. 17-24.
153. Srikanth, B.G. and G. Amarnath, *Characterization of aluminium reinforced with tungsten carbide particulate and flyash metal matrix composites.* International Journal of Engineering Research & Technology., 2015. **4**(05): p. 623-627.
154. Müller, S., et al., *Properties of sintered P/M aluminium composites.* Proc. EuroPM, 2011: p. 325-330.
155. Sharma, A., Y. Shin, and J.-P. Jung, *Influence of Various Additional Elements in Al Based Filler Alloys For Automotive and Brazing Industry.* 대한용접· 접합학회지, 2015. **33**(5): p. 1-8.
156. Kent, D., G. Schaffer, and J. Drennan, *Age hardening of a sintered Al–Cu–Mg–Si–(Sn) alloy.* Materials Science and Engineering: A, 2005. **405**(1): p. 65-73.
157. Abdulsahib, Y.M., *Effect of Copper Addition on the Microstructure and Mechanical Properties of Al-Si Alloy.* Al-Qadisiya Journal For Engineering Sciences, 2014: p. 366-381.
158. Oh, M.C. and A. Byungmin, *Effect of Mg composition on sintering behaviors and mechanical properties of Al–Cu–Mg alloy.* Transactions of Nonferrous Metals Society of China, 2014. **24**: p. s53-s58.
159. Salleh, M.S., M.Z. Omar, and J. Syarif, *The effects of Mg addition on the microstructure and mechanical properties of thixoformed Al–5% Si–Cu alloys.* Journal of Alloys and Compounds, 2015. **621**: p. 121-130.
160. Thirugnanam, A., et al., *Effect of Mg on the fracture characteristics of cast Al–7Si–Mg alloys.* Materials Science and Engineering: A, 2007. **445**: p. 405-414.
161. Nnakwo, K.C., et al., *Effect of magnesium and manganese on the secondary phase and mechanical properties of aluminium-4% copper alloy.* International Journal of Engineering Research & Technology., 2014. **3**(8): p. 1267-1276.
162. Nam, S.W. and D.H. Lee, *The effect of Mn on the mechanical behavior of Al alloys.* Metals and Materials International, 2000. **6**(1): p. 13-16.
163. Saud, S.N., et al., *Effects of Mn additions on the structure, mechanical properties, and corrosion behavior of Cu-Al-Ni shape memory alloys.* Journal of materials engineering and performance, 2014. **23**(10): p. 3620-3629.
164. Ji, S., et al., *Effect of iron on the microstructure and mechanical property of Al–Mg–Si–Mn and Al–Mg–Si diecast alloys.* Materials Science and Engineering: A, 2013. **564**: p. 130-139.
165. Davami, P., N. Varahram, and S. Kim, *On the effect of hydrogen and Fe on reproducibility of tensile properties in cast Al–Si–Mg alloys.* Materials Science and Engineering: A, 2013. **565**: p. 278-284.
166. Dons, A.L., et al., *On the effect of additions of Cu and Mg on the ductility of AlSi foundry alloys cast with a cooling rate of approximately 3K/s.* Materials Science and Engineering: A, 2005. **413**: p. 561-566.
167. Haruna, A.I. and I.U. Abhulimen, *Effect Of Macro Additions Of Zinc And Nickel On The Mechanical And Microstructural Properties Of A Modified 7xxx Aluminium Alloy.* International Journal of Scientific & Technology Research, 2014. **3**(9): p. 94-99.

168. Kalhapure, M.G. and P.M. Dighe, *Impact of silicon content on mechanical properties of aluminum alloys.* Int. J. Sci. Res, 2015. **4**: p. 38-40.
169. Kumar, V., H. Mehdi, and A. Kumar, *Effect of Silicon content on the Mechanical Properties of Aluminum Alloy.* International Research Journal of Engineering and Technology, 2015. **2**(4): p. 1326-1330.
170. Mathai, B., et al., *Effect of Silicon on Microstructure and Mechanical Properties of Al-Si Piston Alloys.* International Journal of Engineering Trends and Technology, 2015. **29**(6): p. 299-303.
171. Elzanaty, H., *Effect of different Si content on the mechanical properties in al-based alloy*. International Journal of Research in Engineering & Technology (IMPACT: IJRET), 2014. **2**(7): p. 49-54.
172. Savaşkan, T. and A. Aydıner, *Effects of silicon content on the mechanical and tribological properties of monotectoid-based zinc–aluminium–silicon alloys.* Wear, 2004. **257**(3): p. 377-388.
173. Kumari, S.S., R. Pillai, and B. Pai, *Role of calcium in aluminium based alloys and composites.* International materials reviews, 2005. **50**(4): p. 216-238.
174. Mondal, D., et al., *Effect of calcium addition on the microstructure and compressive deformation behaviour of 7178 aluminium alloy.* Materials & Design, 2011. **32**(5): p. 2803-2812.
175. Belov, N.A., E.A. Naumova, and T.K. Akopyan, *Effect of Calcium on Structure, Phase Composition and Hardening of Al-Zn-Mg Alloys Containing up to 12wt.% Zn.* Materials Research, 2015. **18**(6): p. 1384-1391.
176. Jaradeh, M. and T. Carlberg, *Effect of titanium additions on the microstructure of DC-cast aluminium alloys.* Materials Science and Engineering: A, 2005. **413**: p. 277-282.
177. Hirsch, J., *Recent development in aluminium for automotive applications.* Transactions of Nonferrous Metals Society of China, 2014. **24**(7): p. 1995-2002.
178. Meng, Y., et al., *Effect of vanadium on the microstructures and mechanical properties of an Al–Mg–Si–Cu–Cr–Ti alloy of 6XXX series.* Journal of Alloys and Compounds, 2013. **573**: p. 102-111.
179. Zhang, J.-c., et al., *Effect of Zr addition on microstructure and properties of Al–Mn–Si–Zn-based alloy.* Transactions of Nonferrous Metals Society of China, 2014. **24**(12): p. 3872-3878.
180. Kashyap, K., *Effect of zirconium addition on the recrystallization behaviour of a commercial Al-Cu-Mg alloy.* Bulletin of Materials Science, 2001. **24**(6): p. 643-648.
181. Easton, M. and D. Stjohn, *Grain refinement of aluminum alloys: Part I. the nucleant and solute paradigms—a review of the literature.* Metallurgical and Materials Transactions A, 1999. **30**(6): p. 1613-1623.
182. Easton, M. and D. StJohn, *Grain refinement of aluminum alloys: Part II. Confirmation of, and a mechanism for, the solute paradigm.* Metallurgical and Materials Transactions A, 1999. **30**(6): p. 1625-1633.
183. Schaffer, G., et al., *The effect of trace elements on the sintering of an Al–Zn–Mg–Cu alloy.* Acta materialia, 2001. **49**(14): p. 2671-2678.
184. Sercombe, T. and G. Schaffer, *On the use of trace additions of Sn to enhance sintered 2xxx series Al powder alloys.* Materials Science and Engineering: A, 1999. **268**(1): p. 32-39.
185. Kaufman, J.G. and E.L. Rooy, *Aluminum alloy castings: properties, processes, and applications*. 2004: Asm International.
186. Ahmed, G.S., et al., *Microstructure Analysis and Evaluation of Mechanical Properties of Nickel Based Super Alloy CCA617.* Materials Today: Proceedings, 2015. **2**(4-5): p. 1260-1269.
187. Naeem, H.T., et al., *The influence of nickel and tin additives on the microstructural and mechanical properties of Al-Zn-Mg-Cu Alloys.* Advances in Materials Science and Engineering, 2014. **2014**.
188. Ramnath, B.V., et al., *Aluminium metal matrix composites–a review.* Rev. Adv. Mater. Sci, 2014. **38**(5): p. 55-60.

189. Rahman, M.H. and H.M. Al Rashed, *Characterization of silicon carbide reinforced aluminum matrix composites.* Procedia Engineering, 2014. **90**: p. 103-109.
190. Sujan, D., et al., *Physio-mechanical Properties of Aluminium Metal Matrix Composites Reinforced with Al2O3 and SiC.* World Academy of Science, Engineering and Technology, International Journal of Chemical, Molecular, Nuclear, Materials and Metallurgical Engineering, 2012. **6**(8): p. 678-681.
191. Kok, M., *Production and mechanical properties of Al 2 O 3 particle-reinforced 2024 aluminium alloy composites.* Journal of Materials Processing Technology, 2005. **161**(3): p. 381-387.
192. Yılmaz, O. and S. Buytoz, *Abrasive wear of Al 2 O 3-reinforced aluminium-based MMCs.* Composites Science and Technology, 2001. **61**(16): p. 2381-2392.
193. Swamy, A., et al., *Effect of particulate reinforcements on the mechanical properties of Al6061-WC and Al6061-Gr MMCs.* Journal of Minerals and Materials Characterization and Engineering, 2011. **10**(12): p. 1141-1152.
194. Dyzia, M. and J. Śleziona, *Aluminium matrix composites reinforced with AlN particles formed by in situ reaction.* Archives of Materials Science and Engineering, 2008. **31**(1): p. 17-20.
195. Wang, J., et al., *Properties of submicron AlN particulate reinforced aluminum matrix composite.* Materials & Design, 2009. **30**(1): p. 78-81.
196. Oñoro, J., *High-temperature mechanical properties of aluminium alloys reinforced with titanium diboride (TiB 2) particles.* Rare Metals, 2011. **30**(2): p. 200-205.
197. Suresh, S., N. Shenbag, and V. Moorthi, *Aluminium-titanium diboride (Al-TiB2) metal matrix composites: challenges and opportunities.* Procedia Engineering, 2012. **38**: p. 89-97.
198. Okafor, E. and V. Aigbodion, *Effect of Zircon Silicate Reinforcements on the Microstructure and Properties of as Cast Al-4.5 Cu Matrix Particulate Composites Synthesized via Squeeze Cast Route.* Tribology in Industry, 2010. **32**(2): p. 31-37.
199. Shirvanimoghaddam, K., et al., *Effect of B 4 C, TiB 2 and ZrSiO 4 ceramic particles on mechanical properties of aluminium matrix composites: experimental investigation and predictive modelling.* Ceramics International, 2016. **42**(5): p. 6206-6220.
200. Thandalam, S.K., S. Ramanathan, and S. Sundarrajan, *Synthesis, microstructural and mechanical properties of ex situ zircon particles (ZrSiO 4) reinforced Metal Matrix Composites (MMCs): a review.* Journal of Materials Research and Technology, 2015. **4**(3): p. 333-347.
201. Madheswaran, K., S. Sugumar, and B. Elamvazhudi, *Mechanical Characterization of Aluminium–Boron Carbide Composites with Influence of Calcium Carbide Particles.* International Journal of Emerging Technology and Advanced Engineering, 2015. **5**(7): p. 492-496.
202. Gopal Krishna, U., K. Sreenivas Rao, and B. Vasudeva, *Effect of boron carbide reinforcement on aluminium matrix composites.* International Journal of Metallurgical & Materials Science and Engineering (IJMMSE) ISSN: p. 41-48.
203. Ghasali, E., et al., *Investigation on microstructural and mechanical properties of B 4 C–aluminum matrix composites prepared by microwave sintering.* Journal of Materials Research and Technology, 2015. **4**(4): p. 411-415.
204. Patidar, D. and R. Rana, *Effect of B 4 C particle reinforcement on the various properties of aluminium matrix composites: a survey paper.* Materials Today: Proceedings, 2017. **4**(2): p. 2981-2988.
205. Nie, C.-Z., et al., *Production of boron carbide reinforced 2024 aluminum matrix composites by mechanical alloying.* Materials transactions, 2007. **48**(5): p. 990-995.
206. Elgallad, E., et al., *Effects of additives on the microstructures and tensile properties of a new Al-Cu based alloy intended for automotive castings.* AFS Transactions, American Foundary Society, Paper, 2010: p. 10-42.
207. Davami, P., S. Kim, and N. Varahram, *Effects of hydrogen and oxides on tensile properties of Al–Si–Mg cast alloys.* Materials Science and Engineering: A, 2012. **552**: p. 36-47.

208. Rana, R., R. Purohit, and S. Das, *Reviews on the influences of alloying elements on the microstructure and mechanical properties of aluminum alloys and aluminum alloy composites.* International Journal of Scientific and Research Publications, 2012. **2**(6): p. 1-7.
209. Molina, R., P. Amalberto, and M. Rosso, *Mechanical characterization of aluminium alloys for high temperature applications Part 2: Al-Cu, Al-Mg alloys.* Metallurgical Science and Technology, 2011. **29**(2): p. 5-13.
210. Zeren, M., *Effect of copper and silicon content on mechanical properties in Al–Cu–Si–Mg alloys.* Journal of Materials Processing Technology, 2005. **169**(2): p. 292-298.
211. Remøe, M.S., et al., *The effect of alloying elements on the ductility of Al-Mg-Si alloys.* Materials Science and Engineering: A, 2017. **693**: p. 60-72.
212. Schodek, D.L., P. Ferreira, and M.F. Ashby, *Nanomaterials, nanotechnologies and design: an introduction for engineers and architects*. 2009: Butterworth-Heinemann.
213. Youseffi, M. and N. Showaiter, *PM processing of elemental and prealloyed 6061 aluminium alloy with and without common lubricants and sintering aids.* Powder metallurgy, 2006. **49**(3): p. 240-252.
214. Castellanos, A., *The relationship between attractive interparticle forces and bulk behaviour in dry and uncharged fine powders.* Advances in Physics, 2005. **54**(4): p. 263-376.
215. Kruth, J.-P., et al., *Binding mechanisms in selective laser sintering and selective laser melting.* Rapid prototyping journal, 2005. **11**(1): p. 26-36.
216. Aifantis, E.C., *Gradient effects at macro, micro, and nano scales.* Journal of the Mechanical Behavior of Materials, 1994. **5**(3): p. 355-375.
217. Cervantes-Uc, J.M., et al., *Thermal degradation of commercially available organoclays studied by TGA–FTIR.* Thermochimica Acta, 2007. **457**(1): p. 92-102.
218. *Assessed Al-Cu phase diagram*. [cited 2012 15 September]; Available from: http://d2vlcm61l7u1fs.cloudfront.net/media%2F94a%2F94a938af-387c-4c1b-9615-1e4a2edf3fcf%2Fphp3bADjW.png.
219. Mai, T. and A. Spowage, *Characterisation of dissimilar joints in laser welding of steel–kovar, copper–steel and copper–aluminium.* Materials Science and Engineering: A, 2004. **374**(1): p. 224-233.
220. Padmavathi, C., A. Upadhyaya, and D. Agrawal, *Effect of atmosphere and heating mode on sintering of 6711 and 7775 alloys.* Materials Research Innovations, 2011. **15**(4): p. 294-301.
221. Fouad, M.J. and M.K. Abbass, *Fabrication and Characterization of Al-Si Matrix Hybrid composites Reinforced with Nanoparticles Al 2 O 3+ TiO 2.* 2016.
222. Min, K.H., et al., *Liquid phase sintering of the commercial 2xxx series Al blended powder.* Journal of alloys and compounds, 2006. **419**(1): p. 290-293.
223. Ganesh, N.R. *Powder Metallurgy – Basics and Applications*. [cited 2017 8 July]; Available from: www.iitg.ernet.in/engfac/ganu/public_html/Powdermetallurgy.pdf.
224. Yei, D.-R., et al., *Enhanced thermal properties of PS nanocomposites formed from inorganic POSS-treated montmorillonite.* Polymer, 2004. **45**(8): p. 2633-2640.
225. Wikipedia-Contributors. *Archimedes' principle*. 21 July 2017 August 9, 2017]; Available from: https://en.wikipedia.org/w/index.php?title=Archimedes%27_principle&oldid=791621957.
226. Baniassadi, M., et al., *Mechanical and thermal behavior of nanoclay based polymer nanocomposites using statistical homogenization approach.* Composites science and technology, 2011. **71**(16): p. 1930-1935.
227. Sahin, Y., *Preparation and some properties of SiC particle reinforced aluminium alloy composites.* Materials & design, 2003. **24**(8): p. 671-679.
228. *Surface Roughness - MiSUMi*. [cited 2011 12 June]; Available from: http://vn.misumi-ec.com/pdf/tech/press/pr1167_1168.pdf.
229. Lumley, R., T. Sercombe, and G. Schaffer, *Surface oxide and the role of magnesium during the sintering of aluminum.* Metallurgical and Materials Transactions A, 1999. **30**(2): p. 457-463.

230. Lumley, R. and G. Schaffer, *The effect of solubility and particle size on liquid phase sintering.* Scripta Materialia, 1996. **35**(5): p. 589-595.
231. Zuzana, O., et al., *Effect of thermal treatment on the bentonite properties.* Arh. Teh. Nauke, 2012. **7**: p. 49-56.
232. Önal, M. and Y. Sarıkaya, *Thermal behavior of a bentonite.* Journal of Thermal Analysis and Calorimetry, 2007. **90**(1): p. 167-172.
233. *What is Bentonite? What is Montmorillonite II Clay Minerals*. [cited 2015 September 26]; Available from: http://www.eytonsearth.org/bentonite-montmorillonite.php.
234. Dontsova, K.M., et al., *Influence of Exchangeable Cations on Water Adsorption by Soil Clays.* Soil Science Society of America Journal, 2004. **68**: p. 1218-1227.
235. Da Silva, R.A. and D.J. Guerra, *Use of natural and modified kaolinite/ilite as adsorbent for removal methylene blue dye from aqueous solution.* Journal of the Chilean Chemical Society, 2013. **58**(1): p. 1517-1519.
236. Bukka, K., J. Miller, and J. Shabtai, *FTIR study of deuterated montmorillonites: Structural features relevant to pillared clay stability.* Clays and Clay Minerals, 1992. **40**(1): p. 92-102.
237. *Functional groups: O-Si-H and Si-H* [FTIR spectra] [cited 2017 14 August]; Available from: http://cdn.iopscience.com/images/1402-4896/87/3/035701/Full/pscr453228f7_online.jpg.
238. Holtzer, M., A. Bobrowski, and B. Grabowska, *Montmorillonite: a comparison of methods for its determination in foundry bentonites.* Metalurgija, 2011. **50**(2): p. 119-122.
239. Szabo, L., et al., *Spectroscopic and theoretical study of amlodipine besylate.* Journal of Molecular Structure, 2009. **924**: p. 385-392.
240. *Silicones – Compounds and Properties*. [cited 2015 30 September]; Available from: https://www.wacker.com/cms/media/publications/downloads/6415_EN.pdf.
241. German, R.M. *An Update on the Theory of Supersolidus Liquid Phase Sintering*. in *Proceedings Sintering*. 2003.
242. Ferkel, H. and R. Hellmig, *Effect of nanopowder deagglomeration on the densities of nanocrystalline ceramic green bodies and their sintering behaviour.* Nanostructured Materials, 1999. **11**(5): p. 617-622.
243. Wikipedia-Contributors. *Second law of thermodynamics*. 3 August 2017 [cited 2017 8 August]; Available from: https://en.wikipedia.org/w/index.php?title=Second_law_of_thermodynamics&oldid=793682783.
244. Vander Voort, G.F. and J. Asensio-Lozano, *The al-si phase diagram.* Microscopy and Microanalysis, 2009. **15**(S2): p. 60-61.
245. Wikipedia-Contributors. *Entropy*. 1 August 2017 8 August 2016]; Available from: https://en.wikipedia.org/w/index.php?title=Entropy&oldid=793415618.
246. Qu, X.-h., et al., *Review of metal matrix composites with high thermal conductivity for thermal management applications.* Progress in Natural Science: Materials International, 2011. **21**(3): p. 189-197.
247. Wikipedia-Contributors. *Silicon*. 2017 August 15, 2017 [cited 2017 August 14]; Available from: https://en.wikipedia.org/w/index.php?title=Silicon&oldid=795473947.
248. Wikipedia-Contributors. *Silicon dioxide*. 2017 August 12, 2017 [cited 2017 August 14]; Available from: https://en.wikipedia.org/w/index.php?title=Silicon_dioxide&oldid=795240472.
249. Kirkpatrick, A.T. *Heat transfer mechanisms*. [cited 2015 24 August]; Available from: https://www.engr.colostate.edu/~allan/heat_trans/page4/page4f.html.
250. Kirkpatrick, A.T. *Heat transfer resistance modelling*. [cited 2015 24 August]; Available from: https://www.engr.colostate.edu/~allan/heat_trans/page4/page4f.html.
251. Wikipedia-Contributors. *Copper*. 6 August 2017 [cited 2017 8 August]; Available from: https://en.wikipedia.org/w/index.php?title=Copper&oldid=794267723.

252. Wikipedia-Contributors. *Magnesium*. 1 August 2017 8 August 2017]; Available from: https://en.wikipedia.org/w/index.php?title=Magnesium&oldid=793344151.
253. Song, G. and A. Atrens, *Understanding Magnesium Corrosion.* Advanced Engineering Materials, 2003. **5**(12): p. 837-858.
254. *Modulus of Elasticity or Young's Modulus - and Tensile Modulus for common Materials*. August 8, 2017]; Available from: http://www.engineeringtoolbox.com/young-modulus-d_417.html.
255. Schaffer, G., et al., *The effect of the atmosphere and the role of pore filling on the sintering of aluminium.* Acta Materialia, 2006. **54**(1): p. 131-138.
256. Schaffer, G. *Powder processed aluminium alloys*. in *Materials forum*. 2004.
257. Kimura, A., et al., *Reduction mechanism of surface oxide in aluminum alloy powders containing magnesium studied by x-ray photoelectron spectroscopy using synchrotron radiation.* Applied physics letters, 1997. **70**(26): p. 3615-3617.
258. Kondoh, K., A. Kimura, and R. Watanabe, *Effect of Mg on sintering phenomenon of aluminium alloy powder particle.* Powder Metallurgy, 2001. **44**(2): p. 161-164.
259. *How and why alloying elements are added to aluminum.* July 14, 2017; Available from: http://www.alcotec.com/us/en/education/knowledge/qa/How-and-why-alloying-elements-are-added-to-aluminum.cfm.
260. Lu, S.-Z. and A. Hellawell, *The mechanism of silicon modification in aluminum-silicon alloys: impurity induced twinning.* Metallurgical Transactions A, 1987. **18**(10): p. 1721-1733.
261. McCaldin, J. and H. Sankur, *Diffusivity and Solubility of Si in the Al Metallization of Integrated Circuits.* Applied Physics Letters, 1971. **19**(12): p. 524-527.
262. Wikipedia-Contributors. *Magnesium*. 2017 August, 1 [cited 2017 August 17]; Available from: https://en.wikipedia.org/w/index.php?title=Magnesium&oldid=793344151.

APPENDICES:

Appendix A1: Supplier's Information Sheet for *AMB-2712* Al alloy.

Appendix A2: Supplier's Information Sheet for *AMB-2906* Al alloy.

Appendix A3: Supplier's Information Sheet for *AMB-6711* Al alloy.

Appendix B1: Supplier's Information Sheet for *Nanofil 116*.

Appendix B2: Supplier's Information Sheet for *Cloisite Ca^{++}DEV*.

AMPAL, INC.

408 US Highway 202
Flemington, New Jersey 08822

Telephone: (908) 782-5454
Fax: (908) 782-3489

ALUMINUM POWDER (AL-3.8Cu-0.75Si-1.0Mg)
AMPALLOY AMB 2712

CHEMICAL ANALYSIS:

Al	= BALANCE
Cu	= 3.6 – 4%
Si	= 0.6 – 0.9%
Mg	= 0.8 – 1.2%

LUBRICATED PROPERTIES 1.5% Acrawax		
Briquetting Pressure T.S.I	Green Density g/cc	Green Strength P.S.I
6	2.4	400
8	2.53	675
12	2.55	700
14	2.6	775

SINTERED PROPERTIES (2.65 g/cc sintered density)			
NO HEAT TREAT		HEAT TREATED	
Temp. F	Hardness R/H	Temp. F	Hardness R/H
1075	96		
1100	97	1100	111
1150	96	1150	107
1175	78	1175	N/A

The graphical illustrations of MECHANICAL PROPERTIES DATA show the results obtained from laboratory tests of sintered compacts. The test specimens used were Metal Powder Industries Federation (M.P.I.F) Standard Transverse bars and Tensile bars.

Test bars were sintered on graphite for 30 minutes at the temperature shown, in pure nitrogen atmosphere having a dew point of minus 40F. Heat treated bars were additionally heated for 30 minutes at 950 F, quenched in cold water and aged for 20 hours at 350 F.

AMPALLOY AMB 2712 - SINTERED PROPERTIES

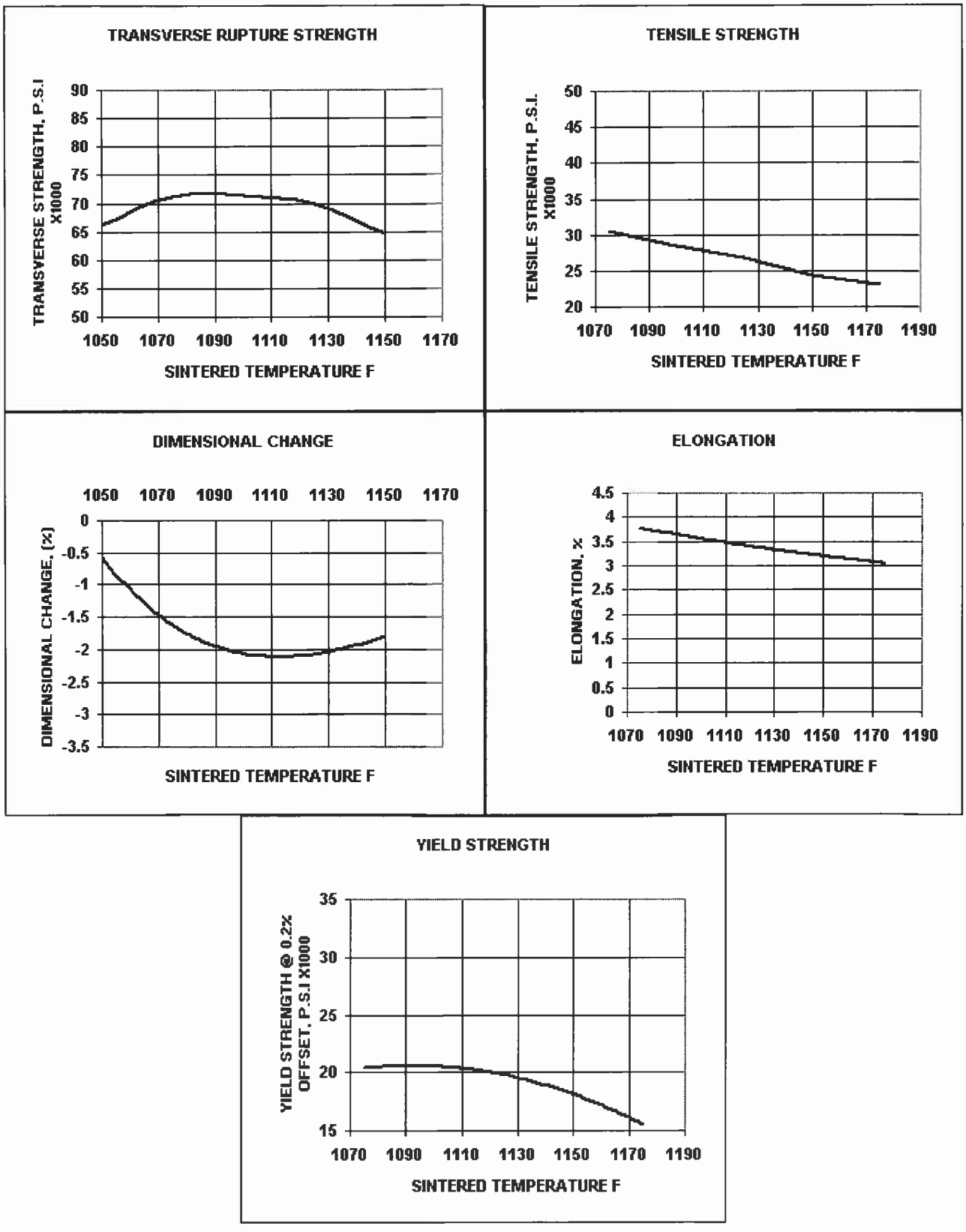

All graphical presentations of data represent average of data produced at a green density of 2.55g/cc. Sintering temperatures are shown on each graph.

AMPALLOY AMB 2712 - HEAT TREATED PROPERTIES

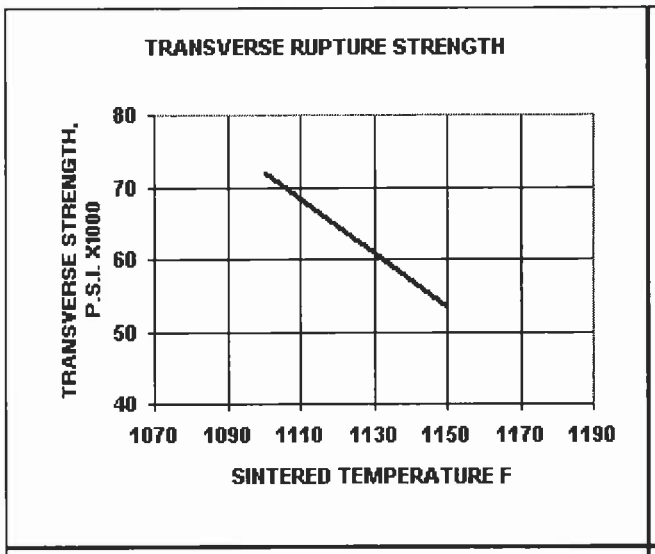

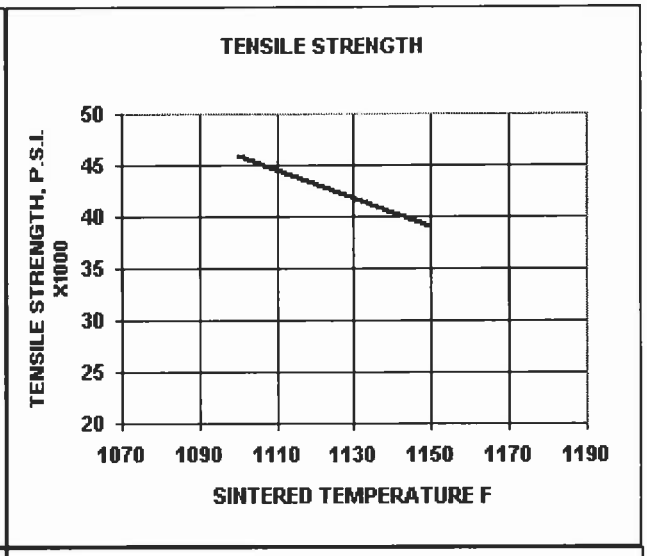

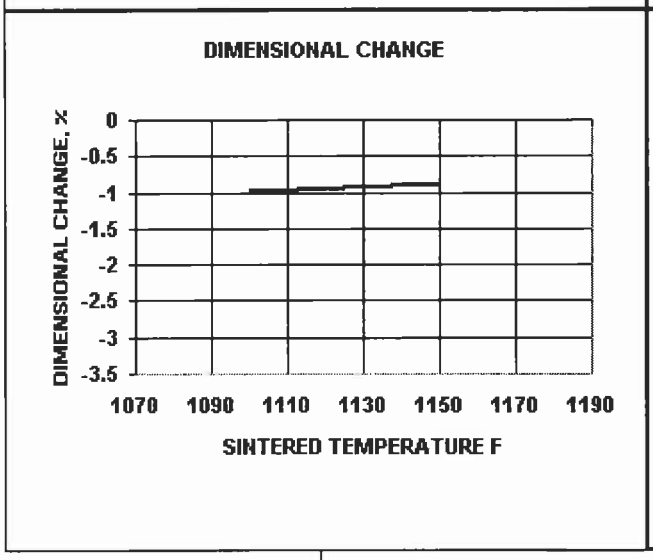

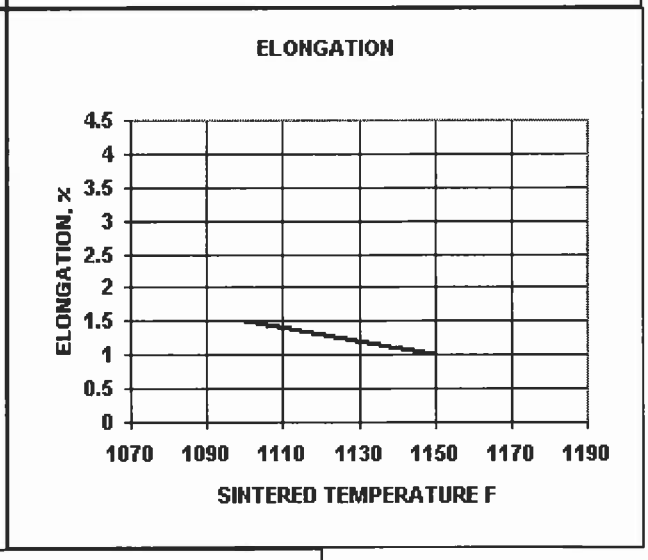

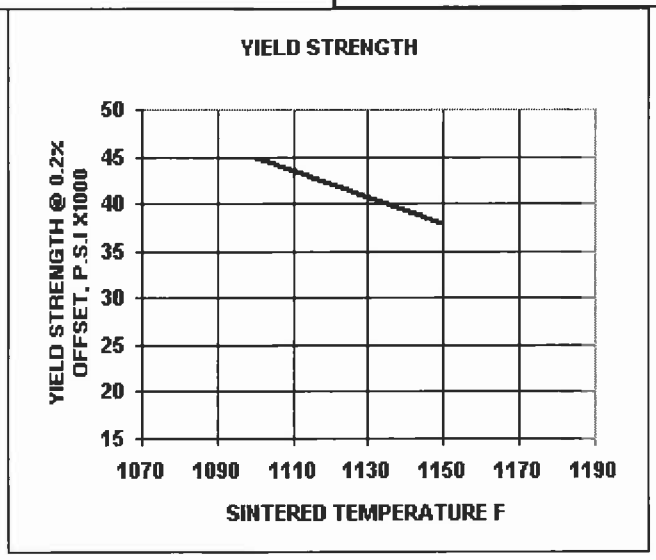

All graphical presentations of data represent average of data produced at 10, 20, and 30TSI compacting pressures.
Sintering temperatures are shown on each graph.

AMPAL, INC.

P.O. Box 2270
Flemington, New Jersey 08822

Telephone: (908) 782-5454
Fax: (908) 782-3489

AMPALLOY AMB 2905

CERAMIC REINFORCED ALUMINUM POWDER (AL-2.98Cu-0.26Si-1.2Mg-0.6Sn)

METALLIC COMPONENTS (wt. %) :

Al = BALANCE
Cu = 2.8 – 3.2
Si = 0.15 – 0.35
Mg = 1.0 – 1.4
Sn = 0.45 – 0.75

NON METALLIC COMPONENTS (vol. %) :

Ceramic = 5 %

LUBRICATED PROPERTIES
1.5% Lubricant

Briquetting Pressure T.S.I	Green Density g/cc	Green Strength P.S.I
15	2.61	1400
20	2.66	1500
25	2.67	1530

SINTERED PROPERTIES
(Sintering temperature 1150F)
NO HEAT TREAT

Briquetting Pressure T.S.I	Sintered Density g/cc	Rockwell Hardness B Scale
15	2.73	42
20	2.73	42
25	2.73	37

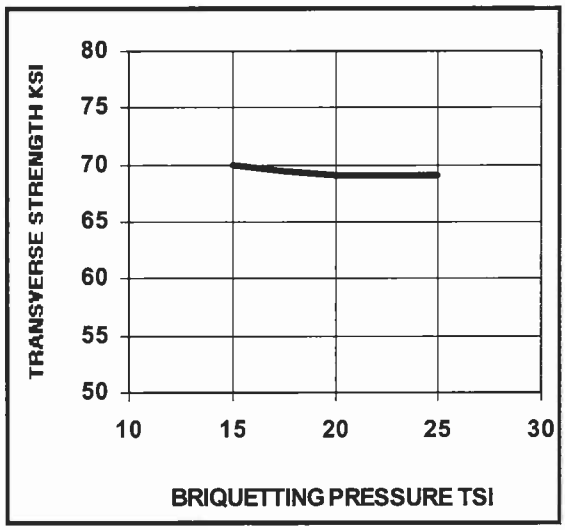

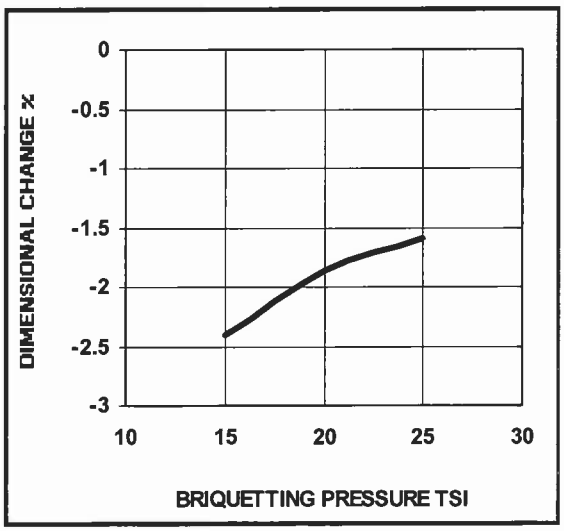

The graphical illustrations of MECHANICAL PROPERTIES DATA show the results obtained from laboratory tests of sintered compacts. The test specimens used were Metal Powder Industries Federation (M.P.I.F) Standard Transverse bars. Test bars were sintered on graphite for 45 minutes at 1150F, in pure nitrogen atmosphere having a dew point of minus -40F.

AMPAL, INC.

408 US Highway 202
Flemington, New Jersey 08822

Telephone: (908) 782-5454
Fax: (908) 782-3489

ALUMINUM POWDER (AL-0.25Cu-0.8Si-1.0Mg)
AMPALLOY AMB 6711

CHEMICAL ANALYSIS:

Al = BALANCE
Cu = 0.15 – 0.35%
Si = 0.65 – 0.9%
Mg = 0.8 – 1.2%

LUBRICATED PROPERTIES 1.5% Acrawax		
Briquetting Pressure T.S.I	Green Density g/cc	Green Strength P.S.I
6	2.3	400
8	2.45	650
11	2.47	700
14	2.53	800

SINTERED PROPERTIES (2.62 g/cc sintered density)			
NO HEAT TREAT		HEAT TREATED	
Temp. F	Hardness R/H	Temp. F	Hardness R/H
1125	62		
1100	76	1100	98
1150	78	1150	103
1175	80	1175	N/A

The graphical illustrations of MECHANICAL PROPERTIES DATA show the results obtained from laboratory tests of sintered compacts. The test specimens used were Metal Powder Industries Federation (M.P.I.F) Standard Transverse bars and Tensile bars.

Test bars were sintered on graphite for 30 minutes at the temperature shown, in pure nitrogen atmosphere having a dew point of minus 40F. Heat treated bars were additionally heated for 30 minutes at 950 F, quenched in cold water and aged for 20 hours at 350 F.

AMPALLOY AMB 6711 - SINTERED PROPERTIES

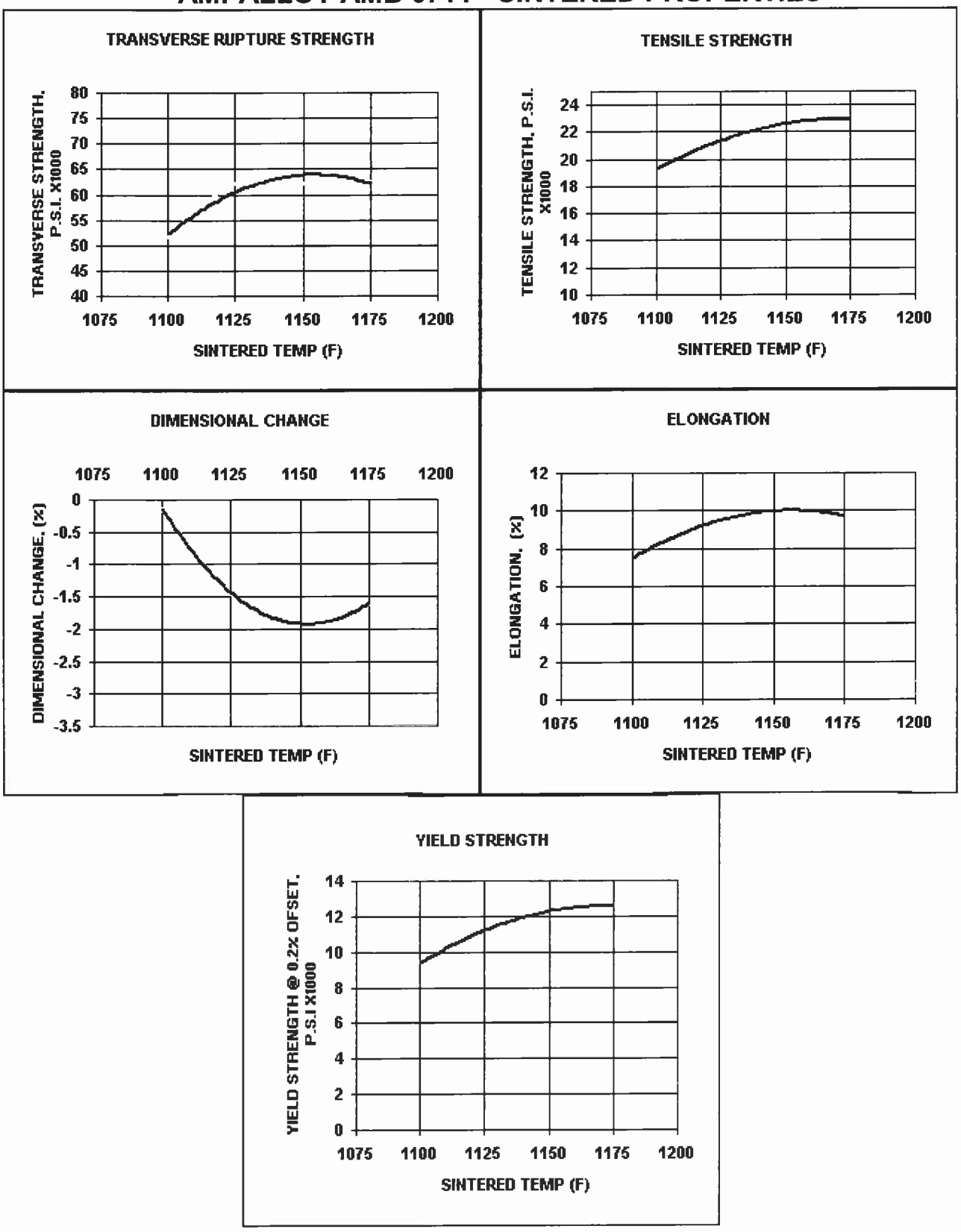

All graphical presentations of data represent average of data produced at a green density of 2.50g/cc. Sintered temperatures are shown on each graph.

AMPALLOY AMB 6711 - HEAT TREATED PROPERTIES

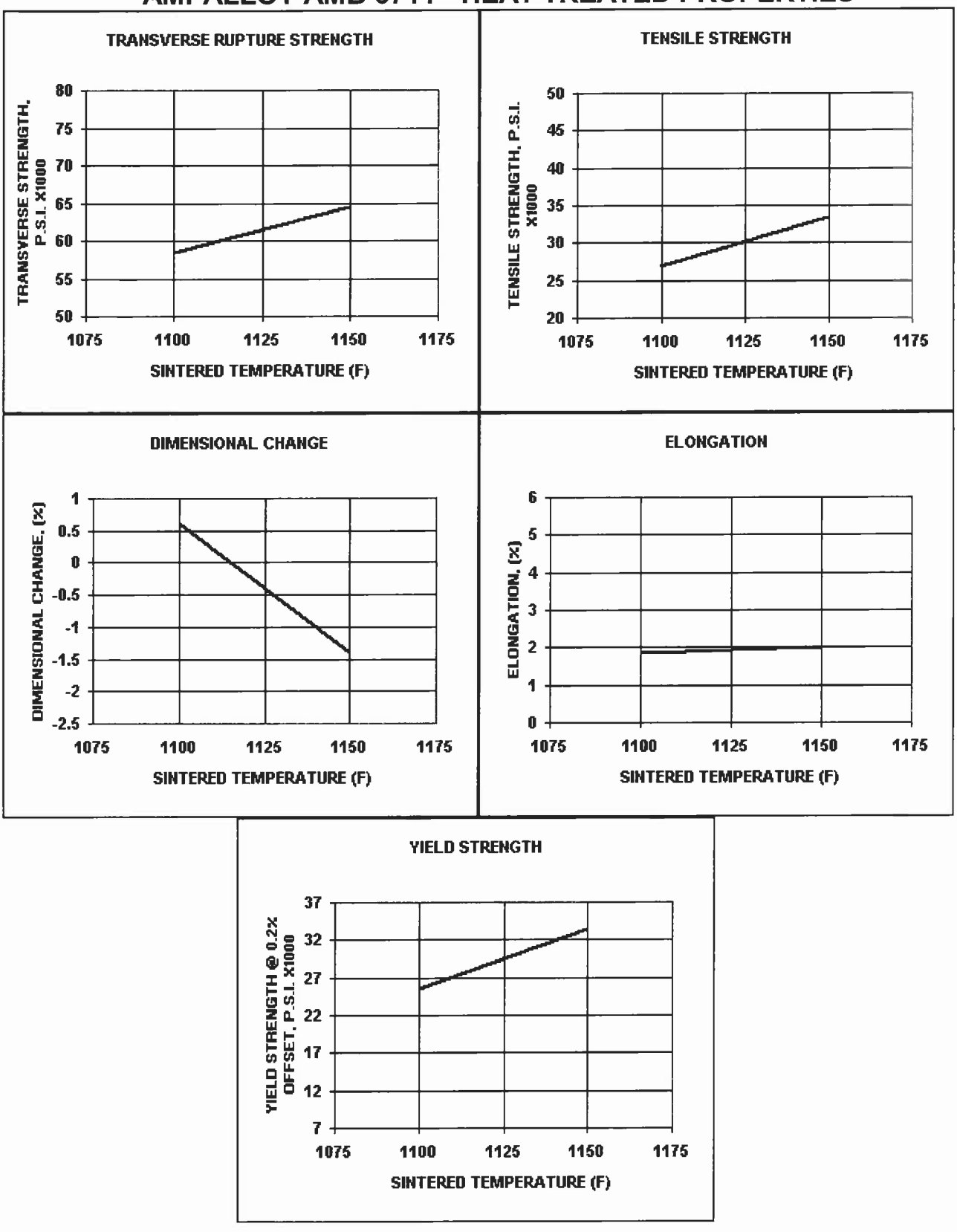

All graphical presentations of data represent average data produced at 10,20, and 30 TSI compacting pressures. Sintering temperatures are shown on each graph.

SOUTHERN CLAY PRODUCTS / A SUBSIDIARY OF ROCKWOOD SPECIALTIES, INC.

PRODUCT BULLETIN/Nanofil®

Southern Clay Products, Inc.
1212 Church Street
Gonzales, TX 78629
Phone: 800-324-2891
Fax: 830-672-1903
www.scprod.com

Nanofil® 116

Description:
Nanofil 116 is a natural montmorillonite.

Designed Used:
Nanofil 116 is an additive for plastics and rubber to improve various physical properties, such as reinforcement, CLTE, synergistic flame retardant and barrier.

Typical Properties:

Product Form:	Powder
Color:	Off White
Bulk Density:	340g/l
Median Particle Size:	12µm
Loss on Ignition:	8%
Moisture Content:	11%
Modifier Content:	none
Interlayer Spacing:	1.25nm
Modifier:	none
Cation Exchange Capacity:	116meq/100g clay

For additional information or technical assistance contact Southern Clay Products, Inc. toll free at 800-324-2891.

Southern Clay Products, Inc.
1212 Church Street
Gonzales, TX 78629
Phone: 800-324-2891
Fax: 830-672-1903
www.scprod.com

Cloisite® Ca^{++}DEV
Typical Physical Properties Bulletin

Description:
Cloisite® Ca^{++}DEV is a natural montmorillonite.

Designed Used:
Cloisite® Ca^{++}DEV is an additive for plastics to improve various plastic physical properties, such as reinforcement, HDT, CLTE and barrier.

Typical Properties:

Treatment/Properties:	Organic Modifier (1)	Modifier Concentration	% Moisture	% Weight Loss on Ignition
Cloisite® Ca^{++}DEV	None	None	<9%	7%

Typical Dry Particle Sizes: (microns, by volume)

10% less than:	50% less than:	90% less than:
2µm	10µm	25µm

Color: Off White

Density:

Loose Bulk, lbs/ft^3	Packed Bulk, lbs/ft^3	Density, g/cc
24.65	39.02	2.8

X Ray Results: d_{001} = 11.7Å

For additional information or technical assistance contact Southern Clay Products, Inc. toll free at 800-324-2891.